Holocene climate variability revealed using geochemistry and Computed Tomography scanning of stalagmites from the North Atlantic Basin

WALCZAK, IZABELA,WERONIKA

Holocene climate variability revealed using geochemistry and Computed Tomography scanning of stalagmites from the North Atlantic Basin

Izabela Weronika Walczak

This thesis is submitted in partial fulfilment of the requirements for the degree of Doctor of Philosophy

Department of Earth Sciences
Durham University

2016

Abstract

The reliable prediction of the future climate change requires high-quality densely distributed climate records that clarify natural climate variability and its recent modulation by anthropogenic impacts. Stalagmites can meet those requirements; however, conservation concerns require new non-destructive techniques to preserve the natural environment of the caves. This thesis discusses two high-resolution Holocene climate reconstructions built using i) geochemical analyses of a Bermudan stalagmite and ii) novel and non-destructive Computed Tomography data from a Spanish stalagmite, as well as iii) supporting cave monitoring data. Considered together, these efforts provide a complementary view of diverse aspects of climate change across the North Atlantic, and provide insights into how anthropogenic CO_2 emissions may further affect climate.

Monitoring of environmental conditions took place at Leamington Cave (Bermuda) and Conch Bar Caves (Turks and Caicos Islands). To our knowledge, these are the first long-term monitoring efforts at coastal sites near sea level. The results of continuous monitoring of these two near shore caves in the tropical western North Atlantic are not dissimilar to previous results derived from inland caves. The microclimate and ventilation dynamics of Leamington Cave and Conch Bar Caves are controlled mainly by seasonal temperature differences between outside and cave air, wind, and rainfall totals. However, because hydrological connections with the sea, the microclimate of these near shore caves is also modulated by the seawater temperature, and sea level fluctuations.

Following from the cave monitoring efforts, one stalagmite from Leamington Cave was collected. The $\delta^{18}O$ of stalagmite BER-SWI-13 provides an annually-resolved rainfall record for the last 700 years. The record suggests that the tropical cyclone activity in Bermuda following the Industrial Revolution has not exceeded its longer-term natural variability. Higher tropical cyclone activity during Bermuda's pre-colonisation period is associated with more El Niño events and positive NAO phase and reflects the northeast-ward tropical cyclone tracks migration that coincides with the low TC activity in the Caribbean Sea.

Finally, one stalagmite from southern Spain was used in a pilot study to assess the applicability of CT scanning to speleothem-based climate reconstruction. Internal density variability of stalagmite REF-07 (from Refugio Cave) was used to create a time-series record of stalagmite density, which was then linked to climate. The record reveals Holocene climate variability in southern Iberia, and suggests that the current Mediterranean climate in southern Iberia was initially emplaced at approximately 5.3 ka BP following gradual southward migration of the North Atlantic Subtropical High.

Table of Contents

List of figures

List of tables

List of appendices

Declaration and copyright

I declare that this thesis, which I submit for the degree of Doctor of Philosophy at Durham University is my own work and is not the same as any work that has previously been submitted at this or any other university for any degree, diploma or other qualification.

Izabela W. Walczak
Durham University
30th June 2016

Acknowledgements

First and foremost I would like to thank my supervisor *James Baldini* and *European Research Council* (grant number (240167) for supporting and funding my PhD project, field trips to Belize, Bermuda and Turks and Caicos, conference attendances (EGU 2013 in Vienna, Goldschmidt 2014 in Sacramento, KR 7 in Melbourne) that enabled me to pursue my academic and personal interests in caves, meet like-minded people and share my research results with fellow scientists. Also without my supervisor's unwavering support and encouragement, this thesis would not have been possible.

I would like to express my gratitude to all people directly engaged with the HURRICANE Project: *Colin Macpherson,* for making the stable isotope lab available for me to perform analysis of my samples; *Lisa Baldini*, for all her help with analysing Refugio Cave's and Bermuda stalagmites; *Brian Frappier*, for performing stable isotope analysis on over of my 3000 samples from Bermuda; *David Richards, Dan Nita* and *Chris Standish* for U-series dating of my stalagmites from Bermuda, Spain and Turks and Caicos Islands; *Franzi Lechleitner,* for teaching me how to perform radiocarbon dating; *Harriet Ridley*, for all your help and guidance with stalagmite milling and stable isotope analysis; *Alex Baker* and *Bob Jamieson* for all your support. Special thanks go to *Jo Peterkin* for training me in using the mass-spectrometer. I also extend my gratitude to all of my field assistants: *Harriet Ridley, Bob Jamieson, Franzi Lechleitner, Al Cook, Przemek Wolfram*, without whom all of my field trips to Belize, Bermuda and Turks and Caicos would be boring, harder and less fruitful.

Special thanks go to *Bermuda Aquarium*, *Gil Nolan* and *Robbie Smith* for allowing me to conduct my research in Bermuda, taking me caving and engaging me in all of the local events that made my time in Bermuda unforgettable.

I would also like to thank all the postgrad students and staff from the Durham University Earth Science Department that I met over the last four years, especially my departmental desk neighbours: *Bakey, Liz, Harriet, Claire, Josh* and *Erin* for all your support, shared fun, desk beers, cakes, plant jungle, and kindness.

Many thanks to all my Polish friends that I crossed paths with in Durham: *Sabina, Zuza, Dawid, Grzesiek, Aneta* and especially *Marek*. You guys always cheer me up and thanks to all our conversations over beer in every pub in Durham, I felt like I was back in Poland. I am also grateful to *Agnieszka Gajda* for her patience and all the help with ArcGIS. Many thanks to all my closest friends in Poland: *Magda, Prezes, Kasia, Olga, Jarek, Grzesiek*, for always being my friends regardless where I live and how far I am from Krakow. Dzięki!

Thanks to all my friends in DUSA: *Al, Zara, Pete, Alex BJ, Liv, Hugh, JC, Hannah and Ian, Jossie*, and many others, for all the caving trips, skiing, socials and shared fun.

I am also really grateful to *Áine O'Driscoll* and *Cillian Burke* for introducing me into the world of caving back in Ireland. Without you two, I would probably never got interested in caves, learnt SRT and did my caving-related PhD. Go raibh maith agat!

Finally, I would like to express my deepest gratitude to *Przemek* for your constant support regardless the situation and *Al* for being there for me during the last stages of my PhD.

Na sam koniec chciałabym podziękować mojej mamie i siostrze za cierpliwość i ciągłe wsparcie.

Chapter 1

Introduction and background

1.1. Thesis aims and overview

The study included in this thesis has been part of HURRICANE Project based at Durham University funded by European Research Council that aims to develop high-resolution Atlantic tropical cyclone activity records for at least 500 years using speleothems, significantly lengthening existing datasets. The records will be used to reconstruct TC trajectory shifts and to understand mechanisms controlling them. This thesis contributes to this project by providing the high-resolution climate reconstruction from Leamington Cave in Bermuda covering the last 700 years supported by continuous cave monitoring that confirmed the site suitability for this purpose. Also this thesis provides the results of the other near-shore cave monitoring in Turks and Caicos Islands, and the results of using a novel technique in paleoclimate reconstruction on the example of stalagmite from El Refugio Cave in Spain. The aim of this thesis is to increase the spatial coverage of Holocene palaeoclimate data from terrestrial archives in Caribbean and Mediterranean regions and to develop a novel non-destructive technique of obtaining proxy data.

This thesis consists of six chapters described briefly below:

- **Chapter 1** includes thesis rationale and gives general information about the available proxy and mechanisms controlling the climate in the North Atlantic Basin.
- **Chapter 2** provides the general information about four cave sites located in the North Atlantic basin that were studied in this thesis. The chapter also describes the sites' regional geology and present climate.

- **Chapter 3** shows the results of continuous cave monitoring of two near-shore tropical caves: Conch Bar Caves in Turks and Caicos Islands, and Leamington Cave in Bermuda.
- **Chapter 4** reveals the results of CT scanning the un-sectioned stalagmite from El Refugio Cave in Spain and uses the information about stalagmite density to decipher climate changes in western Mediterranean during the Holocene. The version of the chapter was published in a Special Issue of *Quaternary Science Reviews*, "Novel approaches to and new insights from speleothem-based climate reconstructions" edited by Corinne Wong and Daniel Breecker.
- **Chapter 5** presents the results of the longest available high-resolution geochemical analysis of a stalagmite from Leamington Cave, Bermuda using over 3000 data points that reveals the climate variability and related tropical cyclone activity in the North Atlantic since AD 1312 spanning the period of Little Ice Age and post-industrial period.
- **Chapter 6** is a synthesis of the work presented in this thesis, its implications, and a discussion of the future outlook and acts to draw together the implications of the three studies.

1.2. Thesis rationale

The most recent Intergovernmental Panel on Climate Change (IPCC) fourth assessment report states that human influence on the climate system is clear, and recent anthropogenic emissions of greenhouse gases are the highest in history. The report also says that recent climate changes, especially since the 1950s, have had widespread impacts on human and natural systems. Anthropogenic greenhouse gas

emissions have increased since the pre-industrial era, driven largely by economic and population growth that has led to atmospheric concentrations of carbon dioxide (CO_2), methane (CH_4) and nitrous oxide (N_2O) that are unprecedented in at least the last 800,000 years. Also since the 1950s, changes in many extreme weather and climate events have been observed, e.g. an increase in warm temperature events, an extreme in high sea levels, and an increase in the number of heavy precipitation events in a number of regions (IPCC, 2014).

Many climate projections (e.g. IPCC (2014), Knutson et al. (2010)), especially focusing on the future intensity, frequency and geographical distribution of tropical cyclones (TCs) are based on the instrumental data (e.g. the National Hurricane Centre's North Atlantic hurricane database known as HURDAT) collected since the industrial era (since ca. 1850). To make better future climate predictions, it is essential, though, to first understand the natural climate variability before the industrial era. This can be achieved by using the proxy data from well-dated archives, e.g. speleothems, corals, sediment cores, that can preserve the climate signal. Recently, the number of TC reconstructions in the North Atlantic basin is increasing; however mostly they are relatively low-resolution and based on sediment cores (e.g. Donnelly and Woodruff (2007) and Liu and Fearn (2000)), tree rings (e.g. Miller et al. (2006)) or corals (e.g. Hetzinger et al. (2008)). Thus, there is a need for more high-resolution accurately dated speleothem-based TC reconstructions in the North Atlantic basin that could extend instrumental and historical records; and aid in understanding the impact of climate change on the large-scale circulation of the North Atlantic.

The oxygen and carbon stable isotopes of ancient speleothems commonly used in climate reconstructions, are usually gleaned from a single plane cut through a sample and typically attempt to follow the stalagmite's growth axis in two dimensions. However, this approach ignores possible growth axis shifts that could occur out of this plane which in turn could dramatically affect climate interpretations, for example through off-axis stable isotope kinetic enrichment (Mickler et al., 2004b, Mickler et al., 2006). Hence, developing better techniques for extracting the climate signal from speleothems are necessary.

This thesis focuses on climate reconstructions using speleothems from the North Atlantic basin and developing a novel technique of extracting the climate signal using Computed Tomography (CT) scanning.

1.3. Speleothems as climate archives

Speleothems are one of the paleoclimate archives that can provide long, continuous, precisely U-series dated and high-resolution time series, unaffected by post-depositional diagenetic alternation. They are crystalline deposits of calcium carbonate ($CaCO_3$) formed in karstic caves. Speleothem precipitation is induced by degassing of CO_2 from percolating waters from overlying soil and bedrock surfaces. The external seasons can affect the quantity and chemistry of dripping water and may cause variation in CO_2 concentration of the cave atmosphere, sometimes associated with differing patterns of air circulation. This leads to seasonal variations in speleothem precipitation (Fairchild et al., 2006). The shape and diameter of speleothem depends on many factors, including water flow rate, water supersaturation, drop fall height (Fairchild et al., 2006). Those factors, that can be

linked to exterior climate, also control stalagmite petrography (Frisia, 2015) and density (more in Chapter 4).

Speleothems are widespread so their records have a direct relevance to regional climates and environments, and may also contribute to archaeological investigations. They contain several proxy parameters and many different techniques can be used to extract the climate signal, including the analysis of stable isotopes (especially oxygen and carbon), trace elements and petrography, making the speleothems a very reliable source of information about the past climates. There are some weaknesses to speleothem-based climate reconstructions that include insufficient understanding of the meaning of proxy variables, and frequently relying on only one proxy without presenting the data for others (Fairchild and Baker, 2012).

1.3.1. Stable isotope composition

The analyses of stable isotope composition are the most widely used in stalagmite-based palaeoclimate reconstructions. Usually oxygen (e.g. Kennett et al. (2012)) and carbon stable isotope ratios (e.g. Ridley et al. (2015a)) from stalagmites are interpreted as a climate proxy, however, recently, analyses of other stable isotope ratios are getting more recognition, e.g. calcium (Owen et al., 2016) and magnesium (Galy et al., 2002). In this thesis both oxygen and carbon stable isotopes are used to reconstruct past climate variability.

Speleothems made of $CaCO_3$ can isotopically exchange with water:

Eq. 1-1

$$^1/_3 CaC^{18}O_3 + H_2{}^{16}O \leftrightarrow {}^1/_3 CaC^{16}O_3 + H_2{}^{18}O$$

The ***oxygen stable isotope ratio*** ($\delta^{18}O$) is commonly measured in speleothems and interpreted as a rainfall proxy (Fensterer, 2011, Winter et al., 2011). Under equilibrium conditions, the $\delta^{18}O$ values of speleothem carbonate is related to the $\delta^{18}O$ value of drip water and the cave temperature through its control on equilibrium fractionation between water and calcite (Hendy, 1971). Fractionation occurs during the degassing of CO_2 in the cave air and speleothem precipitation. The $\delta^{18}O$ is calculated from the ratio of heavy (^{18}O) to light (^{16}O) oxygen isotopes of the sample (R_{sample}) relative to the standard ($R_{standard}$), as follows:

Eq. 1-2

$$\delta^{18}O = \left(\frac{R_{sample}}{R_{standard}} - 1\right) * 1000\ ‰$$

where the $R_{standard}$ for speleothems is Vienna Pee Dee Belemnite (VPDB).

Speleothems are deposits formed by precipitation from seepage water entering the roof or walls of the cave that ultimately reflects the $\delta^{18}O$ of meteoric waters and therefore can reflect the $\delta^{18}O$ of precipitation. The $\delta^{18}O$ of the rainfall, and hence the speleothem, varies due to fractionation occurring during phase change and diffusive exchange of isotopes between rain and vapour. Because $H_2{}^{18}O$ has lower saturation vapor pressures than $H_2{}^{16}O$, stable isotope ratios are lower in vapour than in the parent water. This difference is expressed by a fractionation factor α_{eq}, where $\alpha_{eq} = \frac{R_{liquid}}{R_{vapor}}$, where R is a isotope ratio. Under the conditions of isotopic equilibrium at 25^0C, the $\delta^{18}O$ values of the vapour phase are 10‰ lower than that of a liquid phase (Majzoub, 1971). Therefore during the condensation, heavy isotopes are concentrated in the condensate, and isotope ratios in vapor are decreased. When raindrops fall, their isotope ratio is not in equilibrium with the surrounding vapor,

and diffusive isotope exchange takes place. Because heavy isotopes diffuse to the condensate preferentially and falling raindrops encounter isotopically richer vapor near the ground, the isotope ratio of rain increases as it falls and reaches the ground with much higher isotope ratios then when it formed at the cloud base (Miyake et al., 1968). This exchange process also lowers the isotope ratio of the ambient vapor near the ground with time, which in turn leads to a temporal decrease of isotope ratios of rain during a storm.

Dansgaard (1964) described general effects that appeared to result in gradual $\delta^{18}O$ decrease of meteoric precipitation: (1) towards higher latitudes (***latitude effect***), (2) with increasing altitude related to the decrease in saturation vapour pressure with altitude (***altitude effect***), (3) with increasing distance from the coast (***continental effect***), (4) with increasing amount of rainfall (***amount effect***), and (5) with temperature increase in the tropics (Vuille et al., 2003) and decrease in mid-latitudes (***temperature effect***). Some studies suggested that in the tropics $\delta^{18}O$ depends significantly on the precipitation amount, whereas the isotope ratios of meteoric waters only exhibit a weak correlation with surface air temperature (Vuille et al., 2003). This relationship is based on monthly composite samples, such as those recorded in the Global Network of Isotopes in Precipitation (GNIP). Despite of strong negative correlation between monthly $\delta^{18}O$ and precipitation, the role of precipitation amount in daily-scale isotope variability in the tropical regions like Central America is minor (Sánchez-Murillo et al., 2016). Moreover the shift from air temperature to precipitation amount controlling oxygen stable isotopic ratios is generally noted around 30^{o}N/S (Bowen, 2008) which might affect the $\delta^{18}O$ signal in regions like Bermuda (32^{o}N).

Many studies (Frappier et al., 2007, Haig et al., 2014, Malmquist, 1997) reveal stalagmites are capable of recording TC precipitation. However, according to the principles of stable isotope meteorology described above, a particular location might not be sensitive to all tropical cyclones that passed the site. TCs are distinguished from normal tropical weather not only by their strong winds and intense rainfall but also by the anomalously low $\delta^{18}O$ contents of their rains that reach the surface, being a result of the amount effect (Lawrence and Gedzelman, 1996). The TCs rainfall is depleted in ^{18}O by over 6‰ relative to average monsoonal precipitation, owing to the recycling of water within the system, high condensation efficiency and large size and longevity of such cyclones as intense convective systems (Lawrence et al., 1998).

The $\delta^{18}O$ during tropical cyclone event not only varies with time but also varies spatially within the cyclone system. Stable isotope analysis of rain and water vapor samples collected during flights in Hurricane Olivia (1994), Opal (1995), Marilyn (1995) and Hortense (1995) revealed that at all flight levels over the sea (850-475 hPa) the lowest $\delta^{18}O$ occurred in or near regions of stratiform (formed along the fronts) rains between about 50 and 250 km from the eye. However, in the eyewall isotope ratios increased, where evaporation and isotope equilibrium of sea spray supplies the eyewall with up to 50% of its water vapor (Gedzelman et al., 2003).

The ***stable carbon isotope ratios*** ($\delta^{13}C$) are another measure commonly analysed in speleothems along with the $\delta^{18}O$ values, however they are often unreported due to their ambiguity in interpretation. Factors affecting speleothem $\delta^{13}C$ depends on the sources of carbon that include: 1) atmospheric CO_2, 2) the relative proportions of C_3 and C_4 vegetation above caves (Dorale, 1998), 3) the soil/vegetation productivity

affected by temperature and precipitation (Genty et al., 2006), 4) carbon isotope fractionation during decomposition of soil organic matter (Baker et al., 2011), 5) the proportion of host rock carbon (Fairchild et al., 2006), 6) in-cave kinetic effects (Mickler et al., 2004a, Mattey et al., 2010) and 7) cave air pCO_2 changes and thus the ventilation efficiency (Boch et al., 2011, Mattey et al., 2010). Despite of this, they tend to be interpreted as an archive of vegetation changes above the cave (Dorale, 1998) because of small fractionation between HCO_3^- and $CaCO_3$ during the $CaCO_3$ precipitation. Thus the variability of $\delta^{13}C$ comes from the fact that carbon isotope compositions in speleothem are derived from CO_2 dissolved in the drip water, and the fact that soil CO_2 is produced by plant respiration and organic matter decomposition. The $\delta^{13}C$ values are thus higher where C_4 vegetation dominates in the soil. In the locations where the past vegetation is not affected by anthropogenic activity and/or is not experiencing temporal shifts in vegetation type (e.g. from C_4 to C_3), the $\delta^{13}C$ is sensitive to climate changes through alternating the ecosystem's carbon budget (Frappier et al., 2002, Ridley et al., 2015a). The density of vegetation above the cave also controls the $\delta^{13}C$, as in the absence of soil cover, the dissolution of limestone occurs by reaction with atmospheric CO_2, leading to higher $\delta^{13}C$ values of DIC in recharge water compared to that produced under C_3- and C_4-based soils (Frumkin et al., 2000). More information about formation of $\delta^{13}C$ in speleothems in open and closed system can be found in Dulinski and Rozanski (1990).

1.3.2. Stalagmite density

X-ray computed tomography (CT scanning) is a non-destructive technique commonly applied in medicine, and recently also in geosciences (Carlson et al., 2003, Ketcham and Carlson, 2001, Mees et al., 2003). CT images (termed slices) are

created by directing a planar fan beam at an object from multiply angular orientations. They correspond to what would be observed if the object were cut open along the image plane. The greyscale in CT images correspond to relative X-ray attenuation, which is a function of elemental composition and density. A series of continuous slices for an object allows for a complete three-dimensional volume projection (Mickler et al., 2004b). More information about different types of CT scanners can be found in Ketcham and Carlson (2001).

The interpretation of the obtained CT images can be complicated by various artifacts like beam hardening, ring artifacts, or streaks traversing the longest axes of the object. Beam hardening is the most frequently encountered artefact which causes the edges of an object to appear brighter than the centre. The simplest remedy for that would be to use a high energetic X-ray beam to ensure that beam hardening is negligible. However, most geological materials are attenuating enough that beam hardening is noticeable, unless the sample is quite small (Ketcham and Carlson, 2001).

CT scanning, through internal three-dimensional density mapping of opaque objects, is able to provide information about stalagmite growth axis shifts (Mickler et al., 2004b) and internal porosity (Zisu et al., 2012). Moreover, CT scanning provides rapidly acquired quantitative information about stalagmite density, a variable that until now could be obtained at low spatial resolution only through calculations based on the mass of cut stalagmite blocks (Zhang et al., 2010). Despite numerous studies using CT scanning to derive quantitative density data from sediment cores (Tanaka

et al., 2011, Wirth et al., 2013, Mees et al., 2003), the technique has not previously been used to derive time-series data from stalagmites.

The relationship between stalagmite density and environmental factors such as meteoric precipitation, temperature, soil, and vegetation above a cave, is complex. These factors directly control water flow dynamics, and consequently drip-water saturation state (with respect to calcium carbonate) that is the predominant determinant of stalagmite density (Zhang et al., 2010, Dreybrodt, 2008, Frisia et al., 2000). In addition, cave ventilation regimes also complicate it by affecting the intensity of CO_2 degassing from drip-water entering a cave (Boch et al., 2011, Mattey et al., 2010). However, because environmental change during stalagmite growth drives calcite density variability, stalagmite calcite density is interpretable in terms of climate (Zhang et al., 2010). In a study of the East Asian Monsoon, Zhang et al. (2010) demonstrated that rainfall amounts (inferred from stalagmite $\delta^{18}O$) and calcite density variations (derived by conventional non-CT scanning methods) were positively correlated, which is also consistent with studies of calcite textures (Frisia et al., 2000, Frisia, 2015). By calculating stalagmite density from the measured mass of stalagmite blocks cut every 5 mm, Zhang et al. (2010) achieved a resolution of 87 years. CT scanning therefore offers a novel means to produce comparable density data quickly and non-destructively, and at a considerably higher spatiotemporal resolution than is achievable using conventional density measurements.

1.3.3. Other proxies

Many other proxies are available from stalagmite archives including trace elements (Boch et al. (2011), Ortega et al. (2005)) and petrography (e.g. Frisia (2015))

analysis. Among these, trace elements are probably the most commonly used and usually interpreted as climate proxy (Huang et al., 2001) and/or reflection of ***prior calcite precipitation*** (PCP), that is a consequence of water degassing into air spaces before the drip reaches the cave. Because the trace elements were not measured as a part of this study, there are not discussed further here.

1.4. Climate controls in the North Atlantic Basin

The climate of the North Atlantic Basin is influenced by many atmospheric processes including oscillations like the Atlantic Multidecadal Oscillation, the North Atlantic Oscillation, the El Niño–Southern Oscillation, and natural global wind distributions e.g. the ***Intertropical Convergence Zone*** (ITCZ) where trade winds converge near the Equator and Westerlies, prevailing winds from the west toward the east in the mid-latitudes. The Atlantic Ocean has been suggested as an important driver of climate variability both in western Europe and North America on multidecadal timescales, probably related to thermohaline circulation (Sutton and Hodson, 2005, Knight et al., 2006, Goldenberg et al., 2001).

The ***Atlantic Multidecadal Oscillation*** (AMO) index is defined as the average sea surface temperature (SSTs) in the region from 0^0 to 60^0N, 80^0W to 0^0, detrended to isolate the natural variability. The index values calculated based on the observed data since AD 1856 are provided by National Oceanic and Atmospheric Administration (NOAA) (Bender et al., 2010). During the instrumental record, the AMO exhibits a 65-80 year cycle with a 0.4^0C SSTs range. The warm phases of AMO occurred during 1860-1880 and 1940-1960, and cool phases during 1905-1925 and 1970-1990 (Bender et al., 2010). A tree-ring based AMO reconstruction extends this record to

AD 1567 (Gray et al., 2004). Studies show that the primary source of this multidecadal AMO variability is the changes in the strength of the thermohaline circulation. The correlations between temperature based indices during the period 1961-2010 and AMO suggest that temperature variability and, to a lesser extent, precipitation extremes are related to the AMO signal of the North Atlantic SSTs (Stephenson et al., 2014).

The ***North Atlantic Oscillation*** (NAO) is one of the most prominent and recurrent patterns of seasonal and interdecadal atmospheric circulation variability associated with changes in the surface westerlies across the North Atlantic to Europe (McCloskey et al., 2013, Hurrell, 1995). The NAO phase is calculated based on the surface pressure data between Iceland Low and ***North Atlantic Subtropical High*** (NASH). The resulting index is a measure of the strength of the westerly flow and is also an indicator for winter climate in Europe (Wanner et al., 2001). Positive NAO phase (intensified NASH and deeper Iceland Low) is associated with strong westerlies that lead to unsteady weather conditions over Western and Central Europe, characterized by succession of low pressure centres and warmer and wetter conditions over Northern Europe and dryer conditions over Southern Europe. During the negative NAO phase (weak NASH and shallower Iceland Low) meridional pressure gradient is reduced, hence weaker westerlies over the North Atlantic and Western Europe lead to unsteady weather and wetter conditions in Southern Europe, and dryer and colder conditions over Northern Europe, typically associated with a blocking (stationary high) situation extending from Eastern to Western/Central Europe (Pinto and Raible, 2012). Many studies show that NAO phase also affects tropical cyclones track (Elsner et al., 2000) and vegetation activity in the following

spring and summer seasons (Gouveia et al., 2008). The NOAA provides monthly mean NAO index since January 1950. In general the decades between 1950 and 1970 were characterised by negative NAO index (weaker NASH) unlike the decades between 1970 and 1994. Many NAO reconstructions exist extending the instrumental record to mid-Holocene (e.g. Trouet et al. (2009), Baker et al. (2015), Olsen et al. (2012), Ortega et al. (2005).

The ***El Niño–Southern Oscillation*** (ENSO) is one of the largest drivers of interannual variability in a present-day global climate. It is a climate phenomenon on the timescale of two to seven years (Collins et al., 2010), consisting of two, warm (El Niño) and cold (La Niña), phases related to SSTs anomalies in the tropical Pacific. The El Niño event is associated with positive SSTs anomalies in the central and east-central equatorial Pacific that weakens the Walker circulation and shifts it eastward. This leads to weaker trade winds that would normally push the warm water westward, so consequently, waters in the central and eastern Pacific heat up and the thermocline tilt diminishes preventing upwelling. This results in stronger upper-level westerlies winds over the Caribbean. Many studies show that ENSO affects rainfall in the Caribbean and North Atlantic region (Giannini et al., 2001, Jury et al., 2007, Klotzbach, 2011b, Rodrigues and McPhaden, 2014) and seasonal levels of Atlantic basic TC activity (Klotzbach, 2011b, Klotzbach, 2011a) but also the strength of the monsoons in east Asia (e.g. Rodysill et al. (2013)) and coral mortality (Yu et al., 2012). NOAA provides historical ENSO record only since AD 1950, but a variety of proxies have been used to reconstruct ENSO variability during the Holocene (e.g. Li et al. (2013), Cobb et al. (2003), Moy et al. (2002), McGregor et al. (2013)) indicating that the most intense ENSO activity during the last millennium occurred

during the mid-seventeenth century. Despite considerable progress in understanding the impact of climate change on many processes that contribute to ENSO activity, the future ENSO variability is unclear (Collins et al., 2010).

Most of the instrumental records of the climate variables and oscillations mentioned above that are incorporated in future climate projections, started less than two centuries ago. Also since AD 1850, the concentrations of naturally occurring greenhouse gasses (GHG) like carbon dioxide (CO_2), methane (CH_4) and nitrous oxide (N_2O) have increased substantially and are attributed to human activities since the Industrial Revolution. The increased GHG are responsible for climate and ocean warming, diminishing of amounts of snow and ice, and sea level rise (IPCC, 2014). Understanding the past climate changes before the Industrial Revolution, that would reflect natural climate variability, is essential in the future climate changes predictions. The low-lying Caribbean area and North Atlantic islands are particularly sensitive to observed global warming, according to the IPCC 2014 report, because it increases not only air and sea surface temperature but also can change the precipitation amount and increase the frequency of extreme events and result in sea level rise (Table 1.1). This could pose a threat to the survival of mangroves in Bermuda, as they are unable to tolerate increased water depth at the seaward margin (Ellison, 1996).

Table 1.1. Potential impacts of climate changes in the Caribbean area.

Potential climate change impact	Effects
Temperature increase	• Loss of terrestrial and marine species • Reduced fish stocks • Human health impacts including heat stress and increased vector borne disease
Increased extreme events	• Damage to physical infrastructure and natural assets such as coral reefs and vegetation
Increased sea surface temperature	• Coral bleaching • Ocean acidification • Movement of marine species away from traditional habitats
Sea level rise	• Erosion of coastal areas including beaches, wetlands and coastal settlements • Saline intrusion
Changes in precipitation	• Freshwater shortages and drought • Changes in water quality • Human health impacts increased vector borne disease

Source: Turks and Caicos Islands Climate Change Policy

Chapter 2

Cave study sites in the North Atlantic Basin

2.1. Introduction

This thesis presents research based on four different cave sites located within the North Atlantic Basin: (1) El Refugio Cave, Spain, (2) Leamington Cave, Bermuda, (3) Conch Bar Caves, Turks and Caicos Islands and (4) Yok Balum Cave, Belize. The first site is located on the northeast side of the NASH system (also known as Azores High or Bermuda High), where air subsidence produces stable conditions and aridity. The latter three sites are situated on the western and southwestern flank of the NASH, where air convergence and uplifting promotes instability. As a result those regions experience different climates according to the Köppen-Geiger classification (Peel et al., 2007) (Figure 2.1).

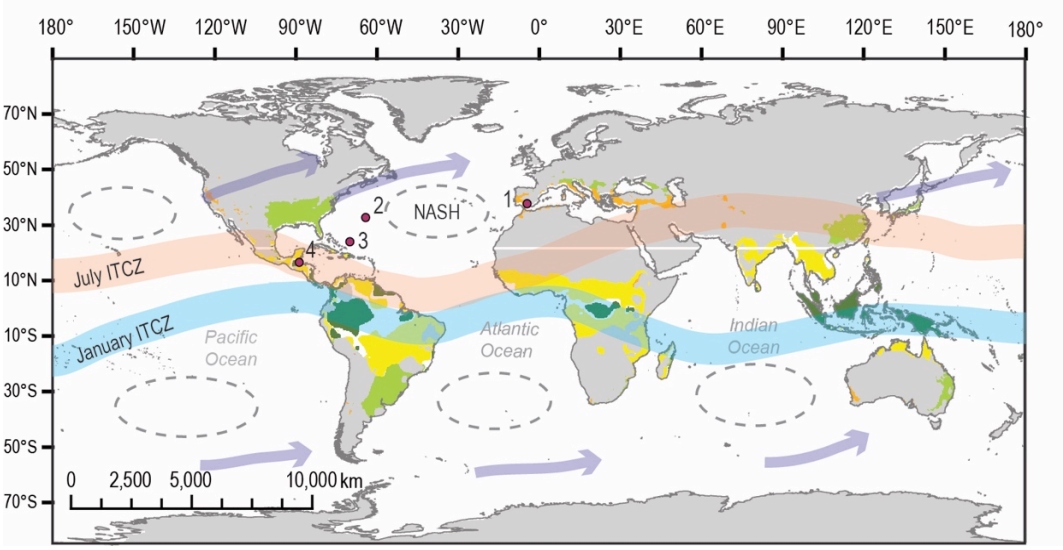

Figure 2.1. The study sites location in the global context: (1) Refugio Cave, Spain; (2) Leamington Cave, Bermuda, (3) Conch Bar Caves, Turks and Caicos Island and (4) Yok Balum Cave, Belize. The distribution of the climate types characteristic to the studied sites are based on the Köppen-Geiger classification (Peel et al., 2007): orange – temperate climate with dry and hot summer (Csa; Mediterranean); light green – temperate climate without dry season with hot summer (Cfa); yellow – tropical savannah (Aw); dark green – tropical rainforest (Af). July and January location of ITCZ marked as orange and blue stripes,

respectively. Subtropical highs, including NASH marked as grey dashed ovals. Westerlies marked as dark blue arrows.

All sites are influenced to certain extent by NASH intensity (as measured by NAO index) and displacement. Refugio Cave and Leamington Cave sites are also sensitive to westerlies migration, whereas Conch Bar Caves and Yok Balum cave are more affected by the ITCZ position shifts (Figure 2.1).

All the study sites can be defined as relatively warm caves with mean air temperature above 18^{o}C. Leamington Cave and Conch Bar Caves are located near sea level and formed in the relatively young and immature Pleistocene limestone, whereas El Refugio Cave and Yok Balum Cave are situated at higher elevation and formed in much older limestone of Mesozoic age (Table 2.1).

Table 2.1. The cave sites characteristics and the study summary.

	El Refugio Cave, Spain	**Leamington Cave, Bermuda**	**Conch Bar Caves, Turks and Caicos**	**Yok Balum Cave, Belize**
Location	36^{o} 35' N, 4^{o}35 'W	32^{o} 20' N, 64^{o} 42' W	21^{o} 49' N, 71^{o} 47' W	16^{o} 12' N, 89^{o} 4' W
Altitude (a.s.l)	690 m	18 m	13 m	366 m
Bedrock	Dolomitic marble (Triassic)	Eolianite limestone (Pleistocene)	Oolitic limestone (Pleistocene)	Limestone (Cretaceous)
Vegetation	Shrubs	Forest and shrubs	scarse	Tropical rainforest
Sea connection	no	yes	yes	no
Current climate[1]	Mediterranean (Csa)	humid subtropical (Cfa)	tropical savannah (Aw)	tropical rainforest (Af)
Tcave[2]**/Tair**[3] **(**^{o}**C)**	18.5 [3]	22.5 [2]	24.6 [2]	22.8 [3]
Mean total precipitation (mm)[3]	534	1410	604	3000
Cave monitoring period	2003 – 2006 [6]	12/ 03/ 2013 – 10/ 12/ 2015 (32 months)	19/ 04/ 2011 – 3/ 03/ 2013 (23 months)	2011 - present [4]
Collected stalagmites	REF-07	BER-SWI-13, BER-STO-13	TC-EMP-12	YOK-K, YOK-L [5]
Techniques used	CT scanning U-series dating	CT scanning Stable isotope analysis U-series dating ^{14}C dating	CT scanning Stable isotope analysis U-series dating	CT scanning U-series dating
Climate reconstruction period	2.975-9.239 ka BP	0.500 ka BP - present	n/a	n/a [5]

[1] climate type based on Köppen-Geiger classification (Peel et al., 2007).

[2] based on the cave monitoring results discussed later in this thesis.
[3] based on the data published from the nearest weather station discussed later in this thesis.
[4] the cave monitoring results between April 2011 and June 2013 are published in Ridley et al. (2015b).
[5] other stalagmites (YOK-G, YOK-I) were collected from Yok Balum cave and climate reconstructions based on them are published in Ridley et al. (2015a) and Kennett et al. (2012) respectively.
[6] the cave monitoring results published in Mudarra et al. (2009).

2.2. El Refugio Cave, Spain

El Refugio Cave is located near the western boundary of the Sierra de Mijas mountain range, five km from the Mediterranean coast in Andalusia, Spain (Figure 2.2). El Refugio Cave was discovered in 1997 and surveyed in 2002 (Mainake, 2002) (Figure 2.3). The cave comprises approximately 65 m of passages with the first nine meters separated from the cave interior by a three meter high flowstone deposit that impedes air circulation to inner chambers (Figure 2.3). El Refugio Cave monitoring between 2003 and 2006 reveals a small degree of seasonal cave air exchange (mean seasonal cave air pCO_2 variance less than 1000 ppm) with increased ventilation and low pCO_2 concentrations in the winter (Mudarra et al., 2009).

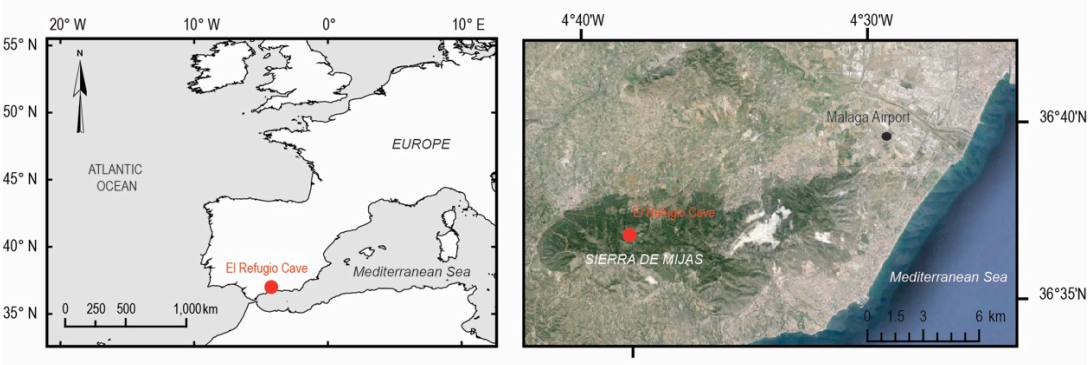

Figure 2.2. Location of Refugio Cave in Europe (left) and in relation to Malaga Airport (right).

2.2.1. Regional geology

The Sierra de Mijas are mainly built of a 300 m thick Triassic white dolomitic marble unit (Andreo et al., 1998) and principally formed by ESE-WNW folds. The

area lies close to the present-day convergence zone between the Eurasian and African Plates that is characterised by moderate magnitude seismic activity (Gràcia et al., 2010). Most of the caves in the Sierra de Mijas are small cavities with subvertical development (Andreo et al., 1998).

2.2.1. Regional climate

At present, the regional climate is Mediterranean-type (Csa) (Peel et al., 2007) (Figure 2.1), and is strongly seasonal, with hot-dry summers and cool-wet winters (October-April). At the meteorological station at Malaga Airport (5 m.a.s.l., 14 km from El Refugio Cave) annual mean air temperature during the period 1981-2010 was 18.5°C, and winter (October-April) precipitation represented 90% of the mean annual precipitation of 534 mm (Agencia Estatal de Meteorología (AEMET)). The isotopic content of rainwater and groundwater reflects a mixed Atlantic and Mediterranean origin (Andreo et al., 2004).

The vegetation above the Refugio Cave comprises mainly Mediterranean shrubs (Figure 2.4).

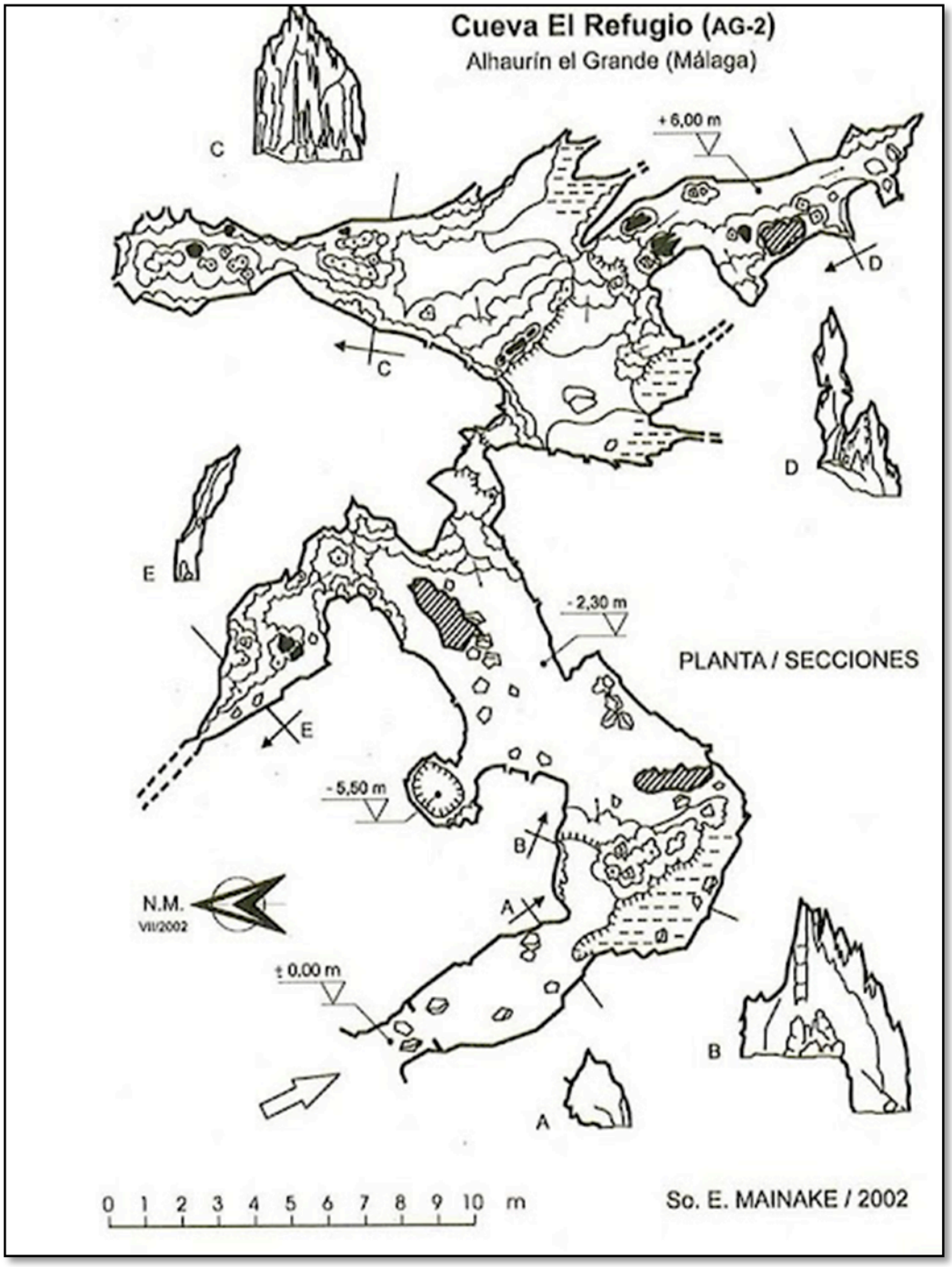

Figure 2.3. El Refugio cave survey (Mainake, 2002).

Figure 2.4. Typical vegetation cover in the Sierra de Mijas mountains, where El Refugio Cave is located (photo: Lisa Baldini).

2.3. Leamington Cave, Bermuda

Leamington Cave (32°20'N, 64°42'W, entrance at 18 m a.s.l.), located in Hamilton Parish, NE Bermuda (Figure 2.5), was chosen as a study site due to its abundance of active speleothems (Figure 2.6 and Figure 2.7), limited access by a public and close proximity to the Bermuda International Airport, where meteorological observations are taken by the Bermuda Weather Service. The cave, formed in the oldest eolianite limestone, the Walsingham Formation, was discovered in AD 1914 and was open to the public until 1990s (personal communication, Gil Nolan). Since then the access to the cave is gained only after obtaining a permit from the landlord. The cave is connected with the ocean via Harrington Sound (Figure 2.7). The vegetation above

the cave comprises mainly trees and bushes (Figure 2.8). There is also little underground freshwater, so the residents depend on capturing rainfall on roofs for their water supply.

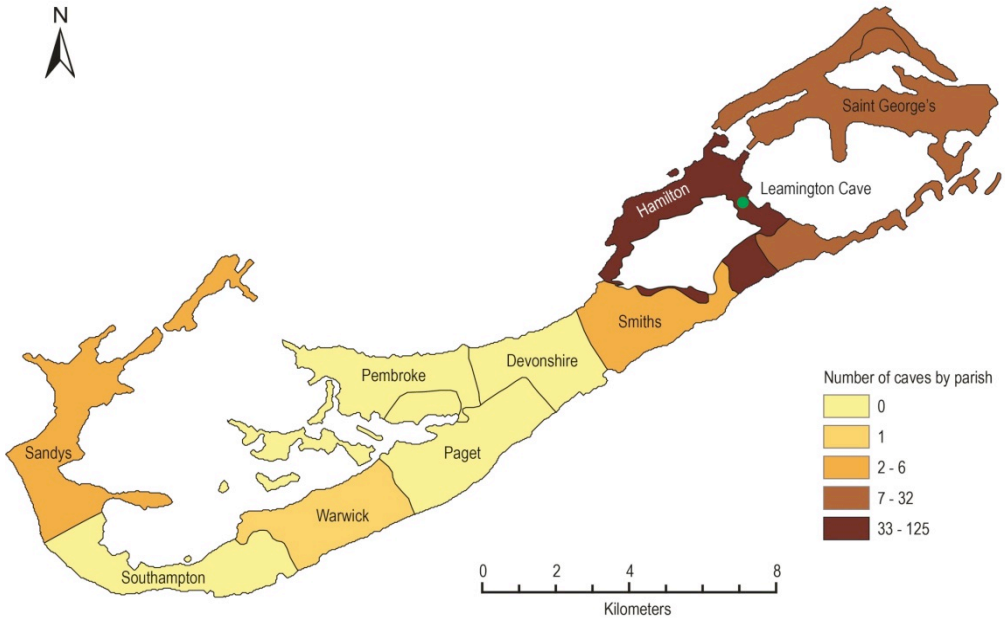

Figure 2.5. Number of caves by parish. Adapted from Illiffe (2003).

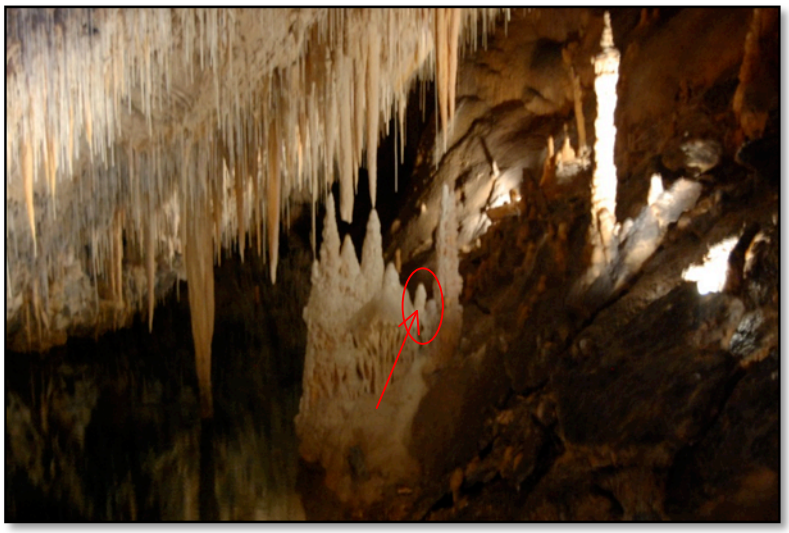

Figure 2.6. Stalagmite BER-SWI-13 (red arrow) in Leamington Cave before collection.

Figure 2.7. An abundance of soda straws and stalactites hanging over the pool connecting Leamington Cave with the sea.

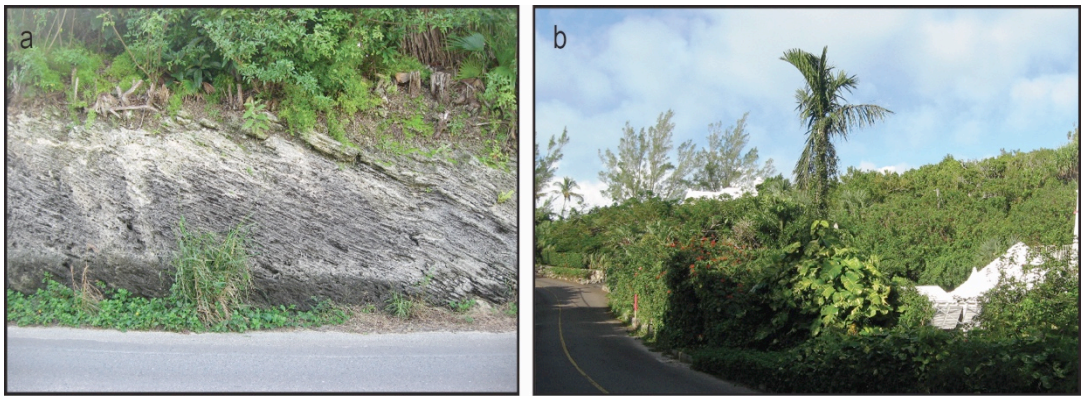

Figure 2.8. The area near the Leamington Cave: (a) an outcrop of the Walsingham formation and (b) vegetation cover.

2.3.1. Regional geology

Bermuda is a group of islands located at the western margin of the Sargasso Sea in the North Atlantic Ocean covering an area of roughly 55 km^2 (Figure 2.9a). The islands have a volcanic basalt core capped by alternating marine and eolian limestones (eolianites) developed during late Quaternary sea level fluctuations (Figure 2.10). Bermuda comprises six eolianite limestone formations (Figure 2.10).

The oldest and most compact unit, the Walsingham Formation (Figure 2.8a), hosts the highest number of discovered caves (Illiffe, 2009). Most of Bermuda caves began forming during Pleistocene glacial periods, when the Bermuda platform was exposed due to a lower sea level, allowing rainwater to percolate through the porous dunes and marine limestone (Figure 2.10). With a warmer climate and associated sea level rise, the platform was drowned (Figure 2.10b) allowing many sediment-producing organisms to thrive resulting in marine limestone deposition. Existing caves were drowned, but newer ones formed in the harder, cemented eolian limestone of the former dunes.

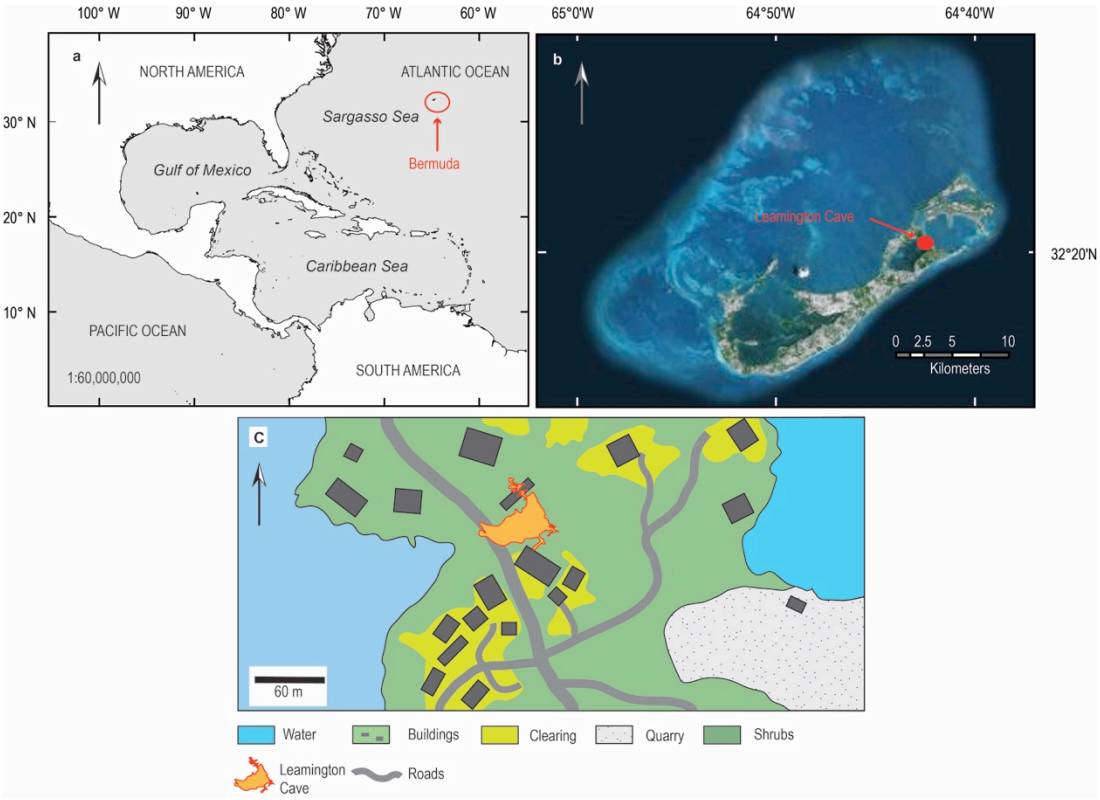

Figure 2.9. The location of a) Bermuda, b) Leamington Cave in Bermuda, and c) a schematic illustrating the environment above the Leamington Cave.

In present day Bermuda the surface alignment of joints is either a NE/SW trend or a NW/SE trend. Most caves in Bermuda show a similar trend in their alignment. The

Bermuda island platform is tectonically stable, and is therefore considered a benchmark for global sea level changes during the Pleistocene (Rowe et al., 2014).

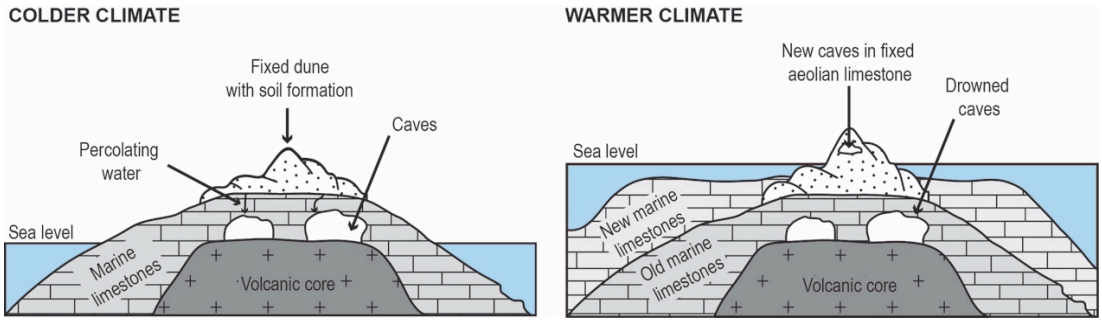

Figure 2.10. Bermuda during sea level lowstands (colder climate) and sea level highstands (warmer climate). Source: Chandler (2006a). Adapted by Izabela Walczak.

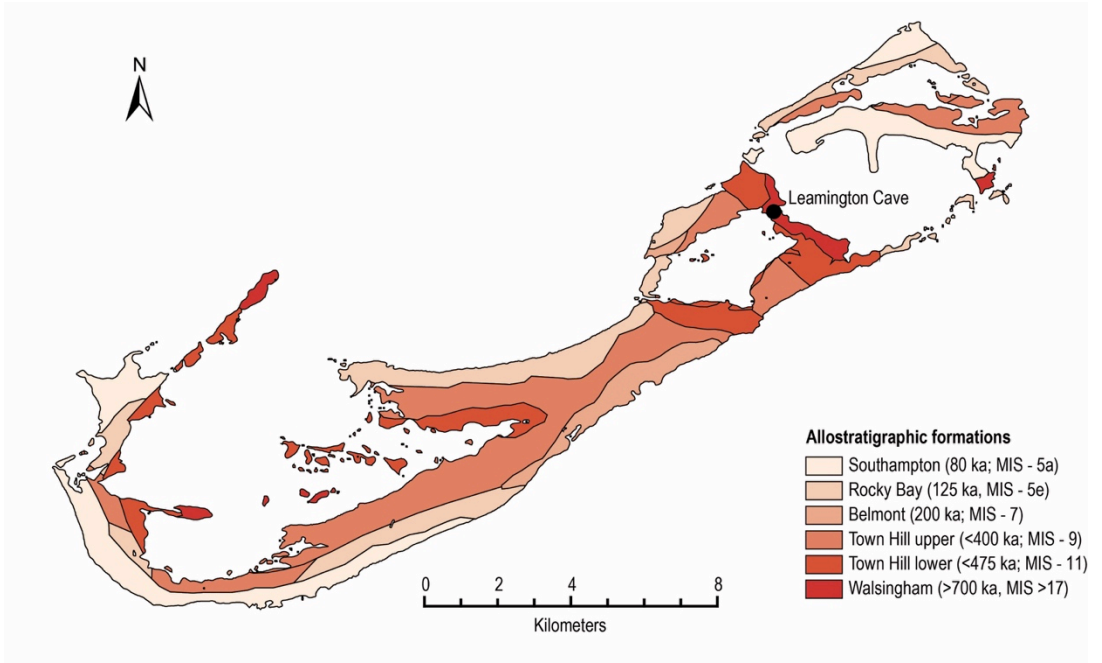

Figure 2.11. The simplified geological map of Bermuda (Chandler, 2006b). Age of eolianite formations after Rowe and Bristow (2015). Adapted by Izabela Walczak.

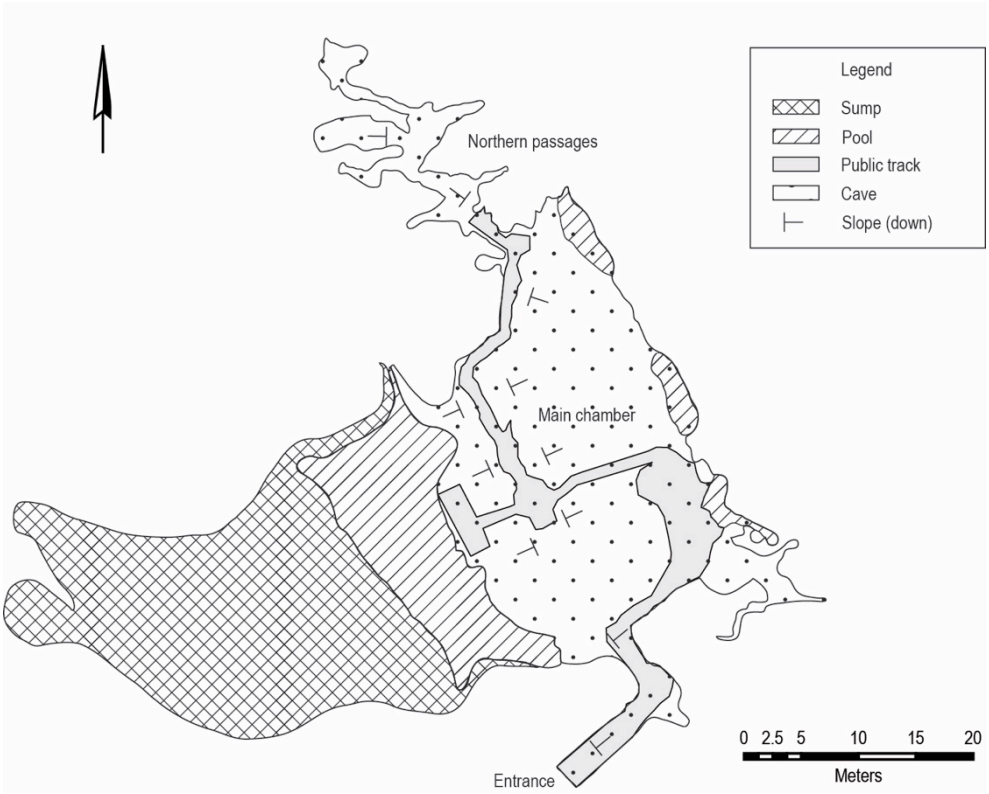

Figure 2.12. Leamington Cave plan. Survey by members of the Bermuda Cave Diving Association.

2.3.2. Present climate and hydrology

At present the archipelago experiences a subtropical climate (Cfa in Köppen-Geiger classification (Peel et al., 2007)) with evenly distributed precipitation throughout the seasons and hot summers, and lies within a hurricane (tropical cyclone) belt. The hurricane season in Bermuda officially runs from June to November. Apart from tropical cyclones, Bermuda also frequently experiences subtropical and extratropical cyclone activity (Guishard et al., 2007). The meteorological data recorded at the Bermuda International Airport from 1949 to 1999 (The Bermuda Weather Service, 2000) indicates that mean annual air temperature (T_{out}) was 22^{o}C ranging from 17.7^{o}C in February to 27.2^{o}C in August (Figure 2.13a) and mean annual precipitation sum (PP) was 1410 mm. The precipitation sum during the hurricane season accounts for ~55% of total annual rainfall in Bermuda (based on the period between 1949-

1999, The Bermuda Weather Service (2000)). The driest months are April and May (mean monthly PP ~ 86 mm) and wettest is October (mean monthly precipitation total ~161 mm) (Figure 2.13a**).** During the last 65 years, the highest (1916 mm) and lowest (943 mm) annual precipitation totals were recorded in 1962 and 1975, respectively. No tropical storm affected Bermuda in 1962, and therefore the high rainfall total in that year reflects another phenomenon. Most of the year, winds prevail from the SW and SSW, except for September and October when they prevail from east (Figure 2.14). The mean annual SSTs between 1949 and 1999 was 22.8^{o}C ranging from 18.4^{o}C (March) to 28.2^{o}C (August).

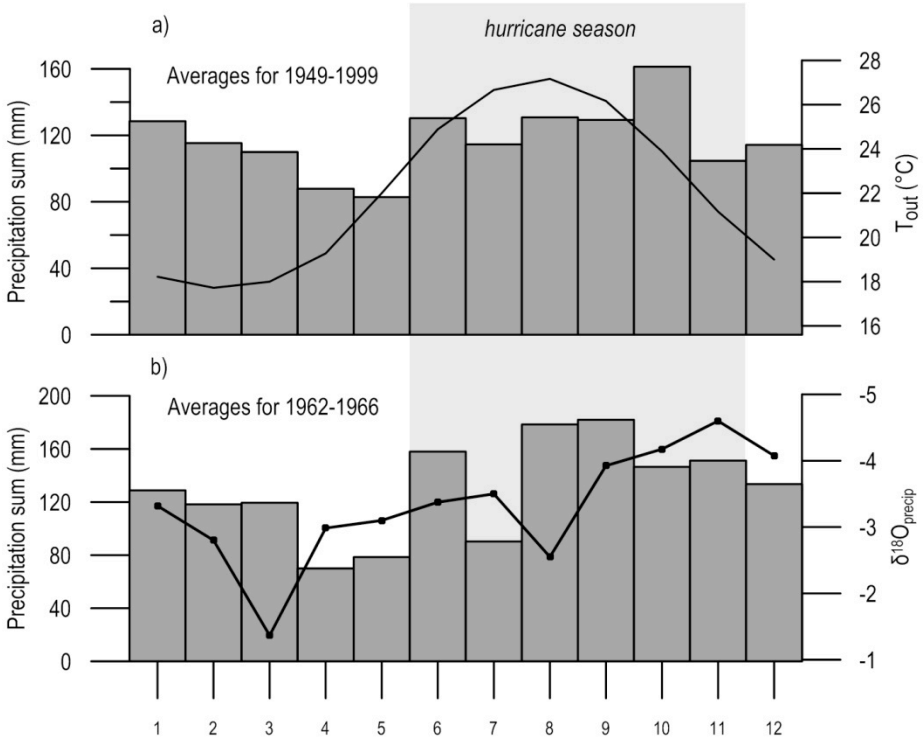

Figure 2.13. Bermuda climatology: a) The mean monthly precipitation sum (bars) and the air temperature (line) from 1949 to 1999 observed at Bermuda International Airport; b) mean monthly precipitation totals and $\delta^{18}O_{rainfall}$ (‰, SMOW) observed in Bermuda from 1962 to 1966 (source: GNIP).

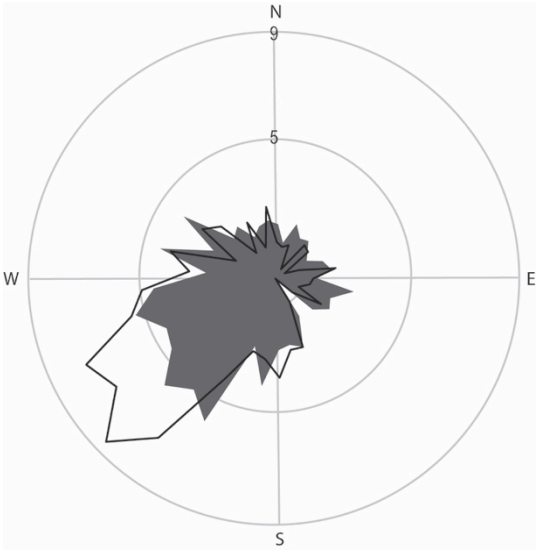

Figure 2.14. Wind rose plot for Bermuda based on the data between August 2006 and June 2014. The % of wind direction occurrence (grey shading) and % of total rainfall amount from that direction (black line).

The Global Network of Isotopes in Precipitation (GNIP) provides monthly $\delta^{18}O_{precip}$ data between January 1962 and February 1966 for Bermuda (Figure 2.15b). The mean $\delta^{18}O_{rainfall}$ for the whole available GNIP dataset is -3.55‰. The lowest $\delta^{18}O_{precip}$ values (below -4‰) during this four-year interval occurred from October to December, coinciding with the hurricane season, and the highest values (above -2.5‰) occurred in March and August. During a year, $\delta^{18}O_{precip}$ values above the average (-3.36‰) coincide with lower monthly precipitation totals (between January and May and in July). The August $\delta^{18}O_{precip}$ increased despite of high rainfall totals in that month which could be related to high contribution of sea spray. The monthly $\delta^{18}O_{precip}$ shows a weak negative correlation (r = -0.23), however insignificant, with the monthly precipitation totals (the slope of the trendline is -0.004‰/mm) and no correlation with the mean monthly temperature (r = 0.08) (Figure 2.15). This suggests that the amount effect, rather than the air temperature, probably controls the oxygen isotopic composition of precipitation in Bermuda. The comparison between

precipitation totals during GNIP observations and the whole available precipitation record from the Bermuda International Airport station reveals that the four-year GNIP record coincided with relatively wetter conditions, particularly in June and October.

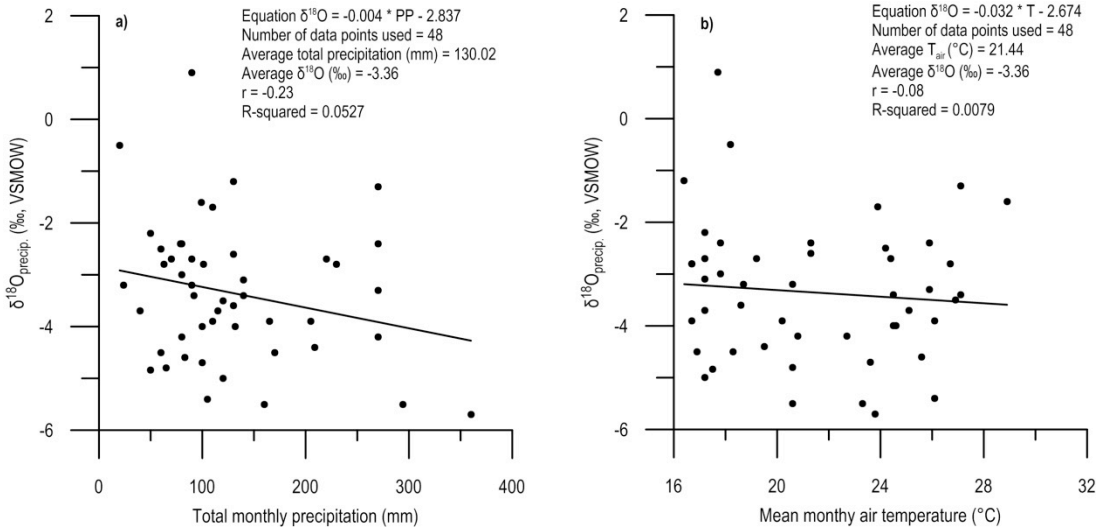

Figure 2.15. Relationship between (a) total monthly precipitation and $\delta^{18}O_{precip.}$, (b) mean monthly air temperature and $\delta^{18}O_{precip}$ based on dataset from the GNIP station in Bermuda between 1962 and 1966 (n=48).

Bermuda is located outside the main development region for hurricanes, however the islands are frequently threatened by TC formed at low latitudes and tracked northward. A historical record of tropical storms and hurricanes that affected Bermuda since its colonisation in AD 1609 is provided by Terry Tucker (Tucker, 1982).

At present climatic and hydrographic conditions around Bermuda are influenced by the Gulf Stream, the North Atlantic Oscillation (NAO), the tropical Atlantic variability (TAV), and Atlantic Meridional Overturning Circulation (AMOC) that all strongly influence local SSTs (Marshall et al., 2001). The TAV is defined as the

covariation of the SSTs gradient across the equator (ΔT_{eq}) and the weakening/strengthening of trade winds. Increased rainfall in the northern Caribbean is associated with El Niño events (Jury et al., 2007) and positive AMO index (Fensterer et al., 2012, Winter et al., 2011, Burn et al., 2016).

2.3.3. Vegetation changes

Bermuda was uninhabited until 1609, when the H.M.S. Sea Venture wrecked on local reefs, effectively starting the islands colonial period. The islands are therefore an important location for evaluating anthropogenic impacts.

Pollen records from Mangrove Lake, Bermuda, (Watts and Hansen, 1986) show that cedar (*Juniperus)* forest, recorded at the time of settlement in the 17th Century, was the predominant vegetation cover over the Holocene. Mangroves (*Rhizophora)*, as well as coral-algal reef communities in Bermuda (currently the most northern in the world) were established 3 ka BP (Ellison, 1996, Watts and Hansen, 1986) when sea-level rise slowed from 26 cm per 100 years to 7 cm per 100 years. Prior to the establishment of corals (between 5 and 2.1 ka) Bermuda was a marsh wetland (Ellison, 1996). Mangroves are the only remaining native forest areas in Bermuda. The unique native dryland forest, composed largely of the endemics Bermuda cedar (*Juniperus bermudiana*), Bermuda palmetto (*Sabal bermudiana*) and Bermuda olivewood (*Elaeodendron laneanum*), has been entirely lost owing to urbanisation, introduction of aggressive exotic species, and the cedar blight beginning in 1946 (Challinor and Wingate, 1971, Rueger and von Wallmenich, 1996).

Since colonization began in 1609, Bermuda cedar was extensively used for housing, framing and furniture, and for the construction of vessels and sloops due to cedar's lightness, high resistance to rot, and strength; this resulted in the decrease in relative abundance of Bermuda cedar (*Juniperus bermudiana*) in the pollen record, coinciding with an increase in Bermuda palmetto (*Sabal bermudiana*) pollen also attributable to colonisation (the palmetto was used for roof thatching on early houses, basketry, woven hats for export, food, and the production of an alcoholic beverage called 'bibby') (Rueger and von Wallmenich, 1996).

Intense vegetation changes in Bermuda since human colonisation in 1609 suggest that pollen records at this site are possibly unreliable source of climate variability over the last few hundred years. Historical records are notoriously unreliable making it essential to obtain climate proxy records from different materials like speleothems.

2.4. Conch Bar Caves, Turks and Caicos Islands

Conch Bar Caves is the largest above-ground cave system in the Bahamian archipelago, and is located on Middle Caicos, the largest island in the Turks and Caicos Islands (Figure 2.16). Since the 1880s the cave was exploited for guano (bat manure) that was later exported from the Turks and Caicos to the UK for use as a fertilizer. Carved and painted names and dates from the guano mining period are still apparent in the cave today. Currently, the caves are inhabited by four species of bats, which number approximately 1000-1500 individuals, with many bats roosting directly over pools in the cave. Therefore guano likely provides an important food resource for aquatic fauna (Kornicker et al., 2008). At present Conch Bar Caves are only used as a tourist site which is tightly controlled by the Turks and Caicos

National Trust. The caves are easily accessed on foot from the road but vehicle access is restricted.

The vegetation above the cave is sparse, mainly consisting of shrubs and bushes supported by an extremely thin soil (Figure 2.18).

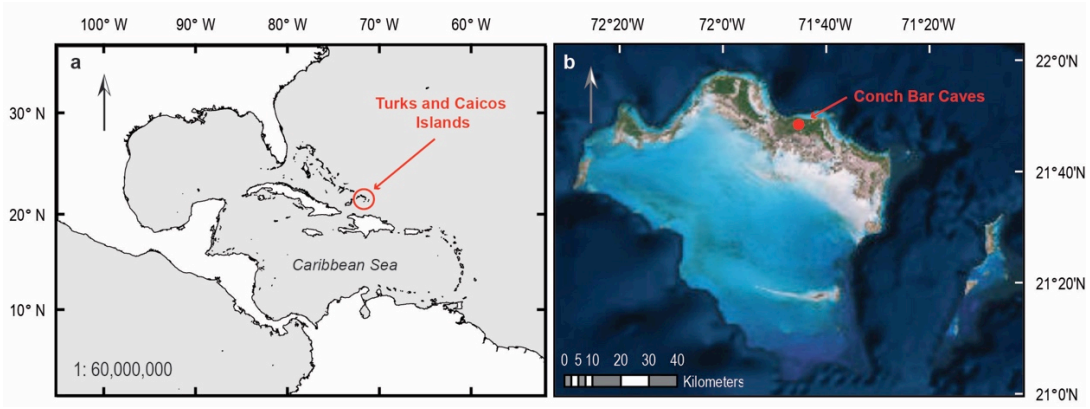

Figure 2.16. Location of a) Turks and Caicos Islands and b) Conch Bar Caves in the Turks and Caicos archipelago.

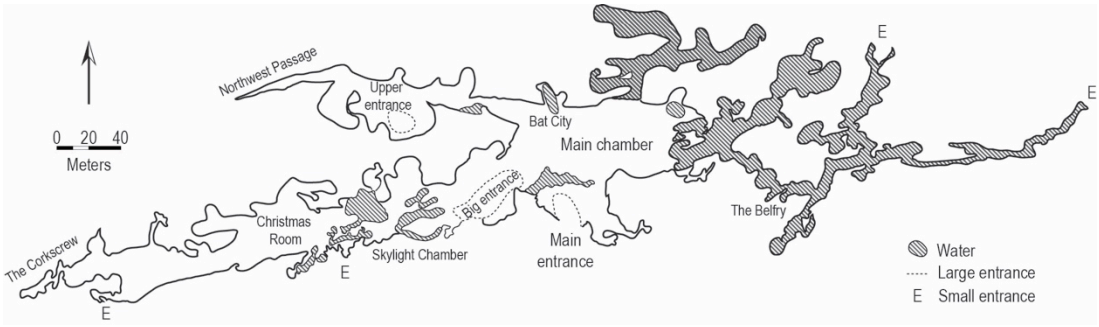

Figure 2.17. A schematic plan view of Conch Bar Caves. Adapted from Smart et al. (2008).

Figure 2.18. The wide main entrance to Conch Bar Caves, a typical example of a flank margin cave. The cave system has numerous other entrances not visible in the image.

2.4.1. Regional geology

The Conch Bar Cave system comprises of more than 3.3 km of surveyed passages (Cheng et al., 2000) (Figure 2.16). The cave system developed in young carbonates that are diagenetically immature. The caves are partly flooded by the ocean, and consequently water level fluctuation reflect local sea level. Conch Bar Cave is an excellent example of a flank margin cave, which develops at the flanks of freshwater lens where freshwater mixes with seawater and produces unique dissolutional features in carbonate rocks (Figure 2.19). This is a result of a property of carbonate geochemistry, where two different waters, both saturated with respect to $CaCO_3$, mix to result in an undersaturated solution. This causes localised and substantial dissolution of carbonate bedrock, termed ‘mixing corrosion’ or ‘mixing dissolution’ (Mylroie, 2012). Flank margin caves are also a great source of information about past sea-stands (Figure 2.20), because freshwater lens track sea level. Six cave levels are apparent in Conch Bar caves: four above current sea level and two below (Moseley et al., 2007). The uppermost level is comprised of discontinuous relict cave

passages at 12–16 m above present sea level. The main level is the most extensive part of the cave with the rock floor at 2–6 m above sea level. The next level consists of partially flooded rooms with rock bottom down to 2 m below sea level, while the lowest section of the cave is completely submerged with water depths of up to 15 m (Kornicker et al., 2008). Although there is no direct connection with the sea, water levels in the cave vary tidally up to about 80 cm (Figure 2.21). This can also affect stalagmite growth which ceases when the cave is flooded during the high sea-stands (during the interglacial periods). Moreover, if the mixing zone between freshwater (brackish) and saltwater (marine) is located at the stalagmite elevation, it may cause dissolution of the secondary calcite that builds speleothems.

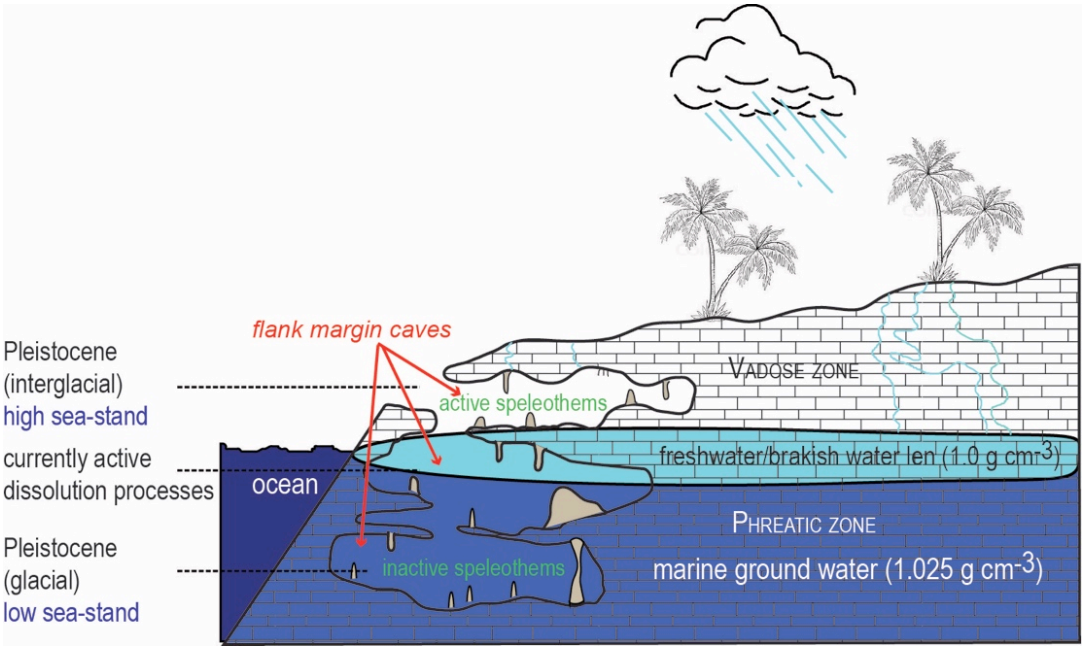

Figure 2.19. Cartoon diagram of a freshwater lens in a carbonate island, illustrating flank margin cave development during different sea-stands in the lens margin, under the flank of the enclosing landmass.

Figure 2.20. Conch Bar Caves as an example of flank margin cave. Photo shows two cave levels indicating the height of the sea stands.

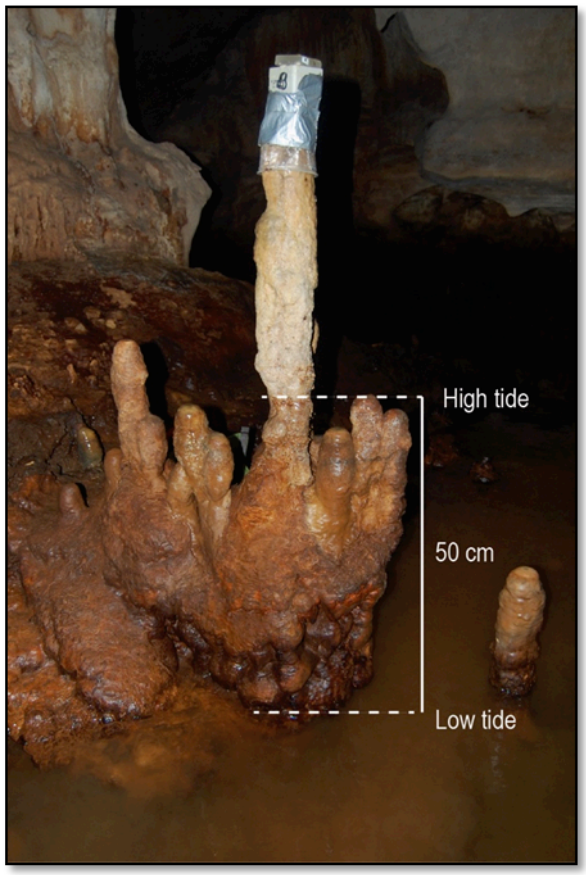

Figure 2.21. Water level changes around the location of stalagmite TC-EMP-12 in Conch Bar Caves before the sample collection.

2.4.2. Present climate

Turks and Caicos Islands experience tropical savannah climate (Aw), which is the second most common climate type by land area after arid desert hot (BWh), accounting for 11.5% and 14.2%, respectively (Peel et al., 2007). Most of the islands are affected by the Atlantic trade winds (Halkitis et al., 1980) moderated by the warm Antilles Current. Effective rainfall is typically negative over the year, and particularly between November and February. A small peak in May and a broad peak between September and October (P – E ~ 0) is a result of seasonal storms, separated by a weak deficit in July. Months with intense TCs tend to have SSTs anomalies > +0.5°C east of Bermuda, which amplifies the upper high and westward track of these storms. The average return period of hurricanes above category 3 is ~20 years usually following a west-northwest path following development east of the Antilles and passage north of Puerto Rico (Li et al., 2013).

Mean annual precipitation at Conch Bar is 676 mm, with mean monthly rainfall above 50 mm between September and December (considered the 'wet season'). Mean annual temperature is 25.9°C, ranging from 23.4°C in January to 28.2°C in August (Figure 2.22). The months of minimum and maximum SST around Turks and Caicos Islands are March and October, respectively (Giry et al., 2012).

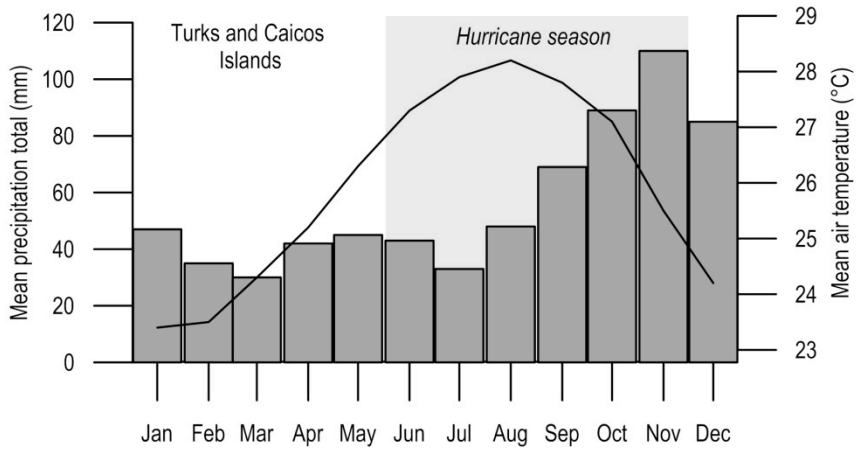

Figure 2.22. Mean monthly precipitation and air temperature in Turks and Caicos Islands. Data from Climate-data.org.

2.5. Yok Balum Cave, Belize

Yok Balum Cave is located in the Toledo District of southern Belize in Central America, 30 km northwest from the town of Punta Gorda (Figure 2.23). The climate archives preserved in the cave's speleothems (Kennett et al., 2012, Ridley et al., 2015a) are important for the near archaeological sites (e.g. Uxbenká) that date back to 60 cal years BC that are associated with a Pre-Classic Maya period (Culleton et al., 2012) (Figure 2.24). The cave extends approximately 540 m as a main trunk passage from a small opening in the west (the main entrance) to a larger, more elevated opening to the south. The second entrance resulted from cave collapse at least 44,000 ± 3300 years BP probably associated with tectonic activity (Ridley et al., 2015b). Mean T_{cave} oscillates around 22.3°C (±0.5°C). Yok Balum Cave is a well-ventilated, dynamic cave system (mean pCO_2 of 461 ppm) that ventilates seasonally driven by thermally induced inside-outside air density differences (Ridley et al., 2015b). The cave is well-decorated with actively growing speleothems (Figure 2.25).

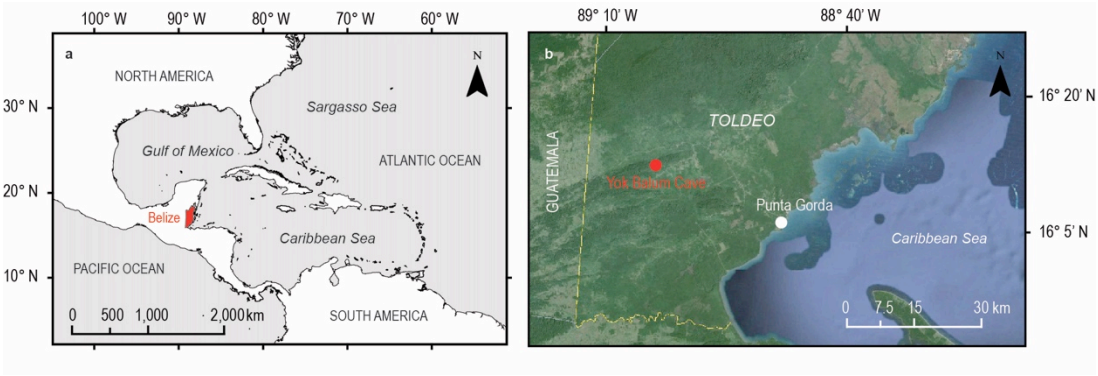

Figure 2.23. The location of a) Belize and b) Yok Balum Cave within the Toledo District.

Figure 2.24. Yok Balum Cave is located close to many important Classic Maya Centres.

2.5.1. Regional geology

Yok Balum Cave developed within the tectonically uplifted Cretaceous Campur limestone formation (Kennett et al., 2012, Miller, 1996), which originates from deposition of evaporates and marine carbonates throughout the Caribbean, around the granite intrusions of the Maya Mountains to the north. Yok Balum Cave is situated in one of the eight identified karst areas in Belize described as K-T fault ridges of 300 km^2 area trending southwest to northeast and rising above plains of the Toledo series (the Quaternary shales, mudstones and sandstones) (Miller, 1996). The cave is located ca. 100 km north of the divergent boundary between the North American and Caribbean Plates, and northeast of the subduction zone between those

plates and the Cocos Plate. The latter boundary is the dominant source of regional seismic activity that affects the cave area occasionally (Ridley et al., 2015b).

Figure 2.25. Stalagmites of Yok Balum Cave, which is rich in actively growing speleothems.

2.5.2. Present climate

Currently southern Belize experiences tropical rainforest climate (Af) with the temperature of the coldest month above 18^{o}C and precipitation of the driest month above 60 mm (Peel et al., 2007). The total annual precipitation in Belize ranges from 1300 mm in the north to 4500 mm in the south. 80% of the total annual precipitation occurs during the wet season (May through January) and is a direct result of seasonal ITCZ migration (Kennett et al., 2012) (Figure 2.26). Most of the moisture comes from the Caribbean Sea as a result of trade wind convergence with a small contribution coming from the Pacific Ocean (Kennett et al., 2012). The climate of Belize is also affected by the TCs and large-scale convective systems that can bring heavy localised rain to southern Belize.

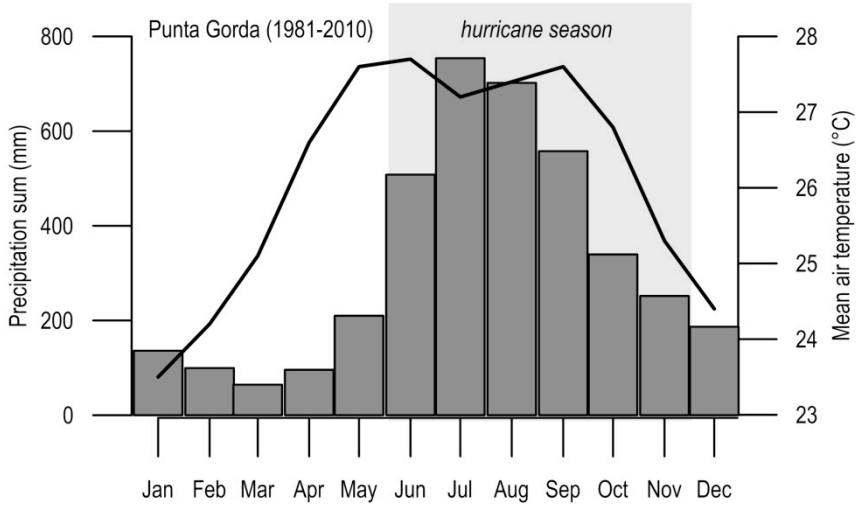

Figure 2.26. Mean monthly air temperature and precipitation totals between 1981-2010 at the Agricultural Station in Punta Gorda Town (Toledo) (National Meteorological Service of Belize, 2016).

2.6. Summary

All the study sites except Refugio Cave were continuously monitored for cave air temperature, drip rates, cave pCO_2, and barometric pressure for at least two years. The results of Yok Balum cave monitoring are published in Ridley et al. (2015b)(Appendix C) and some results of Refugio Cave monitoring are available from Mudarra et al. (2009). The results arising from Conch Bar Caves and Leamington Cave monitoring will be discussed in Chapter 3. From each site at least one stalagmite was collected for further analysis. All the collected stalagmites were CT scanned and dated, except for stalagmite YOK-K from Yok Balum Cave; results are discussed in Chapter 4. Stalagmites TC-EMP-12 and BER-SWI-13 were also analysed for stable carbon and oxygen isotope compositions and these results are discussed in the Chapter 4 and 5. Climate reconstructions based on previously published proxy data combined with new records produced from stalagmites REF-07 and BER-SWI-13 are discussed in Chapters 4 and 5, respectively. The climate

reconstruction from stalagmite TC-EMP-12, despite available $\delta^{18}O$ and $\delta^{13}C$ data, was not pursued due to very large age uncertainties, discussed in the Chapter 3.

Chapter 3

Monitoring of near shore tropical caves

3.1. Introduction

Most of the information about the cave air circulation and climatology comes from the monitoring of inland caves located in karst areas that are well above sea level (e.g. Crag Cave in Ireland (Sherwin and Baldini, 2011), Natural Bridge Caves in Texas (Cowan et al., 2013), Obir Caves in Austria (Spötl et al., 2005), St. Michael's Cave in Gibraltar (Mattey et al., 2010), Yok Balum Cave in Belize (Ridley et al., 2015b), and many others). Their monitoring studies indicate that seasonal cave ventilation, expressed by e.g. CO_2 or radon concentration variations, is usually triggered by the air density differences between outside and cave air resulting in convective air circulation. The main cave-air CO_2 sources are CO_2 degassing from vadose and phreatic water, animal and human respiration, and decaying organic material (e.g. bat guano) within the caves. The understanding of the mechanism controlling seasonal and interannual cave-air CO_2 concentration is essential for interpreting paleoclimate archives, because the cave-air CO_2 fluctuations regulate the degassing of CO_2 from drip water and thus influence the speleothem deposition rate and potentially the uptake of chemical proxies that could potentially cause biases (Baldini et al., 2008, Spötl et al., 2005, Banner et al., 2007, Cowan et al., 2013). The mechanisms controlling cave ventilation and climatology in temperate inland cave environments are well described as opposed to tropical near shore island caves (Gamble et al., 2000). Fairchild and Baker (2012) predict that rainfall variations may influence circulation in those caves.

Here, we present the results of continuous tropical island cave monitoring from Conch Bar Caves (Turks and Caicos Islands) and Leamington Cave (Bermuda). Both

caves are developed in immature Pleistocene limestones, located on small islands (total land area less than 130 km^2), are very close (less than 500 m) to the sea shore, and are at low altitudes (less than 20 m a.s.l.) in the tropical western North Atlantic Basin. More information about each cave site can be found in the Chapter 2. We also evaluate the suitability of stalagmites from near-shore caves for paleoclimate reconstructions with a special focus on their ability to record tropical cyclone signal.

3.2. Methods

Conch Bar Caves (CBC) and Leamington Cave (LC) were continuously monitored for cave air pCO_2, air temperature (T_{cave}), cave air barometric pressure (p_{cave}), cave relative humidity (RH) and drip rate from April 2011 to March 2013, and from March 2013 to December 2015, respectively (Table 3.1). All the monitoring equipment in CBC was placed in one location, on a dripstone formation dubbed the 'Island' in the cave's northern passage with standing brackish water situated ~500 m from the nearest shoreline on Middle Caicos Island (Figure 3.1 and Figure 3.2). In LC, the loggers were distributed evenly throughout the cave (Figure 3.3). All the monitoring data are presented here in the Atlantic Standard Time (UTC-4).

The cave air pCO_2 was recorded every three hours using a Vaisala CARBOCAP Carbon Dioxide GMP343 Probe (± 3 ppm + 1% of reading) linked to Vaisala MI70 Indicator and powered by two Duracell MN918 Lantern batteries wired in parallel. In LC, the logger was placed ca. 90 m from the entrance, in the northern cave passages (Figure 3.3, orange circle) and recorded the data from March 11, 2013 to November 19, 2013.

P_{cave} and T_{cave} were measured continuously at hourly intervals by BaroTROLL loggers, with temperature range between -20 and +80°C (with an accuracy of ±0.1°C and a resolution of 0.01°C), and pressure range between 0 and 1.14 bar (with an accuracy of ±0.1 FS and a resolution of ±0.005% FS). In LC, the loggers were located ca. 36 m (in the main chamber) and 90 m (next to Vaisala logger) from the entrance (Figure 3.3, black circles). In CBC, one logger was located on the 'Island' and the other one outside of the cave, measuring also air temperature (T_{out}).

Table 3.1 Cave climate characteristics recorded during Conch Bar Caves and Leamington Cave monitoring.

Variable	Logger	Logging interval
drip rate	Stalagmate Plus Mk2b automated drip loggers	Hourly[1,2]
cave air pCO_2	Vaisala CARBOCAP® Carbon Dioxide Probe GMP343	3 hours (Apr 2011-Jun 2012)[1]
		3 hours (Mar-Nov 2013)[2]
		12 hours (June 2012-March 2013)[1]
T_{cave}	Tinytag Plus 2 - TGP-4500 logger	Hourly[1,2]
RH	Tinytag Plus 2 - TGP-4500 logger	Hourly[1,2,]
p_{cave} , p_{out}	BaroTROLL	Hourly[1,2]

[1] Conch Bar Caves
[2] Leamington Cave

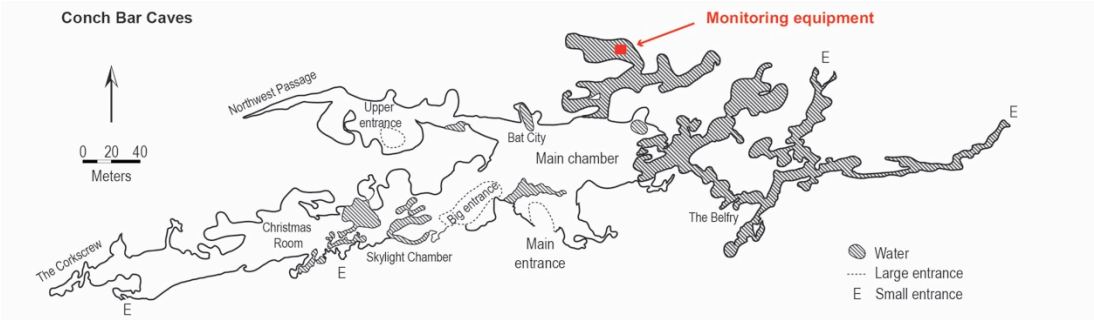

Figure 3.1. The location of monitoring equipment in the Conch Bar Caves, Turks and Caicos Islands. Adapted from Smart et al. (2008).

Figure 3.2. Conch Bar Caves monitoring island: the location of Vaisala, Barotroll, Tinytag and Stalagmate loggers.

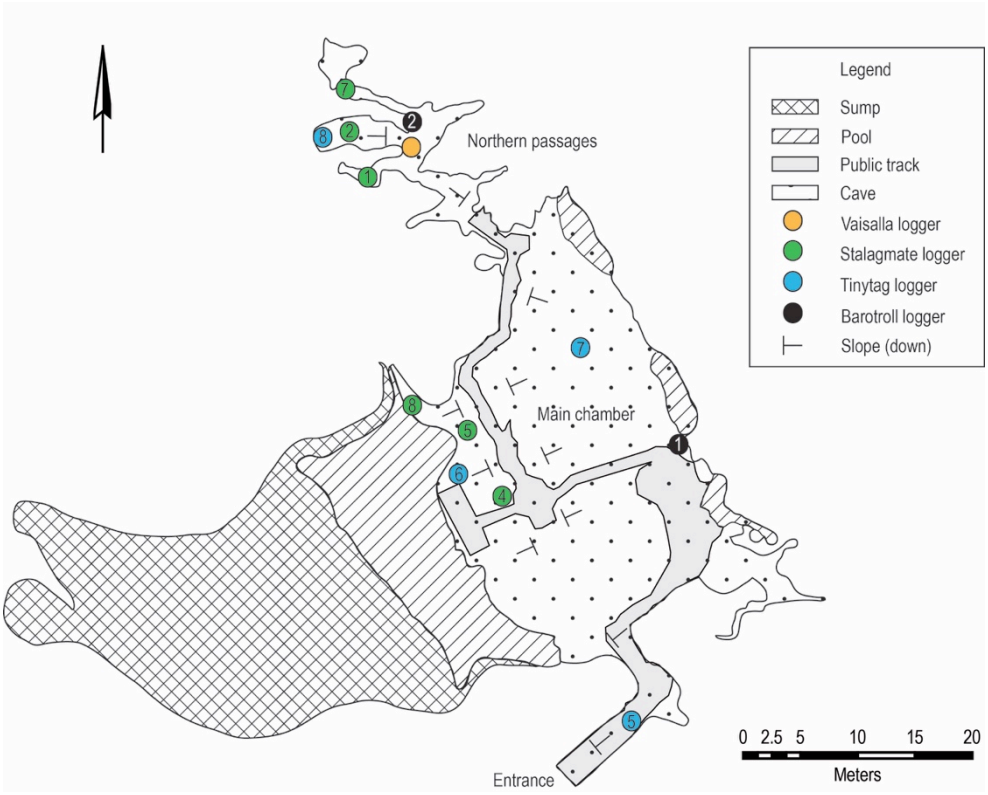

Figure 3.3 Distribution of monitoring loggers within Leamington Cave. Surveyed by members of the Bermuda Cave Diving Association. Sketched by Robert Power, 1986. Adapted by Izabela Walczak.

T_{cave} and RH were recorded by TinyTag Plus2 - TGP-4500 loggers also at hourly intervals. The Tinytag logger records temperature observations between -25 and +85°C with an accuracy of ±0.4°C at 25°C, and a resolution of 0.01°C. The reading range for relative humidity is 0 to 100%, with ±3% accuracy at 25°C and a resolution better than 0.3% RH. In LC, the loggers were distributed evenly throughout the cave (Figure 3.3, blue circles).

The drip rate feeding stalagmites of potential interest were recorded by three (in CBC) and six (in LC) Stalagmate Plus Mk2b automated drip loggers at hourly intervals. In LC, three of them (#4, #5, #8) were placed in the main chamber, close to the pool and the remaining three loggers (#1, #2, #7) were placed in the cave's northern passages (Figure 3.3, green circles and Figure 3.5). Based on the drip rate in CBC and LC and their responsiveness to rainfall (Figure 3.10) discussed later, stalagmites TC-EMP-13 ('the Emperor', Figure 3.4a) from CBC and stalagmites BER-STO-13 ('Stormy', 674 mm long, Figure 3.5a) and BER-SWI-13 ('Swizzle', 190 mm long, Figure 3.5b) from LC, were collected for further analysis. Other stalagmites are not discussed further in the thesis.

In Turks and Caicos Islands, the Driptych Pluvimate logger was placed in the rain gauge outside the CBC to monitor rainfall. However due to its frequent clogging and hence its unreliability to record the precise rainfall rate, we only use the information about the timing of the rainfall here rather than its rate.

Figure 3.4. The locations of monitored drip rate in Conch Bar Caves: (a) 'Emperor' (collected stalagmite TC-EMP-12), (b) 'Nipple', (c) 'Cleatus'. Darker colouring at the base of stalagmites marks the highest tide level.

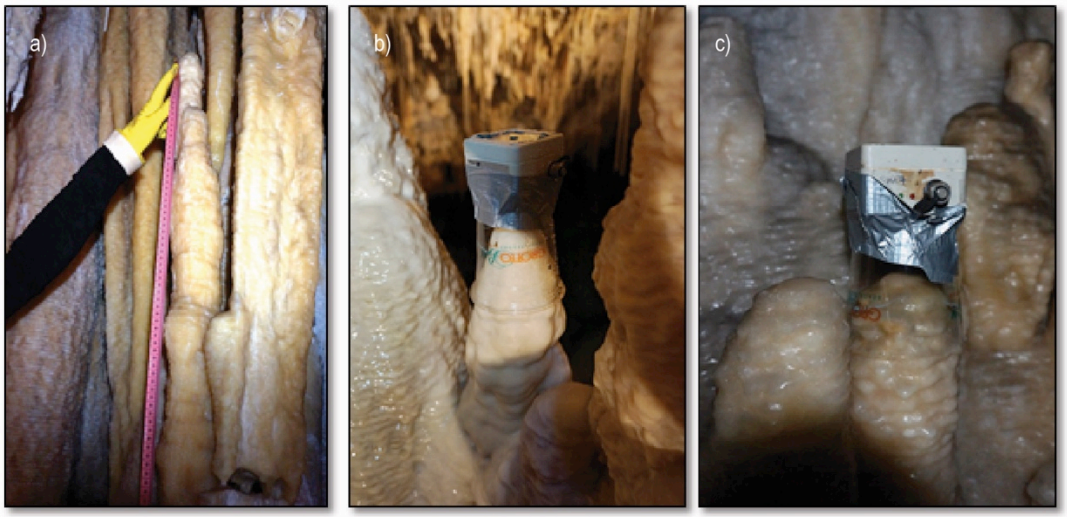

Figure 3.5. The locations of the monitored drip rate in Leamington Cave: (a) Stalagmate logger #8 ('Stormy'), (b) Stalagmate logger #5 ('Swizzle'), (c) Stalagmate logger #7.

Mean sea level data at hourly intervals during caves monitoring period were downloaded at Local Standard Time from NOAA Tides and Currents (https://tidesandcurrents.noaa.gov/) from the closest station. CBC monitoring results were compared with the mean sea level data from Arecibo, Puerto Rico (18^0 28.8' N; 66^0 42.1' W) and LC data with the water level data from the station located in St.

George's Island, Bermuda (32º 22.4' N, 64º 42.2' W). Both stations are characterised by a mixed semidiurnal tidal pattern (the high and low tides differing in height) (Ross, 1995). These raw data have not been subjected to the National Ocean Service's quality control and are released for use as preliminary data with appropriate caution. However, in this study we are predominantly interested in the timing of the peak and low water levels, rather than its actual height.

Weather station data about rainfall data from Turks and Caicos Island are not available, however sea surface temperatures (SSTs) were obtained from NOAA Tides and Currents for Virginia Keys, USA, since SSTs data from Arecibo were incomplete during CBC monitoring period. The information about daily air temperatures (T_{out}), SSTs, wind direction, wind speed and rainfall in Bermuda comes from the Bermuda Weather Service website (http://weather.bm/) recorded at the Bermuda International Airport located 2 km east from the LC.

Monthly North Atlantic Oscillation index (NAO) and Atlantic Meridional Oscillation index (AMO) data were downloaded from NOAA Climate Prediction Centre (http://www.cpc.ncep.noaa.gov/).

3.3. Results

3.3.1. Leamington Cave, Bermuda

The temperature monitoring across the cave indicates that variance in temperature decreases from the entrance to the rear of the cave, as expected. The mean cave temperature (T_{LC}) by the pool recorded by the Tinytag #6 (Figure 3.3), an area where later stalagmites were collected from, ranges from 20.8ºC (December-June, defined

here as a 'cool season') to 24.7°C (July-November, defined here as a 'warm season'). The mean annual T_{LC} is ~22.5°C corresponding to the mean annual temperature in Bermuda. During the Leamington Cave monitoring period that spans over almost three years, the daily mean T_{LC} strongly, positively correlates with daily mean SSTs ($r = 0.83$, $p < 0.01$) and hence outside temperature (T_{out}) ($r = 0.81$, $p < 0.01$) recorded at the Bermuda International Airport (Figure 3.6c).

Over longer time period (between 2000 and 2015), mean monthly T_{out} at Bermuda strongly positively correlates with local monthly SSTs ($r = 0.99$, $p < 0.01$), with mean monthly AMO index ($r = 0.46$, $p < 0.01$) and negatively with NAO index ($r = -0.24$, $p < 0.01$, Figure 3.6d). This suggests that T_{cave} is controlled by the same mechanisms that control the SSTs and T_{out}. Thus, successful T_{cave} reconstruction from speleothems is interpretable in terms of SSTs/T_{out}/AMO index and to lesser extent as NAO index.

Tinytag logger #8 (Figure 3.3) at the back of the cave recorded continuous 100% of humidity during the monitoring period (Figure 3.6b, blue line). The Tinytag logger #6 located by the pool (Figure 3.3) recorded continuous 100% of humidity mostly in the cool season, and during the warm season the humidity there falls down to zero or varies (Figure 3.6b, black line), almost certainly reflecting a technical fault in the logger.

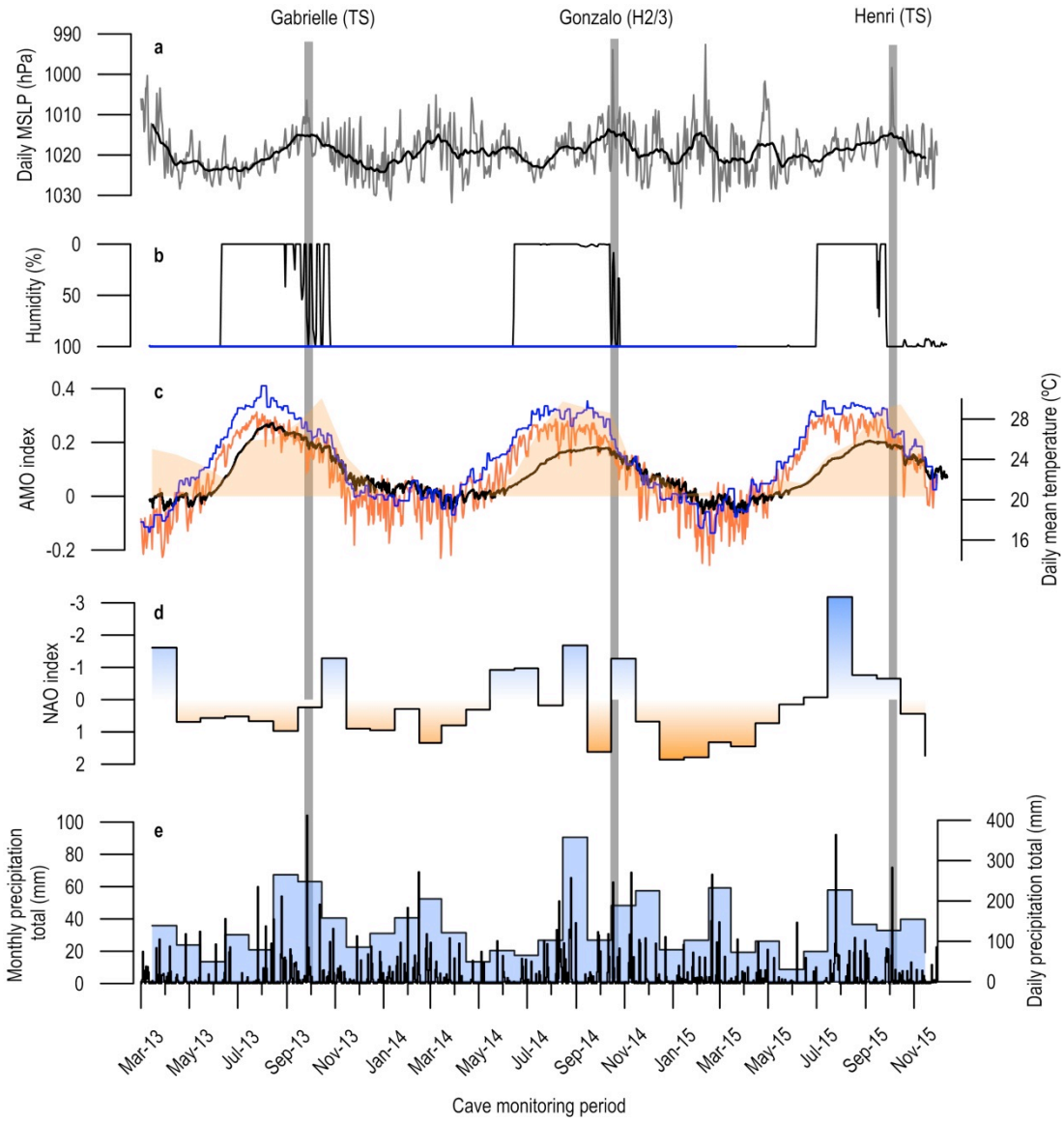

Figure 3.6. Climatology during the Leamington Cave monitoring period. (a) Daily mean sea level pressure (grey line) observed at the Bermuda International Airport by the Bermuda Weather Service with 31-point running average (black line). Grey bars point to the time of TCs passing. Note that y-axis is reversed. (b) The cave humidity recorded by the Tinytag loggers #6 (black line) and #8 (blue line). Note that y-axis axis is reversed. (c) The mean monthly AMO index calculated from the Kaplan SST dataset. Orange shading indicates positive phase. Daily SSTs (blue line) and T_{out} (orange line) observed at the Bermuda International Airport by the Bermuda Weather Service. T_{cave} (black thick line) recorded by the Tinytag logger #6 by the pool. (d) monthly NAO index; (e) Daily (black bars) and monthly (blue bars) precipitation totals observed at the Bermuda International Airport by the Bermuda Weather Service.

Daily precipitation totals are correlated negatively with daily mean sea level pressure ($r = -0.33$, $p < 0.01$) and positively with SSTs ($r = 0.51$, $p < 0.01$) and T_{out} ($r = 0.49$, $p < 0.01$) (Figure 3.6), suggesting dominance of the convective rainfall.

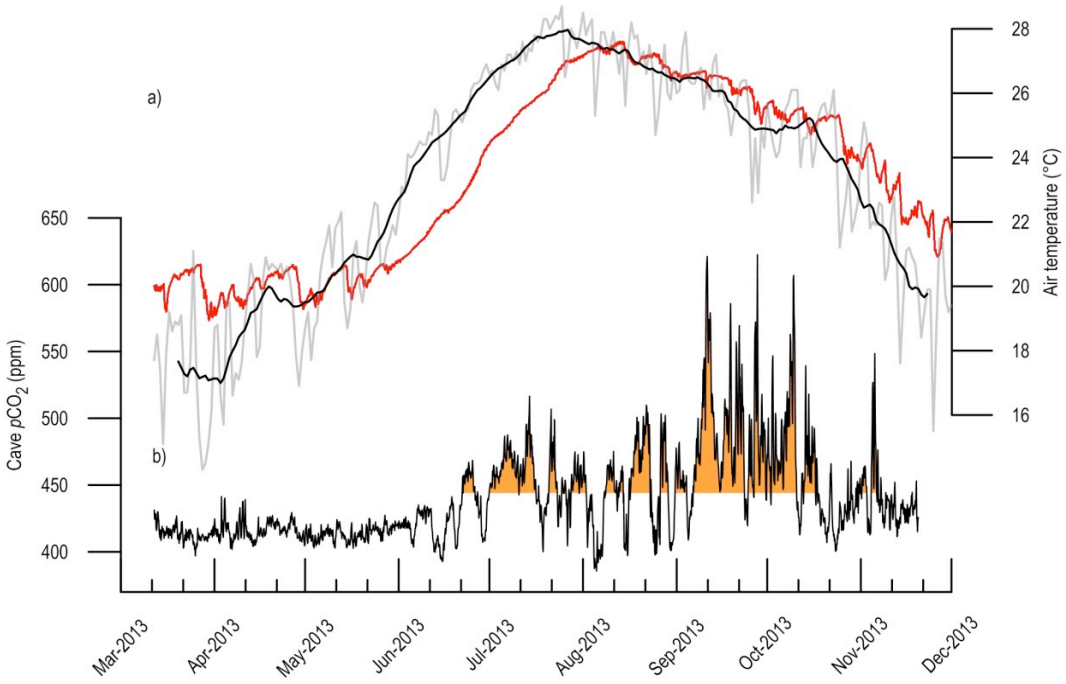

Figure 3.7. Cave and climate monitoring data from March 2013 to November 2013. (a) hourly T_{cave} recorded by Tinytag logger #6 (red line), daily mean T_{out} recorded at Bermuda International Airport (grey line) with 17-days running average (black line). (b) cave pCO_2 recorded at 3 hour intervals. Orange shading indicates pCO_2 concentration over mean of 444 ppm.

The mean cave pCO_2 from March to November 2013 of 444 ppm ($\sigma = 34$ ppm, $n = 334$), approximates Mauna Loa atmospheric pCO_2 (mean air pCO_2 = 396 ppm over the same time interval) and suggests very efficient cave ventilation. The minimum and maximum values of cave pCO_2 recorded during monitoring period were 385 (on 5th August 2013 at 12:00) and 622.5 ppm (on 27th September 2013 at 18:00), respectively. The time interval of the highest, above the mean (orange shading in Figure 3.7), cave pCO_2 occurs in the warm season and coincides with the rapid T_{LC}

increase from ~22 to ~26ºC from the mid-June to August, and stays elevated until the mid-October. The correlation between mean daily pCO_2 and daily mean T_{out} and T_{LC} (measured by Vaisala logger) is 0.29 ($n = 253$, $p < 0.001$). The cave pCO_2 below the mean is recorded from March to June (cool season) suggesting common in mid-latitudes winter-dominated cave ventilation driven by convective mixing (Fairchild and Baker, 2012). Due to pCO_2 logger failure from December 2013, the cave pCO_2 variability from December to March is unknown. However, cave pCO_2 is probably low, controlled by the same mechanisms as during the period between March and June. Temporal pCO_2 variability in the cool season is low (mean March-June pCO_2 = 417 ppm, σ = 11 ppm) unlike in the warm season characterised by higher temporal variability (mean July-October pCO_2 = 463 ppm, σ = 33 ppm) that is common in other caves as well (e.g. Ridley et al. (2015b)).

Spectral analysis of 3-hourly LC pCO_2 data was performed using the software PAST (Hammer et al., 2001). PAST automatically detrends the data prior to analysis. The LC pCO_2 data revealed peaks at 24 and 12 hours, corresponding to tidal pattern. However both peaks are below 95% confidence (Figure 3.8). Lower correlation in LC could be a result of Vaisalla logger location at the back of the cave, further away from the water making it less sensitive to water level changes in comparison to CBC. Also positive correlation exists between mean daily water level at Bermuda International Airport and mean daily cave pCO_2 ($r = 0.29$, $n = 253$, $p < 0.01$) for the whole monitoring period. This suggests that daily ventilation is also controlled by the tide levels.

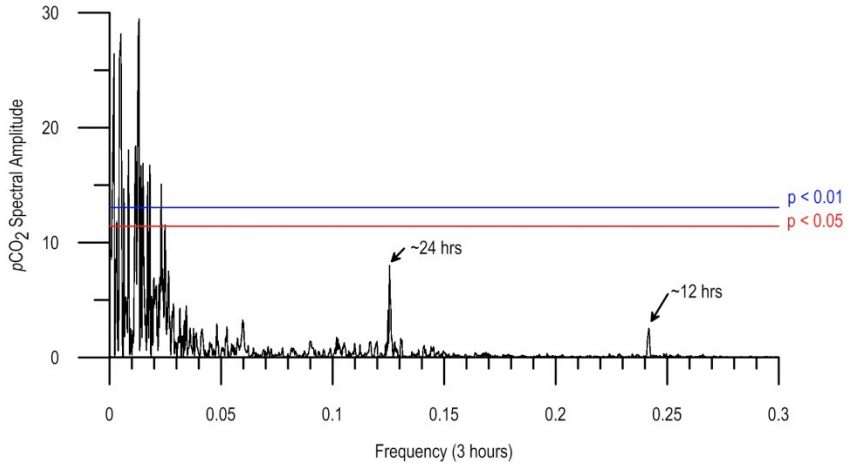

Figure 3.8. Results of spectral analysis of the Leamington Cave pCO_2.

Another factor affecting LC pCO_2 is the wind direction ($r = -0.22$, $p < 0.01$) and speed ($r = -0.17$, $p < 0.01$). The cave entrance points towards SW and hence the lowest pCO_2 (< 420 ppm) occurs when the wind is coming from SW (210-240°) direction (Figure 3.9b) which also brings the strongest winds (> 10 m/s) to Bermuda (Figure 3.9a) and over 30% of annual rainfall (Figure 2.14), mostly associated with the winter low-pressure (~30% of total SW wind occur between December and February) or summer tropical cyclones (> 33% of total SW wind occur between June and August) transit. However no correlation was found between the daily rainfall sum and cave-air pCO_2. The mean highest (> 450 ppm) cave-air pCO_2 is associated with the winds from NNE and SE-E.

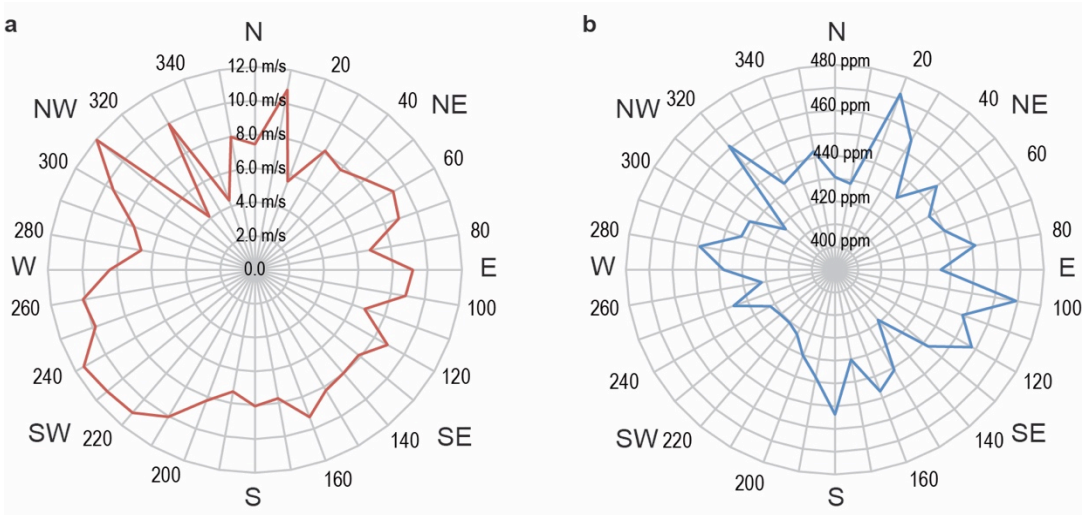

Figure 3.9. Distribution of: a) wind speed (m/s) (red line) and b) LC pCO_2 (ppm) (blue line) in relation to the wind direction in Bermuda during the monitoring period.

Only at four drip rate monitoring locations (#4, #5, #7 and #8) (Figure 3.3), the dripping was recorded. No recorded dripping at the locations #1 and #2 is probably associated with a lack of rainfall infiltration due to house building directly above those stalagmite locations. The drip sums recorded at locations #7 and #5 ('Swizzle') show a similar pattern: increased drip rate coinciding with the two rainfall peaks between September-November 2013 and February-April 2014 (Figure 3.10). Due to Stalagmate loggers malfunctioning at those two locations after May 2014, drip sum monitoring could not be extended into the next year to see if the pattern continues. The absolute drip rate values are higher at the location #5 than in #7, suggesting decreased rainfall infiltration at the location #7 due to near house location above the site.

During drip rate monitoring, three tropical cyclones (Gabrielle 2013, Faye 2014 and Gonzalo 2014) passed the cave site. During the passing of Gabrielle (of tropical storm intensity), on 11th September 2013, the daily rainfall sum reached 13.21 mm

that was reflected in the increased drip rate only at the location #7. Both hurricanes, Faye (cat. 1) and Gonzalo (cat. 2/3), that occurred in October 2014 made landfall in Bermuda and resulted in 54.4 mm (sum between 10 and 12th October) and 73.4 mm (sum between 17 an 19th October) of rainfall, respectively. Since the loggers at locations #5 and #7 at that time were malfunctioning, only logger #8 managed to record increased drip rates during both TC transit. However, the highest daily precipitation sum (104.14 mm) during the cave monitoring period was recorded at Bermuda International Airport on 26th September 2013 and was not associated with a tropical cyclone but with the low pressure transit. This resulted in the increased drip rate at the locations #5 and #7. This suggests that despite of dwellings proximity to LC, the drips in the cave are still sensitive to increased rainfall associated with the tropical cyclones or low pressure systems passing.

Based on the drip sensitivity to rainfall and stalagmites lengths, two of them at the locations #5 (named ‘Swizzle’) and #8 (named ‘Stormy’) were collected for the further analysis.

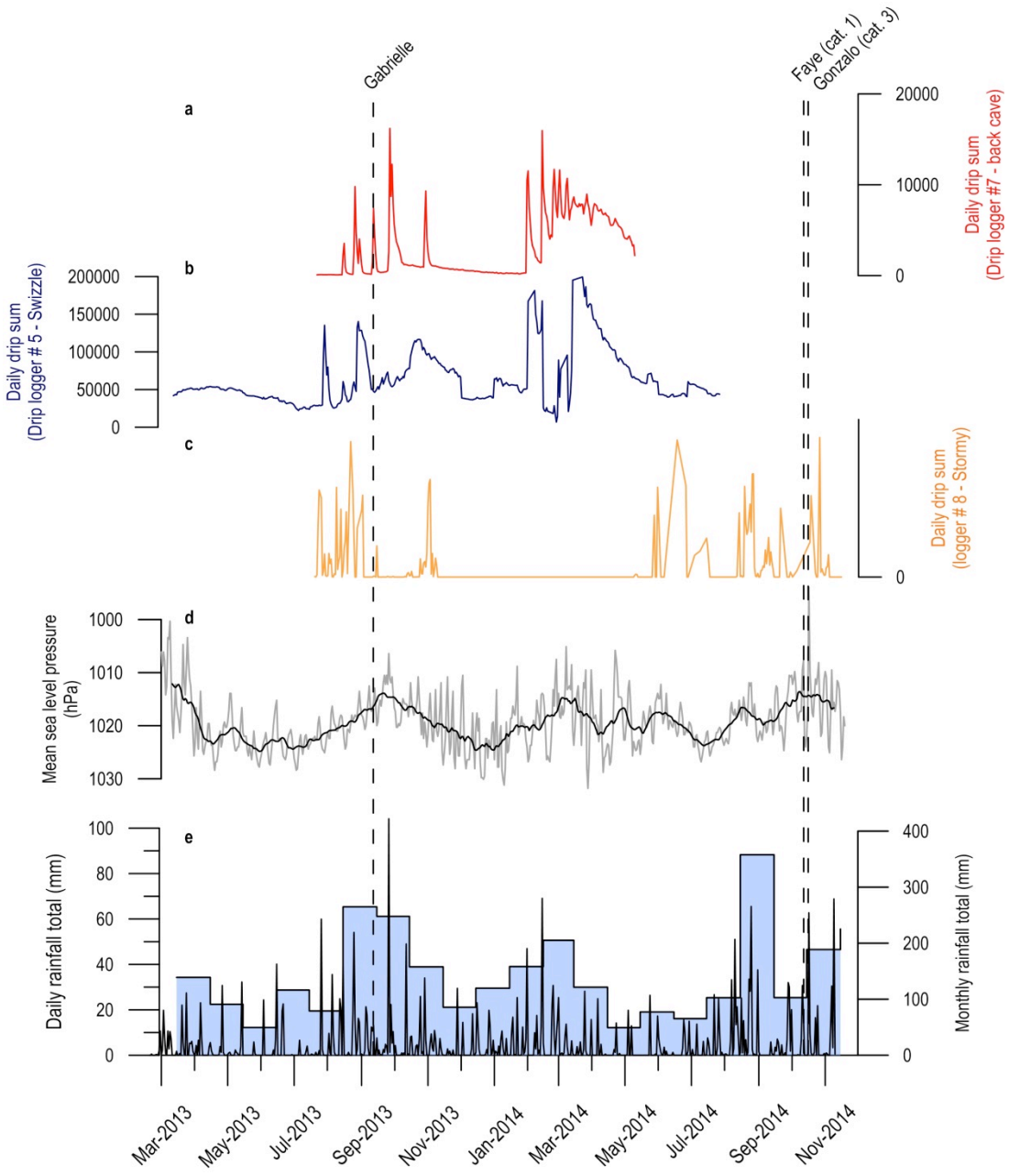

Figure 3.10. Daily drip sum recorded at three different locations in the Leamington Cave: (a) by Stalagmate #7, (b) by Stalagmate #5 (location of 'Swizzle'), (c) by Stalagmate #8 (location of 'Stormy') during the monitoring period, (d) Daily mean sea level pressure (grey) with 21-point running average (black line), (e) Daily (black line) and monthly (blue bars) rainfall sum observed at Bermuda International Airport. Note that Y-axis was clipped in b) and c), so the plot reveals the timing of the drip sum peaks rather than its actual drip sum.

3.3.2. Conch Bar Caves, Turks and Caicos Islands

Over the monitoring period mean T_{out} (recorded by the Barotroll logger) was 26.9^{0}C (σ = 3.9^{0}C), ranging between 15.8 and 40.6^{0}C, and the mean cave air temperature (T_{CBC}) recorded by Vaisala logger, was 24.6^{0}C (σ = 0.3^{0}C), ranging between 24.0 and 25.1^{0}C (Figure 3.12e). Over this two-year monitoring period, T_{CBC} values show a steady increase from June to November, overlapping the hurricane season, and are generally above the mean, hence defined here as a 'warm/hurricane season' (Figure 3.12e). From November to May T_{CBC} values decrease and are generally below the mean, hence defined here as 'cool season'.

Loggers detected our presence during each field work in the form of T_{CBC} increase by ~0.3-2.3^{0}C. Due to efficient cave ventilation, every time T_{CBC} returned to normal (mean for the last few days before the trip) within three hours.

The mean daily T_{CBC} strongly correlates with mean daily T_{out} ($r = 0.49$, $p < 0.01$), SSTs in Virginia Keys ($r = 0.52$, $p < 0.01$, $n = 685$) and AMO index ($r = 0.51$, $p < 0.05$). Negative correlation exists between T_{CBC} and NAO index ($r = -0.40$, $p < 0.05$) (Figure 3.12g).

The daily cave temperature variability corresponds to water level fluctuations at Arecibo, Puerto Rico (Figure 3.13e and f) that show mixed semidiurnal tidal pattern. As a result, the rise (decrease) in air temperature corresponds to high (low) tide. The correlation between T_{CBC} and water level in the cool season is positive and generally strong ($r > 0.4$) (Figure 3.15). During the hurricane season, the correlation is weaker ($-0.4 < r < 0.4$). The spectral analysis using software PAST (Hammer et al., 2001) of

the hourly recorded cave temperature (Figure 3.11) measured by Barotroll logger yields periodicities of 12 and 24 hours (however below 95% confidence level) further corroborates the link between T_{CBC} and water level (Figure 3.13e and f).

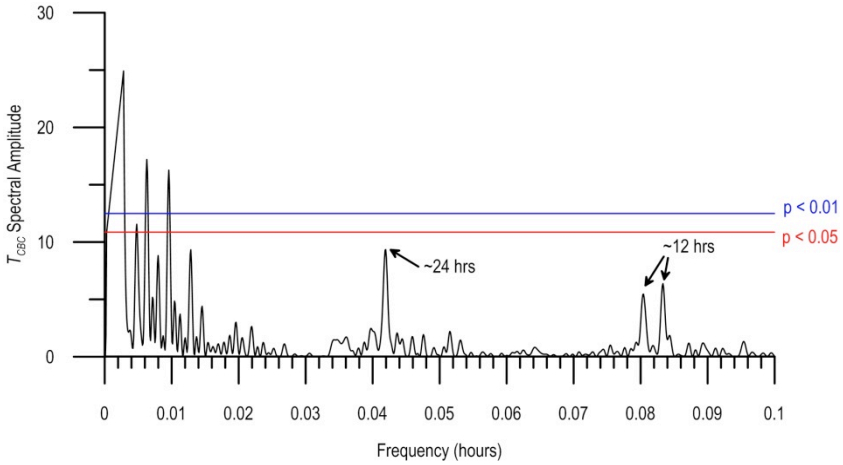

Figure 3.11. Results of spectral analysis of T_{CBC}.

The concentration of pCO_2 in the cave shows seasonal variability. During the monitoring period, the mean pCO_2 in Conch Bar Caves was 505 ppm (σ = 82 ppm). The lowest pCO_2 concentration (403.9 ppm) recorded during monitoring period occurred on August 24, 2011, at 23:00 during Hurricane Irene's (cat. 3) transit (Figure 3.12 and Figure 3.16). Cave air pCO_2 in Conch Bar Cave reaches a maximum (over 900 ppm) in the summer (May-June) and autumn (October-November) (Figure 3.12). The lowest pCO_2 values and the smallest difference between outside and cave air temperature occur during the cool season (Figure 3.15). The daily variability in cool season is much lower than during the rest of the year. This suggests strong ventilation during winter months due to sinking of cold, low pCO_2 surface air into the cave. Also low cave air pCO_2 values (mean = 444 ppm, σ = 19 ppm calculated for period between December and March) coincide with positive NAO phase (Figure 3.12f and g) and low sea CO_2 saturation (Bates et al., 1998) due to deep mixing layer

that could result in seawater acting as a CO_2 sink and contribute to lowering of the cave pCO_2 values.

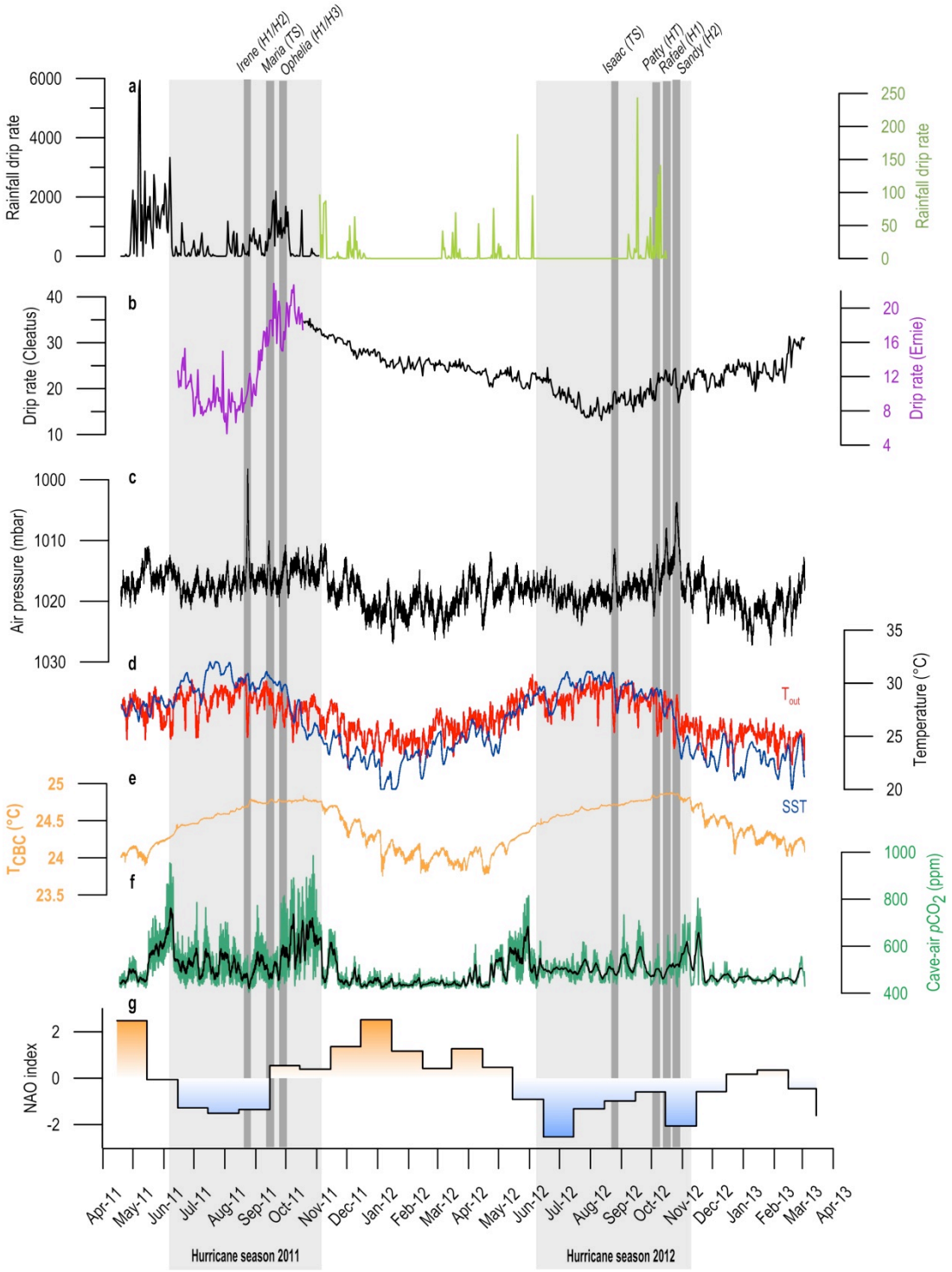

Figure 3.12. Meteorological and hydrological time series over the Conch Bar Caves monitoring period: (a) daily rainfall drip rate measured outside of the cave. Due to logger malfunctioning, we only consider the timing of the precipitation not its amount; (b) cave

daily average drip rate measured at Cleatus (black line) and Ernie (purple line) locations; (c) hourly pressure values measured outside the cave, (d) 25-point running average of hourly SSTs at Virginia Keys, Florida, USA (blue line) and T_{out} measured outside the cave (blue line), (e) T_{CBC} recorded at 3 hours interval, (f) cave pCO_2 concentration values recorded at 3 hours interval (green line) with a 13-point running average; (g) monthly NAO index. Grey bars indicate tropical cyclones with its intensity according Saffir-Simpson scale at the time of the island passing. Grey background indicates hurricane season.

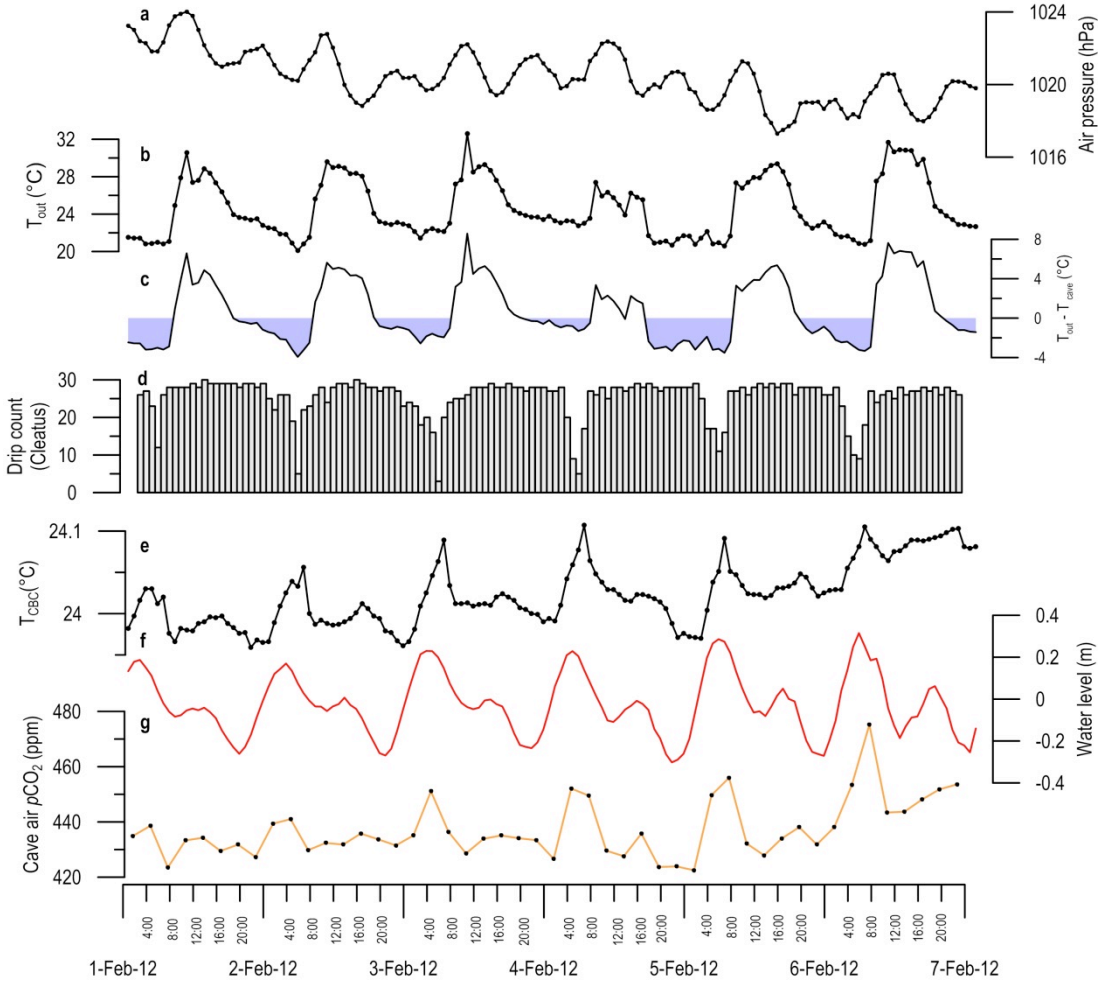

Figure 3.13. Cave monitoring results between 1st and 7th February 2012: (a) hourly air pressure values measured outside of CBC; (b) hourly air temperature values measured outside of CBC by Barotroll logger; (c) the temperature difference between outside and cave air. Blue shading indicates $T_{out} < T_{CBC}$; (d) hourly drip count at Cleatus location; (e) hourly cave temperature; (f) hourly water level measured at Arecibo, Puerto Rico (red line); (g) pCO_2 concentration values measured at three hours intervals.

Spectral analysis performed using software PAST on hourly pCO_2 data revealed significant peaks above the 99% confidence limit centred at 12 and 24 hours (, similarly to T_{CBC}, that suggests pCO_2 fluctuating with tides (Figure 3.13f and g). However, events like strong tropical cyclones transit can disturb those cycles (Figure 3.16f). Positive correlation (r = 0.21, p <0.01) exists between mean daily water level at Arecibo, Puerto Rico and pCO_2 in CBC, that is stronger (r > 0.3) in a cooler season (Figure 3.15b). Sparse vegetation above the cave likely does not contribute much to soil CO_2 and hence to CO_2 concentration in vadose water which suggests that dominant source of cave air CO_2 possibly comes from degassing from CO_2-rich groundwater. In CBC, groundwater is mainly seawater so factors controlling CO_2 concentration in seawater like marine plant and animal activity or atmospheric CO_2 concentration, also control cave pCO_2.

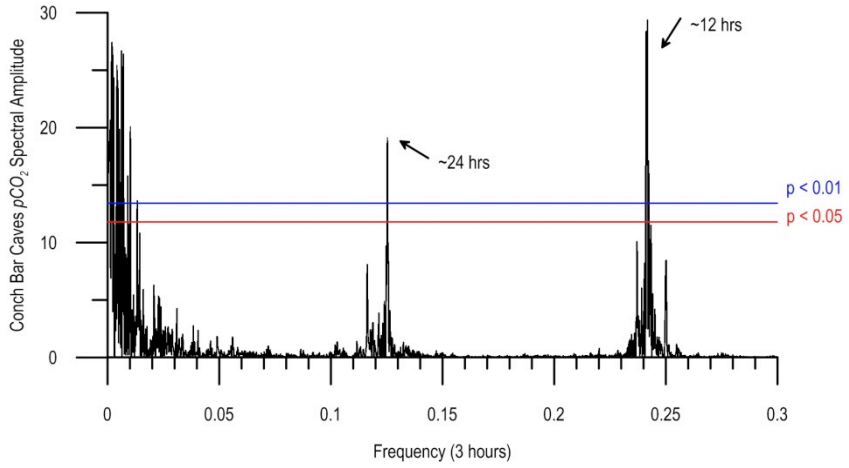

Figure 3.14. Results of spectral analysis of Conch Bar Caves hourly recorded pCO_2.

During the year, the period of lowest p_{cave} (<1018 hPa) occurred, as expected, during the second part of hurricane season (defined by NOAA, National Weather Service as period from June 1 to November 30 in the Atlantic, Caribbean, and the Gulf of Mexico) from September to November (Figure 3.12c). During the CBC monitoring

period, seven tropical cyclones passed the site that significantly depressed the cave air pressure (Figure 3.12c). The lowest recorded p_{cave} (998.2 hPa on Aug 24, 2011 at 4:00 GMT-5) occurred during Hurricane Irene passing in late August 2011 (Figure 3.16c). Air pressure higher than the mean of 1018 hPa occurs in a cool season, between December and March, coinciding with the generally positive NAO phase suggesting strong North Atlantic Subtropical High (NASH) and anticyclonic weather. The other peak in air pressure occurs in June (in 2011) and between June and August (in 2012). Summer peak in p_{cave} is probably associated with the intensification and expansion of the NASH that causes the Caribbean mid-summer drought (Gamble et al., 2008). The highest p_{cave} recorded (1027.3 hPa) during the cave monitoring period occurred on January 9 and January 28, 2013.

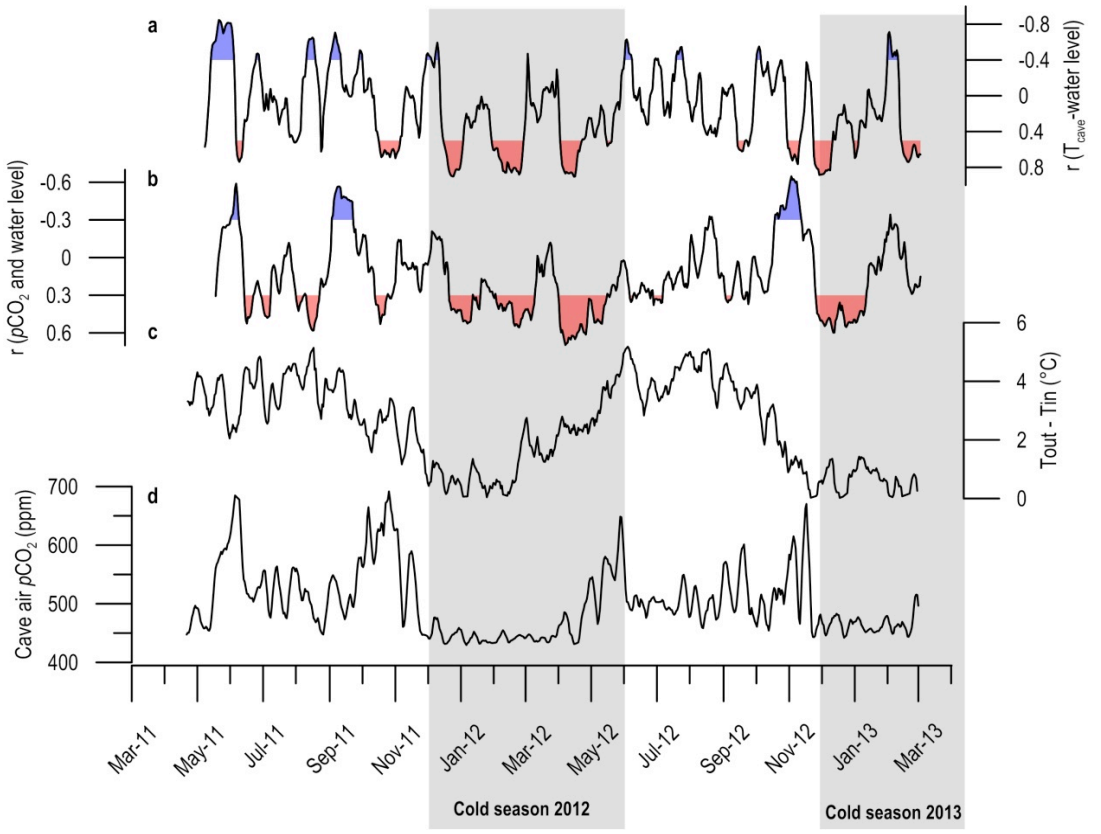

Figure 3.15. The 20-point running average of correlation between: (a) cave temperature and water level; (b) pCO_2 and water level**.** Plot (c) shows the daily difference in temperature

between outside and cave air. Plot (d) shows 5-point running average of cave pCO_2. Grey background indicates cold season.

The comparison of combined drip rate from two locations (Cleatus – black line and Emperor – purple line, Figure 3.12b) with rainfall (Figure 3.12a) recorded outside the cave reveals high CBC sensitivity to rainfall. Peaks in rainfall occur towards the end of hurricane season (September and October). In cool season rainfall is sporadic and hence the drip rate in CBC steadily decreases from the end of hurricane season (November) until the next hurricane season (Figure 3.12b). The rainfall data also reveals bimodal rainfall pattern with peaks in May/June and October/November suggesting mid-summer drought in between those peaks (Gamble et al., 2008).
The drip rate at 'Nipple' location was close to zero during the whole monitoring period; hence it is not shown on the graphs.

On a daily scale, the drip rate at Cleatus site decreases to almost zero during the high tide, suggesting temporal site flooding by the incoming tide (Figure 3.13d and Figure 3.16b). Spectral analysis of Cleatus hourly drip sum reveals periodicity at ~24, ~12, ~8, ~6 hours further corroborating that conclusion. Despite of recorded rainfall during hurricane Irene transit, the drip rate at Cleatus stayed stable (Figure 3.16b).

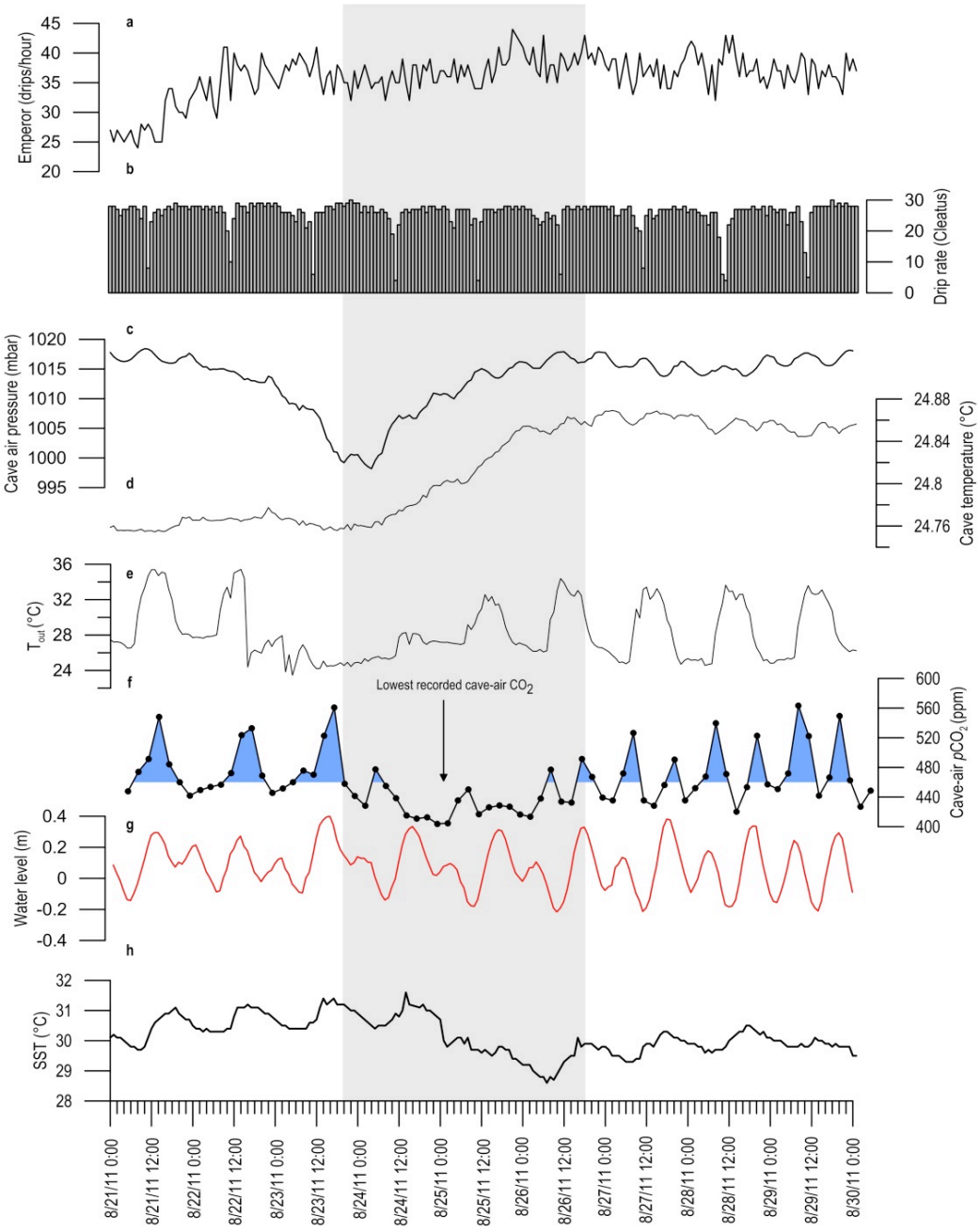

Figure 3.16. Cave monitoring results during Hurricane Irene passing between Aug 21 and Aug 30, 2011: a) drip sum at the Emperor location; b) drip sum at Cleatus location; c) hourly cave air pressure values; d) hourly cave temperature values; e) outside air temperature values; f) cave pCO_2 recorded three hours intervals, blue shading indicates values above mean; g) water level at Arecibo, Puerto Rico; h) SSTs measured at Virginia Key, USA. Grey shading indicates hurricane eye passing over Turks and Caicos Islands.

3.4. Discussion

3.4.1. Thermal conditions

Monitoring of two near-shore island caves located in the western Atlantic revealed that the presence of the brackish water impacts the temperature in a cave system, similarly to streams and lakes in inland caves. Strong positive correlation between near-shore cave temperature and regional SSTs and AMO phase suggests that successful cave temperature reconstruction from speleothems is interpretable in terms of SSTs and AMO index. However, the biggest difference between influence of the present water in near shore caves and inland caves is the tidal pulse that creates the cyclical pattern in the cave water temperature and the cave air above the water (Figure 3.13). This correlation between the cave temperature and tides is also observed in the other tropical caves, e.g. in Crescent Top Cave on San Salvador Island, Bahamas (Gamble et al., 2000). The temperature in the caves is also controlled by the tropical cyclones transit that results in a T_{cave} decrease before and during the storm and T_{cave} increase after the storm.

3.4.2. Cave ventilation

Similarly to inland caves (e.g. Kowalczk and Froelich (2010), Ridley et al. (2015b), Baldini et al. (2008), Spötl et al. (2005), Przylibski (1999), Frisia et al. (2005), Oster et al. (2012), Cowan et al. (2013)), LC and CBC are characterised by winter-dominated ventilation. The seasonal ventilation differences are driven by density differences between outside and cave air caused by seasonal differences in outside temperatures. Both caves, LC and CBC, reveal low (elevated) pCO_2 values with low (higher) temporal variability during the cold (warm) season. However diurnal CO_2

variability in near shore caves is also controlled by additional factors like: 1) the tide cycles, 2) the wind speed and its direction, 3) and associated rainfall.

Unlike inland caves, near shore caves reveal bimodal cave pCO_2 concentration distribution (similarly to the rainfall) with peaks in May-June and Oct-Nov in CBC and July and September in LC (Figure 3.17). High positive correlations between monthly pCO_2 and regional SSTs (r = 0.62 for CBC and r = 0.77 for LC) suggest that seawater temperature that controls CO_2 sea-air fluxes (Bates et al., 1998), could also seasonally act as a sink or source of CO_2 in the cave air.

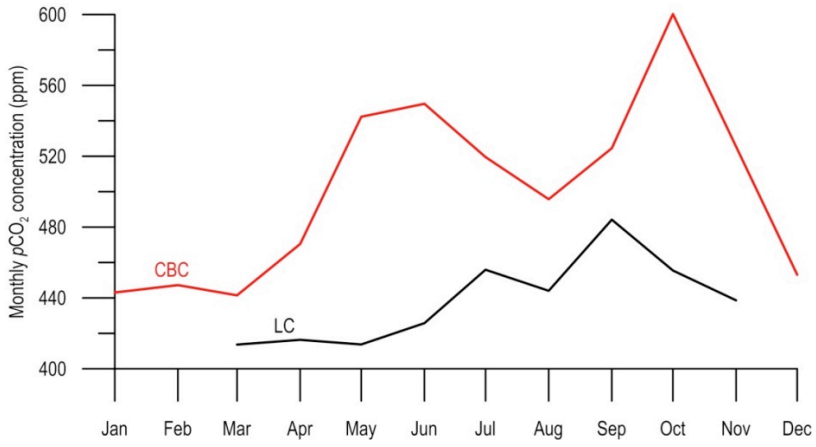

Figure 3.17. Monthly pCO_2 concentrations in Conch Bar Caves (red line; calculated between April 2011 and March 2013) and Leamington Cave (black line; calculated between March and November 2013) showing bimodal distribution.

3.4.3. Implications for paleoclimate studies

The seasonality in pCO_2 values can influence the saturation state for carbonate minerals, causing significant variations in growth rate or allowing corrosion to occur during a particular season (Fairchild and Baker, 2012). The mean annual pCO_2 value in CBC is slightly higher than in LC; however both show relatively low annual pCO_2

values (< 505 ppm) in comparison to inland caves e.g. Crag Cave (~3700 ppm, (Baldini, 2010)), Natural Bridge Caverns (~4935 ppm, (Cowan et al., 2013)), Obir Caves (~942 ppm, Spötl et al. (2005) suggesting very efficient ventilation that is favourable for all year round calcite precipitation making seasonal bias caused by cave-air CO_2 unlikely. Because seasonal variations in pCO_2 values are relatively low, the changes in water supply and drip rate exert a primarily control on calcite deposition rates within near-shore caves, making their stalagmites very sensitive to climate changes above the cave. Due to high correlation of present cave temperature and SSTs, the changes in the North Atlantic SSTs may also be recorded in stalagmites along with the rainfall amount.

Common presence of seawater in the near shore caves that fluctuates with tides and storm surges can result in temporal stalagmite flooding and their growth cessation. This suggests that the isotopic signal produced by the rainfall associated with the most intense tropical cyclones might not be recorded.

3.5. Conclusions

The results of almost five-years (in total) continuous monitoring of two near shore caves in the tropical western North Atlantic show a lot of similarities with the inland caves. The microclimate and ventilation dynamics of Leamington Cave and Conch Bar Caves, are controlled mainly by 1) seasonal temperature differences between outside and cave air (like inland caves), 2) wind and associated rainfall, but because of the connection of phreatic water with seawater, the microclimate of near shore caves is also modulated by 3) the seawater temperature, and 4) water level

fluctuations that further corroborates the results of flank margin caves monitoring in Bahamas and Puerto Rico (Gamble et al., 2000).

Daily and seasonal efficient ventilation of near shore caves suggests that they are favourable environment for speleothem formation. This also implies that seasonal changes in water supply and drip rate exert a primarily control on calcite deposition rates within near-shore caves, rather net CO_2 flux to the cave, as opposed to some inland caves (e.g. Kowalczk and Froelich (2010)). However, projected sea-level rise associated with global warming may result in the near-shore caves flooding that would inhibit speleothem growth and make those caves inaccessible for tourists.

Future research in near shore caves should focus on other factors that play role in calcite deposition like the seasonal concentration of calcium in the drip water that could bias climate signal incorporated in stalagmites.

Chapter 4

Reconstructing high-resolution climate using CT scanning of unsectioned stalagmites: a case study identifying the mid-Holocene onset of the Mediterranean climate in southern Iberia[1]

[1] A version of this chapter is published as: Walczak, I. W. *et al.* Reconstructing high-resolution climate using CT scanning of unsectioned stalagmites: A case study identifying the mid-Holocene onset of the Mediterranean climate in southern Iberia. *Quaternary Science Reviews* **127**, 117-128.

Abstract

The forcing mechanisms responsible for the mid-Holocene onset of the Mediterranean-type climate in south-western Europe are currently unclear, but understanding these is critical for accurate climate projections under future greenhouse gas-induced warming. Additionally, regional studies that present conflicting patterns for the onset and advancement of Mediterranean climatic conditions complicate definitively ascribing causality. Here, we use a new high resolution stalagmite density record obtained non-destructively using Computed Tomography (CT) scanning to reconstruct southern Iberian climate between 9.3 and 2.9 ka BP. We suggest that stalagmite density can be used as a water-excess proxy, with lower densities associated with more variable drip rates, possibly reflecting increased seasonality consistent with expectations from previous studies of speleothem textures and crystal fabrics. Our results reveal an early Holocene humid interval and mid-Holocene year-round aridity that preceded the onset of Mediterranean climate at 5.3 ka BP in southern Iberia. Using this new dataset combined with previously published results, we link the gradual advancement of Mediterranean climate to the southward migration of the North Atlantic Subtropical High induced by an orbitally driven decrease in Northern Hemisphere insolation. Future anthropogenic warming could result in a reversal of this trend, a northward migration of the North Atlantic Subtropical High, and a return to year-round aridity in south-western Europe.

4.1. Introduction

Stalagmites are excellent climate archives because they yield multi-proxy information (e.g. stable isotope, trace element, and petrographic information) constrained by a radiometric chronology. Additionally, at relatively undisturbed sites, they can complement palaeoclimate information from well dated archives (e.g. sediment core-based studies) (Fairchild et al., 2006, Henderson, 2006). High-resolution stalagmite climate reconstructions are usually based on information gleaned from a single plane cut through the sample, and typically attempt to follow the stalagmite's growth axis in two dimensions. However, this approach ignores possible growth axis shifts that could occur out of this plane which in turn could dramatically affect climate interpretations, for example through off-axis stable isotope kinetic enrichment (Mickler et al., 2004b). To date, no high-resolution stalagmite climate proxy research has taken account of such three-dimensional growth axis shifts, which can occur due to changes in infiltration pathway, lateral growth of soda straws, following subsidence of cave floors and/or seismic activity (Becker et al., 2006). Taking these potential shifts into account is particularly important in seismically active areas, like southern Iberia, which lies close to the convergence zone between the Eurasian and African Plates (Gràcia et al., 2010). X-ray computed tomography (CT scanning) through internal three-dimensional density mapping of opaque objects, is able to provide information about stalagmite growth axis shifts (Mickler et al., 2004b) and internal porosity (Zisu et al., 2012). More information about CT scanning can be found in Chapter 1.

The southern Iberian Peninsula is currently characterised by a Mediterranean climate (Csa in Köppen-Geiger classification, Peel et al. (2007)), with dry (precipitation of the driest month in summer is less than 40 mm) and hot (temperature of the hottest month is over 22^0C) summers and wet winters caused by the seasonal meridional migration of the North Atlantic Subtropical High (NASH) (Harding et al., 2009). The NASH (often also referred to as the Bermuda or Azores High (Davis et al., 1997)) is the semi-permanent subtropical anticyclone over the North Atlantic Ocean basin that forms at the descending limb of Hadley cell circulation. The NASH exerts a major influence on the present-day weather and climate of Iberia by controlling the latitude of North Atlantic westerlies (Marshall et al., 2001, Tzedakis et al., 2009). The contrast between winter and summer precipitation in Iberia is due largely to the tendency for the NASH to migrate northwards over Iberia in summer (resulting in hot, dry conditions) and to migrate southwards in winter (bringing increased rainfall with the westerlies) (Harding et al., 2009, Trigo et al., 2004). In the present day, interannual variability in the strength and position of the NASH is linked to the state of the North Atlantic Oscillation (NAO) (Souza and Cavalcanti, 2009).

Several studies suggest that the western Mediterranean region, located at critical geographic and atmospheric boundaries, has experienced abrupt climatic shifts over the Holocene (Dorado Valiño et al., 2002, Pérez-Obiol et al., 2011, Jambrina-Enríquez et al., 2014, Jalut et al., 2009, Roberts et al., 2011, Moreno et al., 2011, Anderson et al., 2011, García-Alix et al., 2012, Jiménez-Moreno and Anderson, 2012, Fletcher et al., 2013, Baldini, 2007, Carrión, 2002). Jalut et al. (2009) examined circum-Mediterranean pollen data to derive three climatic phases for the Holocene: i) the early Holocene (11.5-7 ka BP) characterised by increased rainfall,

ii) the mid-Holocene (7-5.5 ka BP), characterised by increased variability, linked to decreasing Northern Hemisphere insolation, and iii) the late Holocene, characterised by the onset of a drying trend at ~5.5 ka BP. This drying trend may reflect decreased annual rainfall induced by substantially lower summer rainfall, with winters remaining cool and wet. Typically this transition into seasonal aridity is interpreted as the Holocene onset of the Mediterranean climate in Iberia. Existing Iberian pollen and lake sediment records (Figure 4.1) reveal considerable variability in the timing and character of these phases thereby, impeding our understanding of Holocene climate in the region (Dorado Valiño et al., 2002, Pérez-Obiol et al., 2011, Jambrina-Enríquez et al., 2014, Jalut et al., 2009, Roberts et al., 2011, Moreno et al., 2011, Anderson et al., 2011, García-Alix et al., 2012, Jiménez-Moreno and Anderson, 2012, Carrión et al., 2010). Thus, the spatiotemporal pattern of Mediterranean climate advancement within the Iberian Peninsula has remained difficult to constrain. Studies along the eastern transect of the Iberian eastern margin concluded that the Mediterranean climate advanced from the south (beginning at 10 ka BP) towards the north (between 3.3 and 1 ka BP) (Jalut et al., 2000, Jalut et al., 1997). This contrasts with Magny et al. (2013) who argued for maximum (minimum) summer dryness north (south) of 40^{0}N in the central Mediterranean (during the early to mid-Holocene). Using a combination of lacustrine and marine records along a north-south transect in the central Mediterranean, Magny et al. (2013) highlighted contrasting patterns of palaeohydrological change south and north of 40^{0}N that developed in response to a combination of orbital, ice-sheet and solar forcings. Many Iberian climate reconstructions are pollen-based and are often hampered by substantial chronological uncertainties. Adding to this complexity, archaeological evidence indicates substantially increased human activity in the region since 7.5-7 ka

BP (Pérez-Obiol et al., 2011) that may have compromised the link between pollen assemblages and paleoclimatic conditions at some sites. Increased sclerophyllous (adapted to prevent moisture loss) pollen assemblages, interpreted as reflecting the onset of Mediterranean climate (Jalut et al., 1997), could instead partly reflect deforestation and other anthropogenic factors. Although general Holocene climate shifts in the western Mediterranean have been proposed, the regional patterns, especially in southern Iberia, and the underlying forcing mechanisms for this variability remain unclear (Carrión et al., 2010). New well-dated records from this region of southern Spain are therefore crucial to reconstruct Mediterranean climate advancement (supplementing pollen data) and to better understand the links between Iberian climate and North Atlantic atmospheric dynamics.

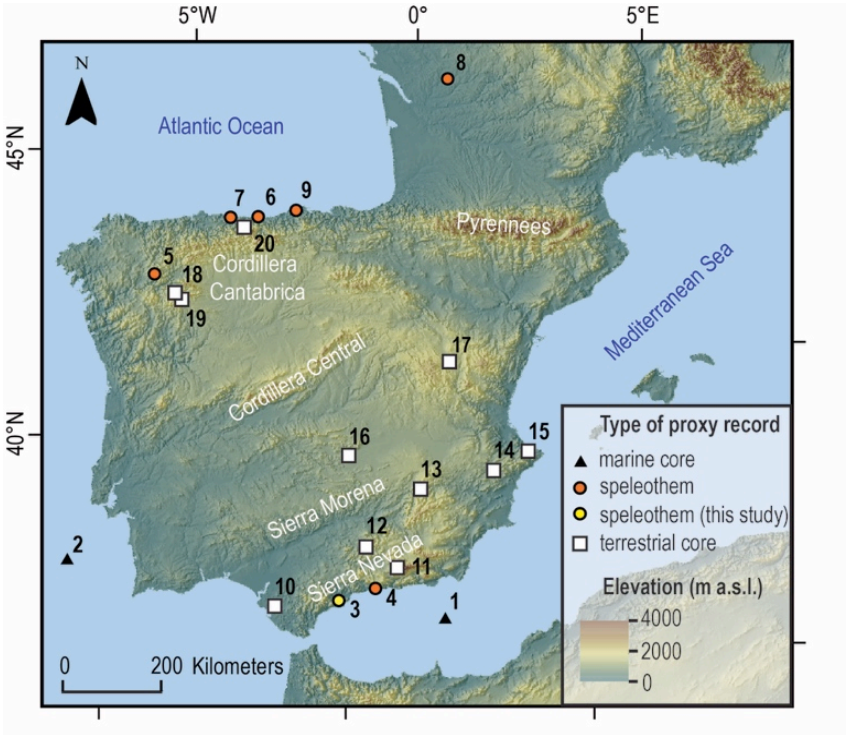

Figure 4.1 Location of palaeoclimate proxy records mentioned in the text. Marine cores (black triangles): (1) MD95-2043 (Fletcher et al., 2013), (2) MD95-2042 (Chabaud et al., 2014); speleothems from (3) El Refugio Cave (this study, yellow circle); speleothems (red circle) from (4) Nerja Cave (McMillan, 2006), (5) Cova de Arcoia (Railsback et al., 2011),

(6) Pindal (Stoll et al., 2013), (7) Cueva Rosa (Stoll et al., 2013), (8) Villars Cave (Genty et al., 2006) (9) La Garma Cave (Baldini, 2007, Baldini et al., 2015); terrestrial cores (white squares) from (10) Laguna de Medina (Reed et al., 2001), (11) Borreguiles de la Virgen (García-Alix et al., 2012), (12) Laguna de Rio Seco (Anderson et al., 2011), (13) Siles (Carrión, 2002), (14) Salinas (Burjachs and Riera, 1995), (15) Cabo de Gata (Jalut et al., 2000), (16) La Mancha Plain (Dorado Valiño et al., 2002), (17) Villarquemado (Aranbarri et al., 2014), (18) Sanabria Lake (Jambrina-Enríquez et al., 2014), (19) Laguna de la Roya (Allen et al., 1996), (20) Lago Enol (Moreno et al., 2011).

Stalagmite-based Holocene climate reconstructions in the western Mediterranean are scarce, and are mostly from the northern Iberian Peninsula (Stoll et al., 2013, Railsback et al., 2011, Baldini, 2007, Domínguez-Villar et al., 2008, Martín-Chivelet et al., 2011), the Mediterranean-influenced region of south-eastern France (McDermott et al., 1999, McMillan et al., 2005, Genty et al., 2006) and coastal central Italy (Zanchetta et al., 2007). Currently, the most complete stalagmite-based regional palaeoclimate reconstructions are from caves in northern Iberia and southern Iberia is underrepresented in this respect.

Here we reconstruct Holocene climate variability in southern Iberia using a novel, non-destructive method of generating a high-resolution stalagmite calcite density record using Computed Tomography of an unsectioned stalagmite (REF-07) from El Refugio Cave. We also present the first precise radiometric stalagmite chronology created without sectioning the sample, which tracks the stalagmite growth axis in three dimensions. We then compare this new record with other Northern Hemisphere proxy records spanning 10°N to 70°N, to clarify the mechanisms underlying Mediterranean climate advancement and discuss the implications for Mediterranean climate under continued anthropogenic warming in the future.

4.2. Methods

4.2.1. Sample

In this study, we used the 36-cm tall, unsectioned stalagmite REF-07 collected from the floor of the main chamber of El Refugio Cave, approximately 20 m from the entrance and on the interior side of a 3 m high flowstone deposit that impedes air circulation from the cave exterior. The stalagmite was deposited on the calcified surface of a breakdown block along with several other stalagmites of similar height and dimensions. Stalagmite REF-07 was CT scanned and then U-series dated (typical 2σ analytical age errors are between 0.04 and 0.08 ka) without sectioning the sample. CT scanning-derived stalagmite density variations were then used for palaeoclimate reconstruction. Due to widespread over-collection of stalagmites, the REF-07 could be returned to the cave unsectioned and reattached for cultural conservation of the cave site, without generating additional proxy records from a sectioned slab.

4.2.2. CT scanning

Stalagmite REF-07 was CT scanned at North Durham University Hospital, Durham, UK, before and after U-Series powder extraction (Figure 4.2). A Toshiba Aquillion 64 CT Scanner was operated at a tube voltage and current intensity of 135 kV and 80mA, respectively, with small focal spot size (0.9/0.8) and FC30 filter type. The scanner was set to a 0.5 mm slice thickness, with a 0.3 mm overlap between successive scans (slice spacing), resulting in a voxel size of 0.21 x 0.21 x 0.3 mm and a spatial resolution along the growth axis of 0.21 mm. Reconstructed images were exported as 512 x 512 16-bit signed Digital Imaging and Communications in Medicine (DICOM) files.

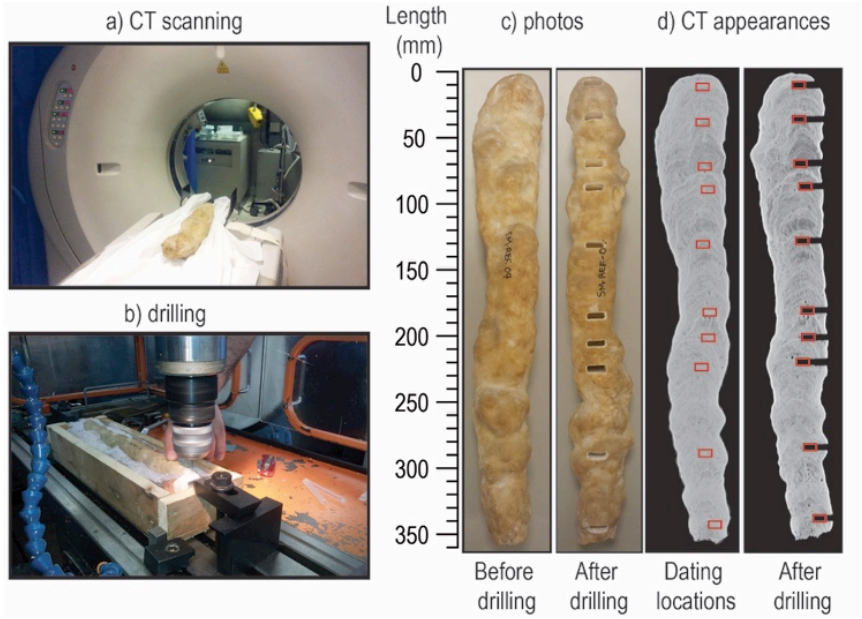

Figure 4.2. Procedure for dating the unsectioned REF-07 stalagmite. (a) CT scanning of REF-07 at North Durham University Hospital, UK; (b) drilling REF-07 to obtain samples for U-Th dating at the Durham University Physics Workshop; (c) photos of REF-07 before drilling and after drilling; (d) CT appearances of REF-07 before drilling with planned dating locations (red rectangles) and CT appearance of REF-07 after drilling.

The CT technique offers a number of significant advantages over conventional techniques, one of which is relatively fast data reproducibility. The technique also allows complete three-dimensional characterisation of a sample (Video S1) rather than a single plane or transect, more insightful understanding of stalagmite growth related to climatic and non-climatic mechanisms, and high-resolution density data that are interpretable in terms of climate. Moreover, by additional scanning using magnetic resonance imaging (MRI), it is possible to map fluid inclusions within stalagmites for palaeowater analysis (Zisu et al., 2012).

4.2.3. U-Th sampling of unsectioned stalagmite

CT visualisations were used to determine precise locations and depths at which to drill for dating powders. Emphasis was placed on dating locations before and after

potential hiatuses that were observable as thin high-density laminae before or after growth axis shifts. We also avoided collecting powder from the core to keep it for potential geochemical analysis if the stalagmite were to be sectioned. To obtain powder samples for U-Th dating, REF-07 was covered in plastic wrap and placed in a rectangular wooden box filled with air-hardening modelling clay (Figure 4.2) to stabilize the sample. The stalagmite was drilled using a Proto-Trak Model Pro1500 milling machine with a three mm diameter carbide drill bit at the Durham University Physics Workshop. All powder milled before reaching the location of the powder for dating was removed by vacuuming. We drilled ten pockets with an area sampled for dating of 14 x 5 x 10 mm size, which gave around 1.3 g of powder per sample that was later dated at the University of Bristol, UK, following the procedure described in Hoffmann et al. (2007). One dating point (REF-07-07) was out of stratigraphic order (Table 1), and was excluded from the age model. Consequently, nine ^{230}Th dates constrain the age-depth relationship (Figure 4.3) produced by COPRA model (COnstructing Proxy Record from Age models) (Breitenbach et al., 2012). This median age model assigns a precise time scale to CT numbers using 2000 Monte Carlo simulations and linear interpolation. COPRA also allows for a reliable and reproducible age reversal definition, hiatus detection, error estimation, and inclusion (if available) of layer counted intervals to improve overall confidence intervals. All dates are reported in ka BP (BP = before 1950 A.D.).

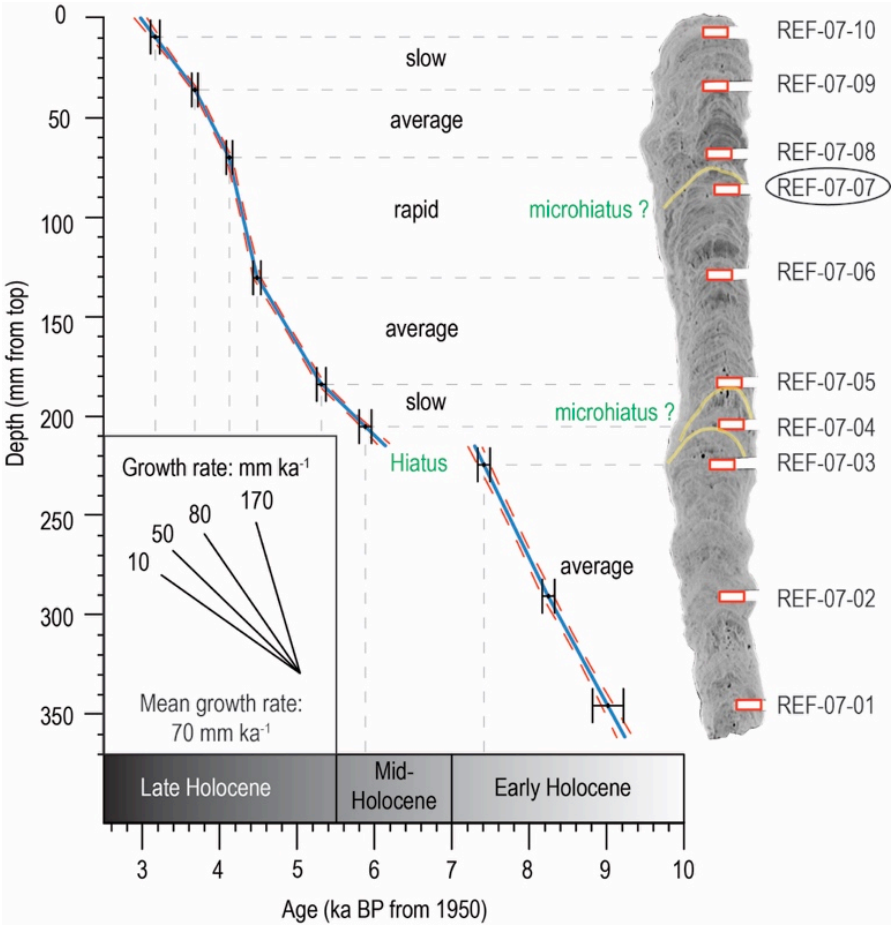

Figure 4.3. COPRA (Breitenbach et al., 2012) median age model for stalagmite REF-07 (blue bold line) with 95% confidence bounds (red dashed lines) constrained by nine U-series dates (black dots with error bars). The circled REF-07-07 date is out of stratigraphic order (see Table 1) and was excluded from the age model. Labels: "slow", "average", "rapid", refer to the growth rates in ranges between 10 and 50 mm ka^{-1}, 50 and 80 km ka^{-1}, 80 and 170 mm ka^{-1}, respectively. CT appearance of REF-07, shown to the right of the depth-age model, was obtained after powder collection for dating. Red rectangles indicate powder collection locations. More details are shown in Table 1. The Holocene subdivision is based on the tripartite model (Jalut et al., 2009) inferred from pollen records.

Table 4.1. U and Th concentrations, isotopic activity ratios and U–Th ages for sub-samples of stalagmite REF-07. Analytical errors are 2σ of the mean. $(^{230}Th/^{238}U) = 1 - e^{-\lambda 230T} + (\delta^{234}U_{measured}/1000)(\lambda_{230}/(\lambda_{230} - \lambda_{234}))(1 - e^{-(\lambda 230 - \lambda 234)}T)$, where T is the age $\delta^{234}U = ((^{234}U/^{238}U) - 1) \times 1000$. Decay constants are 9.1577 x 10^{-6} yr^{-1} for ^{230}Th, 2.826 x 10^{-6} yr^{-1} for ^{234}U (Cheng et al., 2000), and 1.55125 x 10^{-10} yr^{-1} for ^{238}U (Jaffey et al., 1971). *The degree of detrital ^{230}Th contamination is indicated by the measured ($^{230}Th/^{232}Th$); an initial ($^{238}U/^{232}Th$) of 0.8 ± 0.2 is used to obtain a corrected U–Th age.

Lab code	Sample ID	Depth from the top (mm)	^{238}U (ng/g^{-1})	±	^{232}Th (ng/g^{-1})	±	Measured activity ratios						Corrected Age* (ka)	+	-	Corrected Age* (ka from 1950)	$(^{234}U/^{238}U)_{Ai}$	±
							$(^{230}Th/^{232}Th)_A$	±	$(^{230}Th/^{238}U)_A$	±	$(^{234}U/^{238}U)_A$	±						
BIG-UTh-P77	REF-07-10	9.5	190.3	0.8	0.4728	0.0035	36	0.52	0.02955	0.00041	0.9935	0.0016	3.23	0.06	0.06	3.16	0.9934	0.0017
BIG-UTh-P76	REF-07-09	36.1	195.7	0.8	0.0301	0.0004	663	6.56	0.03336	0.00031	0.9903	0.0018	3.74	0.04	0.04	3.68	0.9902	0.0018
BIG-UTh-P75	REF-07-08	70.1	227.7	0.9	0.0742	0.0006	350	3.31	0.03731	0.00034	0.9902	0.0018	4.18	0.04	0.04	4.12	0.9901	0.0018
BIG-UTh-P83	REF-07-07	87.9	256.0	1.1	0.0348	0.0003	2662	14.40	0.11834	0.00063	0.9927	0.0016	13.86	0.08	0.08	13.80	0.9924	0.0017
BIG-UTh-P82	REF-07-06	130.5	230.2	1.0	0.0504	0.0005	564	5.33	0.04047	0.00040	0.9920	0.0018	4.54	0.05	0.05	4.48	0.9919	0.0018
BIG-UTh-P81	REF-07-05	184.1	259.3	1.2	0.2211	0.0017	171	1.28	0.04779	0.00037	0.9911	0.0018	5.37	0.05	0.05	5.31	0.9909	0.0018
BIG-UTh-P80	REF-07-04	205.3	233.5	1.0	0.4266	0.0030	89	0.75	0.05319	0.00042	0.9959	0.0017	5.94	0.06	0.06	5.88	0.9958	0.0017
BIG-UTh-P79	REF-07-03	224.5	191.7	0.8	0.2508	0.0018	155	1.57	0.06630	0.00066	0.9975	0.0019	7.47	0.08	0.08	7.41	0.9974	0.0019
BIG-UTh-P88	REF-07-02	290.5	144.6	0.6	0.2042	0.0016	160	1.42	0.07377	0.00062	1.0023	0.0018	8.31	0.08	0.08	8.24	1.0024	0.0019
BIG-UTh-P87	REF-07-01	345.5	154.5	0.6	0.3072	0.0021	123	0.96	0.08025	0.00061	1.0002	0.0017	9.08	0.08	0.08	9.01	1.0002	0.0018

4.2.4. Data analysis

CT image processing and data analysis was performed using ImageJ software (Abràmoff et al., 2004). The volume rendering produced enabled visualisation of CT numbers as greyscale corresponding to relative X-ray attenuation, which is a function of elemental composition and density (Mickler et al., 2004b). CT numbers, expressed in Hounsfield Units (HU), describe the intensity of the transmitted X-ray beam, and are calculated from relative values of the linear voxel attenuation coefficient ($\mu_1 voxel$) normalised to the reference material of water ($\mu_1 water$), and multiplied by a magnifying integer constant (K): $CT\ number = \frac{K * (\mu_{voxel} - \mu_{water})}{\mu_{water}}$ (Goldman, 2007). To display CT values of REF-07 we converted greyscale values (x) using the relationship described by the equation: $CT\ number = x - 32768$. The relationship between CT number and greyscale needs to be established individually for each scanned sample, as it varies depending on CT scanner settings. CT numbers are used here as an expression of stalagmite density variations.

REF-07 CT visualisations enabled selection of six different planes that virtually section the sample, and three different tracks (each parallel to the growth axis) on each virtual plane provide density data (Figure 4.4). Excluding suspected macrovoids with CT numbers below 1000 HU, the mean CT number on these 18 tracks is 2064 HU, and this value was chosen to define the threshold for determining relatively dense (≥ 2064 HU) versus relatively porous (< 2064 HU) stalagmite calcite.

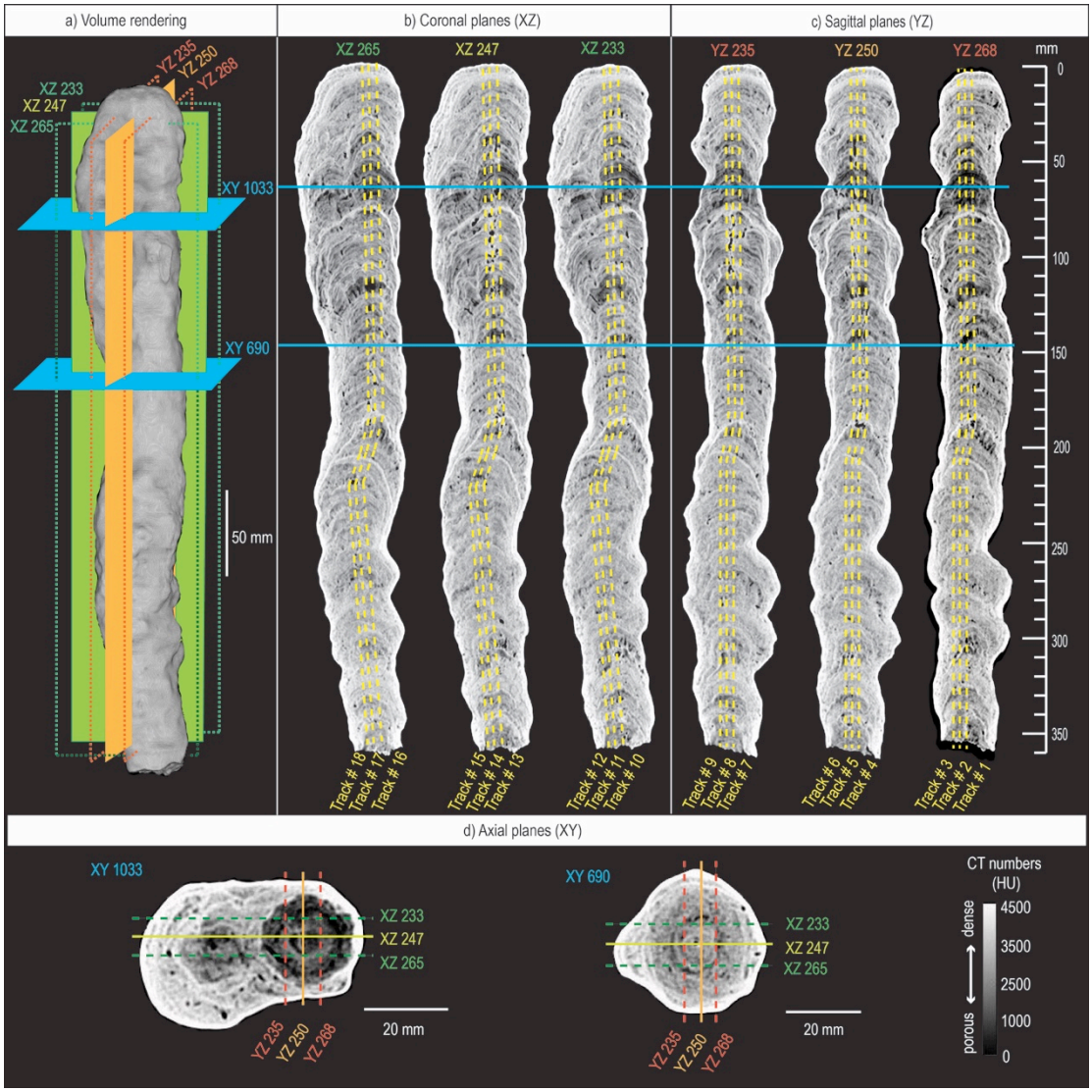

Figure 4.4. CT visualisations of stalagmite REF-07. a) volume rendering with marked virtual sectioning planes that are shown in b) coronal (shades of green); c) sagittal (shades of orange) and d) axial (blue) view. Density data obtained along 18 different tracks (yellow dashed lines in b and c) were averaged to calculate mean CT number shown in Figure 4.7f.

4.3. Results

4.3.1. Age model

To our knowledge, this study presents the first precise (typical 2σ analytical age errors between 0.04 and 0.08 ka; Table 4.1) radiometric stalagmite chronology created without sectioning the sample and the first to track the growth axis in three dimensions (Figure 4.4 and Figure 4.5). Although errors associated with the

'conventional' method (powder samples for dating drilled from a single sectioned plane) are difficult to quantify, some error could arise in cases of unidentified growth axis shifts, and this new technique minimises these errors.

The age model indicates that stalagmite REF-07 grew from 9.25 to 2.97 ka BP with a 70 mm ka^{-1} mean growth rate (Figure 4.3) resulting in a stalagmite density record temporal resolution of ~ five years. The slowest growth (37 mm ka^{-1}) occurred between 5.87 and 5.31 ka BP. This slow growth interval immediately follows a growth hiatus located at 215 mm depth from the top (dated at between 7.30 and 6.14 ka BP). After 4.12 ka BP, REF-07 growth rates decrease steadily until stalagmite growth cessation shortly after the youngest U-Th date at 3.16 ka BP.

4.3.2. Growth axis shifts

Quantitative CT analysis of the internal density structure offers advantages over standard techniques as it provides information about the three-dimensional material density distribution in the sample (Tanaka et al., 2011). This enables identification of any potential growth axis shifts and helps in selecting the optimum sectioning plane for future geochemical and petrographic analysis of the sample.

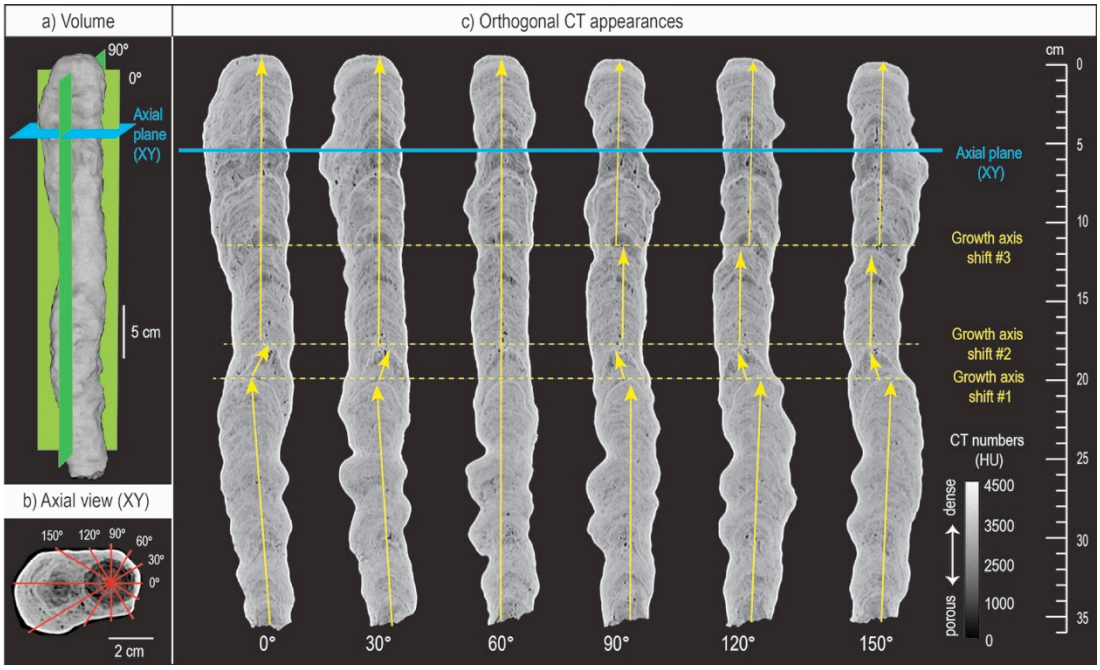

Figure 4.5. REF-07 growth axis shifts revealed by CT scanning: a) 3D volume reconstruction with marked location of axial plane (blue) and two orthogonal views (green); b) axial view at the location is marked as a blue line in c) and as a blue plane in a); c) different orthogonal views depending on the sectioning angle, marked as red lines in b).

Three-dimensional CT images of the REF-07 stalagmite (Video S1), presented in greyscale (the lighter the colour, the denser the material), illustrate its complex internal structure (Figure 4.4 and Figure 4.5). A series of virtual 30° rotations of the sample showing possible sectioning planes reveals three major growth axis shifts (Figure 4.5) at depths of 120, 180 and 210 mm from the top, dated ca. 4.44 ± 0.04 ka BP, ca. 5.36 ± 0.05 ka BP and ca. between 7.30 and 6.14 ka BP (coinciding with a hiatus), respectively.

CT image analysis demonstrates that these three growth axis shifts are not apparent at certain rotation angles (e.g. at 60° or any between 0 and 30°) (Figure 4.5). CT scanning of a stalagmite before sectioning the sample for geochemical analysis

is therefore ideal to avoid sampling off the growth axis, thus minimising off-axis isotopic disequilibrium fractionation effects.

4.3.3. Stalagmite density

CT scanning revealed that stalagmite density during REF-07 growth varied substantially. The lower 150 mm portion of the stalagmite (below the oldest growth axis shift) is relatively dense (mean CT number = 2155 HU), with only minor density variations (σ = 145 HU). Unlike the older part of REF-07, the interval between 50 and 180 mm from the top is characterised by progressively decreasing density (mean CT number = 1918 HU), and substantial density variability (σ = 267 HU). In the upper 50 mm, stalagmite density increases (mean CT number = 2111 HU, σ = 299 HU) and growth rates approximate mean values again. Very high density 'laminae' (over 2400 HU) are present close to 76, 185 and 215 mm from the top of the stalagmite and are dated at 4.16 ka BP, 5.3 ka BP, and at 7.3 ka BP (hiatus), respectively.

4.4. Discussion

4.4.1. Stalagmite density as a climate proxy

In caves with limited seasonal cave air exchange, water-excess and hence drip rate and regime is the dominant control on stalagmite calcite density, with relatively constant and high drip rates promoting denser (columnar open) calcite, and more variable drip rates promoting more porous (columnar microcrystalline or dendritic) calcite (Zhang et al., 2010, Genty and Quinie, 1996, Frisia et al., 2000, Frisia, 2015) due to incomplete crystal coalescence (Figure 4.6). Consequently, a period of constant water excess over several years produces relatively denser stalagmites

(Genty and Quinie, 1996). However, in more vigorously ventilated caves with seasonal cave air pCO_2 shifts of several thousand ppm, cave air pCO_2 variability determines density, with the lower cave air pCO_2 season promoting denser calcite precipitation (Boch et al., 2011, Mattey et al., 2008). Abrupt changes in vegetation cover (e.g. due to brush clearing) can also affect cave air pCO_2 variability, controlling the degree of degassing, and impacting calcite precipitation (Wong and Banner, 2010). However no evidence for past human interferences at Refugio Cave exists. Cave monitoring (Mudarra et al., 2009) between 2003 and 2006 reveals minimal cave air exchange (mean seasonal cave air pCO_2 variability is less than 1000 ppm) with increased ventilation in the winter, which supports a water-excess control on stalagmite density variations at this site. At other monitored cave sites (e.g. Inner Space Cavern in Texas, New St. Michael's Cave in Gibraltar) the degree of ventilation on an interannual basis is thought unlikely to have changed much through time (Banner et al., 2007, Mattey et al., 2010), and this is most likely true for El Refugio Cave as well.

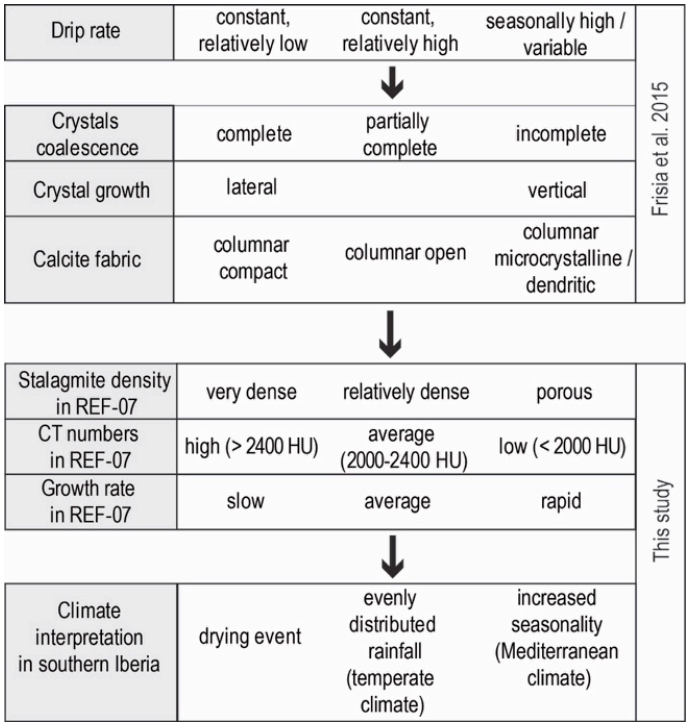

Figure 4.6. Drip rate and flow regime controls on calcite fabric (assuming minimal ventilation effects) from Frisia (2015), and links to stalagmite density derived from CT scanning of REF-07 stalagmite.

High stalagmite density with minor density variations and average growth rates in the lower 150 mm section of REF-07 are interpreted as reflecting relatively high annual rainfall. This suggests more evenly distributed annual rainfall than at present, with a more constant drip rate promoting dense, columnar calcite (*sensu* Frisia et al. (2000)) (Figure 4.6). In contrast, the younger part of the stalagmite, characterised by lower density, suggests decreasing total rainfall and more variable drip rates, possibly reflecting increased seasonality in rainfall. Drip-water characterised by a lower calcite supersaturation and lower *p*H promotes enhanced vertical crystal growth and high abundance of elongated pores, consequently forming more porous calcite (Boch et al., 2011) with a dendritic texture (Frisia et al., 2000). This type of calcite is particularly abundant in the section between 50 and 120 mm.

4.4.2. Holocene climate in the western Mediterranean

Early Holocene

Between 9.2 and 7.3 ka BP (herein referred to as the early Holocene), REF-07 exhibits average growth rates (Figure 4.3) and CT numbers higher than the mean (2064 HU) (Figure 4.7f) suggesting relatively stable drip rates that promoted dense calcite precipitation. This suggests that in the early Holocene, rainfall in southern Iberia was more evenly distributed throughout the year, typical of a more temperate climate lacking a clear dry season. An early Holocene humid phase is also supported by several regional pollen and palaeolimnological records (Moreno et al., 2011, Dorado Valiño et al., 2002, Jambrina-Enríquez et al., 2014, Jalut et al., 2009, Anderson et al., 2011, García-Alix et al., 2012, Jiménez-Moreno and Anderson, 2012, Fletcher et al., 2013, Pérez-Obiol et al., 2011, Reed et al., 2001), the Corchia cave record (Zanchetta et al., 2007) from central Italy (Figure 4.7e), the marine pollen record from Alboran Sea (Combourieu-Nebout et al., 2013), and the recently published gridded mean annual winter precipitation anomalies in parts of coastal SE Iberia

at 9 ka and at 7 ka BP based on pollen data (Mauri et al., 2015). Relatively humid conditions in the early Holocene parts of south-western Iberia coincide with very low flood activity in the southern European Alps (Figure 4.7b) (Wirth et al., 2013), with reconstructed negative winter precipitation anomalies in the Alps (relative to the late preindustrial), particularly around 9 ka and 8 ka BP (Mauri et al., 2015) and high lake levels from Aspvatnet lake, northern Norway (Figure 4.7a), that were interpreted to reflect an increase in winter precipitation (Bakke et al., 2005). This inverse precipitation relationship between the southern Iberia and the southern European Alps differs from the present-day North Atlantic Oscillation (NAO)

teleconnection that results in tight coupling between winter precipitation in these two regions (Comas-Bru and McDermott, 2014). This in turn may suggest that the present-day NAO was established later in the Holocene, and that a northward NASH migration, or its deepening, redirected the westerlies northward bringing moisture to the British Isles and Scandinavia. Humid conditions in southern Iberia combined with drier and/or warmer conditions inferred from records from northern Iberia (Railsback et al., 2011, Allen et al., 1996, Aranbarri et al., 2014, Baldini, 2007), southern France (Genty et al., 2006), the southern Alps (Wirth et al., 2013) and wetter conditions in Norway (Bakke et al., 2005) are consistent with a northward repositioned NASH (Figure 4.8a). Wetter conditions in southern Iberia could have resulted from more Mediterranean derived moisture that did not affect northern Iberia.

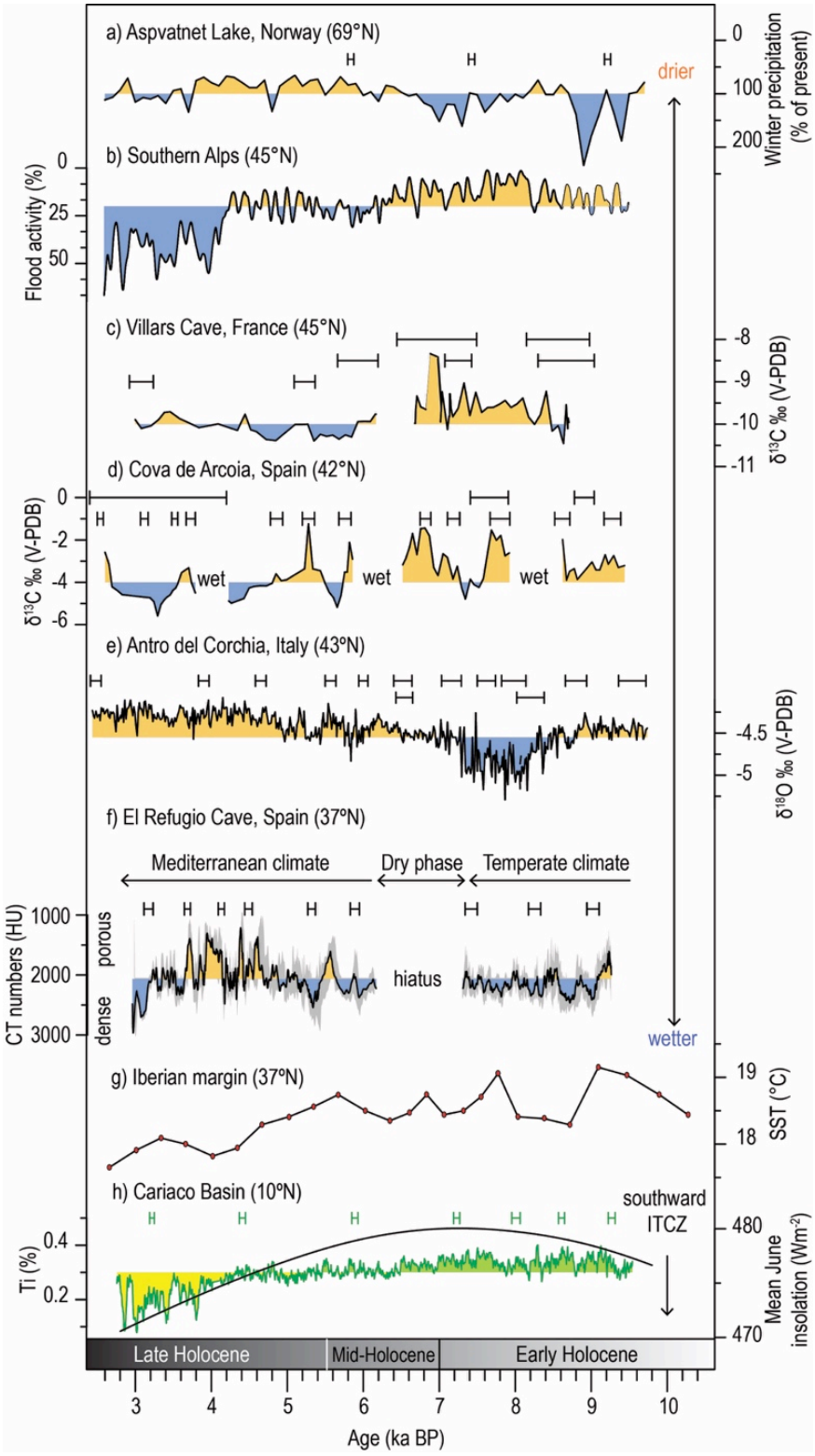

Figure 4.7. Comparison of palaeoclimate reconstructions covering the time interval between 10 and 2.5 ka BP: a) winter precipitation reconstruction from Aspvatnet Lake, Norway (Bakke et al., 2005); b) summer/autumn flood activity reconstruction from the southern European Alps (Wirth et al., 2013); c) precipitation reconstruction from Villars Cave, southern France (Genty et al., 2006); d) precipitation reconstruction from Cova de Arcoia,

Spain (Railsback et al., 2011). In this stalagmite intervals with no data (labelled as 'wet') were interpreted as exceptionally wet due to calcite dissolution caused by higher drip rate and undersaturation of drip-water with respect to calcite; e) precipitation reconstruction from Antro del Corchia, central Italy (low $\delta^{18}O$ values are interpreted to reflect increased winter relative to summer precipitation and vice versa) (Zanchetta et al., 2007); f) precipitation reconstruction from El Refugio Cave, Spain (this study). Blue shading represents CT numbers above the mean calculated for 18 tracks (> 2064 HU), orange shading represents CT numbers below the mean (<2064 HU), grey shading represents 2σ from the average; g) SST reconstruction (stack of deep-sea cores SU8118 and MD952042) from the Iberian margin (Bard, 2002); h) ITCZ reconstruction from Cariaco Basin (Haug et al., 2001) and mean June insolation for $65^{o}N$ (Laskar et al., 2004). Age errors are shown above each record apart from record b) and g). The bottom time division is based on three phases of Holocene climate after Jalut et al. (2009).

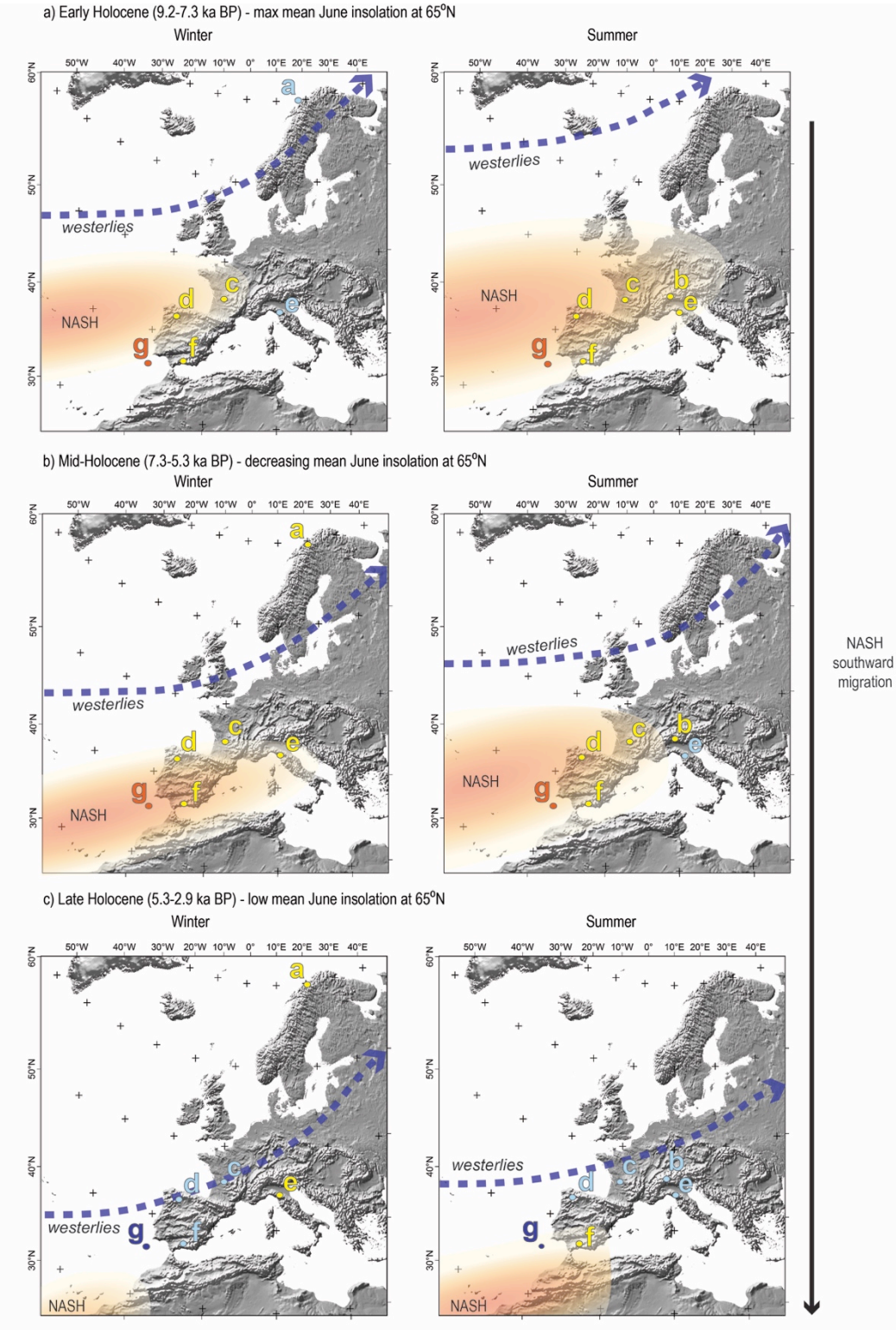

Figure 4.8. Simplified climate interpretation in Europe with southward NASH migration from the early- to late-Holocene based on records plotted in Figure 4.7. Letters correspond to records from Figure 4.7. Letters colour coding: yellow = drier, blue = wetter, red = warmer and dark blue = colder conditions. Record b) is a summer/autumn proxy and therefore is not included in the winter panel.

Mid-Holocene

The mid-Holocene (defined here as 7.3 and 5.3 ka BP) in REF-07 is characterised by a growth hiatus between 7.3 and 6.1 ka BP, followed by relatively slow growth rates between 6.1 and 5.3 ka BP (Figure 4.3), suggesting decreased moisture availability that inhibited stalagmite growth (Figure 4.7f). However, a relatively short but intense interval of stalagmite growth between 6.9 and 6.4 ka BP has been documented at the coastal site of Nerja Cave, approximately 80 km east of El Refugio Cave (Figure 4.1) (McMillan, 2006) indicating regional spatial variability in effective precipitation at this time. Cessation of deposition at Nerja at c. 6.4 ka BP was followed by the beginning of deposition of stalagmite REF-03, another stalagmite from El Refugio Cave that was deposited between 6.5 and 6.2 ka BP (McMillan, 2006) (Figure 4.9). Thus, depositional hiatuses in individual stalagmites may reflect local site-specific hydrological routing effects, and it is difficult to separate these localised drip-water plumbing effects from regional scale climatic effects that influence effective rainfall and the infiltration of water into shallow caves. Nonetheless, considering the available data from El Refugio and Nerja caves together (Figure 4.9), a short period of non-deposition in southern Iberia occurred between c. 7.3 and 6.9 ka. Moisture availability at Nerja in the interval 6.9 to 6.4 ka may also reflect its more coastal and lower altitude location that gave rise to greater moisture availability than at the higher elevation inland El Refugio Cave site. Similar geographic decoupling in terms of winter precipitation is also apparent in the precipitation anomaly reconstructions based on pollen assemblages (Mauri et al., 2015).

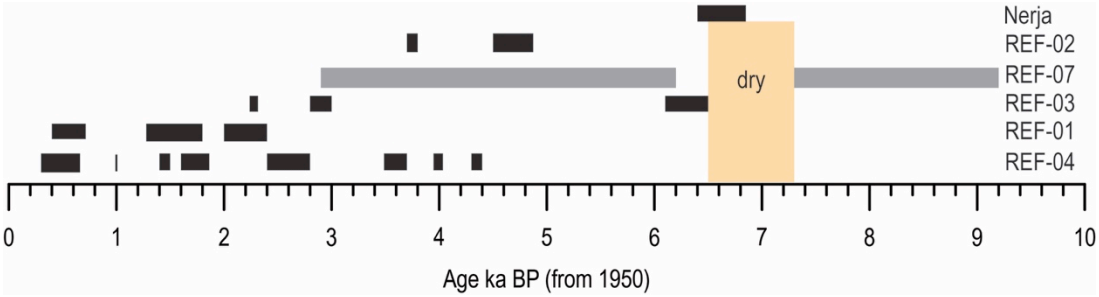

Figure 4.9. Growth periods of stalagmites from Refugio Cave (this study, Baldini (2007), McMillan (2006)) and Nerja Cave (McMillan, 2006).

Regional pollen records suggest a progressive decreasing trend in annual rainfall since ca. 7 ka BP, punctuated by periodically enhanced drought at ca. 7.3 ka BP (Chabaud et al., 2014, Fletcher et al., 2013), ca. 7 ka BP (Jalut et al., 2000), ca. 6.8 ka BP (García-Alix et al., 2012) and ca. 6.5 ka BP (Jiménez-Moreno and Anderson, 2012, García-Alix et al., 2012, Chabaud et al., 2014). This contrasts with some central and north-eastern Iberian regional pollen records (Carrión, 2002, Aranbarri et al., 2014, Fletcher et al., 2007), which suggest increased moisture availability during this interval. This lack of coherence between different records may reflect greater differences in seasonal insolation between the early and mid-Holocene (Wanner et al., 2008), translated into different humidity conditions at sites from higher or lower elevations (Anderson et al., 2011), resulting in complex spatio-temporal patterns of seasonal moisture availability as captured in a recent compilation of pollen data on a regional scale (Mauri et al., 2015). Reed et al. (2001) suggest that a mid-Holocene humidity maximum may have been restricted to the western coast of Iberia, which is also supported by climate models (Roberts et al., 2011) and climate reconstructions (Mauri et al., 2015). Generally dry conditions between 7.3. and 5.8 ka BP suggested by positive $\delta^{13}C$ excursions in the northwest Iberian Cova de Arcoia stalagmite record (Figure 4.7d) (Railsback et al., 2011), the GAR-01 stalagmite record (Baldini,

2007) and a sharp decrease of precipitation after 6 ka BP derived from growth rates of 11 stalagmites (Stoll et al., 2013) support our interpretation of relatively drier conditions across much of Iberia between 7.3 and 5.8 ka BP. Northern Iberian lake sediment records (Jambrina-Enríquez et al., 2014, Moreno et al., 2011) and the pollen-based climate reconstruction from Mauri et al. (2015) further corroborate this interpretation and collectively suggest that relatively drier conditions prevailed in northwestern Iberia during that interval. Together these Iberian climate proxy records suggest that during the mid-Holocene summer aridity existed in both southern and north-western Iberia, although moisture availability in the north was still likely higher (probably from winter westerlies) than in southern Iberia, reflected in the continued growth of northern (Baldini, 2007, Railsback et al., 2011) relative to southern stalagmites between 7.3 and 5.8 ka BP (Figure 4.7d). This suggests that during the mid-Holocene the NASH was located over southern Iberia year round (Figure 4.8b), but south of northern Iberia during the winter. Dry conditions recorded in the Villars stalagmite in southern France (Genty et al., 2006) (Figure 4.7c), low flood activity in the southern Alps (Wirth et al., 2013) (Figure 4.7b), and lower lake-level from the French and Swiss Alps (Magny, 2004), further support our interpretation of a southward shift in NASH from the early- to mid-Holocene (Figure 4.8).

Late Holocene

During the late Holocene (between 5.3 and 3.6 ka BP) REF-07 is characterised by a substantial decrease in stalagmite density (Figure 4.7f). We interpret the occurrence of porous stalagmite calcite together with increasing growth rates since the hiatus interval as reflecting increased drip-water supersaturation with respect to calcite

promoting vertical stalagmite growth associated with lower drip rates (Genty and Quinie, 1996). During the late Holocene, regional lacustrine pollen and sediment records suggest a long-term decreasing trend in annual rainfall in southern Iberia (Anderson et al., 2011, Jiménez-Moreno and Anderson, 2012, García-Alix et al., 2012). An increase in multi-decadal scale stalagmite density variability over this interval suggests the establishment of a modern NAO system at this time. By contrast, in northern Iberia, the stalagmite record from Cova de Arcoia is characterised by lower $\delta^{13}C$ (Figure 4.7d) and $\delta^{18}O$ values and more frequent dissolutional erosional events suggesting overall wetter and perhaps cooler conditions during this interval (Railsback et al., 2011). This suggests that the NASH moved southward from its mid-Holocene central position over Iberia, resulting in repositioned westerlies bringing more moisture over the northern part of the Iberian Peninsula and over southern Europe (Figure 4.8c). This interpretation is supported by increased southern Alps flood activity (Figure 4.7b) and increased rainfall recorded at Villars Cave, southern France, at this time (Figure 4.7c).

Apart from this general decreasing trend in annual rainfall, possibly reflecting increased seasonality (i.e., lower summer rainfall but continued winter rainfall), observed as a stalagmite porosity increase, two very high density (> 2400 HU) "laminae" (yellow lines marked as microhiatuses in Figure 4.3), dated at 4.16 ka BP and 5.3 ka BP, are present during the stalagmite's late Holocene growth. They coincide with the '4.2 ka BP event' (IPCC, 2014) and a short-term drying event in the central Mediterranean centred at 5.2 ka BP (Zanchetta et al., 2014), suggesting that these very high density laminae might indicate the effects of abrupt and short-lived (possibly dry and/or cold) climate change events, although the

climatic expression of these events in Europe is still unclear. Available Iberian pollen records lack evidence for these abrupt climatic events which may reflect their low temporal resolution.

The late Holocene was also the period when the growth of several other dated stalagmites from Refugio Cave initiated (Figure 4.9, Baldini (2007), McMillan (2006)). However, their growth periods are not always overlapping and are often interrupted by several long depositional hiatuses suggesting complicated hydrogeological conditions in the cave. Large regional earthquakes may generate stalagmite growth anomalies (Becker et al., 2006) and/or affect hydrological flow pathways in the cave resulting in on/off switching of stalagmite growth. During the late Holocene, REF-07 CT visualisations reveal two growth axis shifts, dated at 4.44 ± 0.04 ka BP and ca. 5.36 ± 0.05 ka BP, the latter coinciding with published proxy evidence for an earthquake that caused a tsunami in southern Portugal. However, the growth axis shift at 4.44 ka BP, also observed in stalagmite REF-02 from the same cave (Baldini, 2007), does not coincide with any known seismic activity, suggesting an undocumented event or local cave floor subsidence.

Our new Iberian stalagmite record, considered with other western European records, suggests that northwestern Iberia experienced Mediterranean climate-like conditions (dry summers and wet winters) much earlier (during the mid-Holocene) than southern Iberia, and only later (during the late Holocene) transitioned into the more maritime climate particular to the region today. This interpretation contrasts with that inferred from pollen data that the Mediterranean climate zone moved gradually from south to north from the early to the late Holocene (Jalut et al., 1997). However,

our interpretation supports Pérez-Obiol et al. (2011) and Dorado Valiño et al. (2002), who suggested that the onset of Mediterranean climate may follow different patterns according to continentality, altitude, topoclimatology and microhabitats.

In summary, comparison of our southern Iberian climate reconstruction with published moisture balance proxy records spanning 10°N to 70°N places broad constraints on North Atlantic circulation shifts during the Holocene. Combined pollen and chironomid records from northern Norway suggest decreasing winter precipitation from the early Holocene (Figure 4.7a), interpreted as a southward repositioning of the westerlies (Bakke et al., 2005). Similarly, Cariaco sediment data demonstrates a gradual Atlantic Intertropical Convergence Zone (ITCZ) southward movement from its maximum northward location in the early Holocene (Haug et al., 2001) (Figure 4.7h). This southward migration of North Atlantic atmospheric circulation was in response to a gradual orbitally-induced decrease in Northern Hemisphere insolation (Laskar et al., 2004) that is also reflected in Iberian margin sea surface temperature (Figure 4.7g). The ITCZ, approximately tracking the thermal equator, moved progressively southwards resulting in southward migration of Hadley circulation and consequently the NASH (Figure 4.8). In the mid-Holocene, mean NASH position was over central Iberia, resulting in a Mediterranean climate in the north (high pressure in the summer, affected by westerlies in the winter), and a very dry climate in the south (annually persistent high pressure) (Figure 4.8b). The NASH gradually migrated southward since the mid-Holocene, and the onset of a Mediterranean-type climate in southern Iberia was achieved by 5.3 ka BP (Figure 4.8c), albeit with regional heterogeneities. This is consistent with

an abrupt southward migration of the monsoon rain belt in North Africa that terminated the African Humid Period at 5.5 ka BP (deMenocal et al., 2000).

4.5. Conclusions

This study demonstrates the potential of CT scanning to provide high resolution decadal scale climate records from stalagmites. This study suggests that stalagmite density variations derived from CT scanning are accurate reconstruction of the rainfall amount response to oceanic and atmospheric changes. Future work should involve establishing more robust correlations between traditional climate proxies (stable isotopes and trace elements), instrumental climate data and stalagmite density variations.

The high-resolution (CT spatial resolution of 0.21 mm, corresponding to a mean temporal resolution of five years) REF-07 stalagmite density variations obtained using the CT scanning technique reported here, considering together with other European proxy records, reveal Holocene climate variability in southern Iberia, and suggest that the current Mediterranean climate in southern Iberia was initially emplaced at approximately 5.3 ka BP following gradual southward migration of the NASH. These results complement the lower resolution pollen records of the region and help to better constrain climate variability through the Holocene in southern Iberia.

Model projections (Seager et al., 2007, Lu et al., 2007, Rodríguez-Puebla and Nieto, 2010) of future climate under greenhouse gas warming suggest decreased precipitation and soil moisture in the subtropics during the twenty-first century

reflecting a poleward shift of Hadley circulation boundaries. This prediction exists despite the decreasing Northern Hemisphere insolation trend that (without anthropogenic effects) would force the Northern Hemisphere subtropical highs southward. If future northward migration of the NASH does occur, our research suggests that this would cause a return to climate conditions seen during the mid-Holocene, when Mediterranean climate-like conditions prevailed in northern Iberia but southern Iberia experienced aridity. Currently, 56 million people live in the Iberian Peninsula; it is therefore critical to understand how the interplay between greenhouse gas warming, other anthropogenic factors (e.g. SO_4 aerosols), and natural climate variability will reposition the NASH over the next century.

Chapter 5

High-resolution paleoclimate reconstruction from

Bermuda stalagmite spanning last 700 years

5.1. Introduction

On the longer timescales, a negative (cold - La Niña conditions) phase of the El Niño Southern Oscillation (ENSO) (Klotzbach, 2011a, Gray, 1984), a weak vertical shear of the upper-level horizontal winds (Goldenberg et al., 2001, Gray, 1984), positive rainfall anomalies in tropical Africa (Landsea and Gray, 1992, Donnelly and Woodruff, 2007, Klotzbach, 2011a), an increase in sea surface temperatures (SSTs) in the Mean Development Region (MDR) and related positive Atlantic Multidecadal Oscillation (AMO) (Goldenberg et al., 2001, Gray, 1984, Mann et al., 2009), and declines in anthropogenic aerosol levels (Dunstone et al., 2013, Wang et al., 2014) favour the abundance of tropical storms and hurricanes in the North Atlantic Ocean. Dunstone et al. (2013) also suggest that the anthropogenic aerosols forcing could be the dominant cause of historical TCs variability, as they respond much more rapidly to multi-decadal variations in industrial emissions (e.g. rapid economic expansion pre-1914, US and European clean air legislation post-1970s) than GHG. The other factor controlling TCs frequency is the volcanic activity that can reduce the number of TCs formed during the three years following major eruptions compared to the preceding years by the injection of sulphate aerosols into the stratosphere (Guevara-Murua et al., 2015). The volcanic and anthropogenic forcing modulate both ENSO and AMO, thus exert a significant influence on Atlantic hurricane activity (van Hengstum et al., 2015).

Based on best-track data from 1982-2012, Kossin et al. (2014) observed a global average migration of tropical cyclone activity away from the tropics that links to marked changes in the mean meridional structure of environmental vertical wind

shear and potential intensity, and can be plausibly linked to tropical expansion. This implies that Bermuda should experience more hurricanes strike than in the future.

Since AD 1850, 49 tropical cyclones affected Bermuda, out of which 10 were classified as major hurricanes (Figure 5.2). A decade from 1981 to 1990 experienced the highest number of TCs since 1900s, however of low intensity (half of them of tropical storm intensity), unlike a decade from 1921 to 1930 when fewer hurricanes occurred but were of stronger intensity (all classified in category 3). The NOAA data in Bermuda is inconsistent with results indicating enhanced hurricane activity from 1995 to 2005 (Pinto and Raible, 2012, Webster et al., 2005, Goldenberg et al., 2001), which suggests that southward migration of hurricane tracks during that interval.

Currently, most available paleotempestological information comes from the analysis of late Holocene sediment cores from Belize (McCloskey and Keller, 2009, Denommee et al., 2014), the east coast of the USA (Scott et al., 2003, Donnelly et al., 2001b, Donnelly et al., 2004, Donnelly et al., 2001a, Scileppi and Donnelly, 2007, Boldt et al., 2010), the Gulf of Mexico area (Lane et al., 2011b, Liu and Fearn, 2000, Ercolani et al., 2015), Puerto Rico (Donnelly and Woodruff, 2007), the Bahamas (van Hengstum et al., 2014, Toomey et al., 2013, Park, 2012), Cuba (Peros et al., 2015), Barbuda (Burn et al., 2016), Jamaica (Burn and Palmer, 2015), Saint Martin Island (Malaize et al., 2011) and Nicaragua (McCloskey and Liu, 2012) (Figure 5.1).

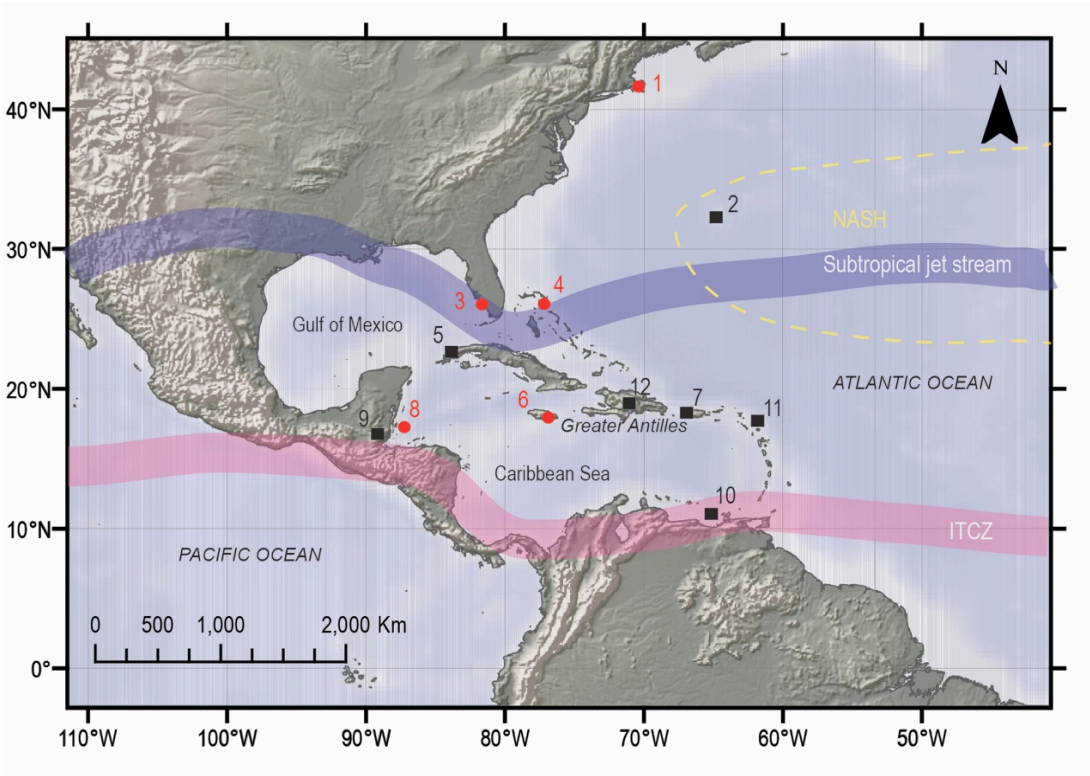

Figure 5.1. Locations of TC activity reconstructions using sediment cores from**:** (1) Salt Pond, Massachusetts (USA) (Donnelly et al., 2015); (3) Southwest Florida (Ercolani et al., 2015); (4) the Bahama Bank (van Hengstum et al., 2014); (6) Jamaica (Burn and Palmer, 2015); (7) Vieques, Puerto Rico (Donnelly and Woodruff, 2007); (8) Blue Hole, Belize (Denommee et al., 2014) marked as red circles. Locations of the other climate reconstructions: (2) the storminess reconstruction from Bermuda cave sediment cores (van Hengstum et al., 2015); (5) climate reconstruction using stalagmite from Cuba (Fensterer et al., 2012); (7) rainfall reconstruction from Puerto Rican stalagmite (Winter et al., 2011); (9) the climate reconstruction using stalagmite from Belize (Kennett et al., 2012); (10) the ITCZ migration reconstruction (Haug et al., 2001) and SSTs reconstruction (Black et al., 2007) from Cariaco Basin; (11) the effective precipitation reconstruction from Barbuda (Burn et al., 2016); (12) climate reconstruction from Dominican Republic (Lane et al., 2011a) are marked as black squares.

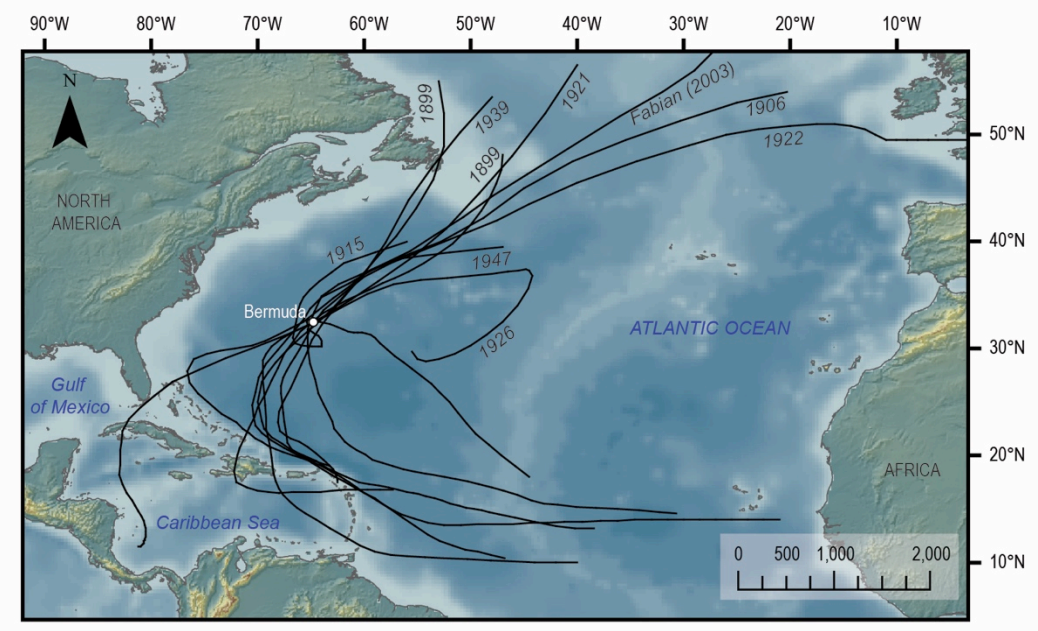

Figure 5.2. Major hurricane (of category higher than 3 in Saffir-Simpson hurricane wind scale) tracks that made landfall in Bermuda between AD 1850 and 2010. Data source: HURDAT.

During the instrumental period, most of the major hurricanes (of category higher than 3 in Saffir-Simpson hurricane wind scale) making landfall in Bermuda are redirected from NW-ward track to NE direction close to Turks and Caicos Islands (around the area of 22°N, 70°W) (Figure 5.2), suggesting that Bermuda rainfall variability associated with TCs should be similar to other rainfall reconstructions from Puerto Rico, Barbuda and Dominican Republic (Figure 5.1).

The number of high-resolution tropical cyclone activity reconstructions spanning the last 1000 years in the North Atlantic Basin has increased in the recent years. Most of them (Ercolani et al., 2015, van Hengstum et al., 2014, Denommee et al., 2014, Burn and Palmer, 2015, Donnelly et al., 2001a, Donnelly et al., 2015) are derived from sediment cores, hence their interpretation can be complicated by difficulties in

distinguishing between storm and tsunami-induces events and possible under-representation of hurricane activity due to erosion.

The analysis of the sediment cores from Walsingham Cavern, Bermuda suggest increased storminess during the Little Ice Age from AD 1250 to 1850 (700 to 100 cal years B.P.) that was linked to negative NAO (Enfield et al., 2001) suggesting weaker NASH. The coral-based studies show a close relationship between NAO phase and regional SSTs exists, persistent for several centuries in Bermuda, whereby more positive regional SSTs coincides with more negative NAO (Goodkin et al., 2008).

Here, we present a new high-resolution paleoclimate reconstruction from Bermuda stalagmite collected from Leamington Cave going back to the beginning of the 14th Century. Due to the site mid-latitude location in the North Atlantic Ocean close to the centre of NASH, Bermuda is ideal location for reconstructing related TC activity, North Atlantic SSTs and general climate circulation. Also because the island was uninhabited before AD 1609, the record contributes to a better understanding of natural climate changes and anthropogenic impact on climate.

5.2. Methods

5.1.1. U-series and radiocarbon dating

The stalagmite BER-SWI-13 was sectioned along the central growth axis (Figure 5.3c) determined using CT appearances (Figure 5.3b), and then polished and cleaned in an ultrasonic bath of deionised water.

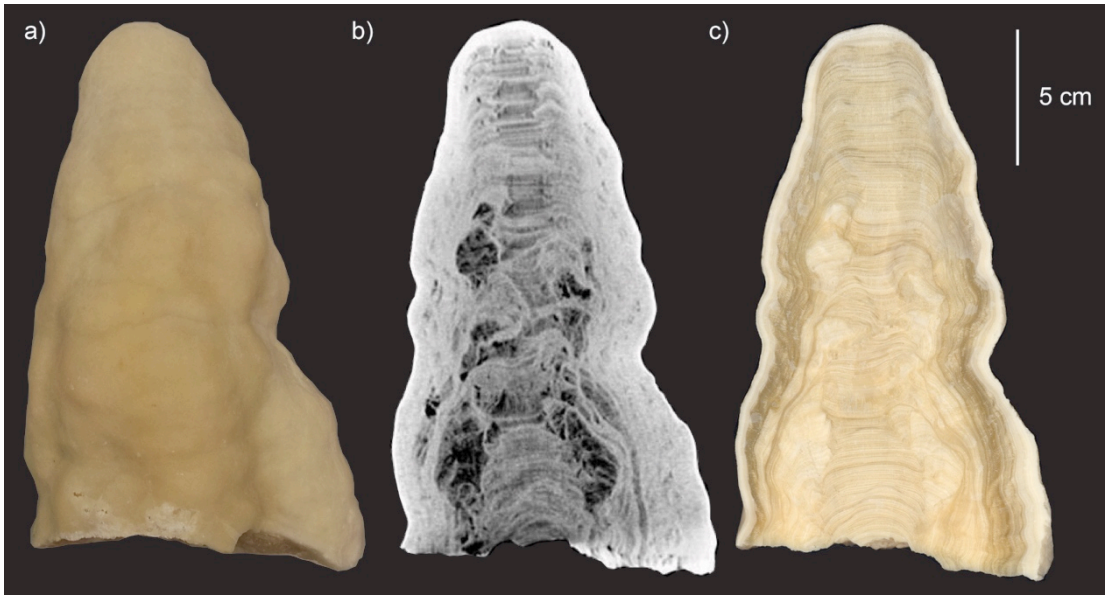

Figure 5.3. Stalagmite BER-SWI-13: a) photo of the stalagmite exterior; b) CT image of a plane XZ 248, c) photo of the sectioned plane corresponding to the CT image in b).

Carbonate powder samples of ~400 mg weight were milled from a polished slab of the stalagmite BER-SWI-13 along the growth axis for U-series dating (Figure 5.5). They were consecutively dated at the Department of Earth Sciences, University of Bristol, and at the St. Andrews Isotope Geochemistry (STAiG) lab using multi-collector-inductively coupled plasma mass spectrometer (MC-ICPMS), following the chemical separation procedure described in Hoffmann et al. (2007). All the dates were in stratigraphic order within the errors. Along the isotope tracks also twenty-five carbonate powder samples of 8-9 mg weight were milled for radiocarbon (^{14}C) dating at ETH Zürich (Table 5.1). The carbonate samples for accelerator mass spectrometry (AMS) ^{14}C measurements were milled along visible growth increments offset from the stable isotope milling track (Figure 5.5) at 5 mm and 10 mm increments for the top 50 mm and the remaining 140 mm, respectively. Carbonate samples were prepared for AMS analysis by acidification to CO_2 using ca. 2 mL 85% H_3PO_4 and then converted to graphite using excess H_2 over Fe catalyst. All ^{14}C

ages were corrected for mass-dependent fractionation. Identification of the initial part of the atmospheric bomb spike at AD 1955 provided both an independent confirmation of the accuracy of the top ^{230}Th dates and a date (AD 1955) to anchor the chronology.

Thirteen U-series dates (Table 5.2), the year of collection (AD 2013) and the year of the bomb spike beginning (AD 1955) (Figure 5.4) were used in the COPRA age model (Breitenbach et al., 2012) to constrain the stalagmite BER-SWI-13 chronology. The ages in Table 5.2 are reported to the year of analysis (2016).

Table 5.1. The ^{14}C data for stalagmite BER-SWI-13. Last column shows ^{14}C dates applying constant DCF correction of 333 years.

Sample ID	Depth from top (mm)	F^{14}C (pMC)	error abs.	^{14}C age (yr)	Error age	^{14}C age (yr) – constant DCF
SWI-14C-01	0	1.0491	0.0032	-385	24	
SWI-14C-02	3	1.0048	0.0031	-38	25	
SWI-14C-03	7.5	0.9598	0.0030	330	25	-3
SWI-14C-04	12.5	0.9521	0.0028	395	24	62
SWI-14C-05	17.5	0.9579	0.0030	345	25	12
SWI-14C-06	22.5	0.9584	0.0029	341	24	8
SWI-14C-07	27.5	0.9569	0.0029	354	25	21
SWI-14C-08	32.5	0.9466	0.0028	441	24	108
SWI-14C-09	37.5	0.9466	0.0029	441	25	108
SWI-14C-10	42.5	0.9448	0.0028	456	24	123
SWI-14C-11	47.5	0.9466	0.0029	441	25	108
SWI-14C-13	57.5	0.9401	0.0030	496	26	163
SWI-14C-15	67.5	0.9300	0.0029	583	25	250
SWI-14C-17	77.5	0.9250	0.0029	627	25	294
SWI-14C-19	87.5	0.9171	0.0029	695	25	362
SWI-14C-21	97.5	0.9193	0.0029	676	25	343
SWI-14C-23	107.5	0.9147	0.0029	716	25	383
SWI-14C-25	117.5	0.9186	0.0029	682	25	349
SWI-14C-27	127.5	0.9183	0.0028	685	24	352
SWI-14C-29	137.5	0.9194	0.0028	675	24	342
SWI-14C-31	147.5	0.9133	0.0027	728	24	395
SWI-14C-33	157.5	0.9113	0.0028	746	25	413

SWI-14C-35	167.5	0.9060	0.0027	793	24	460
SWI-14C-37	177.5	0.9103	0.0028	755	25	422
SWI-14C-39	192.5	0.9024	0.0028	825	25	492

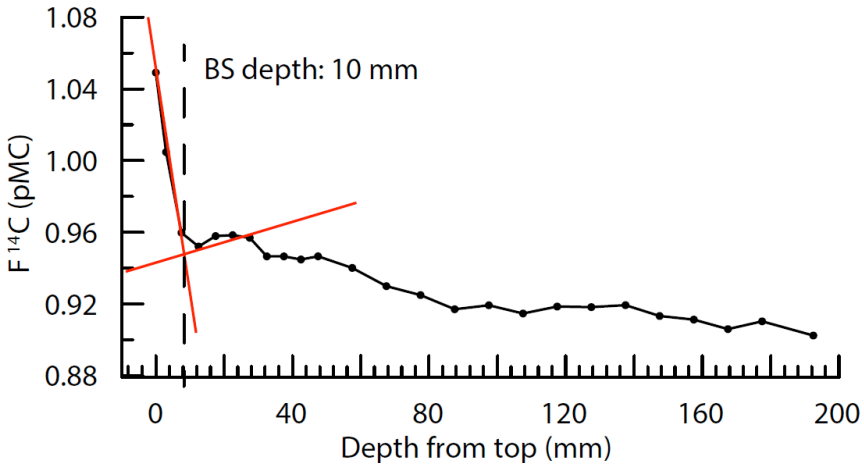

Figure 5.4. Establishing the depth of the bomb spike for stalagmite BER-SWI-13.

Table 5.2. U and Th concentrations, isotopic activity ratios and U–Th ages for sub-samples of stalagmite BER-SWI-13. Analytical errors are 2σ of the mean. $(^{230}Th/^{238}U) = 1 - e^{-\lambda 230T} + (\delta^{234}U_{measured}/1000)(\lambda_{230}/(\lambda_{230} - \lambda_{234}))(1 - e^{-(\lambda 230 - \lambda 234)}T)$, where T is the age $\delta^{234}U = ((^{234}U/^{238}U) - 1) \times 1000$. Decay constants are 9.1577×10^{-6} yr^{-1} for ^{230}Th, 2.826×10^{-6} yr^{-1} for ^{234}U (Cheng et al., 2000), and 1.55125×10^{-10} yr^{-1} for ^{238}U (Jaffey et al., 1971). *The degree of detrital ^{230}Th contamination is indicated by the measured ($^{230}Th/^{232}Th$); an initial ($^{238}U/^{232}Th$) of 0.8 ± 0.2 is used to obtain a corrected U–Th age. Ages are reported to the year of analysis (2016).

Lab code	Sample ID	Depth from the top (mm)	^{238}U (ng/g^{-1})	±	^{232}Th (ng/g^{-1})	±	($^{230}Th/^{232}Th$)	±	($^{230}Th/^{238}U$)	±	($^{234}U/^{238}U$)	±	Corrected Age* (ka)	±	Year AD	($^{234}U/^{238}U$)$_i$	±
dcn435	SWI-UTh-02	15	84.64	0.21	0.0325	8.00E-04	1.26E-04	2.82E-06	2.42E-03	8.75E-05	1.058E+00	1.959E-03	0.132	0.061	1884.1	1.05795	0.00196
dcn437	SWI-UTh-04	35	98.22	0.28	0.0552	1.19E-03	1.84E-04	4.41E-06	3.14E-03	1.05E-04	1.052E+00	1.937E-03	0.184	0.072	1831.9	1.05207	0.00194
dcn439	SWI-UTh-06	57.5	135.52	0.39	0.0341	8.26E-04	8.24E-05	1.98E-06	3.58E-03	6.06E-05	1.054E+00	1.864E-03	0.299	0.038	1717.5	1.05393	0.00187
dcn441	SWI-UTh-08	80	110.57	0.30	0.0219	4.69E-04	6.47E-05	1.42E-06	4.37E-03	1.19E-04	1.061E+00	2.110E-03	0.379	0.040	1637.2	1.06074	0.00211
dcn451	SWI-UTh-10	106	96.80	2.10	0.0177	5.30E-04	5.98E-05	1.25E-06	4.55E-03	1.06E-04	1.061E+00	2.046E-03	0.416	0.028	1599.7	1.06097	0.00205
dcn453	SWI-UTh-12	156	95.29	1.86	0.0458	1.36E-03	1.57E-04	3.66E-06	5.29E-03	1.19E-04	1.062E+00	1.774E-03	0.442	0.051	1573.6	1.06205	0.00178
dcn455	SWI-UTh-14	174	298.62	1.90	0.0641	1.42E-03	7.02E-05	1.48E-06	5.33E-03	8.65E-05	1.057E+00	1.765E-03	0.509	0.024	1507.3	1.05746	0.00177
dcn457	SWI-UTh-16	190	362.36	2.40	0.3557	7.45E-03	3.21E-04	7.44E-06	7.81E-03	1.19E-04	1.057E+00	1.804E-03	0.638	0.087	1378.2	1.05679	0.00181

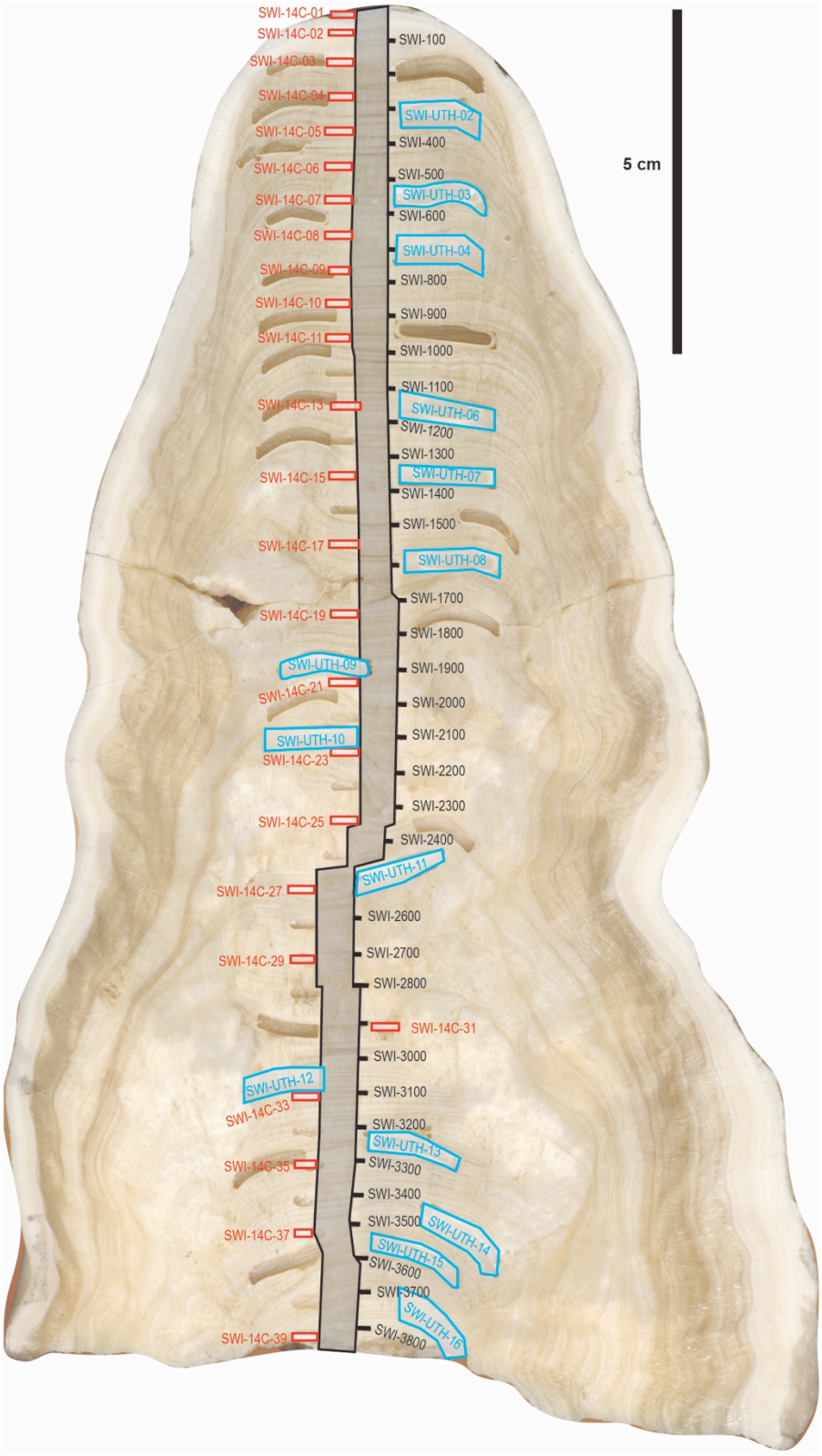

Figure 5.5. Sectioned and polished stalagmite BER-SWI-13 slab with marked locations of ^{14}C (red rectangles) and U-series (blue rectangles) dates considered in the chronology and the stable isotope track (grey wide line). Powders collected from not labelled pits have not yet been analysed.

5.1.2. Geochemical analysis

The 192 mm long stalagmite BER-SWI-13 was milled continuously along the central growth axis at 50μm increments using a computer-controlled ESI/New Wave Micromill at Sir Kingsley Dunham Palaeoclimate Research Lab, Durham University, UK, with a standard 0.8 mm tungsten carbide milling bit (Figure 5.5). Samples were milled to specifications of 0.05 mm width, 5-6 mm length and 0.7-1 mm depth, with the long axis parallel to the growth layers. In total, 3,840 carbonate powder samples were collected but only 3,495 of them were analysed and used here for the interpretation. The carbon and oxygen stable isotope ratios were determined using a Thermo MAT-253 gas isotope ratio mass spectrometer with a Gasbench II coupled to a Kiel IV automated carbonate reaction device at Stable Isotope and Palaeoclimate Analysis Laboratory (SPA Lab), Skidmore College, New York, USA. About 40 stalagmite carbonate samples and 10 reference materials were loaded for each run. Each analysis utilised 30-50 μg of sample powder. Normalizations and corrections were made to IAEA (International Atomic Energy Agency) international reference materials NBS19 (limestone) and LS VEC (lithium carbonate). The analytical error is 0.04‰ for $\delta^{13}C$ and 0.05‰ for $\delta^{18}O$. The carbonate isotope ratios are reported relative to the Vienna PeeDee Belemnite (VPDB) standard.

The stable isotope samples have a mean temporal resolution of two months, however because Bermuda precipitation is distributed more or less evenly throughout the year, no annual geochemical cycles were evident.

5.1. Results

5.1.1. Chronology

The stalagmite BER-SWI-13 grew continuously for 700 years from AD 1312 until the year of collection (AD 2013) (Figure 5.6). Based on the chronology, the mean growth rate is 0.28 mm yr^{-1} which is lower than the growth rate calculated based on the lamina couplets count (342) performed on the polished slab (0.57 mm yr^{-1}) implying that lamina couplets are not annual. Thus lamina count was not included in the chronology. The highest growth rates occurred between AD 1500 and 1600. During the last century the stalagmite growth slowed down that could be a result of the urbanisation near the cave site and associated decreased infiltration.

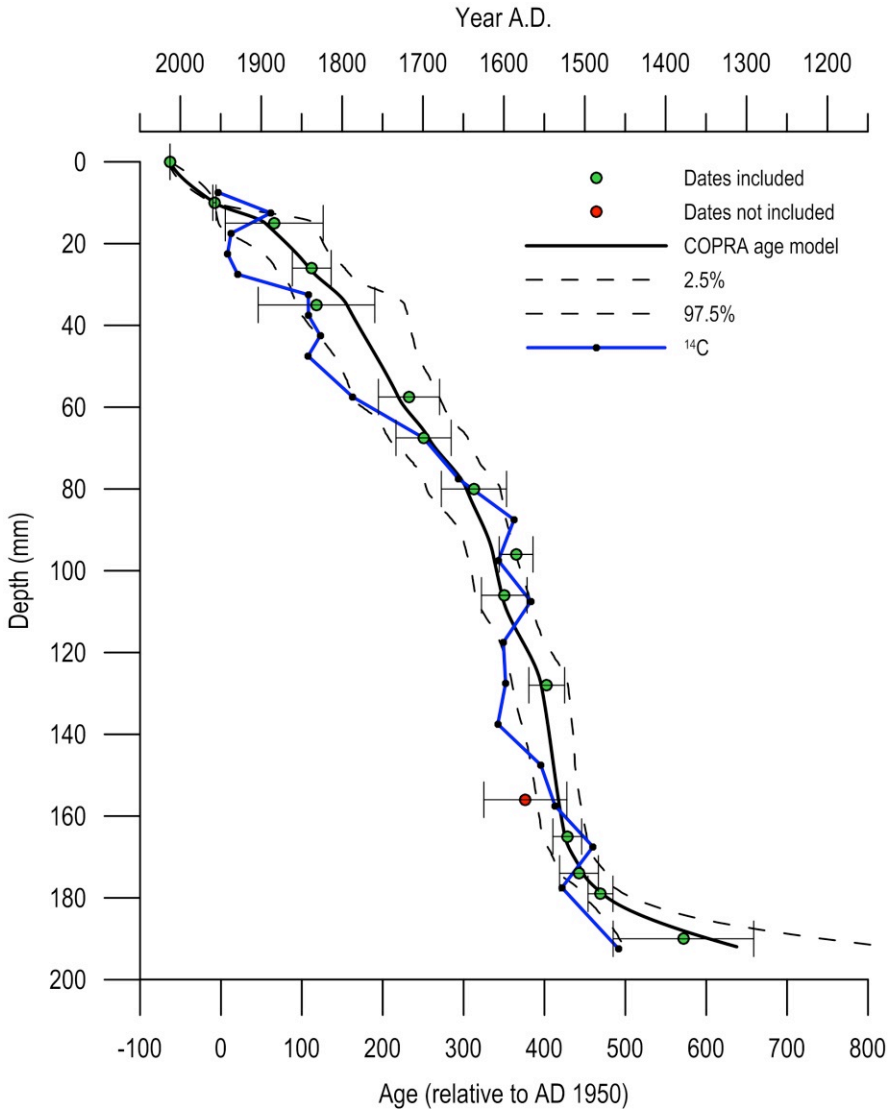

Figure 5.6. The stalagmite BER-SWI-13 age model**.** The COPRA age model (Breitenbach et al., 2012) based on thirteen U-series dates (black line), year of collection (AD 2013) and the beginning of the bomb spike (AD 1955) determined from ^{14}C dates (green dots with error bars). ^{14}C dates after applying constant DCF correction of 333 years (blue line) show similar growth rate to U-series dates-based chronology suggesting that potentially it can be possible to create the age model based only on ^{14}C dates. However this is not discussed further in this thesis. The red dot marks a U-series date not included in the age model.

5.1.2. Speleothem oxygen and carbon stable isotopes

The $\delta^{13}C_{SWI}$ values show higher variability than $\delta^{18}O_{SWI}$ values (Figure 5.7). The mean $\delta^{18}O_{SWI}$ is close to the modelled $\delta^{18}O$ value of meteoric precipitation for

Bermuda calculated using Bowen and Wilkinson (2002) model as a function of latitude (LAT) and altitude (ALT):

$$\delta^{18}O_{precip} = -0.0051(|LAT|)^2 + 0.1805(|LAT|) - 0.002(ALT) - 5.247$$

which is -4.8‰. Both modelled $\delta^{18}O_{precip}$ and mean $\delta^{18}O_{SWI}$ are much lower than $\delta^{18}O_{precip}$ calculated for the whole available GNIP dataset (-3.4‰).

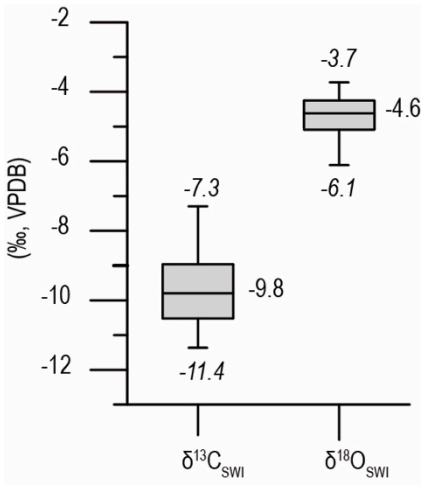

Figure 5.7. The box-whisker plot for stable isotope values from stalagmite BER-SWI-13 showing median, 1st and 3rd quartile, and 5th and 95th percentile. Mean values for $\delta^{13}C_{SWI}$ and $\delta^{18}O_{SWI}$ are -9.8 and -4.6‰, respectively.

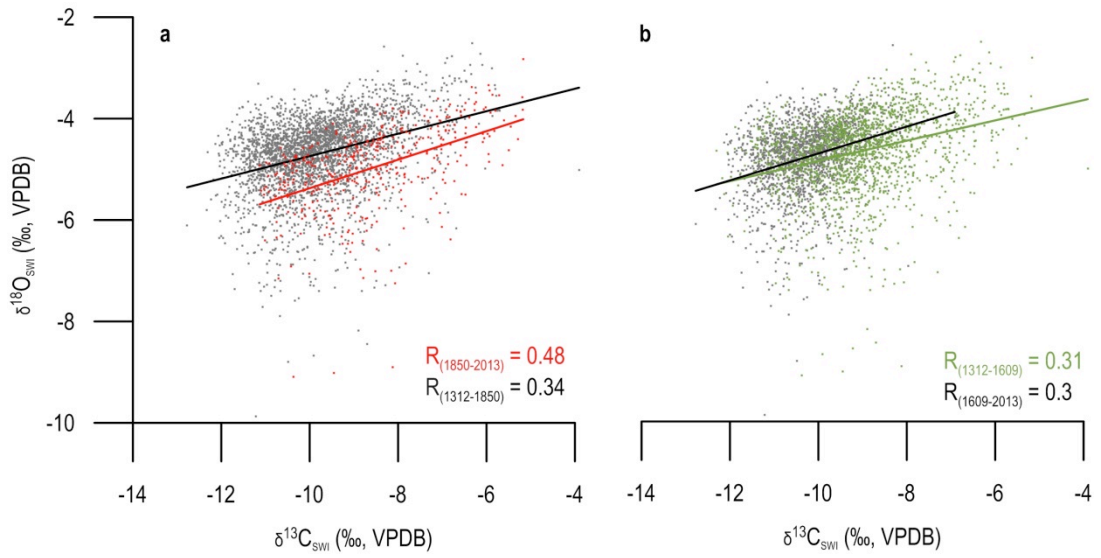

Figure 5.8. Linear correlation between the $\delta^{13}C_{SWI}$ and $\delta^{18}O_{SWI}$ during: a) the pre-industrial (AD 1312-1850; n = 3099) and the industrial era (AD 1850- 2013; n = 394); b) the pre-colonial (from AD 1312-1609, n = 1726) and the post-colonial (AD 1609-2013; n = 1768) period.

$\delta^{13}C_{SWI}$ and $\delta^{18}O_{SWI}$ exhibit a similar weak positive correlation ($r = 0.3$, $p < 0.001$) before and after Bermuda colonisation suggesting little impact of island-wide deforestation on the stable isotope fractionation in the Leamington cave (Figure 5.8b). However, the correlation between $\delta^{13}C_{SWI}$ and $\delta^{18}O_{SWI}$ increases significantly since the Industrial Era ($r = 0.48$) (Figure 5.8a) suggesting increased kinetic isotopic fractionation since AD 1850 (Hendy, 1971).

Only one stable isotope record from a Bermuda stalagmite has been published so far (Malmquist, 1997). The stalagmite $\delta^{18}O$ values from Malmquist (1997) are relatively heavier and have a reduced range of values compared with $\delta^{18}O_{SWI}$. However due to the lack of precise chronological constraints of the older record, the Malmquist (1997) record is not further discussed here.

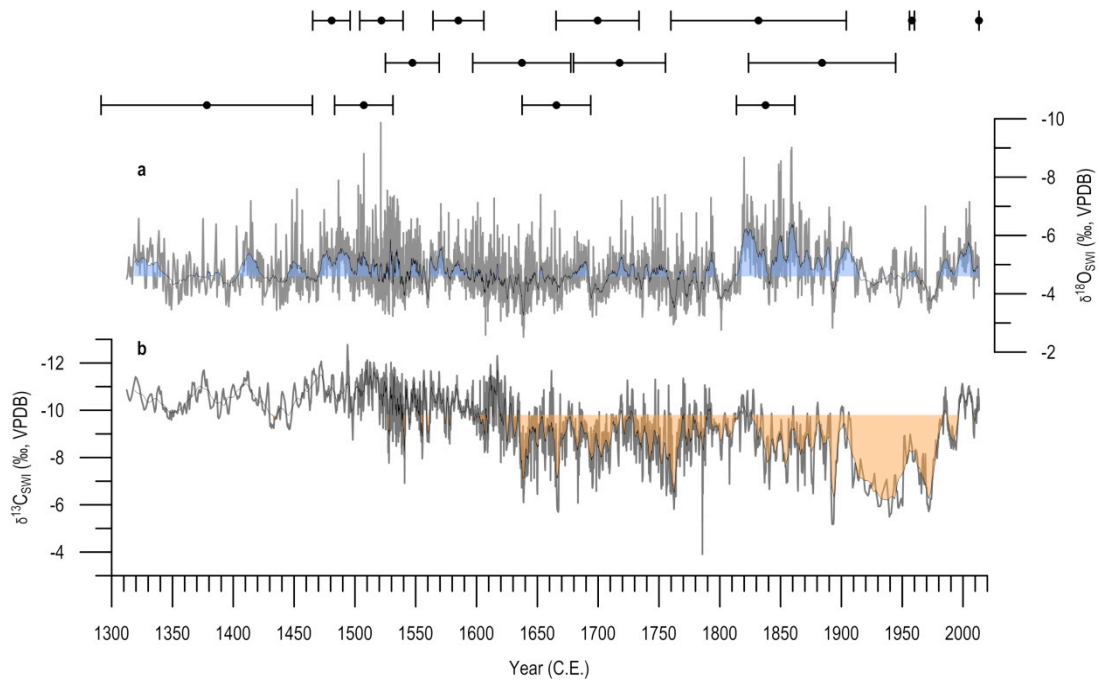

Figure 5.9. The high-resolution stable (a) oxygen and (b) carbon isotope records (grey lines) from stalagmite BER-SWI-13 with 15-point running average (black lines). Blue and orange shading indicate values below and above the mean $\delta^{18}O_{SWI}$ and $\delta^{13}C_{SWI}$ for the whole record, respectively. Above the graphs are dates with error bars used to create chronology of stalagmite BER-SWI-13. Note reversed axes.

The intervals of prolonged, multidecadal lower $\delta^{18}O_{SWI}$ values (below the mean for the whole dataset) occurred: 1) in the last 30 years, 2) between AD 1820 and 1915, and 3) between AD 1400 and 1580 (Figure 5.9a).

The $\delta^{13}C_{SWI}$ values show an abrupt increase above the mean values (calculated for the whole dataset) around AD 1620 and remain elevated until the 1990s (Figure 5.9b). The shift to heavier $\delta^{13}C_{SWI}$ values coincides with the timing of Bermuda colonisation in AD 1609 and is possibly related to extensive deforestation of Bermuda cedar and palmetto used to build vessels and for house thatching, respectively, that resulted in lower soil and plant activity (Rueger and von Wallmenich, 1996).

Table 5.3. Correlation between annually resolved stable oxygen and carbon isotopes from BER-SWI-13 stalagmite and mean annual indices and climate variables during instrumental record (1950-2012 and 2000-2012*). Significant correlations are in bold.

Variable	$\delta^{13}C_{SWI}$	p-value	$\ddot{a}^{18}O_{SWI}$	p-value	n
Rainfall	-0.21	< 0.5	-0.25	< 0.05	63
NAO	0.04	~0.8	0.07	~0.6	63
AMO	**-0.45**	< 0.001	**-0.45**	< 0.001	63
T (Jun-Nov)	0.34	~0.25	0.49	<0.1	13*
T (Dec-May)	0.13	~0.7	0.20	~0.5	13*
T mean	0.3	~0.3	0.44	~0.1	13*
Rainfall (Jun-Nov)	-0.10	~0.8	-0.08	~0.6	13*
Rainfall (Dec-May)	-0.28	~0.4	-0.39	~0.2	13*

At present the annually resolved stable oxygen and carbon isotopes data are strongly negatively correlated with AMO index that expresses the North Atlantic SSTs anomalies (Table 5.3). The comparison of stable isotopes with other instrumental data (e.g. annual and seasonal precipitation total and air temperatures, Figure 5.10) reveals no significant correlations (Table 5.3). Spectral analysis of $\delta^{18}O_{SWI}$ (Figure 5.11) and $\delta^{13}C_{SWI}$ (Figure 5.12) show significant peaks centred at ~86 and ~85 years, respectively, which may be related to the AMO (Gray et al., 2004). Leamington Cave two-year monitoring results (see Chapter 3) also show strong correlations between cave temperature and SSTs and AMO index further corroborating dominant control of air and sea temperature over isotope fractionation at present. In the North Atlantic Basin area, the AMO variability is positively correlated with rainfall amount (Fensterer et al., 2012) and tropical cyclone activity (Klotzbach, 2011b, Winter et al., 2011), hence despite of the weak correlations between $\delta^{18}O_{SWI}$ and rainfall during the limited instrumental climate record that could be result of dating uncertainties or increased kinetic fractionation since the Industrial Revolution, oxygen stable isotope values from Bermuda stalagmite can be used as a rainfall proxy.

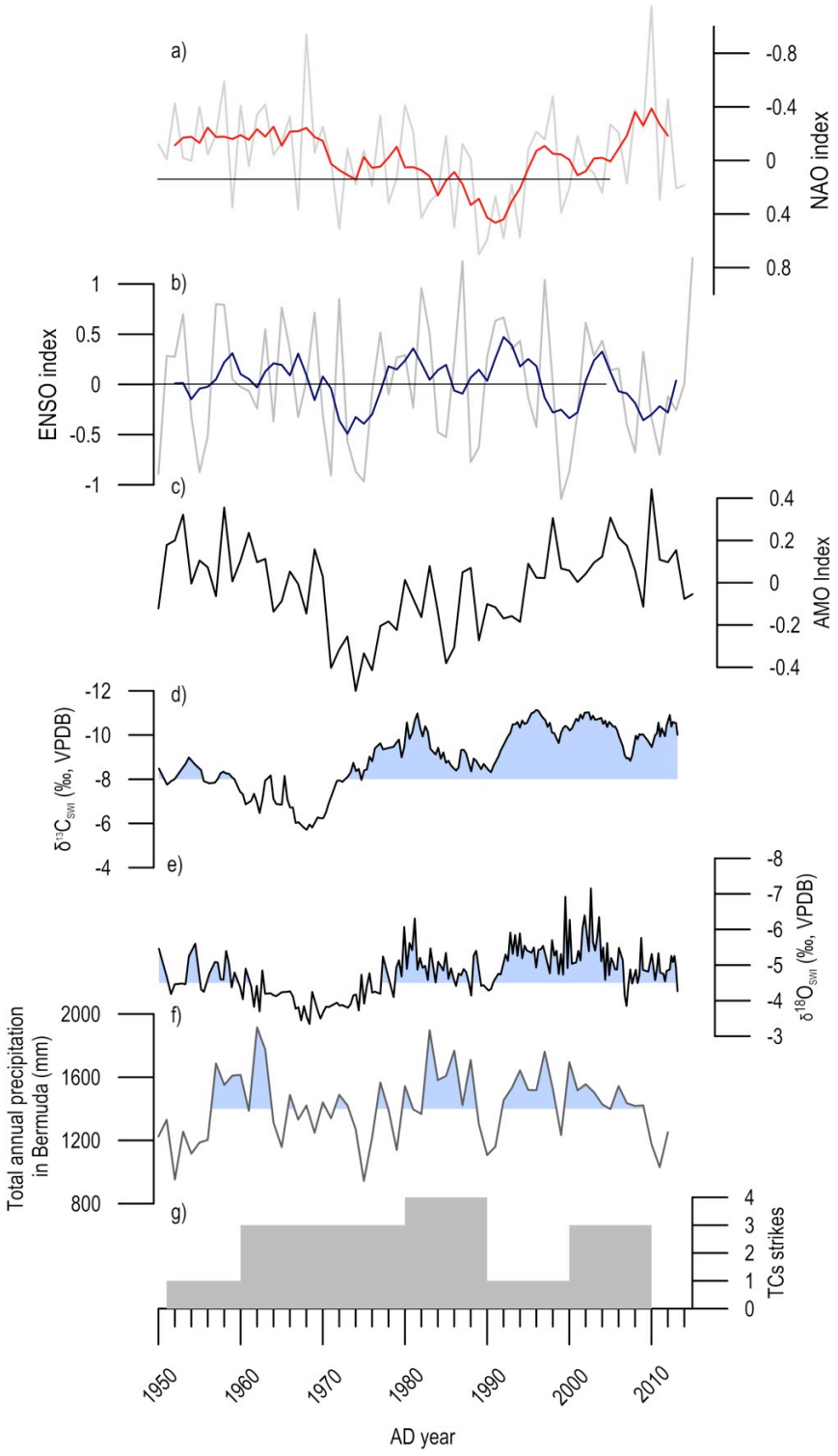

Figure 5.10. The comparison between: a) annual mean NAO index with a 5-year average; b) annual mean ENSO index with 5-year average; c) annual mean AMO index; d) annually resolved $\delta^{13}C_{SWI}$ values; e) annually resolved $\delta^{18}O_{SWI}$ values; f) total annual precipitation in Bermuda and g) decadal sum of tropical cyclones strikes in Bermuda.

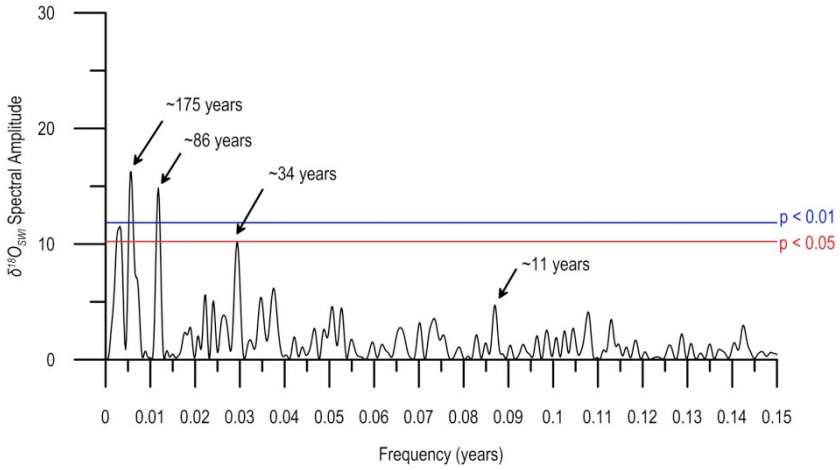

Figure 5.11 Results of spectral analysis of the $\delta^{18}O_{SWI}$ signal.

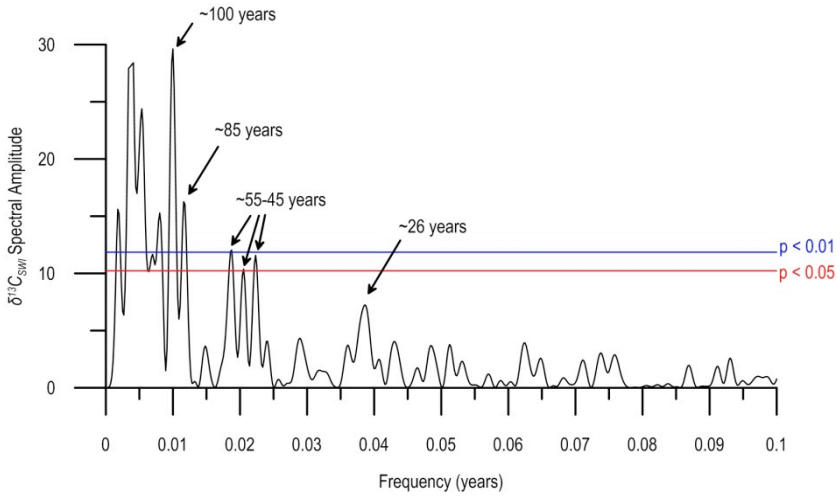

Figure 5.12. Results of spectral analysis of the $\delta^{13}C_{SWI}$ signal.

5.2. Discussion

5.2.1. Pre-colonial period (AD 1300-1600)

Before Bermuda colonisation in AD 1609, the $\delta^{18}O_{SWI}$ show values below the mean, calculated for the whole record, suggesting increased rainfall totals and/or intensity associated with TC activity (Figure 5.14b). Regional records show an increased hurricane activity recorded in the sediment cores from Walsingham Cavern in Bermuda (van Hengstum et al., 2015), the Little Bahama Bank (van Hengstum et al., 2014) and northeast USA (Donnelly et al., 2015) associated with decreased El Niño-like events (Moy et al., 2002) (Figure 5.14a), positive NAO (Olsen et al., 2012,

Trouet et al., 2009) (Figure 5.14g), and increased western North Atlantic SSTs (Saenger et al., 2009) that shifted the average TC track. This northeast-ward TC tracks migration peak in $15^{th}/16^{th}$ century is also observed in the low TC activity in the Caribbean Sea (Denommee et al., 2014).

5.2.2. Little Ice Age (AD 1600-1850)

The beginning of Bermuda colonisation coincides with the peak of the Little Ice Age (LIA). The $\delta^{18}O_{SWI}$ values over that period were isotopically more enriched than calcite that formed during the last 40 years in the Leamington Cave, suggesting drier than present conditions in Bermuda (Figure 5.14b). Also western Cuba (Fensterer et al., 2012) and the Dominican Republic (Lane et al., 2011a) experienced drier conditions and Florida experienced fewer TCs strikes (Ercolani et al., 2015), unlike areas around Caribbean sea (e.g. Belize, Jamaica and Puerto Rico) that show wetter conditions attributed to increased hurricane activity (Burn and Palmer, 2015). Drier/wetter conditions north/south of Greater Antilles also coincide with more negative NAO index that indicates weaker NASH and/or westward NASH centre displacement (Elsner et al., 2000). This coincides with the maximum ITCZ southward migration (Haug et al., 2001) during the last millennia. Despite increased TCs activity south of the Greater Antilles, basin-wide the number of TCs might have decreased as revealed by a combination of a documentary time series of Spanish shipwrecks in the Caribbean with a tree-ring suppression chronology from the Florida Keys (Trouet et al., 2016) that found 75% reduction in decadal-scale Caribbean TC activity between 1645-1715 linked to a reduction in solar irradiance (Maunder minimum).

5.2.3. Modern period (since AD 1850)

Towards the end of the 'Little Ice Age', between AD 1810 and 1900, the $\delta^{18}O_{SWI}$ values are the most isotopically depleted during the whole record that matches with the peak hurricane activity resolved from Bermuda historical records (Tucker, 1982) (Figure 5.14c). Wetter conditions in Bermuda coincide with wetter conditions in western Cuba (Fensterer et al., 2012), and drier conditions south of the Greater Antilles (Burn and Palmer, 2015, Winter et al., 2015).

The first part of the 20th century, until 1950s is characterised by increasing $\delta^{18}O_{SWI}$ values indicating drier conditions and lower TCs activity in Bermuda (Tucker, 1982). Similarly Cuba experiences less rainfall, unlike Puerto Rico (Winter et al., 2011). Since the 1970s, the $\delta^{18}O_{SWI}$ values are decreasing suggesting wetter conditions, coinciding with drying trend in Belize (Kennett et al., 2012).

Since 1940s, the $\delta^{13}C_{SWI}$ values have abruptly decreased from -6‰ to -11‰. This could be related to an increase in the atmospheric pCO_2 since 1950s from 320 ppm to 400 ppm (Figure 5.13). This is supported by Dulinski and Rozanski (1990) that found that carbonate solutions formed under higher pCO_2 precipitate faster and with lower $\delta^{13}C$ values than the solutions formed under lower pCO_2.

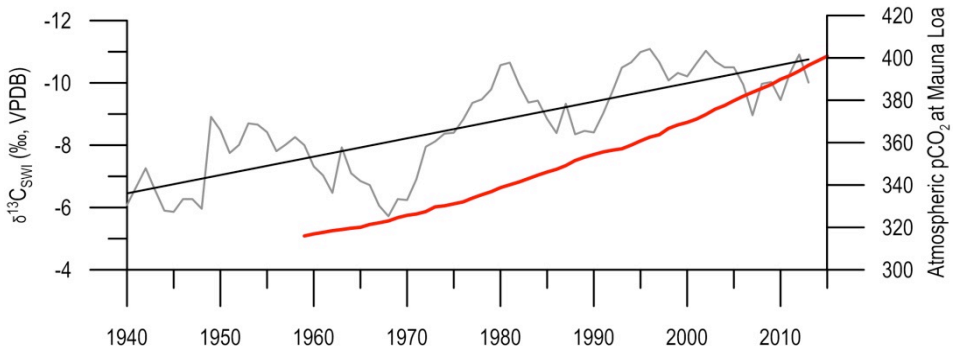

Figure 5.13 The $\delta^{13}C_{SWI}$ values (grey line) with trendline (black line) in comparison to atmospheric pCO_2 values at Mauna Loa.

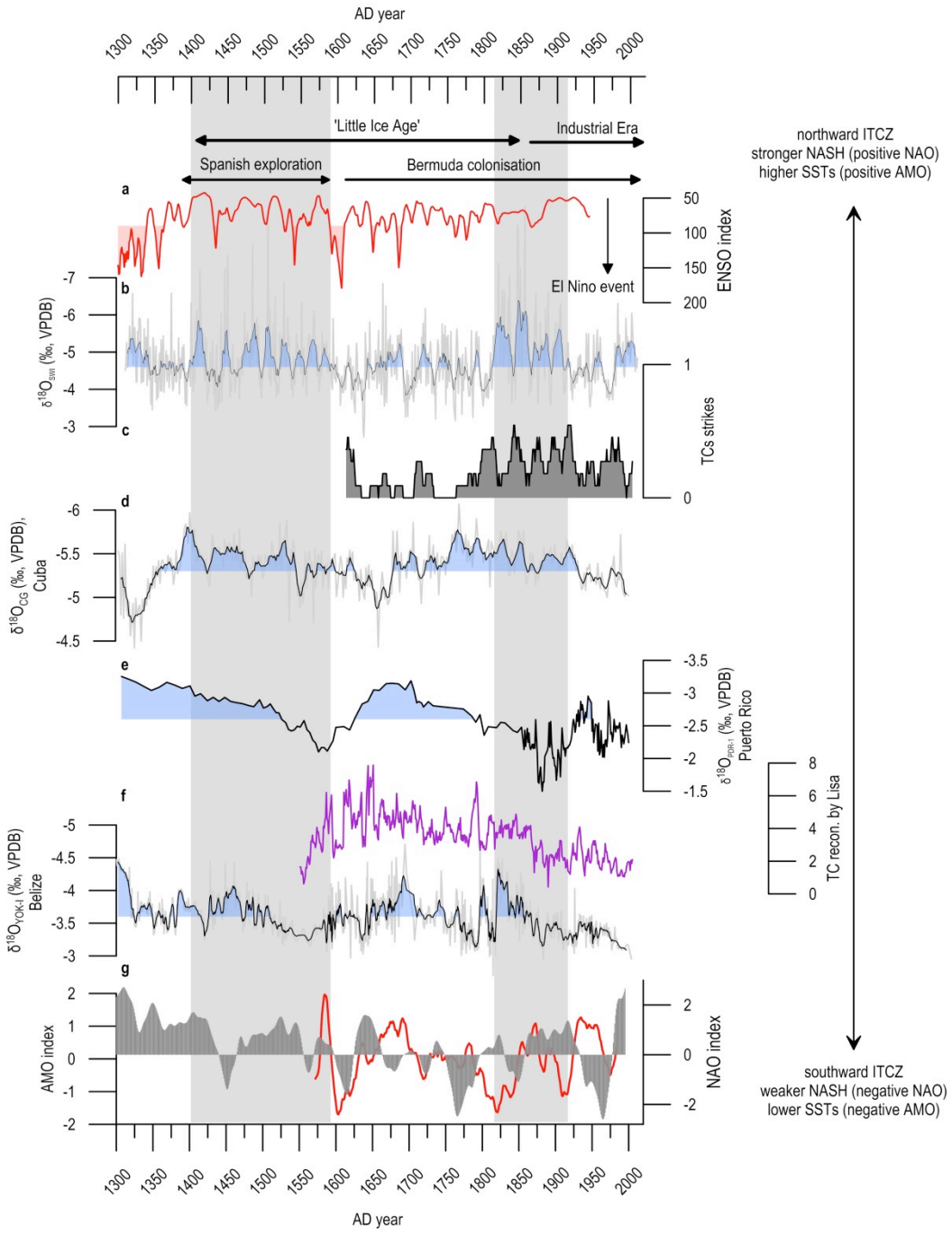

Figure 5.14. Comparison of environmental parameters and proxy-based reconstructions: a) 13-point running average of ENSO reconstruction (Moy et al., 2002); b) $\delta^{18}O_{SWI}$ values from the stalagmite BER-SWI-13 (this study), blue shading indicates values below mean; c) the 11- year running average of TCs strikes in Bermuda (Tucker, 1982); d) the $\delta^{18}O_{SWI}$ values from Cuba stalagmite CG (Fensterer et al., 2012); e) $\delta^{18}O$ values from Puerto Rican stalagmite PDR-1 (Winter et al., 2011); f) $\delta^{18}O$ values from Belize stalagmite YOK-I (Kennett et al., 2012) (black line) and TC activity reconstructions from YOK-G (Baldini – in preparation) (purple line); g) the NAO reconstruction (Trouet et al., 2009) and the AMO reconstruction (Gray et al., 2004) (red line).

5.3. Conclusions

Bermuda stalagmite oxygen stable isotope record reveals two relatively wetter periods in Bermuda: 1) AD 1400-1575 and 2) AD 1825-1925 associated with higher contribution of TC related rainfall. The pre-colonisation increased TC activity in Bermuda is associated with more El Niño-like events and positive NAO-like phase and reflects the northeast-ward TC tracks migration that coincides with the low TC activity in the Caribbean Sea. Our results also confirm that average hurricane activity during the industrial period has not exceeded its longer-term natural variability during the last millennium that corroborates other studies (Burn and Palmer, 2015).

Hurricane activity in Bermuda has been variable over the last 700 years and has been linked to previously known hurricane climate forcings. Increased hurricane activity between the 15 and 16th century and associated winds could have provided suitable conditions for westward Spanish expansion in the North Atlantic region.

Current climate predictions indicate that with greenhouse warming the TC frequency will either decrease or remain unchanged and the TC-related rainfall rates are likely to increase (Knutson et al., 2010).

Chapter 6

Summary and conclusions

6.1. Introduction

This thesis provides two new high-resolution Holocene records from the mid-latitudes located at the eastern and western side of North Atlantic basin based on geochemical analysis and CT scanning of stalagmites from Bermuda and southern Iberia, respectively. Geochemical interpretation of Bermuda stalagmite is supported by high resolution monitoring at the cave site that consequently identified Leamington Cave as a suitable site for paleoclimate study. The work presented is motivated by the need to develop 1) highly resolved and well-constraint climate records from tropical regions to improve understanding of recent tropical climate variability and 2) better techniques to obtain more reliable climate reconstructions.

6.2. Summary

This thesis is written as series of papers, so main conclusions are presented at the chapter's end. This chapter draws together the main conclusions from the other chapters to address the core research topics outlined in Chapter 1 and provides a concise overview of the contribution of this work to tropical paleoclimate research.

The main conclusions in this thesis are:

- the microclimate and ventilation dynamics of Leamington Cave and Conch Bar Caves, are controlled mainly by seasonal temperature differences between outside and cave air, wind and associated rainfall, but because of the connection of phreatic water with seawater, the microclimate of near shore caves is also modulated by the seawater temperature, and water level fluctuations;

- near shore caves are favourable environment for speleothem formation;
- global warming may result in the near-shore caves flooding that would inhibit speleothem growth and make those caves inaccessible for tourists;
- stalagmite density obtained from CT scanning can be used as a water-excess proxy, with lower densities associated with more variable drip rates, possibly reflecting increased seasonality consistent with expectations from previous studies of speleothem textures and crystal fabrics;
- an early Holocene humid interval and mid-Holocene year-round aridity preceded the onset of Mediterranean climate at 5.3 ka BP in southern Iberia.
- the gradual advancement of the Mediterranean climate in southern Iberia is linked to southward migration of the North Atlantic Subtropical High induced by an orbitally driven decrease in Northern Hemisphere insolation;
- Bermuda stalagmite oxygen stable isotope record reveals two relatively wetter periods in Bermuda: 1) AD 1400-1575 and 2) AD 1825-1925 associated with higher contribution of TC related rainfall and more El Nino-like events and more positive NAO-like phase;
- The increased TC-activity during the Industrial Era has not exceeded its longer-term natural variability.

Future work should include more robust correlation between CT-derived stalagmite density values and geochemical data.

Combined, the chapters presented in this thesis present a comprehensive study of recent and Holocene climate variability in the North Atlantic basin based on

speleothem proxy records which are supported by relevant background information from a previously uncharacterised cave.

References

ABRÀMOFF, M. D., MAGALHÃES, P. J. & RAM, S. J. 2004. Image Processing with ImageJ. *Biophotonics International,* 11**,** 36-42.

AGENCIA ESTATAL DE METEOROLOGÍA (AEMET). 2015. *Climatological data* [Online]. http://www.aemet.es/en/portada: Ministerio de Agricultura, Alimentación y Medio Ambiente (MAGRAMA). [Accessed 04-06-2015 2015].

ALLEN, J. R. M., HUNTLEY, B. & WATTS, W. A. 1996. The vegetation and climate of northwest Iberia over the last 14 000 yr. *Journal of Quaternary Science,* 11**,** 125-147.

ANDERSON, R. S., JIMÉNEZ-MORENO, G., CARRIÓN, J. S. & PÉREZ-MARTÍNEZ, C. 2011. Postglacial history of alpine vegetation, fire, and climate from Laguna de Río Seco, Sierra Nevada, southern Spain. *Quaternary Science Reviews,* 30**,** 1615-1629.

ANDREO, B., CARRASCO, F., CUENCA, J., TÉLLEZ, A. & VADILLO, I. 1998. El karst en los mármoles alpujárrides de las sierras Blanca y Mijas (provincia de Málaga). *In:* DURÁN, J. J. & LÓPEZ MARTÍNEZ, J. (eds.) *Karst en Andalucía.* Madrid: Instituto Tecnológico Geominero de España.

ANDREO, B., LIÑÁN, C., CARRASCO, F., JIMÉNEZ DE CISNEROS, C., CABALLERO, F. & MUDRY, J. 2004. Influence of rainfall quantity on the isotopic composition (^{18}O and ^{2}H) of water in mountainous areas. Application for groundwater research in the Yunquera-Nieves karst aquifers (S Spain). *Applied Geochemistry,* 19**,** 561-574.

ARANBARRI, J., GONZÁLEZ-SAMPÉRIZ, P., VALERO-GARCÉS, B., MORENO, A., GIL-ROMERA, G., SEVILLA-CALLEJO, M., GARCÍA-PRIETO, E., DI RITA, F., MATA, M. P., MORELLÓN, M., MAGRI, D., RODRÍGUEZ-LÁZARO, J. & CARRIÓN, J. S. 2014. Rapid climatic changes and resilient vegetation during the Lateglacial and Holocene in a continental region of south-western Europe. *Global and Planetary Change,* 114**,** 50-65.

BAKER, A., C. HELLSTROM, J., KELLY, B. F. J., MARIETHOZ, G. & TROUET, V. 2015. A composite annual-resolution stalagmite record of North Atlantic climate over the last three millennia. *Scientific Reports,* 5**,** 10307.

BAKER, A., WILSON, R., FAIRCHILD, I. J., FRANKE, J., SPÖTL, C., MATTEY, D., TROUET, V. & FULLER, L. 2011. High resolution $\delta^{18}O$ and $\delta^{13}C$ records from an annually laminated Scottish stalagmite and relationship with last millennium climate. *Global and Planetary Change,* 79**,** 303-311.

BAKKE, J., DAHL, S. O., PAASCHE, Ø., LØVLIE, R. & NESJE, A. 2005. Glacier fluctuations, equilibrium-line altitudes and palaeoclimate in Lyngen, northern Norway, during the Lateglacial and Holocene. *The Holocene,* 15**,** 518-540.

BALDINI, J. U. L. 2010. Cave atmosphere controls on stalagmite growth rate and palaeoclimate records. *Geological Society, London, Special Publications,* 336**,** 283-294.

BALDINI, J. U. L., MCDERMOTT, F., HOFFMANN, D. L., RICHARDS, D. A. & CLIPSON, N. 2008. Very high-frequency and seasonal cave atmosphere P_{CO2} variability: Implications for stalagmite growth and oxygen isotope-based paleoclimate records. *Earth and Planetary Science Letters,* 272**,** 118-129.

BALDINI, L. M. 2007. *An Investigation Of The Controls On The Stable Isotope Signature Of Meteoric Precipitation, Cave Seepage Water, And Holocene Stalagmites In Europe.* PhD, University College Dublin.

BALDINI, L. M., MCDERMOTT, F., BALDINI, J. U. L., ARIAS, P., CUETO, M., FAIRCHILD, I. J., HOFFMANN, D. L., MATTEY, D. P., MÜLLER, W., NITA, D. C., ONTAÑÓN, R., GARCIÁ-MONCÓ, C. & RICHARDS, D. A. 2015. Regional temperature, atmospheric circulation, and sea-ice variability within the Younger Dryas Event constrained using a speleothem from northern Iberia. *Earth and Planetary Science Letters,* 419**,** 101-110.

BANNER, J. L., GUILFOYLE, A., JAMES, E. W., STERN, L. A. & MUSGROVE, M. 2007. Seasonal Variations in Modern Speleothem Calcite Growth in Central Texas, U.S.A. *Journal of Sedimentary Research,* 77**,** 615-622.

BARD, E. 2002. Abrupt climate changes over millennial time scales: climate shock. *Physics Today,* 55**,** 32-38.

BATES, N. R., TAKAHASHI, T., CHIPMAN, D. W. & KNAP, A. H. 1998. Variability of pCO_2 on daily to seasonal timescales in the Sargasso Sea near Bermuda. *Journal of Geophysical Research: Oceans,* 103**,** 15567-15585.

BECKER, A., DAVENPORT, C., EICHENBERGER, U., GILLI, E., JEANNIN, P.-Y. & LACAVE, C. 2006. Speleoseismology: A critical perspective. *Journal of Seismology,* 10**,** 371-388.

BENDER, M. A., KNUTSON, T. R., TULEYA, R. E., SIRUTIS, J. J., VECCHI, G. A., GARNER, S. T. & HELD, I. M. 2010. Modeled Impact of Anthropogenic Warming on the Frequency of Intense Atlantic Hurricanes. *Science,* 327**,** 454-458.

BLACK, D. E., ABAHAZI, M. A., THUNELL, R. C., KAPLAN, A., TAPPA, E. J. & PETERSON, L. C. 2007. An 8-century tropical Atlantic SST record from the Cariaco Basin: Baseline variability, twentieth-century warming, and Atlantic hurricane frequency. *Paleoceanography,* 22.

BOCH, R., SPÖTL, C. & FRISIA, S. 2011. Origin and palaeoenvironmental significance of lamination in stalagmites from Katerloch Cave, Austria. *Sedimentology,* 58**,** 508-531.

BOLDT, K. V., LANE, P., WOODRUFF, J. D. & DONNELLY, J. P. 2010. Calibrating a sedimentary record of overwash from Southeastern New England using modeled historic hurricane surges. *Marine Geology,* 275**,** 127-139.

BOWEN, G. J. 2008. Spatial analysis of the intra-annual variation of precipitation isotope ratios and its climatological corollaries. *Journal of Geophysical Research: Atmospheres,* 113.

BOWEN, G. J. & WILKINSON, B. 2002. Spatial distribution of $\delta^{18}O$ in meteoric precipitation. *Geology,* 30**,** 315-318.

BREITENBACH, S. F. M., REHFELD, K., GOSWAMI, B., BALDINI, J. U. L., RIDLEY, H. E., KENNETT, D. J., PRUFER, K. M., AQUINO, V. V., ASMEROM, Y., POLYAK, V. J., CHENG, H., KURTHS, J. & MARWAN, N. 2012. COnstructing Proxy Records from Age models (COPRA). *Clim. Past,* 8**,** 1765-1779.

BURJACHS, F. & RIERA, S. 1995. Canvis vegetals i climàtics durant el neolític a la façana mediterrània ibérica. *Rubricatum,* 1**,** 21-27.

BURN, M. J., HOLMES, J., KENNEDY, L. M., BAIN, A., MARSHALL, J. D. & PERDIKARIS, S. 2016. A sediment-based reconstruction of Caribbean effective precipitation during the 'Little Ice Age' from Freshwater Pond, Barbuda. *The Holocene*.

BURN, M. J. & PALMER, S. E. 2015. Atlantic hurricane activity during the last millennium. *Scientific Reports,* 5**,** 12838.

CARLSON, W. D., ROWE, T., KETCHAM, R. A. & COLBERT, M. W. 2003. Applications of high-resolution X-ray computed tomography in petrology, meteoritics and palaeontology. *Geological Society, London, Special Publications,* 215**,** 7-22.

CARRIÓN, J. S. 2002. Patterns and processes of Late Quaternary environmental change in a montane region of southwestern Europe. *Quaternary Science Reviews,* 21**,** 2047-2066.

CARRIÓN, J. S., FERNÁNDEZ, S., GONZÁLEZ-SAMPÉRIZ, P., GIL-ROMERA, G., BADAL, E., CARRIÓN-MARCO, Y., LÓPEZ-MERINO, L., LÓPEZ-SÁEZ, J. A., FIERRO, E. & BURJACHS, F. 2010. Expected trends and surprises in the Lateglacial and Holocene vegetation history of the Iberian Peninsula and Balearic Islands. *Review of Palaeobotany and Palynology,* 162**,** 458-475.

CHABAUD, L., SÁNCHEZ GOÑI, M. F., DESPRAT, S. & ROSSIGNOL, L. 2014. Land–sea climatic variability in the eastern North Atlantic subtropical region over the last 14,200 years: Atmospheric and oceanic processes at different timescales. *The Holocene,* 24**,** 787-797.

CHALLINOR, D. & WINGATE, D. B. 1971. The struggle for survival of the Bermuda Cedar. *Biological Conservation,* 3**,** 222.

CHANDLER, R. 2006a. Bermuda's Caves. Bermuda Zoological Society.

CHANDLER, R. 2006b. The Geology of Bermuda. Bermuda Zoological Society.

CHENG, H., EDWARDS, R. L., HOFF, J., GALLUP, C. D., RICHARDS, D. A. & ASMEROM, Y. 2000. The half-lives of uranium-234 and thorium-230. *Chemical Geology,* 169**,** 17-33.

COBB, K. M., CHARLES, C. D., CHENG, H. & EDWARDS, R. L. 2003. El Niño/Southern Oscillation and tropical Pacific climate during the last millennium. *Nature,* 424**,** 271-276.

COLLINS, M., AN, S.-I., CAI, W., GANACHAUD, A., GUILYARDI, E., JIN, F.-F., JOCHUM, M., LENGAIGNE, M., POWER, S., TIMMERMANN, A., VECCHI, G. & WITTENBERG, A. 2010. The impact of global warming on the tropical Pacific Ocean and El Nino. *Nature Geosci,* 3**,** 391-397.

COMAS-BRU, L. & MCDERMOTT, F. 2014. Impacts of the EA and SCA patterns on the European twentieth century NAO–winter climate relationship. *Quarterly Journal of the Royal Meteorological Society,* 140**,** 354-363.

COMBOURIEU-NEBOUT, N., PEYRON, O., BOUT-ROUMAZEILLES, V., GORING, S., DORMOY, I., JOANNIN, S., SADORI, L., SIANI, G. & MAGNY, M. 2013. Holocene vegetation and climate changes in the central Mediterranean inferred from a high-resolution marine pollen record (Adriatic Sea). *Clim. Past,* 9**,** 2023-2042.

COWAN, B. D., OSBORNE, M. C. & BANNER, J. L. 2013. Temporal variability of cave-air CO_2 in central Texas. *Journal of Cave and Karst Studies,* 75**,** 38-50.

CULLETON, B. J., PRUFER, K. M. & KENNETT, D. J. 2012. A Bayesian AMS 14C chronology of the Classic Maya Center of Uxbenká, Belize. *Journal of Archaeological Science,* 39**,** 1572-1586.

DANSGAARD, W. 1964. Stable isotope in precipitation. *Tellus,* XVI**,** 436-468.

DAVIS, R. E., HAYDEN, B. P., GAY, D. A., PHILLIPS, W. L. & JONES, G. V. 1997. The North Atlantic Subtropical Anticyclone. *Journal of Climate,* 10**,** 728-744.

DEMENOCAL, P., ORTIZ, J., GUILDERSON, T., ADKINS, J., SARNTHEIN, M., BAKER, L. & YARUSINSKY, M. 2000. Abrupt onset and termination of

the African Humid Period:: rapid climate responses to gradual insolation forcing. *Quaternary Science Reviews,* 19**,** 347-361.

DENOMMEE, K. C., BENTLEY, S. J. & DROXLER, A. W. 2014. Climatic controls on hurricane patterns: a 1200-y near-annual record from Lighthouse Reef, Belize. *Sci. Rep.,* 4.

DOMÍNGUEZ-VILLAR, D., WANG, X., CHENG, H., MARTÍN-CHIVELET, J. & EDWARDS, R. L. 2008. A high-resolution late Holocene speleothem record from Kaite Cave, northern Spain: δ18O variability and possible causes. *Quaternary International,* 187**,** 40-51.

DONNELLY, J. P., BRYANT, S. S., BUTLER, J., DOWLING, J., FAN, L., HAUSMANN, N., NEWBY, P., SHUMAN, B., STERN, J., WESTOVER, K. & WEBB, T. 2001a. 700 yr sedimentary record of intense hurricane landfalls in southern New England. *Geological Society of America Bulletin,* 113**,** 714-727.

DONNELLY, J. P., BUTLER, J., ROLL, S., WENGREN, M. & WEBB III, T. 2004. A backbarrier overwash record of intense storms from Brigantine, New Jersey. *Marine Geology,* 210**,** 107-121.

DONNELLY, J. P., HAWKES, A. D., LANE, P., MACDONALD, D., SHUMAN, B. N., TOOMEY, M. R., VAN HENGSTUM, P. J. & WOODRUFF, J. D. 2015. Climate forcing of unprecedented intense-hurricane activity in the last 2000 years. *Earth's Future,* 3**,** 49-65.

DONNELLY, J. P., ROLL, S., WENGREN, M., BUTLER, J., LEDERER, R. & WEBB III, T. 2001b. Sedimentary evidence of intense hurricane strikes from New Jersey. *Geology,* 29**,** 615–618.

DONNELLY, J. P. & WOODRUFF, J. D. 2007. Intense hurricane activity over the past 5,000 years controlled by El Niño and the West African monsoon. *Nature,* 447**,** 465-468.

DORADO VALIÑO, M., VALDEOLMILLOS RODRíGUEZ, A., BLANCA RUIZ ZAPATA, M., JOSÉ GIL GARCíA, M. & DE BUSTAMANTE GUTIÉRREZ, I. 2002. Climatic changes since the Late-glacial/Holocene transition in La Mancha Plain (South-central Iberian Peninsula, Spain) and their incidence on Las Tablas de Daimiel marshlands. *Quaternary International,* 93–94**,** 73-84.

DORALE, J. A. 1998. Climate and Vegetation History of the Midcontinent from 75 to 25ka: A Speleothem Record from Crevice Cave, Missouri, USA. *Science,* 282**,** 1871-1874.

DREYBRODT, W. 2008. Chemical kinetics, speleothem growth and climate *Boreas,* 28**,** 347-356.

DULINSKI, M. & ROZANSKI, K. 1990. Formation of $^{13}C/^{12}C$ isotope ratios in speleothems: a semi-dynamic model. *Radiocarbon,* 32**,** 7-16.

DUNSTONE, N. J., SMITH, D. M., BOOTH, B. B. B., HERMANSON, L. & EADE, R. 2013. Anthropogenic aerosol forcing of Atlantic tropical storms. *Nature Geosci,* 6**,** 534-539.

ELLISON, J. C. 1996. Pollen Evidence of Late Holocene Mangrove Development in Bermuda. *Global Ecology and Biogeography Letters,* 5**,** 315-326.

ELSNER, J. B., LIU, K. & KOCHER, B. 2000. Spatial Variations in Major U.S. Hurricane Activity: Statistics and a Physical Mechanism. *Climate,* 13**,** 2293-2305.

ENFIELD, D. B., MESTAS-NUNEZ, A. M. & TRIMBLE, P. J. 2001. The Atlantic multidecadal oscillation and its relation to rainfall and river flows in the continental U.S. *Geophysical Research Letters,* 28**,** 2077-2080.

ERCOLANI, C., MULLER, J., COLLINS, J., SAVARESE, M. & SQUICCIMARA, L. 2015. Intense Southwest Florida hurricane landfalls over the past 1000 years. *Quaternary Science Reviews,* 126**,** 17-25.

FAIRCHILD, I. J. & BAKER, A. 2012. *Speleothem Science: From Process To Past Environments*, Blackwell Publishing Ltd.

FAIRCHILD, I. J., SMITH, C. L., BAKER, A., FULLER, L., SPÖTL, C., MATTEY, D., MCDERMOTT, F. & E.I.M.F 2006. Modification and preservation of environmental signals in speleothems. *Earth-Science Reviews,* 75**,** 105-153.

FENSTERER, C. 2011. *Holocene Caribbean climate variability reconstructed from speleothems from western Cuba* Doctor of Natural Sciences, University of Heidelberg.

FENSTERER, C., SCHOLZ, D., HOFFMANN, D., SPÖTL, C., PAJÓN, J. M. & MANGINI, A. 2012. Cuban stalagmite suggests relationship between Caribbean precipitation and the Atlantic Multidecadal Oscillation during the past 1.3 ka. *The Holocene*.

FLETCHER, W. J., BOSKI, T. & MOURA, D. 2007. Palynological evidence for environmental and climatic change in the lower Guadiana valley, Portugal, during the last 13 000 years. *The Holocene,* 17**,** 481-494.

FLETCHER, W. J., DEBRET, M. & GOÑI, M. F. S. 2013. Mid-Holocene emergence of a low-frequency millennial oscillation in western Mediterranean climate: Implications for past dynamics of the North Atlantic atmospheric westerlies. *The Holocene,* 23**,** 153-166.

FRAPPIER, A., SAHAGIAN, D., GONZÁLEZ, L. A. & CARPENTER, S. J. 2002. El Niño Events Recorded by Stalagmite Carbon Isotopes. *Science,* 298**,** 565.

FRAPPIER, A. B., SAHAGIAN, D., CARPENTER, S. J., GONZALEZ, L. A. & FRAPPIER, B. R. 2007. Stalagmite stable isotope record of recent tropical cyclone events. *Geology,* 35**,** 111-114.

FRISIA, S. 2015. Microstratigraphic logging of calcite fabrics in speleothems as tool for palaeoclimate studies. *International Journal of Speleology,* 44**,** 1-16.

FRISIA, S., BORSATO, A., FAIRCHILD, I. J. & MCDERMOTT, F. 2000. Calcite Fabrics, Growth Mechanisms, And Environments Of Formation In Speleothems From The Italian Alps And Southwestern Ireland. *Journal Of Sedimentary Research,* 70**,** 1183-1196.

FRISIA, S., BORSATO, A., SPÖTL, C., VILLA, I. M. & CUCCHI, F. 2005. Climate variability in the SE Alps of Italy over the past 17 000 years reconstructed from a stalagmite record. *Boreas,* 34**,** 445-455.

FRUMKIN, A., FORD, D. C. & SCHWARCZ, H. P. 2000. Paleoclimate and vegetation of the Last Glacial Cycles in Jerusalem from a Speleothem Record. *Global Biogeochemical Cycles,* 14**,** 863-870.

GALY, A., BAR-MATTHEWS, M., HALICZ, L. & O'NIONS, R. K. 2002. Mg isotopic composition of carbonate: insight from speleothem formation. *Earth and Planetary Science Letters,* 201**,** 105-115.

GAMBLE, D. W., DOGWILER, J. T. & MYLROIE, J. 2000. Field assessment of the microclimatology of tropical flank margin caves. *Climate Research,* 16**,** 37-50.

GAMBLE, D. W., PARNELL, D. B. & CURTIS, S. 2008. Spatial variability of the Caribbean mid-summer drought and relation to north Atlantic high circulation. *International Journal of Climatology,* 28**,** 343-350.

GARCÍA-ALIX, A., JIMÉNEZ-MORENO, G., ANDERSON, R. S., JIMÉNEZ ESPEJO, F. & DELGADO HUERTAS, A. 2012. Holocene environmental change in southern Spain deduced from the isotopic record of a high-elevation wetland in Sierra Nevada. *Journal of Paleolimnology,* 48**,** 471-484.

GEDZELMAN, S., LAWRENCE, J., GAMACHE, J., BLACK, M., HINDMAN, E., BLACK, R., DUNION, J., WILLOUGHBY, H. & ZHANG, X. 2003. Probing Hurricanes with Stable Isotopes of Rain and Water Vapor. *Monthly Weather Review,* 131**,** 1112-1127.

GENTY, D., BLAMART, D., GHALEB, B., PLAGNES, V., CAUSSE, C., BAKALOWICZ, M., ZOUARI, K., CHKIR, N., HELLSTROM, J., WAINER, K. & BOURGES, F. 2006. Timing and dynamics of the last deglaciation from European and North African $\delta^{13}C$ stalagmite profiles—comparison with Chinese and South Hemisphere stalagmites. *Quaternary Science Reviews,* 25**,** 2118-2142.

GENTY, D. & QUINIE, Y. 1996. Annually laminated sequences in the internal structure of some Belgian stalagmites — importance for paleoclimatology. *Journal of Sedimentary Research,* 66**,** 275-288.

GIANNINI, A., CANE, M. A. & KUSHNIR, Y. 2001. Interdecadal Changes in the ENSO Teleconnection to the Caribbean Region and the North Atlantic Oscillation. *Journal of Climate,* 14**,** 2867-2879.

GIRY, C., FELIS, T., KÖLLING, M., SCHOLZ, D., WEI, W., LOHMANN, G. & SCHEFFERS, S. 2012. Mid- to late Holocene changes in tropical Atlantic temperature seasonality and interannual to multidecadal variability documented in southern Caribbean corals. *Earth and Planetary Science Letters,* 331–332**,** 187-200.

GOLDENBERG, S. B., LANDSEA, C. W., MESTAS-NUNEZ, A. M. & GRAY, W. M. 2001. The recent increase in Atlantic hurricane activity: Causes and implications. *Science,* 293**,** 474-479.

GOLDMAN, L. W. 2007. Principles of CT and CT Technology. *Journal of Nuclear Medicine Technology,* 35**,** 115-128.

GOODKIN, N. F., HUGHEN, K. A., DONEY, S. C. & CURRY, W. B. 2008. Increased multidecadal variability of the North Atlantic Oscillation since 1781. *Nature Geosci,* 1**,** 844-848.

GOUVEIA, C., TRIGO, R. M., DACAMARA, C. C., LIBONATI, R. & PEREIRA, J. M. C. 2008. The North Atlantic Oscillation and European vegetation dynamics. *International Journal of Climatology,* 28**,** 1835-1847.

GRÀCIA, E., VIZCAINO, A., ESCUTIA, C., ASIOLI, A., RODÉS, Á., PALLÀS, R., GARCIA-ORELLANA, J., LEBREIRO, S. & GOLDFINGER, C. 2010. Holocene earthquake record offshore Portugal (SW Iberia): testing turbidite paleoseismology in a slow-convergence margin. *Quaternary Science Reviews,* 29**,** 1156-1172.

GRAY, S. T., GRAUMLICH, L. J., BETANCOURT, J. L. & PEDERSON, G. T. 2004. A tree-ring based reconstruction of the Atlantic Multidecadal Oscillation since 1567 A.D. *Geophysical Research Letters,* 31**,** n/a-n/a.

GRAY, W. M. 1984. Atlantic Seasonal Hurricane Frequency. Part I: El Niño and 30 mb Quasi-Biennial Oscillation Influences. *Monthly Weather Review,* 112**,** 1649-1668.

GUEVARA-MURUA, A., HENDY, E. J., RUST, A. C. & CASHMAN, K. V. 2015. Consistent decrease in North Atlantic Tropical Cyclone frequency following major volcanic eruptions in the last three centuries. *Geophysical Research Letters,* 42**,** 9425-9432.

GUISHARD, P. M., NELSON, A. E., EVANS, L. J., HART, E. R. & O'CONNELL, G. D. 2007. Bermuda subtropical storms. *Meteorology and Atmospheric Physics,* 97**,** 239-253.

HAIG, J., NOTT, J. & REICHART, G.-J. 2014. Australian tropical cyclone activity lower than at any time over the past 550-1,500 years. *Nature,* 505**,** 667-671.

HALKITIS, M., SMITH, S. & RIGG, K. 1980. *The Climate of the Bahamas*, Bahamas Geographical Association.

HAMMER, Ø., HARPER, D. A. T. & RYAN, P. D. 2001. Past: paleontological statistics software package for education and data analysis. *Palaeontologia Electronica,* 4**,** 1-9.

HARDING, A., PALUTIKOF, J. & HOLT, T. 2009. The climate system. *In:* WOODWARD, J. (ed.) *The Physical Geography of the Mediterranean.* Oxford: Oxford University Press.

HAUG, G. H., HUGHEN, K. A., SIGMAN, D. M., PETERSON, L. C. & RÖHL, U. 2001. Southward Migration of the Intertropical Convergence Zone Through the Holocene. *Science,* 293**,** 1304-1308.

HENDERSON, G. M. 2006. Caving In to New Chronologies. *Science,* 313**,** 620-622.

HENDY, C. H. 1971. The isotopic geochemistry of speleothems—I. The calculation of the effects of different modes of formation on the isotopic composition of speleothems and their applicability as palaeoclimatic indicators. *Geochimica et Cosmochimica Acta,* 35**,** 801-824.

HETZINGER, S., PFEIFFER, M., DULLO, W. C., KEENLYSIDE, N., LATIF, M. & ZINKE, J. 2008. Caribbean coral tracks Atlantic Multidecadal Oscillation and past hurricane activity. *Geology,* 36**,** 11-14.

HOFFMANN, D. L., PRYTULAK, J., RICHARDS, D. A., ELLIOTT, T., COATH, C. D., SMART, P. L. & SCHOLZ, D. 2007. Procedures for accurate U and Th isotope measurements by high precision MC-ICPMS. *International Journal of Mass Spectrometry,* 264**,** 97-109.

HUANG, Y., FAIRCHILD, I. J., BORSATO, A., FRISIA, S., CASSIDY, N. J., MCDERMOTT, F. & HAWKESWORTH, C. J. 2001. Seasonal variations in Sr, Mg and P in modern speleothems (Grotta di Ernesto, Italy). *Chemical Geology,* 175**,** 429-448.

HURRELL, J. W. 1995. Decadal Trends in the North Atlantic Oscillation: Regional Temperatures and Precipitation. *Science,* 269**,** 676-679.

ILLIFFE, T. M. 2003. Submarine caves and cave biology of Bermuda. *NSS News,* August 2013**,** 216-224.

ILLIFFE, T. M. 2009. Bermuda. *In:* PALMER, A. N. P. A. M. V. (ed.) *Caves and karst of the USA*. Huntsville, AL: National Speleological Society.

IPCC 2014. Climate Change 2014: Synthesis Report. Contribution of Working Groups I, II and III to the Fifth Assessment Report of the Intergovernmental Panel on Climate Change. *In:* PACHAURI, R. K. & MEYER, L. A. (eds.). Geneva, Switzerland.

JAFFEY, A. H., FLYNN, K. F., GLENDENIN, L. E., BENTLEY, W. C. & ESSLING, A. M. 1971. Precision measurement of half-lives and specific activities of ^{235}U and ^{238}U. *Physical Review C,* 4**,** 1889-1906.

JALUT, G., DEDOUBAT, J. J., FONTUGNE, M. & OTTO, T. 2009. Holocene circum-Mediterranean vegetation changes: Climate forcing and human impact. *Quaternary International,* 200**,** 4-18.

JALUT, G., ESTEBAN AMAT, A., BONNET, L., GAUQUELIN, T. & FONTUGNE, M. 2000. Holocene climatic changes in the Western Mediterranean, from south-east France to south-east Spain. *Palaeogeography, Palaeoclimatology, Palaeoecology,* 160**,** 255-290.

JALUT, G., ESTEBAN AMAT, A., MORA, S. R. I., FONTUGNE, M., MOOK, R., BONNET, L. & GAUQUELIN, T. 1997. Holocene climatic changes in the western Mediterranean: installation of the Mediterranean climate. *Comptes Rendus de l'Académie des Sciences - Series IIA - Earth and Planetary Science,* 325**,** 327-334.

JAMBRINA-ENRÍQUEZ, M., RICO, M., MORENO, A., LEIRA, M., BERNÁRDEZ, P., PREGO, R., RECIO, C. & VALERO-GARCÉS, B. L. 2014. Timing of deglaciation and postglacial environmental dynamics in NW Iberia: the Sanabria Lake record. *Quaternary Science Reviews,* 94**,** 136-158.

JIMÉNEZ-MORENO, G. & ANDERSON, R. S. 2012. Holocene vegetation and climate change recorded in alpine bog sediments from the Borreguiles de la Virgen, Sierra Nevada, southern Spain. *Quaternary Research,* 77**,** 44-53.

JURY, M., MALMGREN, B. A. & WINTER, A. 2007. Subregional precipitation climate of the Caribbean and relationships with ENSO and NAO. *Journal of Geophysical Research: Atmospheres,* 112**,** n/a-n/a.

KENNETT, D. J., BREITENBACH, S. F. M., AQUINO, V. V., ASMEROM, Y., AWE, J., BALDINI, J. U. L., BARTLEIN, P., CULLETON, B. J., EBERT, C., JAZWA, C., MACRI, M. J., MARWAN, N., POLYAK, V., PRUFER, K. M., RIDLEY, H. E., SODEMANN, H., WINTERHALDER, B. & HAUG, G. H. 2012. Development and Disintegration of Maya Political Systems in Response to Climate Change. *Science,* 338**,** 788-791.

KETCHAM, R. A. & CARLSON, W. D. 2001. Acquisition, optimization and interpretation of X-ray computed tomographic imagery: applications to the geosciences. *Computers & Geosciences,* 27**,** 381-400.

KLOTZBACH, P. J. 2011a. El Niño–Southern Oscillation's Impact on Atlantic Basin Hurricanes and U.S. Landfalls. *Journal of Climate,* 24**,** 1252-1263.

KLOTZBACH, P. J. 2011b. The Influence of El Niño–Southern Oscillation and the Atlantic Multidecadal Oscillation on Caribbean Tropical Cyclone Activity. *Journal of Climate,* 24**,** 721-731.

KNIGHT, J. R., FOLLAND, C. K. & SCAIFE, A. A. 2006. Climate impacts of the Atlantic Multidecadal Oscillation. *Geophysical Research Letters,* 33**,** n/a-n/a.

KNUTSON, T. R., MCBRIDE, J. L., CHAN, J., EMANUEL, K., HOLLAND, G., LANDSEA, C., HELD, I., KOSSIN, J. P., SRIVASTAVA, A. K. & SUGI, M. 2010. Tropical cyclones and climate change. *Nature Geosci,* 3**,** 157-163.

KORNICKER, L. S., ILIFFE, T. M. & HARRISON-NELSON, E. 2008. Ontogeny of Deeveya spiralis Kornicker & Iliffe, 1985, collected in anchialine caves in the Caicos Islands (Crustacea, Ostracoda, Halocyprida, Deeveyidae). *Proceedings of the Biological Society of Washington,* 121**,** 331-353.

KOSSIN, J. P., EMANUEL, K. A. & VECCHI, G. A. 2014. The poleward migration of the location of tropical cyclone maximum intensity. *Nature,* 509**,** 349-352.

KOWALCZK, A. J. & FROELICH, P. N. 2010. Cave air ventilation and CO_2 outgassing by radon-222 modeling: How fast do caves breathe? *Earth and Planetary Science Letters,* 289**,** 209-219.

LANDSEA, C. W. & GRAY, W. M. 1992. The Strong Association between Western Sahelian Monsoon Rainfall and Intense Atlantic Hurricanes. *Journal of Climate,* 5**,** 435-453.

LANE, C. S., HORN, S. P., ORVIS, K. H. & THOMASON, J. M. 2011a. Oxygen isotope evidence of Little Ice Age aridity on the Caribbean slope of the Cordillera Central, Dominican Republic. *Quaternary Research,* 75**,** 461-470.

LANE, P., DONNELLY, J. P., WOODRUFF, J. D. & HAWKES, A. D. 2011b. A decadally-resolved paleohurricane record archived in the late Holocene sediments of a Florida sinkhole. *Marine Geology,* 287**,** 14-30.

LASKAR, J., ROBUTEL, P., JOUTEL, F., GASTINEAU, M., CORREIA, A. C. M. & LEVRARD, B. 2004. A long-term numerical solution for the insolation quantities of the Earth *Astronomy & Astrophysics,* 428**,** 261-285.

LAWRENCE, J. R. & GEDZELMAN, S. D. 1996. Low stable isotope ratios of tropical cyclone rains. *Geophysical Research Letters,* 23**,** 527-530.

LAWRENCE, J. R., GEDZELMAN, S. D., ZHANG, X. & ARNOLD, R. 1998. Stable isotope ratios of rain and vapor in 1995 hurricanes. *Journal of Geophysical Research,* 103**,** 11,381-11,400.

LI, J., XIE, S.-P., COOK, E. R., MORALES, M. S., CHRISTIE, D. A., JOHNSON, N. C., CHEN, F., D/'ARRIGO, R., FOWLER, A. M., GOU, X. & FANG, K. 2013. El Niño modulations over the past seven centuries. *Nature Clim. Change,* 3**,** 822-826.

LIU, K. & FEARN, M. L. 2000. Reconstruction of Prehistoric Landfall Frequencies of Catastrophic Hurricanes in Northwestern Florida from Lake Sediment Records. *Quaternary Research,* 54**,** 238-245.

LU, J., VECCHI, G. A. & REICHLER, T. 2007. Expansion of the Hadley cell under global warming. *Geophysical Research Letters,* 34**,** L06805.

MAGNY, M. 2004. Holocene climate variability as reflected by mid-European lake-level fluctuations and its probable impact on prehistoric human settlements. *Quaternary International,* 113**,** 65-79.

MAGNY, M., COMBOURIEU-NEBOUT, N., DE BEAULIEU, J. L., BOUT-ROUMAZEILLES, V., COLOMBAROLI, D., DESPRAT, S., FRANCKE, A., JOANNIN, S., ORTU, E., PEYRON, O., REVEL, M., SADORI, L., SIANI, G., SICRE, M. A., SAMARTIN, S., SIMONNEAU, A., TINNER, W., VANNIÈRE, B., WAGNER, B., ZANCHETTA, G., ANSELMETTI, F., BRUGIAPAGLIA, E., CHAPRON, E., DEBRET, M., DESMET, M., DIDIER, J., ESSALLAMI, L., GALOP, D., GILLI, A., HAAS, J. N., KALLEL, N., MILLET, L., STOCK, A., TURON, J. L. & WIRTH, S. 2013. North-south palaeohydrological contrasts in the central Mediterranean during the Holocene: tentative synthesis and working hypotheses. *Clim. Past,* 9**,** 2043-2071.

MAINAKE, E. 2002. *Cueva El Refugio (AG-2)*.

MAJZOUB, M. 1971. Fractionation en oxygen-18 et en deuterium entre l'eau et sa vapeur. *Jour. Chim. Phys. ,* 63**,** 563-568.

MALAIZE, B., BERTRAN, P., CARBONEL, P., BONNISSENT, D., CHARLIER, K., GALOP, D., IMBERT, D., SERRAND, N., STOUVENOT, C. & PUJOL, C. 2011. Hurricanes and climate in the Caribbean during the past 3700 years BP. *Holocene,* 21**,** 911-924.

MALMQUIST, D. L. Oxygen isotopes in cave stalagmites as a proxy record of past tropical cyclone activity. 22nd Conference on Hurricanes and Tropical

Meteorology, 1997 Ft. Collins, CO, USA. American Meteorological Society, 393-394.

MANN, M. E., WOODRUFF, J. D., DONNELLY, J. P. & ZHANG, Z. 2009. Atlantic hurricanes and climate over the past 1,500 years. *Nature,* 460**,** 880-883.

MARSHALL, J., KUSHNIR, Y., BATTISTI, D., CHANG, P., CZAJA, A., DICKSON, R., HURRELL, J., MCCARTNEY, M., SARAVANAN, R. & VISBECK, M. 2001. North Atlantic climate variability: phenomena, impacts and mechanisms. *International Journal of Climatology,* 21**,** 1863-1898.

MARTÍN-CHIVELET, J., MUÑOZ-GARCÍA, M. B., EDWARDS, R. L., TURRERO, M. J. & ORTEGA, A. I. 2011. Land surface temperature changes in Northern Iberia since 4000 yr BP, based on $\delta^{13}C$ of speleothems. *Global and Planetary Change,* 77**,** 1-12.

MATTEY, D., LOWRY, D., DUFFET, J., FISHER, R., HODGE, E. & FRISIA, S. 2008. A 53 year seasonally resolved oxygen and carbon isotope record from a modern Gibraltar speleothem: Reconstructed drip water and relationship to local precipitation. *Earth and Planetary Science Letters,* 269**,** 80-95.

MATTEY, D. P., FAIRCHILD, I. J., ATKINSON, T. C., LATIN, J. P., AINSWORTH, M. & DURELL, R. 2010. Seasonal microclimate control of calcite fabrics, stable isotopes and trace elements in modern speleothem from St Michaels Cave, Gibraltar. *Geological Society, London, Special Publications,* 336**,** 323-344.

MAURI, A., DAVIS, B. A. S., COLLINS, P. M. & KAPLAN, J. O. 2015. The climate of Europe during the Holocene: a gridded pollen-based reconstruction and its multi-proxy evaluation. *Quaternary Science Reviews,* 112**,** 109-127.

MCCLOSKEY, T. A., BIANCHETTE, T. A. & LIU, K.-B. 2013. Track Patterns of Landfalling and Coastal Tropical Cyclones in the Atlantic Basin, Their Relationship with the North Atlantic Oscillation (NAO), and the Potential Effect of Global Warming. *American Journal of Climate Change,* 2**,** 12-22.

MCCLOSKEY, T. A. & KELLER, G. 2009. 5000 year sedimentary record of hurricane strikes on the central coast of Belize. *Quaternary International,* 195**,** 53-68.

MCCLOSKEY, T. A. & LIU, K.-B. 2012. A sedimentary-based history of hurricane strikes on the southern Caribbean coast of Nicaragua. *Quaternary Research,* 78**,** 454-464.

MCDERMOTT, F., FRISIA, S., HUANG, Y., LONGINELLI, A., SPIRO, B., HEATON, T. H. E., HAWKESWORTH, C. J., BORSATO, A., KEPPENS, E., FAIRCHILD, I. J., VAN DER BORG, K., VERHEYDEN, S. & SELMO, E. 1999. Holocene climate variability in Europe: Evidence from $\delta^{18}O$, textural and extension-rate variations in three speleothems. *Quaternary Science Reviews,* 18**,** 1021-1038.

MCGREGOR, H. V., FISCHER, M. J., GAGAN, M. K., FINK, D., PHIPPS, S. J., WONG, H. & WOODROFFE, C. D. 2013. A weak El Nino/Southern Oscillation with delayed seasonal growth around 4,300 years ago. *Nature Geosci,* 6**,** 949-953.

MCMILLAN, E. A. 2006. *Tests for palaeoaridity in Holocene stalagmites form SW Europe.* PhD, Keele University.

MCMILLAN, E. A., FAIRCHILD, I. J., FRISIA, S., BORSATO, A. & MCDERMOTT, F. 2005. Annual trace element cycles in calcite–aragonite

speleothems: evidence of drought in the western Mediterranean 1200–1100 yr BP. *Journal of Quaternary Science,* 20**,** 423-433.

MEES, F., SWENNEN, R., VAN GEET, M. & JACOBS, P. (eds.) 2003. *Applications of X-ray Computed Tomography in the Geosciences,* London: Geological Society.

MICKLER, P. J., BANNER, J. L., STERN, L., ASMEROM, Y., EDWARDS, R. L. & ITO, E. 2004a. Stable isotope variations in modern tropical speleothems: Evaluating equilibrium vs. kinetic isotope effects. *Geochimica et Cosmochimica Acta,* 68**,** 4381-4393.

MICKLER, P. J., KETCHAM, R. A., COLBERT, M. W. & BANNER, J. L. 2004b. Application of high-resolution X-ray computed tomography in determining the suitability of speleothems for use in paleoclimatic, paleohydrologic reconstructions. *Journal of Cave and Karst Studies,* 66**,** 3-8.

MICKLER, P. J., STERN, L. A. & BANNER, J. L. 2006. Large kinetic isotope effects in modern speleothems. *Geological Society of America Bulletin,* 118**,** 65-81.

MILLER, D. L., MORA, C. I., GRISSINO-MAYER, H. D., MOCK, C. J., UHLE, M. E. & SHARP, Z. 2006. Tree-ring isotope records of tropical cyclone activity. *Proceedings of the National Academy of Sciences,* 103**,** 14294-14297.

MILLER, T. 1996. Geologic and hydrologic controls on karst and cave development in Belize. *Journal of Cave and Karst Studies,* 58**,** 100-120.

MIYAKE, Y., MATSUBAYA, O. & NISHIHARA, C. 1968. An isotopic study on meteoric precipitation. *Pap. Meteor. Geophys.,* 19**,** 243-266.

MORENO, A., LÓPEZ-MERINO, L., LEIRA, M., MARCO-BARBA, J., GONZÁLEZ-SAMPÉRIZ, P., VALERO-GARCÉS, B., LÓPEZ-SÁEZ, J., SANTOS, L., MATA, P. & ITO, E. 2011. Revealing the last 13,500 years of environmental history from the multiproxy record of a mountain lake (Lago Enol, northern Iberian Peninsula). *Journal of Paleolimnology,* 46**,** 327-349.

MOSELEY, G. E., SMART, P. L. & RICHARDS, D. A. 2007. Clues on Middle Caicos. What can the Conch Bar cave system tell us about sea levels in the past? *Times of the Islands,* Winter 2007/2008.

MOY, C. M., SELTZER, G. O., RODBELL, D. T. & ANDERSON, D. M. 2002. Variability of El Nino/Southern Oscillation activity at millennial timescales during the Holocene epoch. *Nature,* 420**,** 162-165.

MUDARRA, M., ANDREO, B., BARBERÁ, J. A. & VADILLO, I. 2009. Monitoring Dripwater Chemistry In Refugio Cave (Southern Spain) As A Contribution To Understand Infiltration And Speleogenetic Processes In Karst Aquifers *17th International Karstological School "Classical Karst"*. Postojna, Slovenia.

MYLROIE, J. E. 2012. Coastal Caves. *In:* WILLIAM, B. W. & DAVID, C. C. (eds.) *Encyclopedia of Caves (Second Edition)*. Amsterdam: Academic Press.

NATIONAL METEOROLOGICAL SERVICE OF BELIZE. 2016. *Climatology Information for a few stations across Belize* [Online]. http://www.hydromet.gov.bz/climatology: National Meteorological Service of Belize. Available: http://www.hydromet.gov.bz/climatology 2016].

OLSEN, J., ANDERSON, N. J. & KNUDSEN, M. F. 2012. Variability of the North Atlantic Oscillation over the past 5,200 years. *Nature Geosci,* 5**,** 808-812.

ORTEGA, R., MAIRE, R., DEVÈS, G. & QUINIF, Y. 2005. High-resolution mapping of uranium and other trace elements in recrystallized aragonite–

calcite speleothems from caves in the Pyrenees (France): Implication for U-series dating. *Earth and Planetary Science Letters,* 237**,** 911-923.

OSTER, J. L., MONTAÑEZ, I. P. & KELLEY, N. P. 2012. Response of a modern cave system to large seasonal precipitation variability. *Geochimica et Cosmochimica Acta,* 91**,** 92-108.

OWEN, R. A., DAY, C. C., HU, C. Y., LIU, Y. H., POINTING, M. D., BLÄTTLER, C. L. & HENDERSON, G. M. 2016. Calcium isotopes in caves as a proxy for aridity: Modern calibration and application to the 8.2 kyr event. *Earth and Planetary Science Letters,* 443**,** 129-138.

PARK, L. E. 2012. Comparing Two Long-Term Hurricane Frequency and Intensity Records from San Salvador Island, Bahamas. *Journal of Coastal Research***,** 891-902.

PEEL, M. C., FINLAYSON, B. L. & MCMAHON, T. A. 2007. Updated world map of the Köppen-Geiger climate classification. *Hydrol. Earth Syst. Sci.,* 11**,** 1633-1644.

PÉREZ-OBIOL, R., JALUT, G., JULIÀ, R., PÈLACHS, A., IRIARTE, M. J., OTTO, T. & HERNÁNDEZ-BELOQUI, B. 2011. Mid-Holocene vegetation and climatic history of the Iberian Peninsula. *The Holocene,* 21**,** 75-93.

PEROS, M., GREGORY, B., MATOS, F., REINHARDT, E. & DESLOGES, J. 2015. Late-Holocene record of lagoon evolution, climate change, and hurricane activity from southeastern Cuba. *The Holocene,* 25**,** 1483-1497.

PINTO, J. G. & RAIBLE, C. C. 2012. Past and recent changes in the North Atlantic oscillation. *Climate Change,* 3**,** 79-90.

PRZYLIBSKI, T. A. 1999. Radon concentration changes in the air of two caves in Poland. *Journal of Environmental Radioactivity,* 45**,** 81-94.

RAILSBACK, L. B., LIANG, F., VIDAL ROMANÍ, J. R., GRANDAL-D'ANGLADE, A., VAQUEIRO RODRÍGUEZ, M., SANTOS FIDALGO, L., FERNÁNDEZ MOSQUERA, D., CHENG, H. & EDWARDS, R. L. 2011. Petrographic and isotopic evidence for Holocene long-term climate change and shorter-term environmental shifts from a stalagmite from the Serra do Courel of northwestern Spain, and implications for climatic history across Europe and the Mediterranean. *Palaeogeography, Palaeoclimatology, Palaeoecology,* 305**,** 172-184.

REED, J. M., STEVENSON, A. C. & JUGGINS, S. 2001. A multi-proxy record of Holocene climatic change in southwestern Spain: the Laguna de Medina, Cádiz. *The Holocene,* 11**,** 707-719.

RIDLEY, H. E., ASMEROM, Y., BALDINI, J. U. L., BREITENBACH, S. F. M., AQUINO, V. V., PRUFER, K. M., CULLETON, B. J., POLYAK, V., LECHLEITNER, F. A., KENNETT, D. J., ZHANG, M., MARWAN, N., MACPHERSON, C. G., BALDINI, L. M., XIAO, T., PETERKIN, J. L., AWE, J. & HAUG, G. H. 2015a. Aerosol forcing of the position of the intertropical convergence zone since ad 1550. *Nature Geosci,* 8**,** 195-200.

RIDLEY, H. E., BALDINI, J. U. L., PRUFER, K. M., WALCZAK, I. W. & BREITENBACH, S. F. M. 2015b. High-resolution monitoring of Yok Balum Cave, Belize: An investigation of seasonal ventilation regimes and the atmospheric and drip-flow response to a local earthquake. *Journal of Cave and Karst Studies,* 77**,** 183-199.

ROBERTS, N., BRAYSHAW, D., KUZUCUOĞLU, C., PEREZ, R. & SADORI, L. 2011. The mid-Holocene climatic transition in the Mediterranean: Causes and consequences. *The Holocene,* 21**,** 3-13.

RODRIGUES, R. R. & MCPHADEN, M. J. 2014. Why did the 2011-12 La Niña cause a severe drought in the Brazilian Northeast? *Geophysical Research Letters*, 2013GL058703.

RODRÍGUEZ-PUEBLA, C. & NIETO, S. 2010. Trends of precipitation over the Iberian Peninsula and the North Atlantic Oscillation under climate change conditions. *International Journal of Climatology,* 30**,** 1807-1815.

RODYSILL, J. R., RUSSELL, J. M., CRAUSBAY, S. D., BIJAKSANA, S., VUILLE, M., EDWARDS, R. L. & CHENG, H. 2013. A severe drought during the last millennium in East Java, Indonesia. *Quaternary Science Reviews,* 80**,** 102-111.

ROSS, D. A. 1995. *Introduction to Oceanography,* New York, HarperCollins.

ROWE, M. P. & BRISTOW, C. S. 2015. Landward-advancing Quaternary eolianites of Bermuda. *Aeolian Research,* 19, Part B**,** 235-249.

ROWE, M. P., WAINER, K. A. I., BRISTOW, C. S. & THOMAS, A. L. 2014. Anomalous MIS 7 sea level recorded on Bermuda. *Quaternary Science Reviews,* 90**,** 47-59.

RUEGER, B. & VON WALLMENICH, T. 1996. Human impact on the forests of Bermuda: the decline of endemic cedar and palmetto since 1609, recorded in the Holocene pollen record of Devonshire Marsh. *Journal of Paleolimnology,* 16**,** 59-66.

SAENGER, C., COHEN, A. L., OPPO, D. W., HALLEY, R. B. & CARILLI, J. E. 2009. Surface-temperature trends and variability in the low-latitude North Atlantic since 1552. *Nature Geosci,* 2**,** 492-495.

SÁNCHEZ-MURILLO, R., BIRKEL, C., WELSH, K., ESQUIVEL-HERNÁNDEZ, G., CORRALES-SALAZAR, J., BOLL, J., BROOKS, E., ROUPSARD, O., SÁENZ-ROSALES, O., KATCHAN, I., ARCE-MESÉN, R., SOULSBY, C. & ARAGUÁS-ARAGUÁS, L. J. 2016. Key drivers controlling stable isotope variations in daily precipitation of Costa Rica: Caribbean Sea versus Eastern Pacific Ocean moisture sources. *Quaternary Science Reviews,* 131, Part B**,** 250-261.

SCILEPPI, E. & DONNELLY, J. P. 2007. Sedimentary evidence of hurricane strikes in western Long Island, New York. *Geochemistry, Geophysics, Geosystems,* 8**,** Q06011.

SCOTT, D. B., COLLINS, E. S., GAYES, P. T. & WRIGHT, E. 2003. Records of prehistoric hurricanes on the South Carolina coast based on micropaleontological and sedimentological evidence, with comparison to other Atlantic Coast records. *Geological Society of America Bulletin,* 115**,** 1027-1039.

SEAGER, R., TING, M., HELD, I., KUSHNIR, Y., LU, J., VECCHI, G., HUANG, H.-P., HARNIK, N., LEETMAA, A., LAU, N.-C., LI, C., VELEZ, J. & NAIK, N. 2007. Model Projections of an Imminent Transition to a More Arid Climate in Southwestern North America. *Science,* 316**,** 1181-1184.

SHERWIN, C. M. & BALDINI, J. U. L. 2011. Cave air and hydrological controls on prior calcite precipitation and stalagmite growth rates: Implications for palaeoclimate reconstructions using speleothems. *Geochimica et Cosmochimica Acta,* 75**,** 3915-3929.

SMART, P. L., MOSELEY, G. E., RICHARDS, D. A. & WHITAKER, F. F. 2008. Past high sea-stands and platform stability: evidence from Conch Bar Cave, Middle Caicos. 203-210.

SOUZA, P. & CAVALCANTI, I. F. A. 2009. Atmospheric centres of action associated with the Atlantic ITCZ position. *International Journal of Climatology,* 29**,** 2091-2105.

SPÖTL, C., FAIRCHILD, I. J. & TOOTH, A. F. 2005. Cave air control on dripwater geochemistry, Obir Caves (Austria): Implications for speleothem deposition in dynamically ventilated caves. *Geochimica et Cosmochimica Acta,* 68**,** 2451-2468.

STEPHENSON, T. S., VINCENT, L. A., ALLEN, T., VAN MEERBEECK, C. J., MCLEAN, N., PETERSON, T. C., TAYLOR, M. A., AARON-MORRISON, A. P., AUGUSTE, T., BERNARD, D., BOEKHOUDT, J. R. I., BLENMAN, R. C., BRAITHWAITE, G. C., BROWN, G., BUTLER, M., CUMBERBATCH, C. J. M., ETIENNE-LEBLANC, S., LAKE, D. E., MARTIN, D. E., MCDONALD, J. L., OZORIA ZARUELA, M., PORTER, A. O., SANTANA RAMIREZ, M., TAMAR, G. A., ROBERTS, B. A., SALLONS MITRO, S., SHAW, A., SPENCE, J. M., WINTER, A. & TROTMAN, A. R. 2014. Changes in extreme temperature and precipitation in the Caribbean region, 1961–2010. *International Journal of Climatology***,** n/a-n/a.

STOLL, H. M., MORENO, A., MENDEZ-VICENTE, A., GONZALEZ-LEMOS, S., JIMENEZ-SANCHEZ, M., DOMINGUEZ-CUESTA, M. J., EDWARDS, R. L., CHENG, H. & WANG, X. 2013. Paleoclimate and growth rates of speleothems in the northwestern Iberian Peninsula over the last two glacial cycles. *Quaternary Research*.

SUTTON, R. T. & HODSON, D. L. R. 2005. Atlantic Ocean Forcing of North American and European Summer Climate. *Science,* 309**,** 115-118.

TANAKA, A., NAKANO, S. & IKEHARA, K. 2011. X-ray CT analysis and density estimation using a sediment core. *Earth Planets Space,* 63**,** 103-110.

THE BERMUDA WEATHER SERVICE. 2000. *Bermuda's Climatology 1949-1999* [Online]. http://www.weather.bm/ClimateReport/data/climatology.html. [Accessed 12/06/2015 2015].

TOOMEY, M. R., CURRY, W. B., DONNELLY, J. P. & VAN HENGSTUM, P. J. 2013. Reconstructing 7000 years of North Atlantic hurricane variability using deep-sea sediment cores from the western Great Bahama Bank. *Paleoceanography,* 28**,** 31-41.

TRIGO, R. M., POZO-VÁZQUEZ, D., OSBORN, T. J., CASTRO-DÍEZ, Y., GÁMIZ-FORTIS, S. & ESTEBAN-PARRA, M. J. 2004. North Atlantic oscillation influence on precipitation, river flow and water resources in the Iberian Peninsula. *International Journal of Climatology,* 24**,** 925-944.

TROUET, V., ESPER, J., GRAHAM, N. E., BAKER, A., SCOURSE, J. D. & FRANK, D. C. 2009. Persistent Positive North Atlantic Oscillation Mode Dominated the Medieval Climate Anomaly. *Science,* 324**,** 78-80.

TROUET, V., HARLEY, G. L. & DOMÍNGUEZ-DELMÁS, M. 2016. Shipwreck rates reveal Caribbean tropical cyclone response to past radiative forcing. *Proceedings of the National Academy of Sciences*.

TUCKER, T. 1982. *Beware the Hurricane! The story of the cyclonic tropical storms that have struck Bermuda 1609-1982,* Bermuda, Island Press Limited.

TZEDAKIS, P. C., PÄLIKE, H., ROUCOUX, K. H. & DE ABREU, L. 2009. Atmospheric methane, southern European vegetation and low-mid latitude links on orbital and millennial timescales. *Earth and Planetary Science Letters,* 277**,** 307-317.

VAN HENGSTUM, P. J., DONNELLY, J. P., KINGSTON, A. W., WILLIAMS, B. E., SCOTT, D. B., REINHARDT, E. G., LITTLE, S. N. & PATTERSON, W. P. 2015. Low-frequency storminess signal at Bermuda linked to cooling events in the North Atlantic region. *Paleoceanography,* 30**,** 52-76.

VAN HENGSTUM, P. J., DONNELLY, J. P., TOOMEY, M. R., ALBURY, N. A., LANE, P. & KAKUK, B. 2014. Heightened hurricane activity on the Little Bahama Bank from 1350 to 1650 AD. *Continental Shelf Research,* 86**,** 103-115.

VUILLE, M., BRADLEY, R. S., WERNER, M., HEALY, R. & KEIMIG, F. 2003. Modeling $\delta^{18}O$ in precipitation over the tropical Americas: 1. Interannual variability and climatic controls. *Journal of Geophysical Research,* 108.

WANG, Y., LEE, K.-H., LIN, Y., LEVY, M. & ZHANG, R. 2014. Distinct effects of anthropogenic aerosols on tropical cyclones. *Nature Clim. Change,* 4**,** 368-373.

WANNER, H., BEER, J. R., BU¨ TIKOFER, J., CROWLEY, T. J., CUBASCH, U., FLU¨ CKIGER, J., GOOSSE, H., GROSJEAN, M., JOOS, F., KAPLAN, J. O., KU¨ TTEL, M., MU¨ LLER, S. A., PRENTICE, I. C., SOLOMINA, O., STOCKER, T. F., TARASOV, P., WAGNER, M. & WIDMANNM, M. 2008. Mid- to Late Holocene climate change: an overview. *Quaternary Science Reviews,* 27**,** 1791-1828.

WANNER, H., BRÖNNIMANN, S., CASTY, C., GYALISTRAS, D., LUTERBACHER, J., SCHMUTZ, C., STEPHENSON, D. B. & XOPLAKI, E. 2001. North Atlantic Oscillation – Concepts And Studies. *Surveys in Geophysics,* 22**,** 321-381.

WATTS, W. A. & HANSEN, B. C. S. 1986. Holocene climate and vegetation of Bermuda. *Pollen et Spores,* 28**,** 355-364.

WEBSTER, P. J., HOLLAND, G. J., CURRY, J. A. & CHANG, H.-R. 2005. Changes in Tropical Cyclone Number, Duration, and Intensity in a Warming Environment. *Science,* 309**,** 1844-1846.

WINTER, A., MILLER, T., KUSHNIR, Y., SINHA, A., TIMMERMANN, A., JURY, M. R., GALLUP, C., CHENG, H. & EDWARDS, R. L. 2011. Evidence for 800 years of North Atlantic multi-decadal variability from a Puerto Rican speleothem. *Earth and Planetary Science Letters,* 308**,** 23-28.

WINTER, A., ZANCHETTIN, D., MILLER, T., KUSHNIR, Y., BLACK, D., LOHMANN, G., BURNETT, A., HAUG, G. H., ESTRELLA-MARTINEZ, J., BREITENBACH, S. F. M., BEAUFORT, L., RUBINO, A. & CHENG, H. 2015. Persistent drying in the tropics linked to natural forcing. *Nat Commun,* 6.

WIRTH, S. B., GLUR, L., GILLI, A. & ANSELMETTI, F. S. 2013. Holocene flood frequency across the Central Alps – solar forcing and evidence for variations in North Atlantic atmospheric circulation. *Quaternary Science Reviews,* 80**,** 112-128.

WONG, C. & BANNER, J. L. 2010. Response of cave air CO_2 and drip water to brush clearing in central Texas: Implications for recharge and soil CO_2 dynamics. *Journal of Geophysical Research: Biogeosciences,* 115**,** G04018.

YU, K., ZHAO, J.-X., SHI, Q. & PRICE, G. J. 2012. Recent massive coral mortality events in the South China Sea: Was global warming and ENSO variability responsible? *Chemical Geology,* 320–321**,** 54-65.

ZANCHETTA, G., BAR-MATTHEWS, M., DRYSDALE, R. N., LIONELLO, P., AYALON, A., HELLSTROM, J. C., ISOLA, I. & REGATTIERI, E. 2014.

Coeval dry events in the central and eastern Mediterranean basin at 5.2 and 5.6ka recorded in Corchia (Italy) and Soreq caves (Israel) speleothems. *Global and Planetary Change,* 122**,** 130-139.

ZANCHETTA, G., DRYSDALE, R. N., HELLSTROM, J. C., FALLICK, A. E., ISOLA, I., GAGAN, M. K. & PARESCHI, M. T. 2007. Enhanced rainfall in the Western Mediterranean during deposition of sapropel S1: stalagmite evidence from Corchia cave (Central Italy). *Quaternary Science Reviews,* 26**,** 279-286.

ZHANG, D., ZHANG, P., SANG, W., CHENG, H., WU, X., YUAN, Y., BAI, Y., WANG, J. & JIA, J. 2010. Implications of stalagmite density for past climate change: An example from stalagmite growth during the last deglaciation from Wanxiang Cave, western Loess Plateau. *Chinese Science Bulletin,* 55**,** 3936-3943.

ZISU, N. S., SCHWARCZ, H. P., KONYER, N., CHOW, T. & NOSEWORTHY, M. D. 2012. Macroholes in stalagmites and the search for lost water. *J. Geophys. Res.,* 117**,** F03020.

Appendix A

Oxygen and carbon stable isotope data

from BER-SWI-13 stalagmite

Year A.D.	Depth from top (mm)	$\delta^{13}C$ (‰ VPDB)	$\delta^{18}O$ (‰ VPDB)
2013.17	0.00	-10.01	-4.26
2013.05	0.05	-10.55	-4.93
2012.94	0.10	-10.56	-5.26
2012.82	0.15	-10.59	-5.09
2012.70	0.20	-10.38	-5.26
2012.57	0.25	-10.91	-4.88
2012.32	0.35	-10.44	-4.84
2012.19	0.40	-9.95	-4.54
2012.06	0.45	-10.11	-4.76
2011.92	0.50	-10.31	-4.77
2011.79	0.55	-9.93	-4.79
2011.65	0.60	-10.57	-5.33
2011.51	0.65	-10.07	-4.87
2011.36	0.70	-10.00	-4.58
2011.07	0.80	-9.45	-5.31
2010.77	0.90	-9.72	-4.82
2010.30	1.05	-10.03	-4.86
2010.14	1.10	-10.01	-5.76
2009.98	1.15	-10.04	-4.72
2009.81	1.20	-9.81	-4.49
2009.64	1.25	-9.97	-4.87
2009.30	1.35	-9.07	-4.48
2009.13	1.40	-8.84	-4.88
2008.96	1.45	-8.96	-4.46
2008.78	1.50	-8.95	-3.85
2008.60	1.55	-9.09	-4.14
2008.42	1.60	-9.50	-5.14
2008.05	1.70	-9.95	-5.48
2007.87	1.75	-10.23	-4.87
2007.68	1.80	-10.39	-4.88
2007.49	1.85	-10.38	-5.07
2007.29	1.90	-10.50	-5.20
2007.10	1.95	-10.59	-4.71
2006.90	2.00	-10.36	-5.62
2006.70	2.05	-10.65	-4.58
2006.50	2.10	-10.50	-5.50
2006.30	2.15	-10.78	-5.11
2006.10	2.20	-10.74	-6.35
2005.89	2.25	-10.71	-5.76
2005.68	2.30	-10.69	-5.41
2005.47	2.35	-10.88	-5.65
2005.26	2.40	-10.70	-7.16
2005.05	2.45	-11.03	-5.39
2004.62	2.55	-11.01	-6.40
2004.40	2.60	-10.75	-6.05
2004.18	2.65	-10.93	-5.13
2003.96	2.70	-10.63	-5.40
2003.73	2.75	-10.74	-5.08
2003.28	2.85	-10.30	-5.03
2003.05	2.90	-10.21	-6.27
2002.82	2.95	-10.35	-4.92
2002.59	3.00	-10.42	-6.92
2002.35	3.05	-10.32	-4.73
2002.12	3.10	-10.09	-5.31
2001.88	3.15	-9.64	-4.75
2001.64	3.20	-9.84	-5.41
2001.40	3.25	-10.08	-5.26
2001.16	3.30	-10.11	-5.70
2000.91	3.35	-10.56	-4.77
2000.42	3.45	-10.67	-5.30
2000.17	3.50	-10.78	-5.54
1999.92	3.55	-10.92	-5.44
1999.67	3.60	-11.09	-5.43
1999.41	3.65	-11.13	-4.93
1999.16	3.70	-11.03	-5.50
1998.90	3.75	-10.99	-5.35
1998.38	3.85	-10.56	-5.41
1998.12	3.90	-10.50	-5.55
1997.86	3.95	-10.66	-5.19
1997.59	4.00	-10.33	-5.89
1997.33	4.05	-10.59	-5.26
1997.06	4.10	-10.49	-5.84
1996.79	4.15	-10.49	-5.31
1996.52	4.20	-10.10	-5.91
1996.25	4.25	-9.94	-5.12
1995.98	4.30	-9.73	-5.30
1995.43	4.40	-9.30	-4.74
1995.15	4.45	-9.02	-4.76
1994.59	4.55	-8.61	-4.53
1994.31	4.60	-8.32	-4.33
1994.03	4.65	-8.41	-4.28
1993.46	4.75	-8.69	-4.43
1993.17	4.80	-8.46	-4.42
1992.59	4.90	-8.83	-5.40
1992.30	4.95	-8.93	-5.27
1992.01	5.00	-8.35	-4.14
1991.72	5.05	-8.74	-4.52
1991.42	5.10	-9.16	-4.80

Year A.D.	Depth from top (mm)	$\delta^{13}C$ (‰ VPDB)	$\delta^{18}O$ (‰ VPDB)
1991.13	5.15	-9.33	-4.89
1990.83	5.20	-9.33	-4.71
1990.53	5.25	-8.54	-4.76
1990.23	5.30	-8.39	-4.41
1989.93	5.35	-8.50	-4.63
1989.63	5.40	-8.63	-4.91
1989.33	5.45	-8.84	-4.61
1989.02	5.50	-8.74	-5.34
1988.72	5.55	-9.22	-4.84
1988.41	5.60	-8.92	-4.98
1988.10	5.65	-9.43	-5.09
1987.79	5.70	-9.12	-4.51
1987.17	5.80	-9.37	-5.47
1986.86	5.85	-10.15	-4.58
1986.55	5.90	-10.40	-4.98
1986.23	5.95	-9.94	-4.92
1985.92	6.00	-10.36	-5.20
1985.60	6.05	-10.98	-4.87
1985.28	6.10	-10.65	-6.31
1984.97	6.15	-10.10	-5.42
1984.65	6.20	-9.83	-5.62
1984.33	6.25	-10.57	-4.89
1984.00	6.30	-9.46	-6.07
1983.68	6.35	-8.99	-4.68
1983.36	6.40	-9.79	-5.14
1983.03	6.45	-9.65	-4.92
1982.71	6.50	-9.47	-4.10
1981.40	6.70	-9.36	-5.24
1981.07	6.75	-9.63	-4.19
1980.40	6.85	-9.40	-4.25
1980.07	6.90	-8.82	-4.23
1979.74	6.95	-9.02	-4.77
1979.40	7.00	-8.45	-4.42
1979.07	7.05	-8.40	-3.91
1978.73	7.10	-7.97	-4.73
1978.40	7.15	-8.47	-3.72
1978.06	7.20	-8.37	-4.17
1977.72	7.25	-8.74	-4.15
1977.38	7.30	-8.30	-3.90
1977.04	7.35	-8.12	-3.80
1976.36	7.45	-7.88	-3.87
1976.01	7.50	-7.95	-3.86
1975.67	7.55	-7.93	-3.94
1974.64	7.70	-6.91	-3.82
1974.29	7.75	-6.50	-3.83
1973.94	7.80	-6.24	-3.68
1973.60	7.85	-6.23	-3.50
1973.25	7.90	-6.27	-3.71
1972.55	8.00	-5.82	-4.25
1972.20	8.05	-5.95	-3.34
1971.85	8.10	-5.72	-3.54
1971.50	8.15	-5.80	-3.85
1971.15	8.20	-5.93	-3.45
1970.80	8.25	-6.06	-3.81
1970.44	8.30	-6.02	-3.77
1970.09	8.35	-6.72	-4.12
1969.73	8.40	-6.72	-4.26
1969.38	8.45	-7.09	-4.25
1969.02	8.50	-8.15	-7.00
1968.67	8.55	-6.85	-4.24
1967.96	8.65	-6.88	-4.13
1967.60	8.70	-7.10	-4.15
1967.24	8.75	-8.17	-4.21
1966.52	8.85	-7.93	-4.19
1966.16	8.90	-7.07	-4.85
1965.81	8.95	-6.47	-3.70
1965.45	9.00	-6.98	-4.42
1965.08	9.05	-7.34	-3.83
1964.72	9.10	-7.03	-4.39
1964.00	9.20	-6.86	-4.90
1963.64	9.25	-7.32	-4.04
1963.28	9.30	-7.44	-4.39
1962.55	9.40	-8.00	-4.79
1962.19	9.45	-8.11	-4.37
1961.82	9.50	-8.25	-5.04
1961.46	9.55	-8.26	-5.40
1961.10	9.60	-8.35	-4.59
1960.73	9.65	-8.27	-4.60
1960.37	9.70	-8.02	-5.07
1960.00	9.75	-7.85	-5.09
1959.27	9.85	-7.81	-4.76
1958.54	9.95	-7.91	-4.25
1958.17	10.00	-8.42	-4.32
1957.40	10.10	-8.66	-5.60
1956.57	10.20	-8.98	-5.25
1956.13	10.25	-8.70	-4.46
1955.67	10.30	-8.48	-4.48
1954.71	10.40	-8.01	-4.46

Year A.D.	Depth from top (mm)	$\delta^{13}C$ (‰ VPDB)	$\delta^{18}O$ (‰ VPDB)
1954.20	10.45	-7.91	-4.18
1953.69	10.50	-7.75	-4.64
1952.61	10.60	-8.48	-5.46
1952.06	10.65	-8.93	-5.15
1951.49	10.70	-8.91	-4.27
1950.31	10.80	-5.96	-4.70
1949.09	10.90	-6.27	-3.83
1947.17	11.05	-5.86	-3.53
1946.51	11.10	-5.90	-3.89
1945.85	11.15	-6.58	-3.94
1945.17	11.20	-6.56	-5.49
1944.48	11.25	-7.26	-4.20
1943.79	11.30	-7.26	-5.58
1943.09	11.35	-6.67	-4.84
1942.38	11.40	-6.48	-5.50
1941.66	11.45	-6.08	-4.31
1940.94	11.50	-5.63	-4.92
1940.21	11.55	-5.61	-4.04
1939.47	11.60	-5.49	-4.62
1938.73	11.65	-6.08	-4.46
1937.23	11.75	-7.08	-4.33
1933.41	12.00	-6.46	-4.92
1932.64	12.05	-6.05	-4.38
1931.86	12.10	-5.94	-4.86
1930.30	12.20	-5.93	-4.35
1929.52	12.25	-6.24	-4.17
1928.74	12.30	-6.46	-4.47
1927.95	12.35	-6.83	-3.97
1927.17	12.40	-7.32	-4.37
1926.39	12.45	-7.04	-4.04
1925.61	12.50	-6.81	-4.51
1924.83	12.55	-6.92	-4.23
1924.05	12.60	-6.71	-4.37
1923.27	12.65	-6.83	-3.72
1922.49	12.70	-6.46	-4.18
1921.72	12.75	-6.39	-3.97
1919.41	12.90	-6.59	-4.73
1918.65	12.95	-7.02	-4.60
1916.40	13.10	-7.70	-5.25
1915.66	13.15	-7.94	-4.84
1914.92	13.20	-7.33	-5.16
1914.19	13.25	-7.02	-4.51
1913.47	13.30	-7.12	-3.96
1912.76	13.35	-7.46	-5.18
1912.05	13.40	-7.60	-4.13
1911.35	13.45	-7.76	-3.88
1910.65	13.50	-7.16	-5.02
1909.97	13.55	-6.93	-5.27
1909.29	13.60	-6.72	-5.23
1908.63	13.65	-8.04	-5.09
1907.97	13.70	-9.13	-6.24
1907.32	13.75	-9.66	-6.30
1906.68	13.80	-9.61	-6.15
1906.06	13.85	-9.92	-5.43
1904.24	14.00	-8.43	-5.76
1903.66	14.05	-8.40	-5.19
1903.10	14.10	-8.56	-5.16
1902.54	14.15	-9.23	-5.42
1902.00	14.20	-9.25	-6.47
1901.47	14.25	-10.13	-4.82
1900.95	14.30	-9.96	-5.23
1900.45	14.35	-10.18	-5.78
1899.50	14.45	-10.03	-5.14
1899.04	14.50	-9.59	-5.03
1898.60	14.55	-9.48	-5.14
1898.18	14.60	-9.21	-4.72
1897.77	14.65	-9.09	-4.93
1897.38	14.70	-8.65	-5.25
1897.00	14.75	-8.56	-4.44
1896.65	14.80	-7.93	-5.59
1896.31	14.85	-7.78	-4.67
1895.99	14.90	-7.85	-5.16
1895.69	14.95	-7.81	-4.27
1895.41	15.00	-7.86	-5.11
1895.14	15.05	-7.23	-3.85
1894.87	15.10	-7.18	-4.78
1894.59	15.15	-6.67	-3.84
1894.05	15.25	-6.33	-3.38
1893.78	15.30	-5.45	-4.16
1893.51	15.35	-5.19	-3.58
1893.23	15.40	-5.29	-4.41
1892.69	15.50	-5.17	-2.83
1892.42	15.55	-5.18	-3.82
1892.14	15.60	-5.34	-3.95
1891.87	15.65	-5.97	-4.30
1891.60	15.70	-6.48	-4.29
1891.33	15.75	-8.46	-4.56
1891.06	15.80	-9.35	-5.78

Year A.D.	Depth from top (mm)	$\delta^{13}C$ (‰ VPDB)	$\delta^{18}O$ (‰ VPDB)
1890.78	15.85	-9.87	-4.93
1890.51	15.90	-9.09	-6.63
1890.24	15.95	-8.99	-4.81
1889.97	16.00	-8.85	-6.97
1889.70	16.05	-9.11	-6.20
1889.42	16.10	-9.57	-5.92
1889.15	16.15	-9.78	-5.39
1888.34	16.30	-9.12	-5.87
1887.79	16.40	-8.77	-5.38
1887.52	16.45	-8.25	-4.92
1886.71	16.60	-7.05	-5.86
1886.44	16.65	-7.87	-6.16
1886.17	16.70	-8.58	-4.50
1885.89	16.75	-8.92	-4.57
1885.62	16.80	-8.49	-4.56
1885.35	16.85	-7.74	-4.29
1885.08	16.90	-8.12	-4.00
1884.81	16.95	-8.73	-4.79
1884.27	17.05	-9.07	-4.75
1884.00	17.10	-9.15	-5.20
1883.73	17.15	-9.14	-5.22
1883.46	17.20	-9.19	-5.13
1883.19	17.25	-9.40	-4.30
1882.65	17.35	-8.41	-4.49
1882.38	17.40	-8.34	-5.30
1881.84	17.50	-9.56	-5.08
1881.57	17.55	-9.53	-5.98
1881.30	17.60	-9.59	-5.30
1881.03	17.65	-9.93	-5.65
1880.77	17.70	-10.07	-5.10
1880.50	17.75	-10.34	-4.76
1880.23	17.80	-10.17	-5.82
1879.96	17.85	-10.14	-4.81
1879.69	17.90	-9.75	-5.81
1878.89	18.05	-8.94	-5.75
1878.62	18.10	-9.09	-5.03
1878.35	18.15	-9.03	-5.22
1877.82	18.25	-8.71	-4.69
1877.55	18.30	-8.38	-4.37
1876.75	18.45	-6.47	-4.57
1876.22	18.55	-7.09	-3.60
1875.96	18.60	-7.12	-4.73
1875.69	18.65	-6.90	-3.97
1875.16	18.75	-7.53	-4.41
1874.90	18.80	-8.72	-5.24
1874.63	18.85	-8.99	-4.73
1874.37	18.90	-9.74	-5.29
1873.58	19.05	-8.93	-4.64
1873.32	19.10	-8.48	-6.58
1873.05	19.15	-8.70	-5.97
1872.53	19.25	-9.20	-4.38
1872.27	19.30	-9.58	-5.43
1872.00	19.35	-9.87	-5.97
1871.48	19.45	-9.53	-5.98
1871.22	19.50	-9.14	-6.47
1870.70	19.60	-8.81	-4.73
1870.44	19.65	-9.03	-4.32
1870.18	19.70	-9.02	-5.57
1869.92	19.75	-6.82	-6.38
1869.66	19.80	-8.86	-6.02
1869.40	19.85	-8.46	-4.64
1868.89	19.95	-8.91	-4.67
1868.63	20.00	-8.40	-4.98
1868.37	20.05	-7.72	-4.70
1868.11	20.10	-7.35	-4.70
1867.86	20.15	-7.34	-4.65
1867.60	20.20	-7.89	-4.56
1867.34	20.25	-7.40	-3.95
1867.09	20.30	-7.82	-6.85
1866.83	20.35	-8.96	-4.97
1866.58	20.40	-8.95	-4.54
1866.32	20.45	-9.41	-4.72
1866.07	20.50	-9.32	-5.18
1865.56	20.60	-8.79	-7.14
1865.30	20.65	-8.34	-4.46
1865.05	20.70	-8.46	-5.08
1864.55	20.80	-8.08	-4.14
1864.29	20.85	-6.58	-3.86
1864.04	20.90	-6.98	-5.20
1863.54	21.00	-9.44	-5.27
1863.29	21.05	-9.50	-5.63
1863.04	21.10	-9.03	-6.27
1862.79	21.15	-8.71	-6.21
1862.54	21.20	-8.59	-6.10
1862.29	21.25	-8.80	-5.96
1861.79	21.35	-8.43	-5.10
1861.30	21.45	-8.60	-4.96
1861.05	21.50	-9.03	-6.45

Year A.D.	Depth from top (mm)	$\delta^{13}C$ (‰ VPDB)	$\delta^{18}O$ (‰ VPDB)
1860.81	21.55	-9.55	-6.28
1860.56	21.60	-9.91	-5.82
1860.31	21.65	-10.17	-5.98
1860.07	21.70	-10.01	-7.06
1859.82	21.75	-9.53	-5.10
1859.58	21.80	-9.28	-6.33
1859.34	21.85	-9.53	-5.51
1859.09	21.90	-9.45	-9.02
1858.85	21.95	-8.51	-7.01
1858.61	22.00	-8.12	-8.91
1858.12	22.10	-8.48	-6.03
1857.88	22.15	-9.08	-4.43
1857.40	22.25	-8.44	-5.51
1857.16	22.30	-8.79	-6.41
1856.92	22.35	-9.29	-5.12
1856.69	22.40	-9.64	-5.83
1856.45	22.45	-9.55	-5.91
1856.21	22.50	-8.11	-5.35
1855.97	22.55	-7.54	-5.15
1855.74	22.60	-6.97	-5.06
1855.50	22.65	-7.13	-5.47
1855.26	22.70	-7.01	-6.14
1854.79	22.80	-6.92	-4.24
1854.56	22.85	-7.23	-4.98
1854.33	22.90	-7.61	-4.53
1854.09	22.95	-7.58	-4.48
1853.86	23.00	-7.87	-5.28
1853.63	23.05	-7.89	-4.56
1853.17	23.15	-8.18	-5.00
1852.94	23.20	-7.94	-5.41
1852.71	23.25	-8.14	-4.55
1852.48	23.30	-8.07	-7.25
1852.25	23.35	-8.04	-4.97
1852.02	23.40	-7.84	-5.72
1851.79	23.45	-8.48	-5.01
1851.56	23.50	-8.50	-5.38
1851.34	23.55	-8.73	-5.97
1851.11	23.60	-8.98	-5.86
1850.89	23.65	-9.17	-4.60
1850.66	23.70	-9.44	-5.81
1850.44	23.75	-9.61	-4.77
1850.21	23.80	-9.22	-8.56
1849.99	23.85	-9.05	-5.91
1849.77	23.90	-8.76	-6.23
1849.55	23.95	-8.84	-5.35
1849.33	24.00	-8.89	-8.18
1849.10	24.05	-9.08	-4.71
1848.88	24.10	-9.09	-5.75
1848.67	24.15	-8.94	-4.58
1848.45	24.20	-8.70	-8.44
1848.23	24.25	-8.99	-4.58
1848.01	24.30	-8.84	-5.94
1847.79	24.35	-8.90	-5.73
1847.58	24.40	-8.86	-4.20
1847.36	24.45	-8.81	-5.00
1847.15	24.50	-8.59	-4.80
1846.93	24.55	-8.44	-6.60
1846.72	24.60	-7.99	-5.29
1846.50	24.65	-7.92	-5.82
1846.29	24.70	-8.19	-5.16
1846.08	24.75	-7.85	-4.43
1845.87	24.80	-7.87	-3.76
1845.45	24.90	-8.25	-3.74
1845.24	24.95	-8.21	-5.07
1845.03	25.00	-8.20	-6.49
1844.62	25.10	-8.22	-5.26
1844.41	25.15	-8.27	-4.95
1844.20	25.20	-8.49	-7.20
1844.00	25.25	-8.59	-5.45
1843.59	25.35	-8.54	-4.45
1843.39	25.40	-8.91	-4.22
1843.18	25.45	-9.20	-6.00
1842.78	25.55	-9.74	-4.35
1842.58	25.60	-9.87	-4.42
1842.38	25.65	-9.39	-4.88
1842.18	25.70	-9.35	-5.49
1841.98	25.75	-8.82	-4.42
1841.79	25.80	-8.22	-4.59
1841.59	25.85	-7.92	-4.76
1841.39	25.90	-8.02	-4.27
1841.20	25.95	-7.59	-4.59
1841.01	26.00	-7.04	-4.89
1840.81	26.05	-6.66	-3.75
1840.61	26.10	-6.87	-3.63
1840.41	26.15	-6.97	-3.64
1840.21	26.20	-7.72	-3.70
1840.00	26.25	-8.38	-3.95
1839.79	26.30	-8.63	-4.99

Year A.D.	Depth from top (mm)	$\delta^{13}C$ (‰ VPDB)	$\delta^{18}O$ (‰ VPDB)
1839.58	26.35	-8.91	-4.72
1839.15	26.45	-8.60	-4.21
1838.71	26.55	-8.85	-4.46
1838.25	26.65	-8.31	-5.61
1838.03	26.70	-8.11	-4.41
1837.79	26.75	-7.40	-5.19
1837.56	26.80	-7.30	-7.05
1837.09	26.90	-7.35	-5.98
1836.85	26.95	-6.93	-5.68
1836.36	27.05	-7.78	-4.16
1836.11	27.10	-8.03	-4.96
1835.86	27.15	-8.65	-5.09
1835.36	27.25	-9.78	-6.40
1834.84	27.35	-9.93	-5.62
1834.59	27.40	-10.08	-6.11
1834.33	27.45	-9.99	-5.17
1834.06	27.50	-10.26	-6.31
1833.80	27.55	-9.59	-5.35
1833.53	27.60	-9.58	-4.52
1833.26	27.65	-8.75	-5.07
1832.99	27.70	-8.83	-4.98
1832.72	27.75	-8.53	-5.46
1832.45	27.80	-8.71	-4.93
1832.18	27.85	-8.80	-4.56
1831.90	27.90	-8.90	-6.18
1831.62	27.95	-8.77	-4.68
1831.34	28.00	-8.43	-5.05
1830.78	28.10	-9.79	-6.37
1830.50	28.15	-9.51	-6.68
1830.22	28.20	-9.16	-5.11
1829.93	28.25	-8.35	-5.08
1829.64	28.30	-8.14	-5.47
1829.35	28.35	-8.06	-4.58
1828.48	28.50	-8.85	-6.24
1828.19	28.55	-10.33	-5.80
1827.60	28.65	-10.88	-4.99
1827.31	28.70	-10.85	-6.66
1827.01	28.75	-10.38	-6.38
1826.71	28.80	-9.86	-7.16
1826.41	28.85	-9.89	-5.91
1826.12	28.90	-9.73	-6.10
1825.82	28.95	-9.43	-7.34
1825.21	29.05	-9.91	-4.68
1824.91	29.10	-9.47	-6.43
1824.61	29.15	-9.36	-5.23
1823.70	29.30	-9.12	-6.41
1823.39	29.35	-9.52	-5.57
1822.78	29.45	-10.83	-6.59
1822.47	29.50	-10.67	-7.40
1822.17	29.55	-10.45	-5.62
1821.55	29.65	-9.36	-5.68
1820.94	29.75	-9.06	-5.12
1820.63	29.80	-9.51	-6.18
1820.32	29.85	-9.80	-5.47
1820.01	29.90	-9.91	-8.68
1819.40	30.00	-10.62	-5.59
1819.09	30.05	-10.28	-6.62
1818.78	30.10	-10.14	-7.05
1818.47	30.15	-10.66	-5.35
1818.16	30.20	-10.61	-5.65
1817.86	30.25	-10.54	-5.05
1817.55	30.30	-10.00	-5.46
1816.62	30.45	-8.25	-3.99
1816.32	30.50	-9.03	-4.65
1816.01	30.55	-9.89	-4.57
1815.71	30.60	-10.16	-5.02
1815.09	30.70	-9.90	-5.44
1814.79	30.75	-9.69	-4.05
1814.48	30.80	-9.63	-4.40
1813.27	31.00	-9.67	-3.99
1812.97	31.05	-9.88	-4.41
1812.67	31.10	-9.71	-5.60
1812.37	31.15	-9.52	-4.34
1812.07	31.20	-9.63	-5.00
1811.77	31.25	-9.86	-4.03
1811.48	31.30	-9.61	-4.98
1811.18	31.35	-9.60	-5.02
1810.89	31.40	-9.63	-4.68
1810.01	31.55	-8.59	-4.40
1809.42	31.65	-8.47	-4.20
1809.13	31.70	-8.66	-3.96
1808.56	31.80	-8.84	-4.43
1808.27	31.85	-9.12	-3.76
1807.99	31.90	-6.88	-3.93
1807.71	31.95	-8.89	-3.86
1807.43	32.00	-9.04	-3.84
1807.15	32.05	-9.22	-4.48
1806.87	32.10	-9.05	-4.50

Year A.D.	Depth from top (mm)	$\delta^{13}C$ (‰ VPDB)	$\delta^{18}O$ (‰ VPDB)
1806.59	32.15	-9.65	-3.88
1806.32	32.20	-9.31	-4.42
1806.04	32.25	-8.90	-4.28
1805.77	32.30	-9.03	-3.88
1805.50	32.35	-9.28	-3.78
1805.23	32.40	-9.17	-4.04
1804.96	32.45	-9.37	-3.84
1804.70	32.50	-9.75	-4.37
1804.17	32.60	-9.89	-4.43
1803.91	32.65	-9.81	-3.93
1803.65	32.70	-9.49	-4.28
1803.39	32.75	-9.77	-4.22
1803.14	32.80	-9.64	-4.06
1802.89	32.85	-9.44	-4.24
1802.64	32.90	-9.29	-3.85
1802.14	33.00	-8.61	-4.70
1801.90	33.05	-8.75	-4.19
1801.65	33.10	-8.08	-3.46
1801.41	33.15	-7.90	-3.55
1801.18	33.20	-7.90	-2.76
1800.94	33.25	-8.13	-3.81
1800.71	33.30	-8.10	-3.51
1800.48	33.35	-8.33	-3.78
1800.25	33.40	-8.72	-3.90
1799.80	33.50	-9.38	-3.93
1799.57	33.55	-9.44	-3.89
1799.36	33.60	-9.36	-3.97
1799.14	33.65	-9.40	-4.03
1798.93	33.70	-9.33	-4.42
1798.71	33.75	-9.38	-4.47
1798.51	33.80	-9.15	-3.83
1798.30	33.85	-9.31	-4.20
1798.10	33.90	-9.20	-4.08
1797.90	33.95	-9.37	-4.65
1797.31	34.10	-9.03	-4.09
1796.94	34.20	-9.43	-4.58
1796.75	34.25	-9.38	-4.16
1796.57	34.30	-9.49	-4.87
1796.39	34.35	-9.48	-4.49
1796.22	34.40	-9.36	-4.50
1795.88	34.50	-9.42	-4.79
1795.55	34.60	-9.41	-4.39
1795.40	34.65	-9.14	-5.41
1795.24	34.70	-9.62	-4.69
1795.09	34.75	-9.24	-4.54
1794.80	34.85	-9.40	-4.13
1794.38	35.00	-8.97	-4.86
1794.25	35.05	-9.13	-5.24
1794.12	35.10	-9.16	-6.56
1793.98	35.15	-9.20	-6.66
1793.85	35.20	-8.87	-5.67
1793.72	35.25	-8.46	-4.72
1793.58	35.30	-8.66	-4.79
1793.45	35.35	-9.02	-4.89
1793.31	35.40	-9.22	-5.29
1793.18	35.45	-9.77	-5.07
1793.04	35.50	-9.98	-4.78
1792.91	35.55	-10.25	-4.59
1792.78	35.60	-9.91	-7.30
1792.64	35.65	-10.30	-5.08
1792.37	35.75	-10.18	-5.55
1792.24	35.80	-9.46	-5.25
1792.10	35.85	-9.22	-5.01
1791.83	35.95	-9.57	-4.55
1791.69	36.00	-10.16	-5.05
1791.56	36.05	-10.58	-4.35
1791.42	36.10	-10.93	-5.47
1791.28	36.15	-10.80	-4.95
1791.15	36.20	-10.07	-4.73
1790.87	36.30	-10.04	-5.06
1790.74	36.35	-9.02	-4.39
1790.60	36.40	-9.58	-4.75
1790.46	36.45	-9.77	-4.06
1790.33	36.50	-10.01	-4.47
1790.05	36.60	-10.22	-5.04
1789.91	36.65	-10.21	-4.84
1789.78	36.70	-10.25	-5.26
1789.50	36.80	-9.53	-4.76
1789.22	36.90	-9.33	-5.48
1789.09	36.95	-9.48	-5.78
1788.67	37.10	-10.91	-5.20
1788.53	37.15	-10.06	-4.77
1788.39	37.20	-8.56	-4.28
1788.25	37.25	-9.29	-4.69
1788.11	37.30	-7.66	-3.91
1787.97	37.35	-9.06	-4.56
1787.83	37.40	-10.86	-4.95
1787.69	37.45	-11.07	-4.94

Year A.D.	Depth from top (mm)	$\delta^{13}C$ (‰ VPDB)	$\delta^{18}O$ (‰ VPDB)
1787.41	37.55	-7.88	-3.24
1787.27	37.60	-8.36	-3.93
1787.13	37.65	-8.70	-4.80
1786.99	37.70	-8.45	-4.02
1786.85	37.75	-8.97	-4.09
1786.71	37.80	-9.06	-4.62
1786.57	37.85	-9.22	-3.76
1786.43	37.90	-9.01	-3.98
1786.29	37.95	-8.91	-4.49
1786.15	38.00	-6.46	-3.28
1786.01	38.05	-9.17	-3.90
1785.87	38.10	-9.04	-3.74
1785.73	38.15	-3.91	-5.02
1785.59	38.20	-8.66	-4.49
1785.44	38.25	-8.75	-5.58
1785.30	38.30	-8.79	-4.15
1785.16	38.35	-9.18	-5.30
1785.02	38.40	-9.24	-4.75
1784.88	38.45	-9.34	-4.62
1784.74	38.50	-9.42	-4.36
1784.59	38.55	-9.63	-4.19
1784.45	38.60	-9.92	-4.40
1784.31	38.65	-9.43	-3.99
1784.17	38.70	-9.51	-3.85
1783.88	38.80	-9.05	-3.64
1783.74	38.85	-8.78	-3.35
1783.60	38.90	-8.75	-3.91
1783.31	39.00	-8.34	-3.84
1783.17	39.05	-8.34	-3.33
1783.03	39.10	-8.10	-3.25
1782.74	39.20	-8.17	-3.72
1782.60	39.25	-8.71	-5.26
1782.45	39.30	-8.92	-3.81
1782.16	39.40	-9.22	-3.79
1782.02	39.45	-9.37	-3.83
1781.88	39.50	-9.49	-3.73
1781.73	39.55	-9.05	-3.95
1781.45	39.65	-8.91	-3.90
1781.30	39.70	-9.00	-3.73
1781.01	39.80	-9.54	-4.12
1780.87	39.85	-10.15	-5.37
1780.72	39.90	-10.23	-6.77
1780.58	39.95	-10.29	-4.83
1780.43	40.00	-8.39	-4.25
1780.29	40.05	-8.24	-4.65
1780.00	40.15	-8.74	-4.73
1779.86	40.20	-8.55	-4.15
1779.57	40.30	-10.03	-4.48
1779.42	40.35	-10.18	-4.69
1779.28	40.40	-10.42	-4.68
1779.13	40.45	-10.14	-5.27
1778.98	40.50	-10.05	-5.35
1778.84	40.55	-9.85	-5.19
1778.69	40.60	-9.34	-4.59
1778.40	40.70	-9.18	-4.75
1778.26	40.75	-9.53	-4.35
1778.11	40.80	-9.49	-4.96
1777.97	40.85	-9.38	-5.16
1777.82	40.90	-9.62	-4.53
1777.67	40.95	-9.66	-4.50
1777.53	41.00	-9.82	-4.35
1777.38	41.05	-9.65	-5.12
1777.24	41.10	-9.59	-4.38
1777.09	41.15	-9.54	-4.29
1776.80	41.25	-8.11	-3.96
1776.65	41.30	-7.96	-4.21
1776.50	41.35	-7.70	-4.20
1776.36	41.40	-8.24	-4.27
1776.21	41.45	-7.69	-3.63
1776.06	41.50	-7.63	-4.49
1775.92	41.55	-8.38	-5.17
1775.77	41.60	-8.32	-3.95
1775.62	41.65	-9.19	-5.41
1775.33	41.75	-10.00	-4.60
1775.18	41.80	-10.27	-4.25
1774.89	41.90	-10.13	-4.46
1774.74	41.95	-8.77	-4.11
1774.60	42.00	-8.28	-3.75
1774.45	42.05	-9.37	-3.97
1774.30	42.10	-9.64	-4.18
1774.16	42.15	-9.79	-4.52
1774.01	42.20	-9.36	-3.80
1773.86	42.25	-8.80	-3.51
1773.71	42.30	-8.51	-5.01
1773.57	42.35	-8.72	-3.81
1773.42	42.40	-9.07	-4.93
1773.27	42.45	-8.52	-3.43
1773.12	42.50	-7.89	-3.85

Year A.D.	Depth from top (mm)	$\delta^{13}C$ (‰ VPDB)	$\delta^{18}O$ (‰ VPDB)
1772.98	42.55	-7.87	-3.77
1772.83	42.60	-8.48	-3.51
1772.68	42.65	-8.50	-3.33
1772.53	42.70	-8.35	-4.40
1772.39	42.75	-8.16	-3.33
1772.24	42.80	-8.21	-3.31
1772.09	42.85	-8.33	-4.61
1771.94	42.90	-8.70	-3.38
1771.65	43.00	-9.69	-4.25
1771.50	43.05	-10.13	-4.62
1771.20	43.15	-11.12	-4.74
1771.06	43.20	-10.90	-4.80
1770.91	43.25	-7.96	-3.71
1770.76	43.30	-7.23	-3.45
1770.61	43.35	-8.81	-4.40
1770.46	43.40	-9.66	-3.99
1770.32	43.45	-10.53	-4.84
1770.17	43.50	-10.98	-4.52
1770.02	43.55	-11.36	-4.74
1769.87	43.60	-11.27	-5.09
1769.72	43.65	-10.11	-5.79
1769.58	43.70	-8.86	-4.06
1769.43	43.75	-9.27	-4.36
1769.28	43.80	-9.54	-4.12
1768.84	43.95	-8.72	-5.20
1768.54	44.05	-10.10	-6.77
1768.39	44.10	-10.06	-4.87
1768.09	44.20	-8.44	-5.37
1767.95	44.25	-8.90	-3.60
1767.65	44.35	-9.04	-4.98
1767.21	44.50	-7.62	-3.89
1767.06	44.55	-7.83	-4.95
1766.91	44.60	-8.42	-4.40
1766.76	44.65	-9.62	-4.26
1766.17	44.85	-9.22	-5.27
1765.87	44.95	-8.35	-4.26
1765.72	45.00	-7.97	-3.80
1765.28	45.15	-8.19	-5.62
1765.13	45.20	-7.99	-4.38
1764.98	45.25	-8.29	-3.64
1764.83	45.30	-9.07	-3.87
1764.68	45.35	-8.76	-6.07
1764.54	45.40	-7.62	-3.99
1764.39	45.45	-8.48	-5.03
1764.24	45.50	-8.37	-3.92
1764.09	45.55	-8.23	-4.50
1763.94	45.60	-6.34	-3.12
1763.80	45.65	-7.52	-3.93
1763.50	45.75	-6.62	-3.21
1763.35	45.80	-6.84	-3.16
1763.20	45.85	-6.90	-3.35
1763.06	45.90	-6.78	-3.32
1762.91	45.95	-6.92	-4.99
1762.76	46.00	-6.50	-3.05
1762.46	46.10	-5.87	-3.01
1762.32	46.15	-5.81	-3.34
1762.17	46.20	-6.17	-4.10
1762.02	46.25	-6.25	-3.39
1761.87	46.30	-6.36	-2.94
1761.72	46.35	-6.44	-4.47
1761.43	46.45	-6.59	-3.54
1761.13	46.55	-7.02	-3.44
1760.99	46.60	-6.95	-3.30
1760.84	46.65	-8.93	-4.74
1760.54	46.75	-6.69	-4.04
1760.39	46.80	-6.70	-4.27
1760.10	46.90	-9.65	-4.01
1759.95	46.95	-6.46	-3.25
1759.66	47.05	-7.20	-3.66
1759.51	47.10	-6.87	-4.75
1759.36	47.15	-9.86	-4.06
1759.22	47.20	-6.55	-3.76
1759.07	47.25	-7.84	-3.24
1758.92	47.30	-6.87	-3.99
1758.77	47.35	-7.09	-4.78
1758.48	47.45	-7.78	-4.20
1758.33	47.50	-8.19	-4.45
1758.19	47.55	-9.76	-4.59
1757.89	47.65	-11.06	-4.52
1757.74	47.70	-9.55	-5.30
1757.60	47.75	-7.75	-4.40
1757.45	47.80	-8.17	-5.56
1757.16	47.90	-7.86	-4.67
1757.01	47.95	-6.87	-4.29
1756.86	48.00	-7.17	-4.60
1756.72	48.05	-7.02	-4.37
1756.57	48.10	-6.76	-4.21
1756.28	48.20	-6.71	-4.67

Year A.D.	Depth from top (mm)	$\delta^{13}C$ (‰ VPDB)	$\delta^{18}O$ (‰ VPDB)
1756.13	48.25	-6.39	-3.62
1755.69	48.40	-7.39	-4.11
1755.40	48.50	-8.76	-4.20
1755.26	48.55	-9.11	-5.42
1755.11	48.60	-9.65	-5.49
1754.96	48.65	-9.79	-7.40
1754.82	48.70	-9.93	-4.28
1754.67	48.75	-9.99	-5.46
1754.38	48.85	-9.77	-4.25
1754.09	48.95	-8.98	-4.42
1753.95	49.00	-9.27	-4.63
1753.36	49.20	-7.97	-5.45
1753.22	49.25	-7.20	-5.37
1753.07	49.30	-6.82	-4.14
1752.79	49.40	-8.12	-4.69
1752.64	49.45	-6.85	-3.76
1752.50	49.50	-7.06	-4.04
1752.06	49.65	-6.67	-4.07
1751.92	49.70	-6.68	-6.16
1751.77	49.75	-6.87	-5.85
1751.63	49.80	-7.22	-5.08
1751.20	49.95	-8.61	-5.40
1751.05	50.00	-8.63	-4.70
1750.91	50.05	-9.26	-4.67
1750.77	50.10	-9.15	-4.81
1750.62	50.15	-9.14	-6.95
1750.48	50.20	-8.95	-4.26
1750.34	50.25	-8.59	-3.59
1750.19	50.30	-8.00	-4.69
1749.91	50.40	-9.24	-4.54
1749.62	50.50	-7.37	-3.43
1749.48	50.55	-10.86	-5.32
1749.34	50.60	-10.18	-5.71
1749.19	50.65	-9.26	-4.36
1749.05	50.70	-8.32	-4.55
1748.91	50.75	-8.53	-7.33
1748.77	50.80	-8.86	-4.51
1748.62	50.85	-8.39	-4.24
1748.48	50.90	-8.07	-4.45
1748.34	50.95	-8.41	-4.55
1748.20	51.00	-8.09	-4.49
1748.06	51.05	-7.69	-4.39
1747.77	51.15	-7.93	-4.13
1747.63	51.20	-7.96	-4.30
1747.49	51.25	-8.39	-4.70
1747.35	51.30	-8.61	-5.47
1747.07	51.40	-10.74	-6.22
1746.92	51.45	-11.31	-5.21
1746.78	51.50	-10.68	-4.83
1746.64	51.55	-9.74	-4.45
1746.50	51.60	-8.59	-3.82
1746.36	51.65	-8.55	-4.26
1746.22	51.70	-9.69	-5.20
1745.94	51.80	-9.58	-4.79
1745.80	51.85	-8.96	-4.59
1745.52	51.95	-8.33	-3.88
1745.38	52.00	-8.01	-5.76
1745.24	52.05	-7.90	-4.24
1745.10	52.10	-8.23	-4.56
1744.96	52.15	-8.45	-4.30
1744.82	52.20	-8.28	-7.28
1744.68	52.25	-8.04	-3.97
1744.41	52.35	-9.27	-4.59
1744.27	52.40	-9.42	-5.49
1744.13	52.45	-8.54	-4.13
1743.99	52.50	-7.89	-4.98
1743.85	52.55	-9.15	-4.91
1743.44	52.70	-8.41	-4.55
1743.30	52.75	-7.86	-4.41
1742.89	52.90	-6.97	-4.16
1742.75	52.95	-7.27	-3.98
1742.61	53.00	-7.02	-4.69
1742.47	53.05	-9.53	-4.62
1742.34	53.10	-7.23	-4.49
1742.06	53.20	-7.32	-4.11
1741.93	53.25	-7.34	-4.05
1741.79	53.30	-7.44	-5.26
1741.65	53.35	-7.33	-4.21
1741.52	53.40	-8.02	-3.91
1741.38	53.45	-8.14	-4.22
1741.25	53.50	-8.45	-4.49
1741.11	53.55	-9.17	-4.73
1740.97	53.60	-9.21	-5.29
1740.70	53.70	-9.80	-5.38
1740.57	53.75	-9.36	-5.06
1740.43	53.80	-9.43	-5.16
1740.30	53.85	-9.45	-4.93
1740.16	53.90	-9.17	-5.28

Year A.D.	Depth from top (mm)	$\delta^{13}C$ (‰ VPDB)	$\delta^{18}O$ (‰ VPDB)
1740.03	53.95	-8.70	-4.93
1739.90	54.00	-8.15	-4.66
1739.76	54.05	-7.96	-4.77
1739.63	54.10	-8.09	-4.82
1739.49	54.15	-8.21	-5.33
1739.23	54.25	-9.03	-5.60
1739.09	54.30	-9.12	-4.76
1738.96	54.35	-9.09	-4.51
1738.43	54.55	-10.28	-4.85
1738.29	54.60	-9.76	-4.59
1738.16	54.65	-9.75	-5.74
1738.03	54.70	-9.45	-4.67
1737.90	54.75	-9.52	-4.52
1737.63	54.85	-9.09	-5.47
1737.50	54.90	-10.08	-4.57
1737.37	54.95	-10.70	-4.63
1737.11	55.05	-9.67	-5.20
1736.98	55.10	-8.64	-4.04
1736.85	55.15	-7.28	-3.57
1736.33	55.35	-6.98	-3.20
1736.20	55.40	-7.69	-3.53
1736.07	55.45	-9.47	-4.23
1735.81	55.55	-8.52	-5.49
1735.68	55.60	-9.69	-4.39
1735.55	55.65	-8.92	-3.86
1735.42	55.70	-8.64	-4.17
1735.16	55.80	-8.33	-4.91
1735.03	55.85	-8.56	-3.98
1734.78	55.95	-9.02	-4.37
1734.65	56.00	-8.94	-4.57
1734.52	56.05	-8.69	-4.03
1734.27	56.15	-7.85	-3.86
1734.14	56.20	-7.77	-3.91
1734.01	56.25	-7.91	-4.47
1733.89	56.30	-8.32	-4.76
1733.76	56.35	-8.75	-4.97
1733.64	56.40	-8.58	-5.30
1733.38	56.50	-9.31	-4.38
1733.26	56.55	-8.78	-5.06
1733.13	56.60	-9.48	-4.67
1733.01	56.65	-9.33	-4.65
1732.88	56.70	-9.56	-4.62
1732.76	56.75	-9.57	-5.48
1732.63	56.80	-9.52	-4.32
1732.51	56.85	-9.27	-4.54
1732.26	56.95	-9.06	-5.12
1732.13	57.00	-8.99	-4.25
1732.01	57.05	-8.54	-4.39
1731.89	57.10	-8.83	-4.49
1731.76	57.15	-9.64	-4.61
1731.64	57.20	-8.95	-4.38
1731.39	57.30	-8.20	-3.90
1731.27	57.35	-7.77	-4.12
1731.03	57.45	-8.60	-4.07
1730.78	57.55	-9.60	-4.85
1730.66	57.60	-10.01	-4.73
1730.53	57.65	-10.02	-4.91
1730.14	57.80	-8.74	-4.43
1730.01	57.85	-8.98	-4.75
1729.74	57.95	-8.12	-5.00
1729.60	58.00	-8.34	-4.33
1729.46	58.05	-8.73	-5.29
1729.32	58.10	-8.70	-4.43
1729.18	58.15	-9.35	-4.45
1729.03	58.20	-9.59	-4.64
1728.89	58.25	-9.52	-4.39
1728.74	58.30	-10.18	-5.12
1728.59	58.35	-10.44	-5.95
1728.44	58.40	-10.83	-5.00
1728.13	58.50	-10.89	-6.64
1727.98	58.55	-10.77	-4.89
1727.82	58.60	-10.90	-6.03
1727.50	58.70	-10.39	-4.97
1727.02	58.85	-8.33	-4.29
1726.85	58.90	-9.45	-4.16
1726.69	58.95	-9.26	-4.48
1726.52	59.00	-9.43	-5.39
1726.35	59.05	-9.57	-4.15
1726.18	59.10	-9.34	-4.75
1726.01	59.15	-10.17	-5.04
1725.84	59.20	-9.73	-4.00
1725.66	59.25	-9.52	-4.07
1725.31	59.35	-8.94	-4.96
1724.78	59.50	-8.65	-4.55
1724.60	59.55	-9.70	-4.76
1724.23	59.65	-11.02	-4.67
1724.05	59.70	-11.27	-4.74
1723.86	59.75	-10.86	-5.02

Year A.D.	Depth from top (mm)	$\delta^{13}C$ (‰ VPDB)	$\delta^{18}O$ (‰ VPDB)
1723.68	59.80	-9.57	-4.86
1723.30	59.90	-8.29	-4.10
1723.11	59.95	-9.78	-4.96
1722.92	60.00	-8.44	-4.24
1722.73	60.05	-9.10	-4.32
1722.54	60.10	-9.49	-6.17
1722.15	60.20	-9.73	-5.02
1721.96	60.25	-9.33	-5.03
1721.77	60.30	-8.76	-4.23
1721.57	60.35	-9.64	-4.85
1721.37	60.40	-8.56	-4.72
1721.17	60.45	-8.61	-4.46
1720.98	60.50	-8.80	-5.06
1720.78	60.55	-8.67	-5.33
1720.58	60.60	-8.49	-4.34
1720.38	60.65	-8.98	-5.20
1720.18	60.70	-9.03	-4.98
1719.97	60.75	-9.76	-4.45
1719.77	60.80	-10.31	-4.81
1719.57	60.85	-10.15	-5.16
1719.36	60.90	-10.12	-5.78
1719.16	60.95	-10.66	-7.20
1718.95	61.00	-10.34	-4.66
1718.75	61.05	-10.16	-6.59
1718.54	61.10	-10.60	-4.74
1718.33	61.15	-10.29	-5.09
1718.13	61.20	-10.07	-5.27
1717.92	61.25	-9.89	-5.25
1717.71	61.30	-10.04	-4.49
1717.29	61.40	-9.84	-5.40
1716.87	61.50	-7.64	-4.51
1716.45	61.60	-8.02	-4.17
1716.24	61.65	-8.27	-4.50
1716.02	61.70	-8.74	-4.36
1715.81	61.75	-9.11	-5.07
1715.60	61.80	-9.47	-4.35
1715.38	61.85	-9.52	-4.75
1715.17	61.90	-9.69	-4.54
1714.96	61.95	-9.51	-5.39
1714.74	62.00	-9.78	-4.44
1714.53	62.05	-8.70	-4.35
1714.32	62.10	-8.83	-4.28
1714.10	62.15	-9.29	-5.29
1713.89	62.20	-9.18	-4.07
1713.67	62.25	-9.52	-4.79
1713.46	62.30	-9.69	-4.80
1713.24	62.35	-9.09	-5.42
1713.02	62.40	-9.47	-4.62
1712.81	62.45	-9.38	-4.28
1712.59	62.50	-9.60	-4.78
1712.38	62.55	-9.71	-5.15
1712.16	62.60	-9.82	-4.47
1711.95	62.65	-9.62	-5.63
1711.73	62.70	-9.45	-4.47
1711.51	62.75	-9.53	-4.18
1711.08	62.85	-9.79	-4.79
1710.87	62.90	-9.83	-4.35
1710.65	62.95	-9.25	-4.50
1710.00	63.10	-8.15	-4.80
1709.79	63.15	-7.66	-5.94
1709.36	63.25	-7.33	-4.06
1709.14	63.30	-7.60	-4.36
1708.93	63.35	-7.97	-5.13
1708.71	63.40	-7.57	-3.87
1708.50	63.45	-9.06	-4.48
1708.29	63.50	-7.76	-5.20
1708.07	63.55	-8.87	-4.63
1707.86	63.60	-8.27	-5.35
1707.64	63.65	-8.75	-3.91
1707.43	63.70	-8.22	-4.00
1707.22	63.75	-8.29	-4.91
1706.80	63.85	-9.83	-4.81
1706.58	63.90	-9.01	-4.13
1706.37	63.95	-7.84	-3.67
1706.16	64.00	-9.43	-4.57
1705.95	64.05	-9.17	-4.55
1705.74	64.10	-9.05	-4.09
1705.53	64.15	-8.75	-3.90
1704.91	64.30	-8.48	-4.79
1704.70	64.35	-8.70	-4.09
1704.49	64.40	-8.37	-3.98
1704.29	64.45	-9.10	-5.01
1704.08	64.50	-8.03	-5.18
1703.88	64.55	-7.47	-3.77
1703.67	64.60	-7.46	-3.73
1703.47	64.65	-7.82	-3.99
1703.27	64.70	-7.71	-3.73
1703.06	64.75	-9.06	-4.35

Year A.D.	Depth from top (mm)	$\delta^{13}C$ (‰ VPDB)	$\delta^{18}O$ (‰ VPDB)
1702.86	64.80	-8.00	-3.82
1702.66	64.85	-8.13	-4.04
1702.46	64.90	-8.27	-3.86
1702.26	64.95	-8.03	-3.71
1702.06	65.00	-8.27	-3.95
1701.87	65.05	-8.10	-3.81
1701.67	65.10	-7.94	-3.89
1701.08	65.25	-7.11	-4.82
1700.89	65.30	-9.94	-4.32
1700.70	65.35	-7.17	-5.05
1700.51	65.40	-7.41	-3.74
1700.12	65.50	-8.55	-3.90
1699.93	65.55	-8.60	-3.78
1699.75	65.60	-8.66	-4.12
1699.56	65.65	-9.55	-4.03
1699.37	65.70	-8.69	-4.37
1699.19	65.75	-8.96	-4.65
1698.82	65.85	-9.61	-4.33
1698.64	65.90	-9.49	-4.17
1698.46	65.95	-6.58	-3.27
1698.28	66.00	-9.54	-4.35
1698.10	66.05	-9.47	-4.19
1697.92	66.10	-9.22	-4.41
1697.75	66.15	-9.15	-4.39
1697.57	66.20	-9.12	-4.04
1697.40	66.25	-9.09	-4.51
1697.22	66.30	-8.99	-4.36
1697.05	66.35	-9.35	-4.90
1696.88	66.40	-8.74	-4.67
1696.55	66.50	-8.38	-4.15
1696.38	66.55	-7.53	-4.04
1696.05	66.65	-9.15	-5.62
1695.89	66.70	-8.12	-3.64
1695.73	66.75	-6.93	-3.87
1695.41	66.85	-6.72	-3.25
1695.25	66.90	-6.71	-3.21
1695.10	66.95	-6.88	-3.46
1694.94	67.00	-8.15	-4.58
1694.79	67.05	-7.78	-3.77
1694.64	67.10	-8.21	-4.09
1694.49	67.15	-9.00	-4.11
1694.34	67.20	-8.91	-3.92
1694.20	67.25	-8.65	-4.21
1694.05	67.30	-9.27	-4.19
1693.91	67.35	-7.91	-4.01
1693.77	67.40	-7.75	-3.59
1693.62	67.45	-7.40	-4.04
1693.49	67.50	-8.27	-3.45
1693.35	67.55	-7.90	-3.67
1693.21	67.60	-7.62	-3.77
1693.07	67.65	-7.58	-4.35
1692.92	67.70	-7.78	-3.61
1692.78	67.75	-7.89	-4.58
1692.49	67.85	-8.40	-4.22
1692.19	67.95	-8.59	-5.84
1691.88	68.05	-8.74	-5.42
1691.73	68.10	-8.91	-4.07
1691.57	68.15	-9.07	-4.59
1691.26	68.25	-9.04	-5.14
1691.10	68.30	-8.84	-4.56
1690.94	68.35	-9.08	-5.18
1690.77	68.40	-8.88	-4.40
1690.61	68.45	-9.39	-5.07
1690.45	68.50	-8.78	-5.02
1690.28	68.55	-9.25	-5.60
1690.11	68.60	-9.49	-5.16
1689.95	68.65	-9.27	-4.91
1689.78	68.70	-9.16	-5.23
1689.60	68.75	-8.43	-4.81
1689.43	68.80	-8.75	-5.61
1689.26	68.85	-8.75	-5.36
1689.09	68.90	-9.25	-5.20
1688.91	68.95	-9.59	-5.26
1688.73	69.00	-8.89	-4.48
1688.56	69.05	-8.84	-4.56
1688.38	69.10	-8.97	-4.89
1688.20	69.15	-9.08	-5.68
1688.02	69.20	-9.04	-4.75
1687.83	69.25	-8.94	-5.00
1687.65	69.30	-9.08	-4.67
1687.47	69.35	-8.87	-5.46
1687.28	69.40	-9.45	-5.01
1687.10	69.45	-9.95	-5.29
1686.91	69.50	-9.76	-4.49
1686.72	69.55	-8.67	-4.89
1686.53	69.60	-10.03	-4.46
1686.34	69.65	-10.02	-5.10
1686.15	69.70	-9.94	-4.60

Year A.D.	Depth from top (mm)	$\delta^{13}C$ (‰ VPDB)	$\delta^{18}O$ (‰ VPDB)
1685.96	69.75	-9.79	-5.71
1685.77	69.80	-9.20	-4.85
1685.57	69.85	-8.47	-5.27
1685.38	69.90	-9.63	-5.13
1685.18	69.95	-9.73	-4.78
1684.99	70.00	-10.06	-5.19
1684.79	70.05	-8.04	-4.20
1684.59	70.10	-10.32	-4.59
1684.39	70.15	-8.77	-5.45
1684.19	70.20	-7.26	-4.39
1683.99	70.25	-9.13	-5.76
1683.79	70.30	-8.61	-4.45
1683.59	70.35	-8.59	-4.95
1683.39	70.40	-6.07	-4.26
1683.18	70.45	-7.95	-4.21
1682.98	70.50	-8.04	-4.45
1682.77	70.55	-8.61	-6.14
1682.57	70.60	-8.74	-4.40
1682.36	70.65	-8.62	-5.02
1682.16	70.70	-8.85	-4.73
1681.95	70.75	-7.93	-4.25
1681.74	70.80	-8.77	-4.76
1681.53	70.85	-8.63	-4.44
1681.32	70.90	-9.65	-4.66
1681.11	70.95	-8.91	-4.71
1680.90	71.00	-9.14	-4.39
1680.69	71.05	-9.10	-5.96
1680.48	71.10	-9.25	-4.40
1680.27	71.15	-8.29	-4.35
1680.05	71.20	-9.00	-4.45
1679.84	71.25	-8.98	-5.19
1679.63	71.30	-9.13	-4.97
1679.41	71.35	-9.27	-5.00
1679.20	71.40	-9.52	-4.15
1678.77	71.50	-9.20	-4.22
1678.55	71.55	-10.27	-4.77
1678.12	71.65	-9.94	-4.51
1677.90	71.70	-8.89	-4.82
1677.68	71.75	-9.62	-4.55
1677.46	71.80	-9.11	-5.20
1677.24	71.85	-9.38	-4.33
1677.02	71.90	-9.53	-4.34
1676.80	71.95	-9.72	-4.07
1676.59	72.00	-9.98	-4.23
1676.37	72.05	-10.10	-4.35
1676.15	72.10	-10.18	-4.67
1675.92	72.15	-10.39	-4.90
1675.48	72.25	-10.06	-4.61
1675.26	72.30	-9.65	-4.60
1675.04	72.35	-9.50	-5.03
1674.82	72.40	-9.44	-4.49
1674.60	72.45	-9.69	-4.78
1674.37	72.50	-9.18	-5.45
1674.15	72.55	-9.45	-4.00
1673.93	72.60	-8.02	-4.23
1673.71	72.65	-9.05	-4.22
1673.49	72.70	-9.50	-4.88
1673.26	72.75	-9.71	-4.34
1673.04	72.80	-9.36	-4.37
1672.82	72.85	-7.66	-4.13
1672.59	72.90	-8.46	-4.44
1672.37	72.95	-9.16	-5.34
1671.92	73.05	-9.26	-4.82
1671.70	73.10	-8.85	-4.45
1671.48	73.15	-9.52	-5.22
1671.25	73.20	-9.42	-4.84
1671.03	73.25	-9.49	-5.23
1670.81	73.30	-8.40	-4.59
1670.58	73.35	-7.91	-3.89
1670.36	73.40	-8.73	-4.35
1670.14	73.45	-8.66	-3.46
1669.92	73.50	-8.48	-4.18
1669.69	73.55	-8.54	-3.79
1669.47	73.60	-8.81	-3.65
1669.25	73.65	-8.89	-4.33
1669.02	73.70	-9.25	-3.93
1668.80	73.75	-10.69	-4.83
1668.58	73.80	-9.60	-5.83
1668.36	73.85	-9.25	-6.24
1668.14	73.90	-9.23	-4.33
1667.91	73.95	-7.77	-3.54
1667.69	74.00	-8.68	-3.74
1667.47	74.05	-5.87	-3.95
1667.25	74.10	-5.70	-3.84
1667.03	74.15	-5.75	-3.85
1666.81	74.20	-5.71	-3.83
1666.59	74.25	-5.80	-3.42
1666.37	74.30	-5.78	-3.55

Year A.D.	Depth from top (mm)	$\delta^{13}C$ (‰ VPDB)	$\delta^{18}O$ (‰ VPDB)
1666.15	74.35	-6.02	-4.99
1665.71	74.45	-7.04	-3.77
1665.49	74.50	-8.75	-4.58
1665.28	74.55	-9.43	-5.16
1665.06	74.60	-9.01	-4.35
1664.84	74.65	-6.77	-4.06
1664.62	74.70	-8.67	-4.99
1664.41	74.75	-9.19	-6.84
1664.19	74.80	-8.15	-4.90
1663.98	74.85	-7.86	-3.33
1663.76	74.90	-8.33	-3.87
1663.33	75.00	-9.15	-4.27
1663.12	75.05	-10.33	-4.24
1662.90	75.10	-10.95	-4.63
1662.69	75.15	-8.30	-4.12
1662.48	75.20	-8.47	-3.86
1662.27	75.25	-8.10	-4.46
1662.06	75.30	-9.19	-4.00
1661.85	75.35	-9.67	-4.24
1661.64	75.40	-11.67	-6.25
1661.43	75.45	-11.07	-5.03
1661.22	75.50	-8.08	-3.90
1661.01	75.55	-8.38	-4.57
1660.80	75.60	-7.03	-3.83
1660.60	75.65	-10.33	-4.44
1660.39	75.70	-10.76	-4.63
1660.19	75.75	-10.12	-5.26
1659.98	75.80	-9.64	-4.73
1659.78	75.85	-8.81	-4.55
1659.57	75.90	-8.50	-3.93
1659.37	75.95	-8.11	-4.17
1659.17	76.00	-8.54	-4.61
1658.97	76.05	-9.26	-4.23
1658.77	76.10	-9.48	-4.32
1658.57	76.15	-9.42	-5.14
1658.37	76.20	-9.65	-5.58
1658.17	76.25	-9.47	-4.37
1657.98	76.30	-9.65	-5.33
1657.78	76.35	-9.24	-4.48
1657.58	76.40	-9.14	-4.32
1657.39	76.45	-9.22	-4.73
1657.20	76.50	-8.94	-4.09
1657.00	76.55	-9.29	-5.14
1656.81	76.60	-7.98	-4.07
1656.62	76.65	-8.04	-4.26
1656.43	76.70	-7.46	-4.03
1656.24	76.75	-7.67	-3.75
1656.05	76.80	-8.00	-4.08
1655.87	76.85	-8.20	-5.08
1655.68	76.90	-8.60	-4.15
1655.50	76.95	-9.07	-4.88
1655.31	77.00	-10.87	-4.83
1655.13	77.05	-10.03	-4.65
1654.95	77.10	-8.17	-3.61
1654.77	77.15	-10.38	-5.04
1654.59	77.20	-10.43	-4.77
1654.41	77.25	-10.45	-5.05
1654.23	77.30	-10.53	-4.98
1654.06	77.35	-8.24	-4.77
1653.71	77.45	-9.83	-4.14
1653.53	77.50	-9.49	-4.40
1653.36	77.55	-9.21	-4.49
1653.19	77.60	-9.92	-5.17
1653.02	77.65	-9.57	-4.74
1652.85	77.70	-9.96	-4.66
1652.69	77.75	-8.82	-7.40
1652.52	77.80	-9.94	-4.62
1652.36	77.85	-9.88	-4.25
1652.19	77.90	-10.18	-4.68
1652.03	77.95	-9.26	-6.23
1651.87	78.00	-9.42	-4.44
1651.71	78.05	-9.31	-4.20
1651.55	78.10	-8.80	-4.21
1651.40	78.15	-8.86	-4.27
1651.24	78.20	-8.78	-3.80
1651.09	78.25	-9.30	-4.28
1650.93	78.30	-9.40	-4.30
1650.78	78.35	-8.93	-4.04
1650.63	78.40	-9.02	-4.35
1650.49	78.45	-9.39	-4.17
1650.34	78.50	-8.24	-4.37
1650.19	78.55	-7.30	-4.08
1650.05	78.60	-6.45	-3.95
1649.91	78.65	-6.58	-3.87
1649.77	78.70	-7.13	-3.64
1649.63	78.75	-10.09	-5.08
1649.49	78.80	-9.05	-4.72
1649.35	78.85	-9.68	-4.27

Year A.D.	Depth from top (mm)	$\delta^{13}C$ (‰ VPDB)	$\delta^{18}O$ (‰ VPDB)
1649.08	78.95	-7.89	-4.13
1648.95	79.00	-8.56	-4.45
1648.82	79.05	-8.99	-4.24
1648.69	79.10	-10.13	-4.84
1648.56	79.15	-9.78	-4.81
1648.44	79.20	-9.75	-4.55
1648.31	79.25	-8.73	-4.82
1648.19	79.30	-8.71	-4.60
1648.07	79.35	-8.97	-4.32
1647.95	79.40	-9.30	-5.43
1647.83	79.45	-10.14	-5.18
1647.72	79.50	-9.17	-4.61
1647.60	79.55	-9.17	-4.65
1647.49	79.60	-9.03	-4.64
1647.38	79.65	-7.13	-4.60
1647.17	79.75	-9.60	-5.03
1647.06	79.80	-9.53	-4.60
1646.96	79.85	-9.17	-4.47
1646.86	79.90	-8.97	-4.42
1646.76	79.95	-8.99	-4.15
1646.66	80.00	-9.44	-4.29
1646.56	80.05	-9.47	-4.82
1646.46	80.10	-9.76	-4.27
1646.36	80.15	-9.49	-5.81
1646.27	80.20	-9.70	-4.41
1646.17	80.25	-9.71	-4.20
1646.07	80.30	-9.16	-4.37
1645.97	80.35	-8.99	-4.12
1645.87	80.40	-8.96	-4.35
1645.77	80.45	-8.85	-5.65
1645.67	80.50	-8.74	-4.03
1645.57	80.55	-8.81	-6.46
1645.47	80.60	-9.37	-4.14
1645.36	80.65	-9.24	-4.02
1645.26	80.70	-9.75	-3.87
1645.16	80.75	-9.52	-5.00
1645.06	80.80	-9.63	-4.08
1644.85	80.90	-7.01	-3.39
1644.75	80.95	-8.91	-4.77
1644.64	81.00	-9.50	-4.10
1644.54	81.05	-9.42	-4.30
1644.43	81.10	-9.06	-4.98
1644.33	81.15	-8.96	-4.32
1644.22	81.20	-8.96	-4.05
1643.90	81.35	-8.81	-6.00
1643.80	81.40	-8.22	-4.30
1643.58	81.50	-9.37	-3.59
1643.47	81.55	-9.82	-4.43
1643.37	81.60	-9.93	-4.41
1643.26	81.65	-9.86	-5.59
1643.15	81.70	-9.54	-4.83
1643.04	81.75	-9.28	-4.09
1642.93	81.80	-8.84	-4.28
1642.82	81.85	-8.30	-3.62
1642.71	81.90	-7.92	-3.77
1642.60	81.95	-7.73	-4.24
1642.49	82.00	-8.01	-3.52
1642.38	82.05	-9.28	-4.27
1642.27	82.10	-7.69	-4.61
1642.16	82.15	-7.32	-6.04
1642.05	82.20	-7.45	-3.32
1641.94	82.25	-7.23	-4.16
1641.83	82.30	-7.55	-3.39
1641.71	82.35	-7.54	-3.90
1641.60	82.40	-7.62	-3.37
1641.38	82.50	-9.01	-4.94
1641.26	82.55	-8.13	-4.36
1641.15	82.60	-8.18	-3.40
1641.04	82.65	-8.54	-5.92
1640.92	82.70	-8.55	-3.85
1640.81	82.75	-8.45	-4.82
1640.70	82.80	-8.65	-4.53
1640.58	82.85	-8.27	-5.77
1640.47	82.90	-7.17	-3.45
1640.35	82.95	-9.01	-5.52
1640.24	83.00	-8.49	-4.99
1640.12	83.05	-8.75	-5.17
1640.01	83.10	-8.73	-3.79
1639.89	83.15	-8.13	-4.86
1639.78	83.20	-7.37	-3.29
1639.66	83.25	-7.56	-4.87
1639.55	83.30	-7.74	-3.30
1639.43	83.35	-7.75	-3.32
1639.31	83.40	-6.85	-4.06
1639.08	83.50	-6.89	-2.81
1638.96	83.55	-6.49	-4.00
1638.85	83.60	-6.78	-2.77
1638.73	83.65	-6.10	-2.94

Year A.D.	Depth from top (mm)	$\delta^{13}C$ (‰ VPDB)	$\delta^{18}O$ (‰ VPDB)
1638.61	83.70	-6.32	-2.51
1638.50	83.75	-6.14	-2.72
1638.26	83.85	-9.34	-4.40
1637.91	84.00	-6.93	-2.90
1637.79	84.05	-7.36	-3.15
1637.67	84.10	-7.50	-3.08
1637.55	84.15	-7.58	-3.80
1637.43	84.20	-7.56	-2.93
1637.32	84.25	-7.49	-4.37
1637.20	84.30	-7.85	-3.80
1637.08	84.35	-6.72	-4.13
1636.96	84.40	-8.11	-3.45
1636.84	84.45	-7.96	-4.79
1636.72	84.50	-7.89	-4.54
1636.60	84.55	-9.02	-4.98
1636.48	84.60	-8.00	-4.68
1636.36	84.65	-9.04	-4.26
1636.24	84.70	-7.54	-3.65
1636.00	84.80	-7.81	-3.31
1635.88	84.85	-7.73	-4.27
1635.77	84.90	-8.10	-3.63
1635.65	84.95	-8.58	-3.80
1635.53	85.00	-9.80	-4.08
1635.41	85.05	-8.62	-4.14
1635.29	85.10	-10.36	-4.95
1635.17	85.15	-8.90	-4.16
1635.05	85.20	-9.18	-5.07
1634.93	85.25	-9.34	-5.05
1634.80	85.30	-9.76	-3.99
1634.68	85.35	-9.87	-4.99
1634.56	85.40	-10.73	-6.38
1634.44	85.45	-10.55	-4.16
1634.32	85.50	-10.56	-4.78
1634.20	85.55	-10.44	-5.21
1634.08	85.60	-10.58	-4.28
1633.84	85.70	-10.36	-4.15
1633.72	85.75	-10.15	-4.78
1633.60	85.80	-9.86	-4.19
1633.48	85.85	-9.53	-4.13
1633.36	85.90	-9.57	-4.28
1633.24	85.95	-9.34	-3.84
1633.00	86.05	-8.95	-4.06
1632.88	86.10	-8.46	-3.74
1632.76	86.15	-8.94	-5.55
1632.64	86.20	-8.86	-4.16
1632.52	86.25	-9.21	-3.57
1632.40	86.30	-8.92	-4.18
1632.28	86.35	-9.00	-4.74
1632.16	86.40	-9.09	-5.62
1632.04	86.45	-9.72	-3.86
1631.92	86.50	-9.60	-5.15
1631.80	86.55	-9.12	-5.16
1631.68	86.60	-9.59	-5.63
1631.56	86.65	-9.35	-5.20
1631.44	86.70	-9.09	-4.18
1631.32	86.75	-8.23	-4.02
1631.20	86.80	-8.49	-3.43
1631.08	86.85	-8.27	-3.88
1630.96	86.90	-8.10	-3.35
1630.84	86.95	-8.31	-3.67
1630.72	87.00	-8.58	-3.84
1630.60	87.05	-8.91	-4.43
1630.48	87.10	-8.99	-4.64
1630.36	87.15	-9.58	-3.97
1630.24	87.20	-9.96	-4.10
1630.12	87.25	-10.36	-4.20
1630.00	87.30	-10.58	-4.24
1629.88	87.35	-10.52	-4.53
1629.76	87.40	-9.87	-3.94
1629.64	87.45	-9.50	-4.23
1629.53	87.50	-9.02	-3.87
1629.41	87.55	-9.06	-4.87
1629.29	87.60	-8.84	-3.84
1629.17	87.65	-8.92	-4.13
1628.93	87.75	-9.38	-4.14
1628.82	87.80	-9.52	-4.26
1628.70	87.85	-9.99	-4.25
1628.58	87.90	-10.33	-4.48
1628.46	87.95	-10.38	-4.73
1628.35	88.00	-10.58	-5.24
1628.23	88.05	-10.70	-4.56
1628.11	88.10	-10.96	-4.57
1627.99	88.15	-10.99	-4.27
1627.88	88.20	-10.66	-4.48
1627.76	88.25	-10.47	-4.60
1627.64	88.30	-10.45	-4.63
1627.53	88.35	-10.78	-4.94
1627.41	88.40	-9.90	-4.54

Year A.D.	Depth from top (mm)	$\delta^{13}C$ (‰ VPDB)	$\delta^{18}O$ (‰ VPDB)
1627.30	88.45	-8.66	-4.46
1627.18	88.50	-10.14	-4.19
1627.06	88.55	-9.60	-4.22
1626.95	88.60	-9.75	-4.32
1626.83	88.65	-9.69	-4.77
1626.72	88.70	-9.69	-5.96
1626.60	88.75	-9.79	-4.80
1626.49	88.80	-9.34	-3.97
1626.37	88.85	-9.15	-3.37
1626.26	88.90	-9.29	-3.84
1626.14	88.95	-9.47	-3.71
1626.03	89.00	-9.36	-3.97
1625.92	89.05	-9.00	-3.85
1625.80	89.10	-8.97	-4.06
1625.69	89.15	-8.61	-4.14
1625.58	89.20	-8.56	-4.48
1625.46	89.25	-8.86	-3.22
1625.35	89.30	-8.66	-3.57
1625.24	89.35	-8.63	-3.77
1625.13	89.40	-8.74	-3.73
1625.02	89.45	-8.46	-4.53
1624.90	89.50	-8.41	-3.89
1624.79	89.55	-8.58	-3.24
1624.68	89.60	-8.36	-3.72
1624.57	89.65	-8.31	-3.43
1624.46	89.70	-8.84	-4.49
1624.35	89.75	-9.02	-3.76
1624.13	89.85	-9.52	-4.03
1624.02	89.90	-10.05	-5.38
1623.91	89.95	-10.36	-4.33
1623.80	90.00	-10.16	-4.66
1623.69	90.05	-10.70	-3.71
1623.58	90.10	-11.16	-5.41
1623.48	90.15	-11.26	-4.33
1623.37	90.20	-11.38	-4.62
1623.26	90.25	-11.46	-4.18
1623.15	90.30	-11.10	-3.99
1623.05	90.35	-10.95	-4.54
1622.94	90.40	-10.54	-4.39
1622.83	90.45	-10.19	-4.52
1622.73	90.50	-9.72	-4.54
1622.62	90.55	-9.40	-5.37
1622.51	90.60	-8.07	-3.73
1622.41	90.65	-8.99	-4.21
1622.30	90.70	-9.30	-4.56
1622.20	90.75	-9.77	-3.99
1622.10	90.80	-10.70	-5.16
1621.99	90.85	-10.18	-4.28
1621.89	90.90	-9.85	-4.50
1621.79	90.95	-9.92	-3.57
1621.68	91.00	-9.97	-3.55
1621.58	91.05	-9.25	-3.92
1621.48	91.10	-8.96	-6.03
1621.38	91.15	-8.86	-3.74
1621.27	91.20	-8.74	-3.93
1621.17	91.25	-8.84	-4.53
1621.07	91.30	-8.93	-3.91
1620.97	91.35	-9.47	-4.35
1620.87	91.40	-9.75	-4.19
1620.67	91.50	-10.35	-5.26
1620.57	91.55	-11.03	-4.30
1620.48	91.60	-11.26	-4.42
1620.38	91.65	-11.28	-4.85
1620.28	91.70	-10.64	-4.73
1620.18	91.75	-9.93	-4.59
1620.09	91.80	-8.71	-4.35
1619.99	91.85	-7.79	-3.65
1619.89	91.90	-7.81	-3.07
1619.80	91.95	-8.38	-5.02
1619.70	92.00	-9.07	-3.67
1619.61	92.05	-9.48	-4.37
1619.51	92.10	-10.48	-4.21
1619.42	92.15	-10.92	-4.47
1619.33	92.20	-10.26	-4.97
1619.23	92.25	-11.16	-4.92
1619.14	92.30	-10.93	-4.50
1619.05	92.35	-10.43	-4.70
1618.96	92.40	-10.53	-4.33
1618.86	92.45	-10.00	-4.01
1618.77	92.50	-10.64	-5.90
1618.68	92.55	-9.04	-4.21
1618.59	92.60	-9.10	-4.03
1618.50	92.65	-9.28	-4.14
1618.41	92.70	-9.71	-4.59
1618.32	92.75	-9.28	-3.72
1618.24	92.80	-10.12	-4.63
1618.15	92.85	-10.31	-4.95
1618.06	92.90	-10.74	-4.13

Year A.D.	Depth from top (mm)	$\delta^{13}C$ (‰ VPDB)	$\delta^{18}O$ (‰ VPDB)
1617.97	92.95	-10.89	-4.72
1617.89	93.00	-10.78	-4.75
1617.80	93.05	-11.42	-4.54
1617.72	93.10	-11.50	-4.48
1617.63	93.15	-11.63	-4.71
1617.55	93.20	-11.38	-5.36
1617.46	93.25	-11.89	-4.62
1617.38	93.30	-11.98	-5.18
1617.30	93.35	-11.82	-5.35
1617.21	93.40	-12.05	-6.35
1617.13	93.45	-12.12	-5.52
1617.05	93.50	-12.31	-4.66
1616.97	93.55	-12.18	-5.20
1616.89	93.60	-12.06	-4.70
1616.81	93.65	-11.45	-5.07
1616.73	93.70	-11.12	-4.72
1616.65	93.75	-11.00	-4.86
1616.57	93.80	-10.78	-4.41
1616.50	93.85	-10.48	-4.56
1616.42	93.90	-10.25	-4.81
1616.34	93.95	-10.23	-4.14
1616.27	94.00	-10.36	-4.84
1616.19	94.05	-9.37	-4.72
1616.12	94.10	-10.83	-4.23
1616.04	94.15	-11.01	-4.04
1615.97	94.20	-11.04	-4.17
1615.82	94.30	-9.87	-4.95
1615.75	94.35	-11.19	-4.46
1615.68	94.40	-11.29	-5.26
1615.61	94.45	-10.95	-3.98
1615.54	94.50	-11.08	-4.92
1615.47	94.55	-10.79	-3.81
1615.40	94.60	-10.87	-4.65
1615.33	94.65	-10.53	-5.11
1615.26	94.70	-10.66	-4.28
1615.19	94.75	-10.64	-4.93
1615.13	94.80	-10.51	-3.99
1615.06	94.85	-10.65	-4.44
1614.99	94.90	-10.71	-4.19
1614.93	94.95	-10.74	-4.36
1614.86	95.00	-11.03	-4.07
1614.80	95.05	-11.03	-4.31
1614.74	95.10	-11.34	-4.45
1614.67	95.15	-11.22	-4.60
1614.61	95.20	-9.34	-4.81
1614.55	95.25	-11.32	-4.23
1614.49	95.30	-10.97	-7.28
1614.43	95.35	-11.36	-4.23
1614.37	95.40	-11.38	-4.55
1614.31	95.45	-11.24	-4.31
1614.25	95.50	-11.25	-4.33
1614.20	95.55	-11.15	-3.99
1614.14	95.60	-10.90	-5.43
1614.08	95.65	-10.82	-4.38
1614.03	95.70	-9.69	-5.00
1613.97	95.75	-9.61	-4.32
1613.87	95.85	-9.13	-4.03
1613.81	95.90	-9.32	-5.13
1613.76	95.95	-9.72	-5.01
1613.71	96.00	-9.68	-4.56
1613.66	96.05	-10.21	-4.38
1613.61	96.10	-10.31	-4.22
1613.55	96.15	-10.21	-3.95
1613.50	96.20	-10.01	-4.11
1613.45	96.25	-9.44	-4.82
1613.40	96.30	-9.44	-3.99
1613.35	96.35	-9.33	-4.02
1613.19	96.50	-9.36	-4.23
1613.14	96.55	-10.11	-4.41
1613.09	96.60	-10.19	-4.61
1613.04	96.65	-10.52	-4.35
1612.99	96.70	-10.43	-4.01
1612.93	96.75	-10.78	-4.73
1612.88	96.80	-11.05	-4.55
1612.83	96.85	-11.28	-4.26
1612.78	96.90	-11.21	-4.37
1612.72	96.95	-11.44	-4.59
1612.67	97.00	-11.44	-4.90
1612.62	97.05	-10.88	-5.55
1612.57	97.10	-11.33	-4.87
1612.51	97.15	-10.86	-5.13
1612.46	97.20	-11.34	-4.23
1612.41	97.25	-11.21	-4.63
1612.35	97.30	-11.14	-4.85
1612.30	97.35	-10.95	-4.39
1612.25	97.40	-10.78	-4.62
1612.20	97.45	-10.40	-4.44
1612.14	97.50	-10.72	-4.31

Year A.D.	Depth from top (mm)	$\delta^{13}C$ (‰ VPDB)	$\delta^{18}O$ (‰ VPDB)
1612.09	97.55	-10.44	-4.82
1612.04	97.60	-10.49	-4.36
1611.98	97.65	-10.19	-5.21
1611.93	97.70	-10.90	-4.49
1611.88	97.75	-11.15	-4.10
1611.82	97.80	-10.51	-6.03
1611.77	97.85	-11.35	-4.21
1611.72	97.90	-11.53	-4.47
1611.66	97.95	-11.66	-4.95
1611.61	98.00	-11.69	-4.41
1611.55	98.05	-11.76	-5.11
1611.50	98.10	-11.94	-5.75
1611.45	98.15	-11.40	-4.60
1611.39	98.20	-11.87	-4.19
1611.34	98.25	-11.62	-6.03
1611.29	98.30	-11.73	-4.64
1611.23	98.35	-11.35	-4.88
1611.18	98.40	-11.36	-4.41
1611.12	98.45	-10.88	-4.24
1611.01	98.55	-11.12	-4.69
1610.96	98.60	-11.01	-4.53
1610.91	98.65	-11.01	-3.89
1610.85	98.70	-11.05	-5.55
1610.80	98.75	-11.19	-4.52
1610.74	98.80	-11.15	-3.83
1610.69	98.85	-10.16	-4.82
1610.63	98.90	-9.85	-4.30
1610.58	98.95	-9.45	-4.84
1610.52	99.00	-11.09	-4.12
1610.47	99.05	-11.18	-4.00
1610.42	99.10	-11.13	-3.91
1610.36	99.15	-11.37	-4.03
1610.31	99.20	-11.21	-4.11
1610.25	99.25	-11.14	-5.75
1610.20	99.30	-10.77	-4.54
1610.14	99.35	-10.55	-4.56
1610.09	99.40	-10.74	-3.76
1610.03	99.45	-11.00	-5.05
1609.98	99.50	-10.72	-4.50
1609.92	99.55	-10.32	-3.87
1609.87	99.60	-10.10	-4.01
1609.81	99.65	-9.59	-3.68
1609.76	99.70	-9.97	-4.67
1609.70	99.75	-9.42	-5.29
1609.65	99.80	-8.77	-4.72
1609.59	99.85	-8.76	-4.51
1609.54	99.90	-9.33	-3.62
1609.48	99.95	-8.97	-4.30
1609.42	100.00	-8.85	-3.76
1609.37	100.05	-8.72	-3.92
1609.31	100.10	-8.46	-3.06
1609.26	100.15	-10.52	-4.84
1609.20	100.20	-8.66	-5.11
1609.15	100.25	-8.21	-4.52
1609.09	100.30	-9.01	-4.64
1609.04	100.35	-8.67	-4.15
1608.98	100.40	-9.26	-3.59
1608.93	100.45	-9.56	-4.47
1608.87	100.50	-9.58	-4.64
1608.82	100.55	-9.86	-4.15
1608.76	100.60	-9.84	-4.29
1608.70	100.65	-11.19	-4.48
1608.65	100.70	-10.27	-4.38
1608.59	100.75	-10.14	-4.57
1608.54	100.80	-10.07	-4.34
1608.48	100.85	-9.31	-4.58
1608.43	100.90	-9.48	-4.72
1608.37	100.95	-8.81	-4.36
1608.31	101.00	-9.53	-4.08
1608.26	101.05	-10.21	-5.03
1608.20	101.10	-9.60	-4.11
1608.15	101.15	-9.33	-4.55
1608.09	101.20	-9.54	-4.95
1608.04	101.25	-9.16	-4.15
1607.98	101.30	-9.90	-5.14
1607.92	101.35	-10.06	-4.70
1607.87	101.40	-9.90	-4.64
1607.81	101.45	-11.20	-4.56
1607.76	101.50	-9.93	-5.26
1607.70	101.55	-10.42	-5.19
1607.64	101.60	-10.37	-4.14
1607.59	101.65	-10.64	-4.64
1607.53	101.70	-10.75	-4.86
1607.48	101.75	-10.42	-4.55
1607.42	101.80	-8.32	-2.58
1607.36	101.85	-10.41	-4.11
1607.31	101.90	-10.26	-4.20
1607.25	101.95	-9.49	-4.15

Year A.D.	Depth from top (mm)	$\delta^{13}C$ (‰ VPDB)	$\delta^{18}O$ (‰ VPDB)
1607.20	102.00	-9.08	-4.24
1607.14	102.05	-9.24	-3.64
1607.08	102.10	-9.22	-4.06
1607.03	102.15	-9.25	-4.09
1606.97	102.20	-9.23	-3.73
1606.92	102.25	-8.90	-3.81
1606.86	102.30	-9.03	-4.99
1606.80	102.35	-9.32	-4.38
1606.75	102.40	-9.36	-4.07
1606.69	102.45	-9.12	-3.79
1606.64	102.50	-9.37	-4.69
1606.58	102.55	-8.22	-3.99
1606.52	102.60	-8.50	-3.86
1606.47	102.65	-8.41	-3.56
1606.41	102.70	-8.78	-3.57
1606.36	102.75	-8.85	-4.86
1606.30	102.80	-8.92	-4.48
1606.25	102.85	-9.11	-3.74
1606.19	102.90	-9.06	-3.56
1606.13	102.95	-11.44	-4.58
1606.08	103.00	-8.93	-4.35
1606.02	103.05	-9.30	-4.01
1605.97	103.10	-9.21	-3.97
1605.91	103.15	-8.99	-4.21
1605.85	103.20	-9.04	-4.21
1605.80	103.25	-9.07	-4.03
1605.74	103.30	-8.78	-5.11
1605.69	103.35	-9.40	-4.13
1605.63	103.40	-9.50	-4.15
1605.57	103.45	-9.52	-4.09
1605.52	103.50	-9.32	-4.34
1605.46	103.55	-9.66	-4.37
1605.35	103.65	-9.46	-4.26
1605.30	103.70	-9.90	-3.99
1605.24	103.75	-9.80	-6.10
1605.18	103.80	-9.93	-5.07
1605.13	103.85	-9.97	-4.37
1605.07	103.90	-9.83	-4.51
1605.02	103.95	-9.55	-4.19
1604.96	104.00	-9.80	-4.13
1604.91	104.05	-9.31	-4.00
1604.85	104.10	-8.99	-4.23
1604.79	104.15	-9.61	-4.21
1604.74	104.20	-9.65	-4.86
1604.68	104.25	-9.50	-4.91
1604.63	104.30	-9.43	-4.26
1604.57	104.35	-9.49	-5.96
1604.52	104.40	-9.66	-4.29
1604.41	104.50	-9.64	-4.40
1604.35	104.55	-9.53	-3.94
1604.29	104.60	-9.63	-4.28
1604.24	104.65	-9.63	-5.01
1604.18	104.70	-9.53	-4.84
1604.13	104.75	-9.45	-4.36
1604.07	104.80	-9.57	-4.49
1604.02	104.85	-9.45	-4.02
1603.96	104.90	-9.33	-4.19
1603.91	104.95	-9.17	-4.29
1603.85	105.00	-8.91	-3.91
1603.80	105.05	-9.14	-4.49
1603.74	105.10	-9.50	-4.50
1603.69	105.15	-9.51	-5.13
1603.63	105.20	-9.77	-4.98
1603.58	105.25	-9.68	-5.16
1603.52	105.30	-9.90	-4.60
1603.47	105.35	-9.66	-4.30
1603.41	105.40	-9.77	-4.43
1603.36	105.45	-9.47	-4.86
1603.25	105.55	-9.47	-6.61
1603.19	105.60	-9.26	-4.43
1603.14	105.65	-8.75	-4.59
1603.08	105.70	-9.16	-4.59
1603.03	105.75	-9.26	-4.46
1602.97	105.80	-9.49	-4.10
1602.92	105.85	-11.25	-4.72
1602.87	105.90	-9.71	-4.73
1602.81	105.95	-9.69	-5.22
1602.76	106.00	-9.89	-4.32
1602.70	106.05	-9.65	-5.19
1602.65	106.10	-9.81	-4.98
1602.59	106.15	-9.81	-4.84
1602.53	106.20	-9.86	-4.97
1602.47	106.25	-9.61	-4.18
1602.42	106.30	-9.04	-4.35
1602.36	106.35	-9.53	-4.35
1602.30	106.40	-9.45	-4.40
1602.24	106.45	-9.76	-5.19
1602.17	106.50	-10.05	-4.47

Year A.D.	Depth from top (mm)	$\delta^{13}C$ (‰ VPDB)	$\delta^{18}O$ (‰ VPDB)
1602.11	106.55	-9.47	-4.98
1602.05	106.60	-10.08	-5.02
1601.98	106.65	-9.90	-4.80
1601.92	106.70	-9.47	-5.02
1601.85	106.75	-9.94	-4.59
1601.79	106.80	-10.03	-5.24
1601.72	106.85	-9.83	-4.20
1601.65	106.90	-9.78	-5.07
1601.58	106.95	-9.88	-4.80
1601.51	107.00	-9.65	-4.54
1601.45	107.05	-9.91	-5.42
1601.37	107.10	-9.87	-4.87
1601.30	107.15	-9.63	-4.21
1601.23	107.20	-9.90	-4.10
1601.16	107.25	-9.99	-4.40
1601.08	107.30	-9.93	-4.37
1601.01	107.35	-10.01	-7.12
1600.94	107.40	-9.93	-3.97
1600.86	107.45	-9.61	-4.16
1600.78	107.50	-10.12	-4.76
1600.71	107.55	-10.24	-4.48
1600.63	107.60	-10.14	-4.69
1600.55	107.65	-9.58	-4.70
1600.47	107.70	-9.47	-4.62
1600.39	107.75	-9.51	-4.19
1600.31	107.80	-9.54	-4.44
1600.23	107.85	-8.95	-4.61
1600.15	107.90	-9.59	-4.32
1600.07	107.95	-9.81	-4.34
1599.98	108.00	-9.86	-5.33
1599.90	108.05	-9.98	-4.70
1599.82	108.10	-9.79	-6.32
1599.73	108.15	-9.79	-4.27
1599.65	108.20	-9.84	-4.33
1599.56	108.25	-9.65	-4.32
1599.47	108.30	-9.68	-4.35
1599.39	108.35	-9.78	-4.38
1599.30	108.40	-9.71	-6.48
1599.21	108.45	-9.92	-4.27
1599.12	108.50	-9.89	-4.37
1599.03	108.55	-9.97	-4.44
1598.94	108.60	-10.19	-4.47
1598.85	108.65	-9.54	-5.00
1598.76	108.70	-9.99	-4.48
1598.67	108.75	-9.95	-4.57
1598.57	108.80	-9.60	-4.50
1598.48	108.85	-10.00	-4.12
1598.39	108.90	-9.40	-4.28
1598.29	108.95	-9.66	-4.78
1598.20	109.00	-9.41	-3.84
1598.10	109.05	-9.56	-4.24
1598.00	109.10	-9.53	-4.73
1597.91	109.15	-9.56	-4.17
1597.81	109.20	-9.46	-4.73
1597.71	109.25	-9.52	-4.57
1597.61	109.30	-9.41	-4.64
1597.51	109.35	-9.41	-4.09
1597.41	109.40	-9.51	-4.78
1597.31	109.45	-9.55	-4.34
1597.21	109.50	-9.56	-3.84
1597.11	109.55	-11.26	-6.65
1597.01	109.60	-9.56	-4.49
1596.91	109.65	-10.51	-6.06
1596.81	109.70	-10.59	-4.86
1596.70	109.75	-10.80	-4.38
1596.60	109.80	-10.79	-4.90
1596.49	109.85	-11.02	-5.13
1596.39	109.90	-10.77	-5.90
1596.28	109.95	-10.75	-4.39
1596.18	110.00	-10.30	-4.59
1596.07	110.05	-10.13	-4.60
1595.96	110.10	-9.97	-4.02
1595.86	110.15	-10.00	-4.70
1595.75	110.20	-9.85	-4.65
1595.64	110.25	-9.79	-6.18
1595.53	110.30	-9.83	-4.09
1595.42	110.35	-9.81	-4.00
1595.31	110.40	-9.85	-3.87
1595.20	110.45	-9.93	-4.60
1595.09	110.50	-9.94	-4.42
1594.98	110.55	-10.06	-4.78
1594.87	110.60	-10.00	-4.30
1594.76	110.65	-9.97	-4.37
1594.64	110.70	-9.76	-4.61
1594.53	110.75	-9.85	-4.49
1594.42	110.80	-9.76	-4.15
1594.30	110.85	-9.60	-4.46
1594.19	110.90	-9.82	-4.09

Year A.D.	Depth from top (mm)	$\delta^{13}C$ (‰ VPDB)	$\delta^{18}O$ (‰ VPDB)
1594.08	110.95	-9.83	-5.77
1593.96	111.00	-9.92	-4.62
1593.84	111.05	-10.05	-4.40
1593.73	111.10	-10.17	-4.43
1593.61	111.15	-10.15	-4.27
1593.49	111.20	-10.20	-4.37
1593.38	111.25	-10.14	-4.53
1593.26	111.30	-10.39	-4.43
1593.14	111.35	-10.71	-5.27
1593.02	111.40	-10.11	-4.27
1592.90	111.45	-10.66	-4.66
1592.78	111.50	-10.35	-4.25
1592.67	111.55	-10.41	-4.61
1592.55	111.60	-10.85	-4.65
1592.42	111.65	-10.72	-4.48
1592.30	111.70	-10.59	-4.84
1592.18	111.75	-10.59	-4.39
1592.06	111.80	-10.38	-4.90
1591.94	111.85	-10.48	-4.62
1591.82	111.90	-10.34	-4.62
1591.69	111.95	-10.18	-5.85
1591.57	112.00	-10.13	-5.44
1591.45	112.05	-10.10	-4.95
1591.32	112.10	-9.97	-3.80
1591.20	112.15	-10.32	-4.94
1591.08	112.20	-10.46	-6.21
1590.95	112.25	-9.86	-4.97
1590.83	112.30	-9.86	-4.44
1590.70	112.35	-9.69	-4.67
1590.57	112.40	-9.68	-4.43
1590.45	112.45	-9.92	-4.79
1590.32	112.50	-9.84	-4.38
1590.20	112.55	-9.81	-4.19
1590.07	112.60	-9.88	-4.61
1589.94	112.65	-9.73	-4.59
1589.81	112.70	-9.97	-4.67
1589.69	112.75	-9.94	-4.56
1589.56	112.80	-9.97	-4.86
1589.43	112.85	-10.17	-4.46
1589.30	112.90	-10.05	-4.88
1589.17	112.95	-10.14	-5.08
1589.04	113.00	-9.99	-4.68
1588.91	113.05	-10.11	-4.83
1588.78	113.10	-9.82	-5.37
1588.65	113.15	-9.96	-4.65
1588.52	113.20	-9.98	-4.85
1588.39	113.25	-9.79	-4.62
1588.26	113.30	-9.90	-5.36
1588.13	113.35	-9.85	-4.26
1587.86	113.45	-9.73	-5.07
1587.73	113.50	-9.65	-4.44
1587.60	113.55	-9.79	-4.54
1587.47	113.60	-9.91	-4.69
1587.33	113.65	-10.20	-5.29
1587.20	113.70	-10.02	-4.69
1587.07	113.75	-10.04	-4.82
1586.93	113.80	-9.97	-4.54
1586.80	113.85	-10.02	-4.62
1586.67	113.90	-10.39	-5.43
1586.53	113.95	-10.03	-5.30
1586.40	114.00	-9.91	-4.88
1586.26	114.05	-10.28	-4.42
1586.13	114.10	-10.14	-4.87
1585.99	114.15	-10.10	-4.48
1585.86	114.20	-10.13	-4.65
1585.72	114.25	-10.30	-5.63
1585.59	114.30	-10.37	-4.56
1585.45	114.35	-10.35	-4.94
1585.32	114.40	-10.14	-5.30
1585.18	114.45	-10.47	-4.67
1585.05	114.50	-10.05	-6.55
1584.91	114.55	-10.33	-4.76
1584.77	114.60	-10.67	-4.96
1584.64	114.65	-10.84	-4.89
1584.50	114.70	-10.85	-4.94
1584.36	114.75	-10.90	-5.23
1584.22	114.80	-10.65	-4.76
1584.09	114.85	-10.84	-5.00
1583.95	114.90	-11.48	-5.95
1583.81	114.95	-11.05	-4.94
1583.67	115.00	-10.83	-4.76
1583.54	115.05	-10.93	-4.67
1583.40	115.10	-10.89	-4.91
1583.26	115.15	-10.99	-4.71
1583.12	115.20	-11.04	-4.93
1582.98	115.25	-11.08	-4.91
1582.85	115.30	-10.97	-4.96
1582.71	115.35	-10.60	-4.79

Year A.D.	Depth from top (mm)	$\delta^{13}C$ (‰ VPDB)	$\delta^{18}O$ (‰ VPDB)
1582.57	115.40	-10.83	-4.91
1582.43	115.45	-10.45	-5.06
1582.29	115.50	-10.44	-5.76
1582.15	115.55	-10.35	-5.43
1582.01	115.60	-10.46	-4.82
1581.87	115.65	-10.08	-4.48
1581.73	115.70	-10.16	-4.98
1581.60	115.75	-10.19	-4.65
1581.46	115.80	-9.96	-5.52
1581.32	115.85	-10.13	-4.82
1581.18	115.90	-10.22	-4.70
1581.04	115.95	-10.28	-4.60
1580.90	116.00	-10.53	-4.65
1580.76	116.05	-10.55	-4.80
1580.62	116.10	-10.55	-4.73
1580.48	116.15	-10.61	-5.00
1580.34	116.20	-10.54	-4.36
1580.20	116.25	-10.79	-4.79
1580.06	116.30	-10.62	-4.91
1579.92	116.35	-10.52	-4.82
1579.78	116.40	-10.55	-4.59
1579.64	116.45	-10.44	-5.01
1579.50	116.50	-10.22	-4.53
1579.36	116.55	-10.28	-4.67
1579.22	116.60	-10.30	-5.03
1579.08	116.65	-10.34	-5.07
1578.94	116.70	-9.99	-5.02
1578.80	116.75	-9.49	-4.94
1578.66	116.80	-9.18	-4.14
1578.52	116.85	-9.38	-4.23
1578.38	116.90	-9.50	-4.25
1578.24	116.95	-9.11	-4.25
1578.10	117.00	-10.16	-5.16
1577.96	117.05	-8.58	-4.49
1577.82	117.10	-8.96	-3.81
1577.68	117.15	-9.66	-4.27
1577.54	117.20	-9.66	-4.23
1577.40	117.25	-9.16	-3.94
1577.26	117.30	-8.79	-4.15
1577.12	117.35	-8.96	-6.78
1576.98	117.40	-9.67	-4.52
1576.84	117.45	-10.45	-4.89
1576.70	117.50	-10.78	-4.77
1576.56	117.55	-10.94	-4.31
1576.42	117.60	-10.87	-4.61
1576.28	117.65	-10.98	-4.60
1576.14	117.70	-11.01	-4.65
1576.00	117.75	-10.92	-4.61
1575.86	117.80	-10.88	-4.69
1575.72	117.85	-10.75	-5.19
1575.58	117.90	-10.56	-4.85
1575.44	117.95	-10.48	-5.20
1575.30	118.00	-10.36	-5.20
1575.16	118.05	-9.98	-4.67
1575.02	118.10	-9.58	-4.81
1574.88	118.15	-8.93	-4.58
1574.75	118.20	-8.86	-4.45
1574.61	118.25	-9.22	-4.17
1574.47	118.30	-9.38	-4.09
1574.33	118.35	-9.32	-4.35
1574.19	118.40	-9.36	-4.91
1574.05	118.45	-9.03	-4.59
1573.91	118.50	-9.07	-4.50
1573.78	118.55	-9.13	-4.57
1573.64	118.60	-9.57	-5.22
1573.50	118.65	-9.75	-6.14
1573.36	118.70	-10.14	-4.56
1573.23	118.75	-9.95	-4.63
1573.09	118.80	-10.59	-5.21
1572.95	118.85	-10.76	-4.92
1572.81	118.90	-10.91	-4.64
1572.68	118.95	-10.84	-4.80
1572.54	119.00	-10.85	-5.14
1572.40	119.05	-10.90	-5.05
1572.27	119.10	-10.66	-5.04
1572.13	119.15	-10.30	-5.46
1572.00	119.20	-10.24	-5.61
1571.86	119.25	-9.98	-5.52
1571.72	119.30	-9.89	-5.51
1571.59	119.35	-10.23	-5.36
1571.45	119.40	-10.39	-5.52
1571.32	119.45	-10.33	-5.53
1571.18	119.50	-10.17	-5.24
1571.05	119.55	-9.97	-4.69
1570.91	119.60	-10.26	-6.63
1570.78	119.65	-10.56	-5.22
1570.65	119.70	-10.71	-7.09
1570.51	119.75	-10.52	-5.08

Year A.D.	Depth from top (mm)	$\delta^{13}C$ (‰ VPDB)	$\delta^{18}O$ (‰ VPDB)
1570.38	119.80	-10.34	-6.10
1570.24	119.85	-10.35	-5.29
1570.11	119.90	-10.15	-4.90
1569.98	119.95	-10.08	-4.91
1569.85	120.00	-10.53	-5.74
1569.71	120.05	-10.96	-5.51
1569.58	120.10	-11.17	-5.06
1569.45	120.15	-11.47	-5.63
1569.32	120.20	-11.63	-5.03
1569.18	120.25	-11.61	-5.75
1569.05	120.30	-11.10	-5.10
1568.92	120.35	-11.20	-6.11
1568.79	120.40	-10.93	-4.90
1568.66	120.45	-10.86	-4.70
1568.53	120.50	-10.94	-5.47
1568.40	120.55	-10.65	-5.22
1568.27	120.60	-10.49	-4.74
1568.14	120.65	-10.39	-4.98
1568.01	120.70	-10.02	-5.28
1567.88	120.75	-10.04	-5.11
1567.75	120.80	-10.10	-4.70
1567.63	120.85	-10.16	-4.72
1567.50	120.90	-10.42	-4.55
1567.37	120.95	-9.66	-5.12
1567.24	121.00	-10.44	-4.54
1567.12	121.05	-10.58	-4.69
1566.99	121.10	-10.67	-4.73
1566.86	121.15	-10.28	-4.73
1566.74	121.20	-10.57	-4.65
1566.61	121.25	-10.26	-4.69
1566.49	121.30	-10.46	-5.46
1566.36	121.35	-10.41	-4.74
1566.24	121.40	-10.32	-4.96
1566.11	121.45	-10.23	-4.80
1565.99	121.50	-10.42	-5.04
1565.86	121.55	-10.16	-4.67
1565.74	121.60	-10.15	-4.75
1565.62	121.65	-10.29	-4.40
1565.49	121.70	-10.33	-4.75
1565.37	121.75	-10.37	-5.01
1565.25	121.80	-10.47	-4.97
1565.13	121.85	-10.45	-4.65
1565.01	121.90	-10.48	-4.68
1564.89	121.95	-10.58	-5.00
1564.76	122.00	-11.02	-5.42
1564.52	122.10	-11.22	-4.82
1564.41	122.15	-11.11	-5.47
1564.29	122.20	-11.14	-5.07
1564.17	122.25	-10.94	-4.90
1564.05	122.30	-10.31	-4.70
1563.93	122.35	-10.57	-5.72
1563.81	122.40	-10.01	-4.27
1563.70	122.45	-10.06	-4.30
1563.58	122.50	-10.54	-4.77
1563.46	122.55	-10.50	-4.95
1563.35	122.60	-10.70	-5.47
1563.23	122.65	-10.50	-5.49
1563.12	122.70	-10.94	-4.69
1563.00	122.75	-11.19	-5.17
1562.89	122.80	-11.36	-5.42
1562.78	122.85	-11.37	-5.66
1562.66	122.90	-11.57	-5.14
1562.55	122.95	-11.66	-5.84
1562.44	123.00	-11.67	-5.21
1562.33	123.05	-11.40	-5.79
1562.22	123.10	-10.81	-5.02
1562.11	123.15	-10.79	-5.41
1561.99	123.20	-10.00	-5.16
1561.88	123.25	-9.55	-4.42
1561.78	123.30	-9.46	-5.05
1561.67	123.35	-9.99	-4.63
1561.56	123.40	-10.01	-4.95
1561.45	123.45	-9.80	-5.15
1561.34	123.50	-9.66	-4.89
1561.24	123.55	-9.45	-4.39
1561.13	123.60	-9.14	-4.21
1561.02	123.65	-8.95	-4.17
1560.92	123.70	-8.77	-4.20
1560.81	123.75	-8.63	-4.49
1560.71	123.80	-8.88	-3.90
1560.60	123.85	-9.04	-3.76
1560.50	123.90	-9.09	-4.09
1560.40	123.95	-9.18	-3.84
1560.30	124.00	-9.35	-4.17
1560.19	124.05	-9.27	-3.67
1560.09	124.10	-9.25	-3.53
1559.99	124.15	-9.30	-3.81
1559.89	124.20	-9.18	-3.83

Year A.D.	Depth from top (mm)	$\delta^{13}C$ (‰ VPDB)	$\delta^{18}O$ (‰ VPDB)
1559.79	124.25	-9.03	-3.67
1559.69	124.30	-8.99	-3.88
1559.59	124.35	-8.68	-3.71
1559.50	124.40	-8.89	-3.87
1559.40	124.45	-8.93	-3.94
1559.30	124.50	-8.97	-3.64
1559.20	124.55	-9.14	-5.19
1559.11	124.60	-9.39	-4.09
1559.01	124.65	-9.64	-4.26
1558.92	124.70	-10.08	-4.26
1558.82	124.75	-10.33	-4.03
1558.73	124.80	-10.45	-4.13
1558.64	124.85	-10.61	-4.15
1558.55	124.90	-10.94	-4.32
1558.45	124.95	-10.86	-4.59
1558.36	125.00	-10.85	-4.49
1558.27	125.05	-10.77	-4.31
1558.18	125.10	-10.60	-4.38
1558.09	125.15	-10.45	-4.75
1558.00	125.20	-10.28	-4.73
1557.92	125.25	-10.09	-4.45
1557.83	125.30	-10.09	-4.65
1557.74	125.35	-10.04	-4.35
1557.66	125.40	-10.03	-4.53
1557.57	125.45	-10.20	-4.45
1557.49	125.50	-10.28	-4.60
1557.40	125.55	-10.48	-4.60
1557.32	125.60	-10.70	-4.83
1557.23	125.65	-11.07	-4.75
1557.15	125.70	-11.12	-5.19
1557.07	125.75	-11.29	-4.51
1556.99	125.80	-11.28	-4.94
1556.91	125.85	-11.38	-4.97
1556.83	125.90	-11.47	-5.02
1556.75	125.95	-11.66	-4.74
1556.67	126.00	-11.35	-4.99
1556.59	126.05	-11.69	-5.46
1556.52	126.10	-11.43	-4.80
1556.44	126.15	-11.24	-4.97
1556.36	126.20	-11.13	-5.12
1556.29	126.25	-11.05	-5.12
1556.22	126.30	-10.65	-4.87
1556.14	126.35	-11.13	-4.91
1556.07	126.40	-10.78	-4.71
1556.00	126.45	-10.03	-4.68
1555.93	126.50	-9.83	-4.73
1555.85	126.55	-9.81	-4.59
1555.78	126.60	-9.36	-4.72
1555.71	126.65	-8.57	-4.80
1555.65	126.70	-8.55	-4.36
1555.58	126.75	-8.35	-4.18
1555.51	126.80	-8.12	-3.97
1555.44	126.85	-8.10	-4.40
1555.38	126.90	-7.95	-4.07
1555.31	126.95	-8.16	-4.29
1555.25	127.00	-8.60	-4.53
1555.19	127.05	-8.92	-4.28
1555.12	127.10	-9.29	-4.39
1555.06	127.15	-9.61	-4.30
1555.00	127.20	-10.06	-4.60
1554.94	127.25	-10.31	-4.59
1554.88	127.30	-10.40	-4.38
1554.82	127.35	-10.15	-4.29
1554.76	127.40	-10.02	-4.62
1554.71	127.45	-9.58	-4.40
1554.65	127.50	-9.19	-4.48
1554.59	127.55	-8.66	-4.51
1554.54	127.60	-8.70	-4.54
1554.49	127.65	-8.83	-4.34
1554.43	127.70	-9.11	-4.96
1554.38	127.75	-9.11	-4.63
1554.33	127.80	-9.16	-5.00
1554.28	127.85	-9.00	-4.12
1554.23	127.90	-9.35	-4.46
1554.18	127.95	-8.93	-5.72
1554.13	128.00	-8.93	-4.35
1554.08	128.05	-8.93	-5.09
1554.03	128.10	-9.15	-4.62
1553.98	128.15	-9.11	-4.27
1553.94	128.20	-9.29	-4.32
1553.89	128.25	-9.31	-4.40
1553.84	128.30	-9.32	-5.11
1553.79	128.35	-9.99	-4.39
1553.75	128.40	-9.97	-4.43
1553.70	128.45	-10.42	-5.00
1553.65	128.50	-10.79	-5.22
1553.60	128.55	-10.73	-4.96
1553.56	128.60	-10.98	-4.70

Year A.D.	Depth from top (mm)	$\delta^{13}C$ (‰ VPDB)	$\delta^{18}O$ (‰ VPDB)
1553.51	128.65	-11.04	-5.00
1553.46	128.70	-11.14	-4.89
1553.42	128.75	-11.21	-5.42
1553.37	128.80	-11.07	-6.33
1553.32	128.85	-11.16	-5.12
1553.27	128.90	-10.96	-4.78
1553.23	128.95	-10.56	-4.84
1553.18	129.00	-10.08	-5.18
1553.13	129.05	-9.88	-4.56
1553.09	129.10	-9.58	-4.90
1553.04	129.15	-9.28	-4.55
1553.00	129.20	-9.23	-4.45
1552.95	129.25	-9.18	-5.43
1552.90	129.30	-9.25	-4.02
1552.86	129.35	-9.62	-4.33
1552.81	129.40	-9.85	-4.33
1552.76	129.45	-10.06	-5.25
1552.72	129.50	-10.14	-4.35
1552.67	129.55	-10.18	-4.47
1552.63	129.60	-10.09	-4.49
1552.58	129.65	-10.03	-4.61
1552.54	129.70	-9.99	-4.55
1552.49	129.75	-10.02	-4.84
1552.44	129.80	-9.94	-4.81
1552.40	129.85	-9.88	-4.42
1552.35	129.90	-9.88	-5.03
1552.31	129.95	-9.84	-4.56
1552.26	130.00	-10.07	-4.89
1552.22	130.05	-9.82	-4.77
1552.17	130.10	-9.84	-5.95
1552.13	130.15	-9.58	-4.82
1552.08	130.20	-9.65	-4.64
1552.04	130.25	-9.71	-4.46
1551.99	130.30	-9.79	-4.34
1551.95	130.35	-9.98	-4.57
1551.90	130.40	-10.03	-4.58
1551.86	130.45	-10.03	-4.59
1551.81	130.50	-10.44	-4.44
1551.77	130.55	-10.57	-4.70
1551.73	130.60	-10.65	-4.62
1551.68	130.65	-10.68	-4.81
1551.64	130.70	-10.89	-4.32
1551.59	130.75	-10.72	-4.69
1551.55	130.80	-10.74	-4.89
1551.50	130.85	-10.60	-6.58
1551.46	130.90	-10.51	-4.56
1551.42	130.95	-10.53	-4.62
1551.37	131.00	-10.43	-4.70
1551.33	131.05	-10.17	-4.73
1551.28	131.10	-10.09	-4.49
1551.24	131.15	-10.07	-6.05
1551.20	131.20	-9.99	-5.04
1551.15	131.25	-10.12	-6.58
1551.11	131.30	-9.93	-4.91
1551.07	131.35	-9.73	-5.13
1551.02	131.40	-9.57	-5.11
1550.98	131.45	-9.81	-5.36
1550.94	131.50	-9.75	-4.22
1550.89	131.55	-9.77	-4.58
1550.85	131.60	-9.93	-4.55
1550.81	131.65	-9.95	-5.51
1550.76	131.70	-10.10	-5.20
1550.72	131.75	-10.16	-4.74
1550.68	131.80	-10.17	-4.66
1550.63	131.85	-10.32	-4.48
1550.59	131.90	-10.38	-4.35
1550.55	131.95	-10.63	-4.67
1550.51	132.00	-10.46	-5.13
1550.46	132.05	-10.41	-4.48
1550.42	132.10	-10.27	-4.48
1550.38	132.15	-10.17	-4.96
1550.34	132.20	-10.23	-5.04
1550.29	132.25	-9.74	-4.60
1550.25	132.30	-9.95	-5.44
1550.21	132.35	-9.90	-4.92
1550.17	132.40	-9.88	-4.55
1550.12	132.45	-9.82	-4.68
1550.08	132.50	-9.96	-4.83
1550.04	132.55	-9.97	-4.75
1550.00	132.60	-10.16	-5.08
1549.96	132.65	-10.28	-4.81
1549.91	132.70	-10.41	-5.15
1549.87	132.75	-10.55	-5.27
1549.83	132.80	-10.58	-5.16
1549.79	132.85	-10.66	-4.92
1549.75	132.90	-10.63	-5.00
1549.71	132.95	-10.75	-5.85
1549.66	133.00	-10.73	-5.77

Year A.D.	Depth from top (mm)	$\delta^{13}C$ (‰ VPDB)	$\delta^{18}O$ (‰ VPDB)
1549.62	133.05	-10.89	-4.58
1549.58	133.10	-10.87	-4.97
1549.54	133.15	-10.80	-6.21
1549.50	133.20	-10.78	-5.14
1549.46	133.25	-10.92	-4.76
1549.42	133.30	-10.69	-4.86
1549.37	133.35	-10.62	-4.84
1549.33	133.40	-10.48	-4.70
1549.29	133.45	-10.51	-4.95
1549.25	133.50	-10.33	-4.79
1549.21	133.55	-10.16	-4.90
1549.17	133.60	-10.29	-5.85
1549.13	133.65	-10.37	-4.99
1549.09	133.70	-10.14	-4.88
1549.05	133.75	-10.35	-4.89
1549.01	133.80	-10.43	-5.57
1548.97	133.85	-10.55	-5.11
1548.93	133.90	-10.56	-5.07
1548.88	133.95	-10.56	-5.23
1548.84	134.00	-10.78	-4.82
1548.80	134.05	-11.00	-5.71
1548.76	134.10	-11.10	-5.18
1548.72	134.15	-11.30	-4.82
1548.68	134.20	-11.33	-5.12
1548.64	134.25	-11.32	-4.96
1548.60	134.30	-11.34	-4.83
1548.56	134.35	-11.32	-5.46
1548.52	134.40	-11.35	-4.95
1548.48	134.45	-11.32	-4.18
1548.44	134.50	-11.36	-5.18
1548.40	134.55	-11.39	-5.22
1548.36	134.60	-11.28	-5.77
1548.32	134.65	-11.11	-5.03
1548.28	134.70	-10.76	-4.90
1548.24	134.75	-10.32	-4.85
1548.20	134.80	-10.50	-4.81
1548.16	134.85	-10.43	-5.17
1548.12	134.90	-10.61	-4.91
1548.08	134.95	-10.65	-5.73
1548.04	135.00	-10.96	-5.15
1548.00	135.05	-11.04	-4.79
1547.96	135.10	-11.23	-5.88
1547.93	135.15	-11.10	-4.67
1547.89	135.20	-11.28	-5.43
1547.85	135.25	-11.12	-5.41
1547.81	135.30	-11.02	-4.92
1547.77	135.35	-11.07	-5.65
1547.73	135.40	-10.88	-5.42
1547.69	135.45	-10.84	-4.69
1547.65	135.50	-10.76	-5.40
1547.61	135.55	-10.59	-5.22
1547.57	135.60	-10.57	-4.66
1547.53	135.65	-10.49	-5.08
1547.49	135.70	-10.50	-5.38
1547.46	135.75	-10.24	-4.83
1547.42	135.80	-10.24	-5.35
1547.38	135.85	-9.97	-4.91
1547.34	135.90	-10.06	-5.47
1547.30	135.95	-10.04	-4.89
1547.26	136.00	-10.25	-4.81
1547.22	136.05	-10.21	-4.71
1547.19	136.10	-10.28	-5.02
1547.15	136.15	-10.38	-4.58
1547.11	136.20	-10.50	-5.19
1547.07	136.25	-10.47	-5.12
1547.03	136.30	-10.69	-5.56
1546.99	136.35	-10.43	-4.68
1546.95	136.40	-10.55	-4.95
1546.92	136.45	-10.67	-5.01
1546.88	136.50	-10.75	-4.87
1546.84	136.55	-10.75	-4.82
1546.80	136.60	-10.71	-4.92
1546.76	136.65	-10.75	-4.76
1546.73	136.70	-10.75	-4.91
1546.69	136.75	-10.68	-5.71
1546.65	136.80	-10.80	-4.64
1546.61	136.85	-10.74	-4.98
1546.57	136.90	-10.71	-5.19
1546.54	136.95	-10.87	-5.01
1546.50	137.00	-10.76	-4.78
1546.46	137.05	-10.81	-5.52
1546.42	137.10	-10.75	-5.82
1546.38	137.15	-10.43	-5.50
1546.35	137.20	-10.47	-5.01
1546.31	137.25	-10.78	-6.56
1546.27	137.30	-10.57	-4.94
1546.23	137.35	-10.29	-5.02
1546.20	137.40	-10.18	-4.45

Year A.D.	Depth from top (mm)	$\delta^{13}C$ (‰ VPDB)	$\delta^{18}O$ (‰ VPDB)
1546.16	137.45	-10.23	-5.14
1546.12	137.50	-10.12	-4.75
1546.08	137.55	-10.11	-4.57
1546.05	137.60	-10.32	-4.66
1546.01	137.65	-10.35	-4.41
1545.97	137.70	-10.07	-4.45
1545.93	137.75	-10.02	-4.87
1545.90	137.80	-9.89	-4.42
1545.86	137.85	-9.94	-4.76
1545.82	137.90	-9.85	-5.09
1545.78	137.95	-9.84	-4.09
1545.75	138.00	-9.86	-4.64
1545.71	138.05	-9.85	-4.33
1545.67	138.10	-9.80	-4.41
1545.64	138.15	-9.46	-6.18
1545.60	138.20	-9.61	-6.06
1545.56	138.25	-9.72	-4.55
1545.53	138.30	-9.58	-4.55
1545.49	138.35	-10.03	-4.54
1545.45	138.40	-9.81	-4.82
1545.41	138.45	-9.59	-4.10
1545.38	138.50	-9.62	-4.83
1545.34	138.55	-9.75	-4.57
1545.30	138.60	-9.36	-4.44
1545.27	138.65	-9.47	-4.85
1545.23	138.70	-9.57	-4.16
1545.19	138.75	-9.43	-4.74
1545.16	138.80	-9.57	-4.42
1545.12	138.85	-9.54	-4.42
1545.08	138.90	-9.52	-4.19
1545.05	138.95	-9.70	-4.27
1545.01	139.00	-10.08	-4.67
1544.97	139.05	-9.56	-4.04
1544.94	139.10	-9.38	-5.14
1544.90	139.15	-9.35	-4.14
1544.86	139.20	-9.25	-6.15
1544.83	139.25	-9.40	-4.62
1544.79	139.30	-9.20	-4.04
1544.76	139.35	-9.35	-4.31
1544.72	139.40	-9.34	-4.39
1544.68	139.45	-9.28	-4.57
1544.65	139.50	-9.39	-4.93
1544.57	139.60	-9.53	-4.41
1544.54	139.65	-9.72	-4.26
1544.50	139.70	-9.64	-4.43
1544.47	139.75	-9.57	-4.77
1544.43	139.80	-9.65	-4.50
1544.39	139.85	-9.69	-4.13
1544.36	139.90	-9.65	-3.96
1544.32	139.95	-9.84	-4.84
1544.29	140.00	-9.93	-4.89
1544.25	140.05	-9.77	-3.88
1544.21	140.10	-9.84	-4.48
1544.18	140.15	-9.97	-4.58
1544.14	140.20	-9.99	-4.25
1544.11	140.25	-10.13	-6.19
1544.07	140.30	-9.89	-4.28
1544.03	140.35	-9.81	-4.47
1544.00	140.40	-9.90	-4.59
1543.96	140.45	-10.01	-4.14
1543.93	140.50	-10.12	-4.75
1543.89	140.55	-10.17	-4.91
1543.86	140.60	-9.91	-4.85
1543.82	140.65	-10.21	-4.27
1543.78	140.70	-10.22	-4.38
1543.75	140.75	-10.23	-4.38
1543.68	140.85	-10.14	-4.92
1543.64	140.90	-10.29	-4.94
1543.61	140.95	-10.07	-4.80
1543.57	141.00	-10.22	-4.98
1543.53	141.05	-10.15	-4.44
1543.50	141.10	-10.21	-4.52
1543.46	141.15	-10.40	-4.29
1543.43	141.20	-10.34	-5.35
1543.39	141.25	-10.47	-4.19
1543.36	141.30	-10.51	-4.56
1543.32	141.35	-10.51	-5.10
1543.29	141.40	-10.30	-4.22
1543.25	141.45	-10.31	-5.77
1543.22	141.50	-10.24	-4.93
1543.18	141.55	-10.28	-4.48
1543.14	141.60	-10.39	-4.70
1543.11	141.65	-10.41	-4.20
1543.04	141.75	-10.75	-5.28
1543.00	141.80	-10.64	-4.63
1542.97	141.85	-10.65	-4.39
1542.93	141.90	-10.84	-4.54
1542.90	141.95	-10.91	-4.71

Year A.D.	Depth from top (mm)	$\delta^{13}C$ (‰ VPDB)	$\delta^{18}O$ (‰ VPDB)
1542.86	142.00	-11.05	-5.34
1542.83	142.05	-10.68	-4.61
1542.79	142.10	-10.80	-4.47
1542.76	142.15	-10.96	-4.55
1542.72	142.20	-11.08	-4.99
1542.69	142.25	-10.99	-4.34
1542.65	142.30	-11.08	-4.31
1542.62	142.35	-11.22	-4.70
1542.58	142.40	-11.05	-5.10
1542.55	142.45	-11.14	-4.49
1542.51	142.50	-10.66	-6.12
1542.48	142.55	-10.82	-4.42
1542.44	142.60	-10.48	-4.42
1542.41	142.65	-10.50	-4.87
1542.37	142.70	-10.44	-4.00
1542.34	142.75	-10.35	-3.96
1542.30	142.80	-10.13	-4.26
1542.27	142.85	-10.19	-4.02
1542.23	142.90	-10.06	-4.88
1542.20	142.95	-10.12	-4.39
1542.16	143.00	-10.36	-3.94
1542.13	143.05	-10.26	-4.21
1542.09	143.10	-10.75	-4.07
1542.06	143.15	-10.64	-4.42
1542.02	143.20	-10.82	-4.63
1541.99	143.25	-10.77	-5.69
1541.95	143.30	-11.08	-4.11
1541.92	143.35	-11.21	-4.49
1541.88	143.40	-11.26	-4.26
1541.85	143.45	-11.25	-4.46
1541.81	143.50	-11.03	-4.31
1541.78	143.55	-11.26	-4.73
1541.74	143.60	-11.15	-4.42
1541.71	143.65	-11.21	-4.49
1541.67	143.70	-11.30	-4.44
1541.64	143.75	-10.37	-5.66
1541.60	143.80	-11.28	-4.47
1541.57	143.85	-10.76	-4.48
1541.53	143.90	-10.82	-4.33
1541.50	143.95	-10.53	-4.57
1541.46	144.00	-9.82	-4.03
1541.43	144.05	-9.68	-3.86
1541.40	144.10	-9.15	-3.81
1541.36	144.15	-8.92	-4.53
1541.33	144.20	-9.03	-4.17
1541.29	144.25	-9.21	-4.36
1541.22	144.35	-9.20	-3.45
1541.19	144.40	-9.46	-3.99
1541.15	144.45	-9.74	-3.89
1541.12	144.50	-10.07	-3.92
1541.08	144.55	-10.00	-4.35
1541.05	144.60	-9.95	-4.22
1541.01	144.65	-9.52	-3.70
1540.98	144.70	-8.76	-3.78
1540.94	144.75	-8.02	-4.05
1540.91	144.80	-7.80	-3.55
1540.87	144.85	-6.91	-4.00
1540.84	144.90	-8.13	-3.85
1540.81	144.95	-8.24	-3.60
1540.77	145.00	-7.93	-4.98
1540.74	145.05	-8.70	-3.80
1540.70	145.10	-8.41	-3.81
1540.67	145.15	-8.95	-4.83
1540.63	145.20	-8.93	-3.91
1540.60	145.25	-8.83	-3.93
1540.56	145.30	-8.53	-3.93
1540.53	145.35	-8.37	-3.76
1540.49	145.40	-8.04	-3.65
1540.46	145.45	-8.26	-4.20
1540.39	145.55	-9.03	-4.49
1540.36	145.60	-8.99	-3.99
1540.32	145.65	-9.50	-4.01
1540.29	145.70	-9.30	-3.93
1540.25	145.75	-9.51	-3.88
1540.22	145.80	-9.27	-4.41
1540.18	145.85	-9.05	-3.87
1540.15	145.90	-8.88	-3.92
1540.11	145.95	-8.57	-3.91
1540.08	146.00	-8.88	-4.21
1540.04	146.05	-8.78	-4.82
1540.01	146.10	-8.90	-5.29
1539.97	146.15	-9.41	-4.51
1539.94	146.20	-9.54	-3.85
1539.91	146.25	-10.26	-6.09
1539.87	146.30	-9.33	-4.10
1539.80	146.40	-8.53	-4.08
1539.77	146.45	-8.67	-4.30
1539.70	146.55	-9.08	-4.00

Year A.D.	Depth from top (mm)	$\delta^{13}C$ (‰ VPDB)	$\delta^{18}O$ (‰ VPDB)
1539.66	146.60	-9.47	-4.14
1539.63	146.65	-9.62	-4.64
1539.59	146.70	-9.77	-3.96
1539.56	146.75	-10.17	-3.84
1539.52	146.80	-9.94	-4.26
1539.49	146.85	-10.48	-5.07
1539.45	146.90	-10.51	-4.54
1539.42	146.95	-10.59	-4.35
1539.39	147.00	-10.58	-4.01
1539.35	147.05	-10.50	-4.50
1539.32	147.10	-10.01	-4.36
1539.28	147.15	-9.42	-4.32
1539.25	147.20	-9.48	-4.43
1539.21	147.25	-9.18	-4.48
1539.18	147.30	-8.93	-4.47
1539.14	147.35	-8.82	-3.72
1539.11	147.40	-8.70	-4.78
1539.07	147.45	-9.17	-4.12
1539.04	147.50	-9.32	-4.35
1539.00	147.55	-9.62	-4.22
1538.97	147.60	-9.76	-4.38
1538.93	147.65	-10.13	-5.57
1538.90	147.70	-10.23	-4.13
1538.86	147.75	-10.67	-4.50
1538.83	147.80	-11.08	-4.99
1538.79	147.85	-11.19	-4.76
1538.76	147.90	-11.55	-4.39
1538.72	147.95	-11.44	-5.30
1538.69	148.00	-11.25	-4.79
1538.65	148.05	-10.53	-4.37
1538.62	148.10	-8.35	-4.01
1538.58	148.15	-8.15	-3.95
1538.55	148.20	-8.96	-4.08
1538.52	148.25	-10.10	-4.35
1538.48	148.30	-10.19	-4.47
1538.45	148.35	-9.94	-5.52
1538.41	148.40	-8.72	-4.45
1538.38	148.45	-8.40	-4.42
1538.34	148.50	-8.59	-4.09
1538.31	148.55	-9.55	-4.33
1538.27	148.60	-9.83	-4.13
1538.24	148.65	-10.02	-4.62
1538.20	148.70	-10.44	-4.62
1538.13	148.80	-9.50	-5.58
1538.10	148.85	-9.29	-5.24
1538.06	148.90	-9.58	-4.23
1538.03	148.95	-9.77	-4.66
1537.99	149.00	-10.05	-4.27
1537.95	149.05	-10.37	-4.31
1537.92	149.10	-10.49	-4.22
1537.88	149.15	-10.60	-4.41
1537.85	149.20	-11.02	-4.06
1537.81	149.25	-10.98	-4.43
1537.78	149.30	-11.14	-4.42
1537.74	149.35	-10.36	-4.28
1537.71	149.40	-10.22	-3.90
1537.67	149.45	-10.43	-4.58
1537.64	149.50	-10.44	-3.88
1537.60	149.55	-10.67	-4.14
1537.57	149.60	-10.93	-5.31
1537.53	149.65	-11.05	-4.14
1537.50	149.70	-10.94	-4.58
1537.46	149.75	-10.78	-4.50
1537.43	149.80	-10.73	-4.36
1537.39	149.85	-10.75	-4.37
1537.36	149.90	-10.76	-4.59
1537.32	149.95	-10.27	-4.86
1537.28	150.00	-10.05	-4.12
1537.25	150.05	-10.07	-3.84
1537.21	150.10	-10.25	-3.97
1537.18	150.15	-10.45	-3.84
1537.11	150.25	-10.52	-5.51
1537.07	150.30	-10.72	-3.90
1537.04	150.35	-11.04	-4.85
1537.00	150.40	-11.17	-4.31
1536.96	150.45	-10.09	-4.42
1536.93	150.50	-9.32	-6.48
1536.89	150.55	-9.12	-4.69
1536.82	150.65	-9.65	-4.16
1536.79	150.70	-9.74	-5.46
1536.75	150.75	-9.67	-4.52
1536.71	150.80	-9.64	-4.51
1536.68	150.85	-9.68	-5.25
1536.64	150.90	-10.03	-4.80
1536.61	150.95	-10.30	-4.68
1536.57	151.00	-9.86	-5.88
1536.54	151.05	-9.55	-5.31
1536.46	151.15	-9.95	-4.95

Year A.D.	Depth from top (mm)	$\delta^{13}C$ (‰ VPDB)	$\delta^{18}O$ (‰ VPDB)
1536.43	151.20	-10.15	-5.57
1536.39	151.25	-10.41	-5.40
1536.36	151.30	-10.65	-5.02
1536.32	151.35	-10.79	-5.07
1536.28	151.40	-10.86	-4.79
1536.25	151.45	-10.58	-4.59
1536.21	151.50	-9.53	-5.31
1536.18	151.55	-8.89	-5.05
1536.14	151.60	-9.12	-5.32
1536.07	151.70	-9.45	-4.29
1536.03	151.75	-10.14	-5.28
1535.99	151.80	-10.62	-4.42
1535.96	151.85	-10.83	-4.79
1535.92	151.90	-11.05	-6.20
1535.89	151.95	-10.95	-4.34
1535.85	152.00	-10.28	-4.29
1535.81	152.05	-9.54	-4.37
1535.78	152.10	-9.64	-4.40
1535.74	152.15	-9.54	-6.34
1535.70	152.20	-8.66	-4.64
1535.67	152.25	-9.41	-7.00
1535.63	152.30	-9.47	-4.21
1535.59	152.35	-10.16	-4.55
1535.56	152.40	-10.61	-6.45
1535.52	152.45	-10.61	-5.90
1535.48	152.50	-11.03	-4.93
1535.45	152.55	-11.25	-5.21
1535.41	152.60	-11.19	-5.16
1535.34	152.70	-9.53	-4.72
1535.30	152.75	-9.39	-4.29
1535.26	152.80	-9.52	-3.85
1535.23	152.85	-9.73	-5.16
1535.19	152.90	-9.99	-4.55
1535.15	152.95	-10.29	-5.76
1535.12	153.00	-10.57	-5.47
1535.08	153.05	-10.91	-5.72
1535.04	153.10	-10.93	-4.51
1535.00	153.15	-11.11	-5.37
1534.97	153.20	-11.15	-7.24
1534.86	153.35	-10.47	-5.20
1534.82	153.40	-11.40	-4.79
1534.74	153.50	-11.06	-5.64
1534.71	153.55	-10.61	-5.79
1534.67	153.60	-10.31	-4.81
1534.63	153.65	-9.88	-6.79
1534.59	153.70	-9.43	-4.06
1534.56	153.75	-8.92	-4.74
1534.52	153.80	-8.95	-5.33
1534.48	153.85	-9.41	-6.25
1534.44	153.90	-9.77	-6.47
1534.41	153.95	-10.25	-5.93
1534.37	154.00	-10.56	-4.10
1534.33	154.05	-10.88	-5.59
1534.26	154.15	-11.13	-5.50
1534.22	154.20	-11.07	-5.32
1534.18	154.25	-10.41	-5.04
1534.10	154.35	-9.63	-5.25
1534.07	154.40	-8.91	-4.74
1534.03	154.45	-8.48	-4.30
1533.99	154.50	-8.77	-6.49
1533.95	154.55	-9.19	-6.39
1533.91	154.60	-9.35	-4.45
1533.88	154.65	-9.87	-5.50
1533.84	154.70	-10.13	-6.26
1533.80	154.75	-10.62	-5.02
1533.76	154.80	-10.79	-6.59
1533.72	154.85	-11.02	-5.31
1533.69	154.90	-11.04	-5.19
1533.65	154.95	-11.15	-5.27
1533.61	155.00	-10.83	-4.79
1533.57	155.05	-10.41	-3.93
1533.53	155.10	-10.05	-5.25
1533.49	155.15	-9.86	-4.63
1533.45	155.20	-9.90	-5.98
1533.42	155.25	-9.63	-4.73
1533.38	155.30	-9.18	-4.85
1533.34	155.35	-9.00	-4.01
1533.30	155.40	-9.07	-4.50
1533.26	155.45	-9.31	-4.31
1533.22	155.50	-9.76	-4.90
1533.18	155.55	-10.36	-4.48
1533.07	155.70	-11.25	-4.44
1533.03	155.75	-11.55	-4.79
1532.99	155.80	-11.73	-5.05
1532.91	155.90	-11.50	-5.87
1532.87	155.95	-11.68	-5.71
1532.83	156.00	-10.79	-5.96
1532.79	156.05	-10.07	-4.14

Year A.D.	Depth from top (mm)	$\delta^{13}C$ (‰ VPDB)	$\delta^{18}O$ (‰ VPDB)
1532.75	156.10	-10.18	-4.38
1532.71	156.15	-10.08	-4.08
1532.67	156.20	-9.52	-4.45
1532.64	156.25	-9.81	-5.02
1532.60	156.30	-10.06	-4.05
1532.56	156.35	-10.01	-4.54
1532.52	156.40	-10.32	-5.48
1532.48	156.45	-10.70	-3.92
1532.44	156.50	-10.86	-3.57
1532.40	156.55	-11.00	-4.64
1532.36	156.60	-11.39	-6.24
1532.32	156.65	-11.36	-5.43
1532.28	156.70	-11.82	-5.06
1532.24	156.75	-11.64	-3.92
1532.20	156.80	-11.70	-7.36
1532.16	156.85	-11.60	-4.38
1532.12	156.90	-11.66	-5.45
1532.08	156.95	-11.78	-5.64
1532.04	157.00	-11.45	-4.85
1532.00	157.05	-11.48	-4.96
1531.96	157.10	-11.52	-4.17
1531.92	157.15	-11.40	-6.66
1531.88	157.20	-11.10	-5.13
1531.84	157.25	-10.79	-5.05
1531.75	157.35	-10.66	-5.04
1531.71	157.40	-10.21	-4.27
1531.67	157.45	-10.15	-4.79
1531.63	157.50	-10.28	-3.84
1531.59	157.55	-10.54	-3.81
1531.55	157.60	-10.82	-4.36
1531.47	157.70	-11.48	-4.71
1531.43	157.75	-11.53	-4.72
1531.39	157.80	-11.47	-4.60
1531.35	157.85	-10.99	-4.46
1531.31	157.90	-10.50	-4.43
1531.26	157.95	-9.66	-4.03
1531.22	158.00	-8.73	-3.23
1531.18	158.05	-8.68	-4.22
1531.14	158.10	-9.31	-4.12
1531.10	158.15	-9.92	-5.06
1531.06	158.20	-10.19	-5.20
1531.02	158.25	-10.08	-4.21
1530.97	158.30	-10.25	-4.37
1530.93	158.35	-10.04	-4.61
1530.89	158.40	-9.98	-5.21
1530.85	158.45	-9.77	-4.10
1530.81	158.50	-10.03	-4.19
1530.77	158.55	-9.99	-7.29
1530.72	158.60	-9.97	-4.96
1530.68	158.65	-10.11	-4.71
1530.64	158.70	-10.40	-6.15
1530.60	158.75	-10.38	-5.78
1530.56	158.80	-10.48	-6.52
1530.51	158.85	-10.53	-5.42
1530.47	158.90	-10.69	-4.56
1530.43	158.95	-11.05	-4.65
1530.39	159.00	-11.30	-4.69
1530.34	159.05	-11.69	-4.39
1530.26	159.15	-11.45	-5.50
1530.22	159.20	-11.20	-5.39
1530.17	159.25	-10.88	-5.70
1530.13	159.30	-10.01	-6.06
1530.09	159.35	-9.46	-4.38
1530.05	159.40	-9.24	-5.65
1530.00	159.45	-9.38	-5.27
1529.96	159.50	-9.94	-4.68
1529.92	159.55	-10.37	-4.76
1529.87	159.60	-10.63	-4.51
1529.83	159.65	-11.06	-4.88
1529.79	159.70	-11.19	-4.90
1529.74	159.75	-11.37	-5.47
1529.70	159.80	-11.53	-6.51
1529.66	159.85	-12.03	-6.02
1529.61	159.90	-11.32	-5.12
1529.57	159.95	-10.09	-4.93
1529.53	160.00	-9.97	-4.97
1529.48	160.05	-9.14	-5.22
1529.40	160.15	-10.38	-6.88
1529.35	160.20	-10.97	-6.87
1529.31	160.25	-11.02	-5.34
1529.27	160.30	-11.57	-5.29
1529.22	160.35	-11.52	-5.26
1529.18	160.40	-11.55	-5.35
1529.13	160.45	-10.90	-5.81
1529.09	160.50	-10.79	-7.33
1529.04	160.55	-11.04	-7.32
1529.00	160.60	-9.86	-4.78
1528.96	160.65	-9.41	-5.60

Year A.D.	Depth from top (mm)	$\delta^{13}C$ (‰ VPDB)	$\delta^{18}O$ (‰ VPDB)
1528.91	160.70	-9.53	-5.91
1528.87	160.75	-9.85	-5.41
1528.82	160.80	-10.14	-4.66
1528.78	160.85	-10.35	-4.52
1528.73	160.90	-10.82	-4.76
1528.69	160.95	-10.71	-4.50
1528.64	161.00	-10.33	-4.53
1528.60	161.05	-10.05	-6.52
1528.55	161.10	-9.52	-4.45
1528.51	161.15	-9.81	-4.78
1528.46	161.20	-9.36	-4.86
1528.42	161.25	-8.92	-4.26
1528.37	161.30	-9.26	-5.08
1528.33	161.35	-9.10	-4.37
1528.28	161.40	-9.52	-4.60
1528.24	161.45	-9.30	-4.84
1528.19	161.50	-9.19	-4.35
1528.15	161.55	-9.10	-3.30
1528.10	161.60	-8.81	-3.57
1528.06	161.65	-7.96	-6.94
1528.01	161.70	-7.77	-3.84
1527.96	161.75	-8.15	-4.32
1527.92	161.80	-9.01	-4.81
1527.87	161.85	-9.44	-3.90
1527.83	161.90	-9.77	-4.85
1527.78	161.95	-10.00	-3.70
1527.73	162.00	-9.91	-5.09
1527.69	162.05	-9.60	-4.68
1527.64	162.10	-9.87	-4.50
1527.59	162.15	-9.61	-5.50
1527.55	162.20	-9.36	-6.99
1527.50	162.25	-9.19	-5.06
1527.45	162.30	-8.57	-3.48
1527.41	162.35	-8.41	-5.45
1527.36	162.40	-8.19	-3.98
1527.31	162.45	-8.41	-3.42
1527.27	162.50	-8.73	-5.31
1527.17	162.60	-9.29	-5.49
1527.13	162.65	-9.41	-4.24
1527.08	162.70	-9.91	-4.99
1527.03	162.75	-10.07	-3.94
1526.98	162.80	-10.43	-5.54
1526.94	162.85	-10.34	-5.14
1526.89	162.90	-10.47	-5.53
1526.84	162.95	-10.48	-5.01
1526.79	163.00	-10.25	-5.11
1526.75	163.05	-10.35	-4.50
1526.70	163.10	-10.25	-7.55
1526.65	163.15	-9.86	-4.68
1526.60	163.20	-9.98	-5.30
1526.56	163.25	-10.06	-4.38
1526.51	163.30	-10.46	-4.35
1526.46	163.35	-10.60	-4.39
1526.41	163.40	-10.74	-4.93
1526.36	163.45	-10.91	-4.34
1526.31	163.50	-11.16	-4.40
1526.27	163.55	-11.38	-4.77
1526.22	163.60	-11.26	-3.98
1526.17	163.65	-11.06	-6.14
1526.12	163.70	-11.07	-4.65
1526.07	163.75	-10.05	-5.01
1526.02	163.80	-10.24	-4.70
1525.97	163.85	-9.98	-4.82
1525.92	163.90	-10.27	-4.53
1525.87	163.95	-10.54	-5.03
1525.83	164.00	-10.83	-5.31
1525.78	164.05	-11.24	-4.76
1525.73	164.10	-11.75	-4.06
1525.68	164.15	-11.80	-4.41
1525.63	164.20	-11.95	-6.35
1525.58	164.25	-11.85	-5.48
1525.53	164.30	-11.68	-4.66
1525.48	164.35	-11.48	-5.78
1525.43	164.40	-10.13	-4.51
1525.38	164.45	-9.87	-4.55
1525.33	164.50	-9.18	-4.04
1525.23	164.60	-9.85	-3.55
1525.13	164.70	-10.40	-3.82
1525.08	164.75	-10.68	-3.90
1525.03	164.80	-10.91	-6.80
1524.98	164.85	-11.17	-4.67
1524.93	164.90	-11.18	-4.08
1524.88	164.95	-11.22	-3.72
1524.82	165.00	-11.16	-3.31
1524.77	165.05	-11.28	-5.14
1524.66	165.15	-11.38	-6.86
1524.61	165.20	-11.47	-4.59
1524.55	165.25	-11.21	-3.80

Year A.D.	Depth from top (mm)	$\delta^{13}C$ (‰ VPDB)	$\delta^{18}O$ (‰ VPDB)
1524.37	165.40	-10.18	-5.09
1524.17	165.55	-10.66	-4.39
1524.10	165.60	-10.99	-6.15
1523.88	165.75	-11.53	-3.77
1523.81	165.80	-11.60	-4.27
1523.73	165.85	-11.59	-3.79
1523.65	165.90	-11.35	-4.19
1523.57	165.95	-11.44	-5.30
1523.49	166.00	-10.72	-3.92
1523.41	166.05	-10.18	-5.52
1523.33	166.10	-9.52	-3.85
1523.24	166.15	-9.24	-4.92
1523.15	166.20	-9.31	-4.89
1523.07	166.25	-9.91	-4.95
1522.98	166.30	-10.35	-3.43
1522.89	166.35	-10.94	-4.34
1522.80	166.40	-11.27	-4.55
1522.70	166.45	-11.38	-4.14
1522.61	166.50	-10.45	-4.53
1522.51	166.55	-10.06	-4.16
1522.42	166.60	-9.91	-3.97
1522.32	166.65	-9.88	-5.90
1522.22	166.70	-10.06	-4.14
1522.12	166.75	-10.25	-3.79
1522.02	166.80	-10.55	-4.28
1521.91	166.85	-10.52	-5.11
1521.81	166.90	-10.76	-4.33
1521.71	166.95	-10.87	-4.71
1521.60	167.00	-10.85	-6.09
1521.49	167.05	-11.22	-5.20
1521.39	167.10	-11.34	-3.87
1521.28	167.15	-11.22	-9.87
1521.17	167.20	-11.17	-4.31
1521.05	167.25	-11.09	-5.35
1520.94	167.30	-10.55	-3.85
1520.83	167.35	-10.29	-5.24
1520.60	167.45	-9.65	-4.42
1520.48	167.50	-9.62	-4.32
1520.36	167.55	-9.40	-4.11
1520.25	167.60	-9.62	-4.24
1520.13	167.65	-9.78	-3.81
1520.01	167.70	-10.53	-4.66
1519.89	167.75	-10.68	-5.24
1519.76	167.80	-10.86	-4.43
1519.64	167.85	-11.10	-3.93
1519.39	167.95	-11.25	-4.18
1519.27	168.00	-11.31	-5.02
1519.14	168.05	-11.39	-3.66
1519.01	168.10	-11.38	-5.87
1518.89	168.15	-11.54	-4.28
1518.76	168.20	-11.53	-4.34
1518.63	168.25	-11.46	-4.04
1518.50	168.30	-11.61	-5.80
1518.37	168.35	-11.51	-3.78
1518.24	168.40	-11.71	-4.55
1518.10	168.45	-11.59	-4.97
1517.97	168.50	-11.56	-5.97
1517.84	168.55	-11.24	-4.79
1517.70	168.60	-11.14	-4.52
1517.57	168.65	-10.76	-5.53
1517.30	168.75	-11.16	-6.49
1517.02	168.85	-10.96	-7.04
1516.88	168.90	-10.95	-3.61
1516.74	168.95	-11.36	-4.61
1516.61	169.00	-11.50	-5.29
1516.47	169.05	-11.58	-4.37
1516.33	169.10	-11.81	-4.22
1516.19	169.15	-11.84	-4.32
1516.04	169.20	-11.72	-4.66
1515.90	169.25	-11.84	-4.66
1515.76	169.30	-11.93	-4.82
1515.62	169.35	-12.02	-4.84
1515.47	169.40	-11.80	-5.71
1515.33	169.45	-11.69	-4.36
1515.19	169.50	-11.78	-5.14
1515.04	169.55	-11.30	-5.27
1514.90	169.60	-10.97	-5.47
1514.75	169.65	-11.24	-6.64
1514.61	169.70	-10.42	-6.88
1514.46	169.75	-10.00	-5.25
1514.32	169.80	-10.83	-5.77
1514.17	169.85	-10.17	-3.88
1514.02	169.90	-10.43	-4.02
1513.88	169.95	-10.47	-4.20
1513.73	170.00	-10.99	-4.52
1513.58	170.05	-10.90	-4.42
1513.44	170.10	-11.10	-4.57
1513.29	170.15	-11.28	-4.03

Year A.D.	Depth from top (mm)	$\delta^{13}C$ (‰ VPDB)	$\delta^{18}O$ (‰ VPDB)
1513.14	170.20	-11.75	-4.59
1512.99	170.25	-11.53	-5.00
1512.84	170.30	-11.85	-4.73
1512.69	170.35	-11.99	-4.48
1512.55	170.40	-12.03	-4.94
1512.40	170.45	-12.04	-4.73
1512.25	170.50	-11.96	-4.46
1512.10	170.55	-11.55	-6.27
1511.95	170.60	-11.05	-4.15
1511.80	170.65	-11.37	-5.43
1511.65	170.70	-10.76	-5.11
1511.50	170.75	-10.21	-4.00
1511.35	170.80	-10.21	-4.08
1511.20	170.85	-10.27	-4.36
1511.05	170.90	-10.52	-4.70
1510.90	170.95	-10.92	-4.41
1510.75	171.00	-10.66	-4.21
1510.61	171.05	-11.26	-5.32
1510.46	171.10	-11.54	-6.16
1510.31	171.15	-11.99	-5.65
1510.16	171.20	-12.13	-4.50
1510.01	171.25	-12.00	-6.32
1509.86	171.30	-11.93	-4.96
1509.71	171.35	-11.90	-5.92
1509.56	171.40	-11.91	-5.60
1509.41	171.45	-11.35	-4.23
1509.27	171.50	-11.08	-4.17
1509.12	171.55	-12.04	-4.53
1508.97	171.60	-11.97	-5.08
1508.82	171.65	-11.79	-4.45
1508.67	171.70	-11.27	-5.40
1508.53	171.75	-11.35	-4.92
1508.09	171.90	-11.61	-4.53
1507.94	171.95	-11.20	-4.65
1507.79	172.00	-11.12	-5.74
1507.65	172.05	-10.96	-4.49
1507.50	172.10	-10.70	-5.73
1507.36	172.15	-10.48	-8.80
1507.21	172.20	-10.34	-5.47
1507.07	172.25	-10.10	-5.93
1506.93	172.30	-9.96	-5.09
1506.78	172.35	-10.21	-4.15
1506.64	172.40	-10.50	-4.31
1506.50	172.45	-10.85	-4.23
1506.36	172.50	-11.15	-5.74
1506.21	172.55	-11.27	-5.61
1506.07	172.60	-11.30	-4.65
1505.93	172.65	-11.74	-7.07
1505.79	172.70	-11.25	-4.70
1505.65	172.75	-10.83	-4.57
1505.51	172.80	-10.48	-4.43
1505.38	172.85	-10.31	-5.23
1505.24	172.90	-9.77	-4.92
1505.10	172.95	-9.82	-5.10
1504.96	173.00	-9.57	-4.59
1504.83	173.05	-11.09	-4.91
1504.69	173.10	-11.11	-7.40
1504.56	173.15	-11.51	-5.61
1504.42	173.20	-11.42	-4.81
1504.29	173.25	-11.25	-5.09
1504.16	173.30	-10.84	-4.78
1504.02	173.35	-10.25	-4.96
1503.89	173.40	-10.20	-4.16
1503.63	173.50	-10.13	-3.92
1503.50	173.55	-10.95	-5.37
1503.37	173.60	-11.16	-5.12
1503.25	173.65	-11.06	-4.54
1503.12	173.70	-10.98	-5.35
1502.99	173.75	-10.91	-4.93
1502.87	173.80	-10.87	-7.50
1502.74	173.85	-11.07	-7.72
1502.62	173.90	-9.82	-4.66
1502.50	173.95	-11.08	-4.37
1502.38	174.00	-11.00	-5.01
1502.25	174.05	-11.11	-4.16
1502.13	174.10	-11.22	-4.80
1501.99	174.15	-11.20	-4.42
1501.86	174.20	-11.30	-4.40
1501.58	174.30	-11.37	-6.19
1501.44	174.35	-11.22	-4.74
1501.14	174.45	-11.18	-4.49
1500.66	174.60	-11.22	-5.34
1500.33	174.70	-10.81	-4.25
1500.16	174.75	-10.72	-4.41
1499.98	174.80	-10.48	-4.07
1499.80	174.85	-10.49	-5.19
1499.62	174.90	-10.65	-3.75
1499.44	174.95	-10.71	-4.48

Year A.D.	Depth from top (mm)	$\delta^{13}C$ (‰ VPDB)	$\delta^{18}O$ (‰ VPDB)
1499.25	175.00	-10.52	-5.88
1499.06	175.05	-10.25	-4.51
1498.87	175.10	-9.81	-4.79
1498.68	175.15	-9.82	-5.52
1498.28	175.25	-8.75	-3.77
1498.07	175.30	-9.08	-5.12
1497.66	175.40	-9.80	-4.37
1497.45	175.45	-10.00	-4.38
1497.23	175.50	-10.45	-5.45
1497.02	175.55	-10.57	-5.22
1496.80	175.60	-9.96	-4.42
1496.35	175.70	-9.93	-4.08
1496.13	175.75	-9.90	-5.62
1495.90	175.80	-9.98	-4.71
1495.67	175.85	-10.36	-5.35
1495.43	175.90	-10.83	-4.38
1495.20	175.95	-11.45	-5.07
1494.96	176.00	-9.68	-5.94
1494.72	176.05	-12.09	-5.50
1494.48	176.10	-11.92	-5.70
1494.24	176.15	-12.23	-5.59
1493.99	176.20	-12.78	-6.11
1493.75	176.25	-12.33	-5.81
1493.50	176.30	-11.67	-4.71
1493.25	176.35	-11.03	-4.91
1492.48	176.50	-10.73	-5.93
1492.22	176.55	-10.44	-4.53
1491.97	176.60	-10.34	-4.76
1491.70	176.65	-10.22	-5.33
1491.44	176.70	-9.91	-5.83
1491.18	176.75	-10.17	-5.05
1490.91	176.80	-10.46	-5.51
1490.38	176.90	-10.47	-5.21
1490.11	176.95	-11.37	-6.23
1489.56	177.05	-11.61	-5.48
1489.29	177.10	-11.41	-5.23
1489.02	177.15	-11.38	-5.13
1488.74	177.20	-11.05	-6.15
1488.46	177.25	-10.79	-5.50
1488.19	177.30	-10.55	-5.71
1487.91	177.35	-10.49	-6.64
1487.63	177.40	-10.60	-5.31
1487.35	177.45	-10.40	-4.93
1487.06	177.50	-10.65	-3.80
1486.78	177.55	-10.54	-4.80
1486.50	177.60	-10.67	-7.89
1486.22	177.65	-10.59	-4.51
1485.93	177.70	-10.65	-4.04
1485.65	177.75	-10.33	-6.25
1485.36	177.80	-10.16	-4.85
1485.07	177.85	-9.99	-4.95
1484.79	177.90	-9.99	-6.13
1484.50	177.95	-9.88	-5.37
1484.21	178.00	-10.06	-5.17
1483.92	178.05	-10.18	-5.62
1483.63	178.10	-10.37	-4.81
1483.34	178.15	-10.70	-4.59
1482.76	178.25	-10.84	-4.36
1482.47	178.30	-11.37	-4.63
1482.18	178.35	-11.48	-5.54
1481.89	178.40	-11.33	-4.06
1481.60	178.45	-11.51	-4.74
1481.31	178.50	-11.42	-4.90
1481.02	178.55	-11.49	-6.24
1480.73	178.60	-11.14	-4.99
1480.44	178.65	-10.74	-5.04
1480.15	178.70	-10.55	-4.95
1479.86	178.75	-10.33	-4.89
1479.57	178.80	-10.34	-4.92
1479.28	178.85	-10.64	-5.54
1478.99	178.90	-10.67	-5.38
1478.71	178.95	-10.64	-5.56
1478.42	179.00	-11.03	-5.11
1478.13	179.05	-10.85	-5.34
1477.83	179.10	-10.87	-4.99
1477.54	179.15	-10.60	-5.25
1477.24	179.20	-10.66	-6.12
1476.93	179.25	-10.55	-4.54
1476.63	179.30	-10.65	-4.99
1476.32	179.35	-10.81	-4.83
1476.00	179.40	-10.59	-5.92
1475.69	179.45	-10.41	-5.47
1475.37	179.50	-10.35	-6.08
1475.04	179.55	-10.36	-5.86
1474.72	179.60	-10.67	-6.89
1474.39	179.65	-10.96	-4.66
1474.05	179.70	-11.24	-4.65
1473.72	179.75	-11.36	-4.70

Year A.D.	Depth from top (mm)	$\delta^{13}C$ (‰ VPDB)	$\delta^{18}O$ (‰ VPDB)
1473.38	179.80	-11.70	-5.05
1473.03	179.85	-11.72	-4.78
1472.69	179.90	-11.84	-5.96
1472.34	179.95	-12.07	-4.34
1471.98	180.00	-11.98	-4.51
1471.63	180.05	-11.92	-6.46
1471.27	180.10	-11.89	-4.69
1470.90	180.15	-11.80	-4.60
1470.54	180.20	-11.50	-4.86
1470.17	180.25	-11.06	-5.11
1469.80	180.30	-10.83	-3.79
1469.42	180.35	-10.76	-4.65
1469.04	180.40	-10.73	-3.78
1468.66	180.45	-10.63	-4.07
1468.27	180.50	-11.10	-3.73
1467.88	180.55	-11.48	-4.64
1467.49	180.60	-11.48	-4.74
1467.10	180.65	-11.52	-4.64
1466.70	180.70	-11.50	-4.41
1466.30	180.75	-11.76	-4.84
1465.89	180.80	-11.58	-4.12
1465.49	180.85	-11.55	-4.32
1465.08	180.90	-11.66	-5.53
1464.66	180.95	-11.38	-4.45
1464.25	181.00	-10.74	-4.53
1463.83	181.05	-10.31	-5.40
1463.40	181.10	-10.26	-4.32
1462.98	181.15	-10.00	-3.90
1462.55	181.20	-10.36	-3.91
1462.12	181.25	-10.55	-3.70
1461.68	181.30	-11.08	-5.52
1461.24	181.35	-11.04	-4.44
1460.80	181.40	-10.94	-4.13
1460.36	181.45	-11.30	-4.52
1459.91	181.50	-11.08	-4.21
1459.46	181.55	-11.13	-5.21
1459.01	181.60	-11.41	-5.06
1458.55	181.65	-11.14	-4.80
1458.09	181.70	-10.51	-4.50
1457.63	181.75	-10.58	-5.42
1457.17	181.80	-10.68	-3.95
1456.70	181.85	-10.74	-6.87
1456.23	181.90	-10.57	-4.14
1455.75	181.95	-10.44	-5.69
1455.28	182.00	-10.28	-3.79
1454.80	182.05	-10.23	-4.31
1454.31	182.10	-10.22	-4.67
1453.83	182.15	-10.13	-3.99
1453.34	182.20	-10.18	-4.75
1452.85	182.25	-10.23	-4.09
1452.35	182.30	-10.33	-7.59
1451.86	182.35	-10.46	-4.07
1451.36	182.40	-10.79	-4.93
1450.85	182.45	-10.96	-6.44
1450.35	182.50	-11.16	-5.28
1449.84	182.55	-10.96	-4.39
1449.33	182.60	-10.75	-4.72
1448.81	182.65	-10.36	-4.57
1448.29	182.70	-9.98	-7.22
1447.77	182.75	-9.65	-4.67
1447.25	182.80	-9.48	-4.30
1446.73	182.85	-9.26	-5.00
1446.20	182.90	-9.18	-4.68
1445.67	182.95	-9.21	-4.11
1445.13	183.00	-9.42	-4.72
1444.60	183.05	-9.29	-3.69
1444.06	183.10	-9.50	-5.01
1443.51	183.15	-9.84	-6.03
1442.97	183.20	-10.09	-3.74
1442.42	183.25	-10.37	-4.55
1441.87	183.30	-10.49	-4.49
1441.32	183.35	-10.65	-3.61
1440.20	183.45	-10.79	-4.21
1439.64	183.50	-10.63	-3.63
1439.08	183.55	-10.05	-5.47
1438.51	183.60	-9.61	-3.49
1437.94	183.65	-9.88	-4.26
1437.37	183.70	-10.17	-5.19
1436.22	183.80	-9.88	-4.84
1435.64	183.85	-9.64	-3.43
1435.05	183.90	-9.73	-6.39
1434.47	183.95	-9.64	-4.46
1433.88	184.00	-9.72	-4.23
1433.29	184.05	-9.24	-3.87
1432.69	184.10	-9.37	-4.82
1432.10	184.15	-9.38	-4.62
1431.50	184.20	-9.24	-5.29
1430.90	184.25	-9.44	-4.34

Year A.D.	Depth from top (mm)	$\delta^{13}C$ (‰ VPDB)	$\delta^{18}O$ (‰ VPDB)
1430.30	184.30	-9.32	-4.44
1429.69	184.35	-9.84	-4.25
1429.08	184.40	-10.71	-4.61
1428.47	184.45	-11.15	-5.00
1427.86	184.50	-10.81	-4.12
1426.00	184.65	-9.80	-3.90
1425.37	184.70	-9.96	-4.05
1424.75	184.75	-10.00	-5.19
1424.12	184.80	-10.02	-3.63
1423.49	184.85	-10.38	-5.30
1422.85	184.90	-10.51	-4.41
1422.22	184.95	-10.64	-5.39
1421.58	185.00	-10.97	-4.22
1420.94	185.05	-10.45	-5.42
1420.29	185.10	-10.21	-4.45
1419.65	185.15	-10.21	-5.51
1419.00	185.20	-10.31	-4.43
1418.35	185.25	-10.49	-5.13
1417.69	185.30	-10.42	-5.15
1417.04	185.35	-10.40	-4.54
1416.38	185.40	-10.43	-4.86
1415.72	185.45	-10.46	-6.44
1415.06	185.50	-10.86	-4.21
1414.39	185.55	-10.78	-7.19
1413.72	185.60	-10.86	-4.53
1413.05	185.65	-11.02	-5.22
1412.38	185.70	-11.61	-5.55
1411.71	185.75	-11.64	-4.65
1411.03	185.80	-11.28	-6.09
1410.35	185.85	-11.23	-6.11
1409.67	185.90	-11.35	-5.83
1408.98	185.95	-11.37	-4.78
1408.30	186.00	-11.05	-5.80
1407.61	186.05	-11.11	-4.21
1406.92	186.10	-11.00	-4.63
1406.22	186.15	-10.99	-4.68
1405.53	186.20	-10.66	-3.95
1404.83	186.25	-10.54	-4.23
1404.13	186.30	-10.59	-4.30
1403.43	186.35	-10.47	-5.10
1402.72	186.40	-10.62	-6.32
1402.01	186.45	-10.70	-4.09
1401.30	186.50	-10.82	-4.08
1400.59	186.55	-11.03	-4.62
1399.88	186.60	-11.09	-4.27
1399.16	186.65	-10.97	-4.55
1398.45	186.70	-10.84	-4.46
1397.73	186.75	-10.55	-4.45
1397.00	186.80	-10.22	-3.98
1396.28	186.85	-9.84	-3.56
1395.55	186.90	-9.86	-4.46
1394.82	186.95	-10.17	-3.84
1394.09	187.00	-10.34	-3.62
1393.36	187.05	-10.54	-4.31
1392.62	187.10	-10.46	-5.20
1391.89	187.15	-10.92	-4.22
1391.15	187.20	-10.76	-4.49
1390.40	187.25	-10.37	-5.13
1389.66	187.30	-9.95	-4.72
1388.92	187.35	-9.75	-4.65
1388.17	187.40	-9.65	-4.30
1387.42	187.45	-9.70	-4.83
1386.67	187.50	-10.66	-3.88
1385.91	187.55	-10.80	-6.39
1385.15	187.60	-10.45	-5.38
1384.40	187.65	-10.42	-4.46
1383.64	187.70	-10.18	-4.56
1381.34	187.85	-10.07	-4.20
1380.57	187.90	-10.34	-4.72
1379.80	187.95	-10.61	-4.51
1379.03	188.00	-10.93	-5.04
1378.26	188.05	-11.31	-4.06
1377.48	188.10	-11.01	-3.97
1376.70	188.15	-11.27	-4.31
1375.92	188.20	-11.70	-4.52
1375.14	188.25	-11.64	-6.58
1374.36	188.30	-11.39	-4.41
1373.57	188.35	-10.79	-4.51
1372.78	188.40	-10.73	-4.39
1371.99	188.45	-10.87	-4.04
1371.20	188.50	-10.74	-4.57
1370.41	188.55	-10.35	-4.91
1369.61	188.60	-10.39	-4.22
1368.81	188.65	-10.71	-4.34
1368.01	188.70	-11.17	-5.03
1367.21	188.75	-11.09	-4.67
1366.41	188.80	-11.18	-4.48
1365.60	188.85	-10.59	-3.92

Year A.D.	Depth from top (mm)	$\delta^{13}C$ (‰ VPDB)	$\delta^{18}O$ (‰ VPDB)
1364.80	188.90	-10.65	-5.25
1363.99	188.95	-10.04	-5.44
1363.18	189.00	-10.82	-5.04
1362.37	189.05	-10.29	-3.95
1361.55	189.10	-9.86	-5.33
1360.73	189.15	-10.09	-3.96
1359.92	189.20	-10.28	-4.06
1359.10	189.25	-10.05	-4.98
1358.28	189.30	-9.82	-4.71
1357.45	189.35	-9.99	-3.79
1356.63	189.40	-10.29	-4.33
1355.80	189.45	-10.34	-3.72
1354.97	189.50	-10.15	-3.65
1354.14	189.55	-9.86	-5.16
1353.31	189.60	-9.92	-4.20
1352.48	189.65	-9.97	-4.62
1351.64	189.70	-9.98	-5.12
1350.80	189.75	-9.73	-5.39
1349.97	189.80	-10.01	-4.20
1349.12	189.85	-9.59	-3.45
1348.28	189.90	-9.97	-4.33
1347.44	189.95	-9.63	-3.60
1346.59	190.00	-9.66	-5.13
1345.75	190.05	-9.73	-4.26
1344.90	190.10	-10.09	-3.67
1344.05	190.15	-9.93	-4.41
1343.19	190.20	-10.12	-5.89
1342.34	190.25	-10.03	-4.10
1341.48	190.30	-10.33	-5.40
1340.63	190.35	-10.81	-5.38
1339.77	190.40	-10.69	-4.58
1338.91	190.45	-11.02	-6.16
1338.05	190.50	-10.91	-5.63
1337.18	190.55	-10.70	-4.21
1336.32	190.60	-10.08	-4.21
1335.45	190.65	-9.91	-4.72
1334.58	190.70	-10.20	-4.17
1333.71	190.75	-10.44	-5.67
1332.84	190.80	-10.69	-5.27
1331.97	190.85	-10.68	-5.91
1330.22	190.95	-10.53	-5.09
1329.34	191.00	-10.33	-5.56
1328.46	191.05	-10.15	-4.21
1327.58	191.10	-10.04	-4.19
1326.70	191.15	-10.02	-5.21
1325.82	191.20	-10.22	-5.66
1324.93	191.25	-10.37	-5.06
1324.04	191.30	-10.58	-5.42
1323.16	191.35	-10.90	-4.66
1322.27	191.40	-11.08	-6.58
1321.38	191.45	-11.23	-4.97
1320.48	191.50	-11.36	-5.02
1319.59	191.55	-11.41	-5.29
1318.70	191.60	-11.18	-5.70
1317.80	191.65	-10.97	-5.07
1316.90	191.70	-10.70	-4.34
1316.00	191.75	-10.51	-4.92
1315.10	191.80	-10.39	-4.59
1314.20	191.85	-10.48	-5.26
1313.30	191.90	-10.66	-4.70
1312.39	191.95	-10.86	-4.51

Appendix B

CT number data derived from stalagmite REF-07

Age (ka BP) - from 1950	Age Error (ka)	Depth from top (mm)	REF-07 mean CT numbers >1000 HU	REF-07 mean CT number st.dev.
2.975	0.082	0.0	2483	205
2.979	0.082	0.2	2862	111
2.983	0.081	0.4	2963	59
2.987	0.081	0.6	2933	83
2.991	0.080	0.8	2854	107
2.995	0.080	1.0	2738	127
2.999	0.079	1.2	2615	136
3.002	0.079	1.4	2510	132
3.008	0.078	1.7	2427	116
3.012	0.078	1.9	2374	111
3.016	0.077	2.1	2322	136
3.020	0.077	2.3	2283	172
3.024	0.076	2.5	2264	201
3.028	0.076	2.7	2293	196
3.032	0.075	2.9	2333	176
3.036	0.075	3.1	2365	130
3.040	0.074	3.3	2382	101
3.044	0.074	3.5	2398	106
3.047	0.074	3.7	2431	140
3.051	0.073	3.9	2463	157
3.055	0.073	4.1	2503	161
3.059	0.072	4.3	2547	148
3.065	0.071	4.6	2613	114
3.069	0.071	4.8	2669	83
3.073	0.070	5.0	2701	70
3.077	0.070	5.2	2696	61
3.081	0.070	5.4	2678	62
3.085	0.069	5.6	2670	68
3.088	0.069	5.8	2676	58
3.092	0.068	6.0	2684	47
3.096	0.068	6.2	2681	57
3.100	0.067	6.4	2664	68
3.104	0.067	6.6	2646	67
3.108	0.066	6.8	2630	63
3.112	0.066	7.0	2617	58
3.116	0.065	7.2	2608	60
3.122	0.065	7.5	2601	67
3.126	0.064	7.7	2589	76
3.129	0.064	7.9	2556	78
3.133	0.063	8.1	2501	72
3.137	0.063	8.3	2436	70
3.141	0.062	8.5	2371	70
3.145	0.062	8.7	2315	73
3.149	0.062	8.9	2260	85

Age (ka BP) - from 1950	Age Error (ka)	Depth from top (mm)	REF-07 mean CT numbers >1000 HU	REF-07 mean CT number st.dev.
3.153	0.061	9.1	2207	99
3.157	0.061	9.3	2165	105
3.161	0.060	9.5	2137	96
3.165	0.060	9.7	2113	85
3.169	0.059	9.9	2102	100
3.172	0.059	10.1	2102	117
3.178	0.058	10.4	2116	125
3.182	0.058	10.6	2126	115
3.186	0.057	10.8	2123	108
3.190	0.057	11.0	2109	96
3.194	0.057	11.2	2095	71
3.198	0.056	11.4	2074	45
3.202	0.056	11.6	2040	67
3.206	0.055	11.8	1983	115
3.210	0.055	12.0	1933	153
3.213	0.054	12.2	1912	165
3.217	0.054	12.4	1926	144
3.221	0.054	12.6	1959	117
3.225	0.053	12.8	1999	98
3.229	0.053	13.0	2040	96
3.233	0.052	13.2	2074	101
3.239	0.052	13.5	2063	88
3.243	0.051	13.7	2016	88
3.247	0.051	13.9	1932	126
3.251	0.051	14.1	1882	165
3.254	0.050	14.3	1881	201
3.258	0.050	14.5	1950	222
3.262	0.049	14.7	2063	217
3.266	0.049	14.9	2165	205
3.270	0.049	15.1	2241	168
3.274	0.048	15.3	2265	135
3.278	0.048	15.5	2260	121
3.282	0.048	15.7	2233	132
3.286	0.047	15.9	2205	159
3.290	0.047	16.1	2192	164
3.296	0.046	16.4	2194	157
3.299	0.046	16.6	2213	130
3.303	0.046	16.8	2240	114
3.307	0.045	17.0	2260	138
3.311	0.045	17.2	2248	183
3.315	0.044	17.4	2191	204
3.319	0.044	17.6	2112	256
3.323	0.044	17.8	2020	293
3.327	0.043	18.0	1941	278

Age (ka BP) - from 1950	Age Error (ka)	Depth from top (mm)	REF-07 mean CT numbers >1000 HU	REF-07 mean CT number st.dev.
3.331	0.043	18.2	1892	254
3.335	0.043	18.4	1881	249
3.338	0.042	18.6	1906	277
3.342	0.042	18.8	1940	290
3.346	0.042	19.0	1978	276
3.352	0.041	19.3	2014	222
3.356	0.041	19.5	2045	176
3.360	0.041	19.7	2063	141
3.364	0.040	19.9	2070	107
3.368	0.040	20.1	2070	100
3.372	0.040	20.3	2073	130
3.376	0.040	20.5	2069	154
3.380	0.039	20.7	2045	172
3.383	0.039	20.9	2007	193
3.387	0.039	21.1	1960	208
3.391	0.039	21.3	1930	227
3.395	0.038	21.5	1926	249
3.399	0.038	21.7	1949	273
3.403	0.038	21.9	2012	269
3.407	0.038	22.1	2091	238
3.413	0.037	22.4	2166	193
3.417	0.037	22.6	2210	149
3.421	0.037	22.8	2201	104
3.424	0.037	23.0	2162	102
3.428	0.036	23.2	2087	133
3.432	0.036	23.4	2010	165
3.436	0.036	23.6	1939	203
3.440	0.036	23.8	1894	251
3.444	0.036	24.0	1874	293
3.448	0.035	24.2	1885	298
3.452	0.035	24.4	1911	270
3.456	0.035	24.6	1981	227
3.460	0.035	24.8	2055	211
3.464	0.035	25.0	2122	204
3.469	0.035	25.3	2134	171
3.473	0.035	25.5	2091	167
3.477	0.034	25.7	2025	216
3.481	0.034	25.9	1950	300
3.485	0.034	26.1	1950	292
3.489	0.034	26.3	1929	334
3.493	0.034	26.5	1948	364
3.497	0.034	26.7	1962	394
3.501	0.034	26.9	2049	358
3.505	0.034	27.1	2149	303

Age (ka BP) - from 1950	Age Error (ka)	Depth from top (mm)	REF-07 mean CT numbers >1000 HU	REF-07 mean CT number st.dev.
3.508	0.034	27.3	2248	245
3.512	0.034	27.5	2308	206
3.516	0.034	27.7	2330	200
3.520	0.034	27.9	2300	225
3.526	0.034	28.2	2256	262
3.530	0.034	28.4	2216	294
3.534	0.034	28.6	2195	289
3.538	0.034	28.8	2202	244
3.542	0.034	29.0	2213	201
3.546	0.034	29.2	2238	165
3.549	0.034	29.4	2268	157
3.553	0.034	29.6	2300	175
3.557	0.034	29.8	2323	189
3.561	0.034	30.0	2331	164
3.565	0.034	30.2	2319	126
3.569	0.034	30.4	2293	111
3.573	0.034	30.6	2251	143
3.577	0.034	30.8	2214	183
3.583	0.035	31.1	2195	206
3.587	0.035	31.3	2214	184
3.590	0.035	31.5	2253	145
3.594	0.035	31.7	2291	125
3.598	0.035	31.9	2311	121
3.602	0.035	32.1	2315	117
3.606	0.035	32.3	2311	111
3.610	0.036	32.5	2294	93
3.614	0.036	32.7	2265	97
3.618	0.036	32.9	2219	129
3.622	0.036	33.1	2168	158
3.626	0.036	33.3	2116	193
3.630	0.037	33.5	2092	199
3.633	0.037	33.7	2072	196
3.637	0.037	33.9	2039	191
3.643	0.037	34.2	1981	206
3.647	0.038	34.4	1921	232
3.651	0.038	34.6	1887	235
3.655	0.038	34.8	1886	237
3.659	0.038	35.0	1901	257
3.663	0.039	35.2	1929	278
3.667	0.039	35.4	1926	255
3.671	0.039	35.6	1881	238
3.674	0.039	35.8	1790	259
3.678	0.040	36.0	1679	320
3.682	0.040	36.2	1594	362

Age (ka BP) - from 1950	Age Error (ka)	Depth from top (mm)	REF-07 mean CT numbers >1000 HU	REF-07 mean CT number st.dev.
3.684	0.039	36.4	1530	377
3.687	0.039	36.6	1503	361
3.689	0.039	36.8	1491	345
3.693	0.039	37.1	1484	343
3.696	0.038	37.3	1456	355
3.698	0.038	37.5	1450	358
3.701	0.038	37.7	1412	348
3.704	0.038	37.9	1409	318
3.706	0.038	38.1	1393	275
3.709	0.037	38.3	1420	254
3.711	0.037	38.5	1440	273
3.714	0.037	38.7	1426	294
3.716	0.037	38.9	1507	281
3.719	0.037	39.1	1577	281
3.722	0.036	39.3	1595	315
3.724	0.036	39.5	1625	303
3.727	0.036	39.7	1649	281
3.731	0.036	40.0	1685	249
3.733	0.035	40.2	1746	230
3.736	0.035	40.4	1814	218
3.738	0.035	40.6	1889	190
3.741	0.035	40.8	1963	176
3.744	0.035	41.0	2038	207
3.746	0.035	41.2	2112	244
3.749	0.034	41.4	2173	249
3.751	0.034	41.6	2214	235
3.754	0.034	41.8	2228	221
3.756	0.034	42.0	2224	221
3.759	0.034	42.2	2214	230
3.762	0.034	42.4	2203	255
3.764	0.033	42.6	2178	288
3.767	0.033	42.8	2144	320
3.771	0.033	43.1	2103	346
3.773	0.033	43.3	2071	372
3.776	0.033	43.5	2119	308
3.778	0.032	43.7	2126	308
3.781	0.032	43.9	2133	325
3.784	0.032	44.1	2147	349
3.786	0.032	44.3	2168	396
3.789	0.032	44.5	2200	430
3.791	0.032	44.7	2233	415
3.794	0.032	44.9	2247	367
3.796	0.031	45.1	2231	326
3.799	0.031	45.3	2132	362

Age (ka BP) - from 1950	Age Error (ka)	Depth from top (mm)	REF-07 mean CT numbers >1000 HU	REF-07 mean CT number st.dev.
3.802	0.031	45.5	2094	349
3.804	0.031	45.7	2037	378
3.808	0.031	46.0	1958	399
3.811	0.031	46.2	1879	423
3.813	0.031	46.4	1802	451
3.816	0.031	46.6	1744	476
3.818	0.030	46.8	1703	486
3.821	0.030	47.0	1676	493
3.824	0.030	47.2	1669	488
3.826	0.030	47.4	1698	459
3.829	0.030	47.6	1749	417
3.831	0.030	47.8	1820	359
3.834	0.030	48.0	1876	308
3.836	0.030	48.2	1912	285
3.839	0.030	48.4	1923	288
3.842	0.030	48.6	1923	288
3.845	0.029	48.9	1926	273
3.848	0.029	49.1	1940	252
3.851	0.029	49.3	1957	226
3.853	0.029	49.5	1984	257
3.856	0.029	49.7	2084	222
3.858	0.029	49.9	2143	225
3.861	0.029	50.1	2164	251
3.864	0.029	50.3	2147	301
3.866	0.029	50.5	2167	241
3.869	0.029	50.7	2106	273
3.871	0.029	50.9	2043	302
3.874	0.029	51.1	1985	331
3.876	0.029	51.3	1839	437
3.879	0.029	51.5	1866	380
3.883	0.029	51.8	1927	337
3.885	0.029	52.0	1838	374
3.888	0.029	52.2	1766	299
3.891	0.029	52.4	1670	206
3.893	0.029	52.6	1554	117
3.896	0.029	52.8	1432	118
3.898	0.029	53.0	1332	168
3.901	0.029	53.2	1318	175
3.904	0.029	53.4	1304	165
3.906	0.029	53.6	1312	162
3.909	0.029	53.8	1322	195
3.911	0.029	54.0	1345	235
3.914	0.029	54.2	1380	251
3.916	0.029	54.4	1403	262

Age (ka BP) - from 1950	Age Error (ka)	Depth from top (mm)	REF-07 mean CT numbers >1000 HU	REF-07 mean CT number st.dev.
3.919	0.029	54.6	1436	249
3.923	0.029	54.9	1425	235
3.925	0.029	55.1	1432	251
3.928	0.029	55.3	1431	275
3.931	0.029	55.5	1433	266
3.933	0.029	55.7	1424	249
3.936	0.029	55.9	1440	209
3.938	0.029	56.1	1452	178
3.941	0.029	56.3	1462	164
3.944	0.029	56.5	1472	170
3.946	0.029	56.7	1490	172
3.949	0.029	56.9	1508	173
3.951	0.029	57.1	1528	177
3.954	0.029	57.3	1535	188
3.956	0.029	57.5	1524	213
3.960	0.030	57.8	1494	243
3.963	0.030	58.0	1440	260
3.965	0.030	58.2	1417	227
3.968	0.030	58.4	1392	190
3.971	0.030	58.6	1406	164
3.973	0.030	58.8	1464	178
3.976	0.030	59.0	1540	204
3.978	0.030	59.2	1554	234
3.981	0.030	59.4	1564	221
3.984	0.030	59.6	1559	212
3.986	0.031	59.8	1600	191
3.989	0.031	60.0	1630	182
3.991	0.031	60.2	1632	191
3.994	0.031	60.4	1619	192
3.998	0.031	60.7	1605	183
4.000	0.031	60.9	1613	172
4.003	0.031	61.1	1630	190
4.005	0.031	61.3	1644	230
4.008	0.032	61.5	1648	261
4.011	0.032	61.7	1648	288
4.013	0.032	61.9	1649	294
4.016	0.032	62.1	1652	300
4.018	0.032	62.3	1657	313
4.021	0.032	62.5	1656	327
4.024	0.032	62.7	1641	337
4.026	0.033	62.9	1611	340
4.029	0.033	63.1	1582	344
4.031	0.033	63.3	1566	345
4.034	0.033	63.5	1570	333

Age (ka BP) - from 1950	Age Error (ka)	Depth from top (mm)	REF-07 mean CT numbers >1000 HU	REF-07 mean CT number st.dev.
4.038	0.033	63.8	1580	319
4.040	0.034	64.0	1596	293
4.043	0.034	64.2	1615	281
4.045	0.034	64.4	1636	281
4.048	0.034	64.6	1641	299
4.051	0.034	64.8	1622	324
4.053	0.034	65.0	1601	362
4.056	0.035	65.2	1623	379
4.058	0.035	65.4	1655	375
4.061	0.035	65.6	1698	353
4.064	0.035	65.8	1749	321
4.066	0.035	66.0	1774	303
4.069	0.035	66.2	1764	321
4.071	0.036	66.4	1784	323
4.075	0.036	66.7	1764	363
4.078	0.036	66.9	1745	400
4.080	0.036	67.1	1726	427
4.083	0.037	67.3	1699	439
4.085	0.037	67.5	1672	437
4.088	0.037	67.7	1642	442
4.091	0.037	67.9	1627	427
4.093	0.037	68.1	1610	392
4.096	0.038	68.3	1586	369
4.098	0.038	68.5	1601	324
4.101	0.038	68.7	1587	290
4.104	0.038	68.9	1581	258
4.106	0.038	69.1	1604	251
4.109	0.039	69.3	1612	235
4.113	0.039	69.6	1618	217
4.115	0.039	69.8	1627	210
4.118	0.039	70.0	1643	219
4.120	0.039	70.2	1646	220
4.121	0.039	70.4	1644	231
4.122	0.039	70.6	1607	247
4.123	0.039	70.8	1621	247
4.124	0.039	71.0	1693	232
4.126	0.039	71.2	1785	213
4.127	0.039	71.4	1885	171
4.128	0.039	71.6	1982	126
4.129	0.038	71.8	2071	113
4.130	0.038	72.0	2130	118
4.132	0.038	72.2	2165	136
4.133	0.038	72.5	2174	193
4.135	0.038	72.7	2155	281

Age (ka BP) - from 1950	Age Error (ka)	Depth from top (mm)	REF-07 mean CT numbers >1000 HU	REF-07 mean CT number st.dev.
4.136	0.038	72.9	2117	366
4.137	0.038	73.1	2146	343
4.138	0.038	73.3	2130	356
4.139	0.037	73.5	2124	351
4.141	0.037	73.7	2111	346
4.142	0.037	73.9	2090	344
4.143	0.037	74.1	2070	335
4.144	0.037	74.3	2067	327
4.145	0.037	74.5	2084	323
4.147	0.037	74.7	2132	333
4.148	0.037	74.9	2199	361
4.149	0.037	75.1	2288	397
4.150	0.037	75.3	2382	377
4.152	0.036	75.6	2450	307
4.153	0.036	75.8	2480	208
4.154	0.036	76.0	2456	149
4.156	0.036	76.2	2402	163
4.157	0.036	76.4	2296	275
4.158	0.036	76.6	2275	234
4.159	0.036	76.8	2244	266
4.160	0.036	77.0	2195	302
4.162	0.036	77.2	2132	325
4.163	0.035	77.4	2047	333
4.164	0.035	77.6	1956	340
4.165	0.035	77.8	1862	332
4.166	0.035	78.0	1786	317
4.168	0.035	78.2	1737	277
4.169	0.035	78.5	1721	254
4.171	0.035	78.7	1738	250
4.172	0.035	78.9	1786	258
4.173	0.035	79.1	1841	269
4.174	0.035	79.3	1901	295
4.175	0.034	79.5	1936	322
4.177	0.034	79.7	1953	348
4.178	0.034	79.9	1954	353
4.179	0.034	80.1	1950	335
4.180	0.034	80.3	1944	305
4.181	0.034	80.5	1928	276
4.183	0.034	80.7	1903	260
4.184	0.034	80.9	1866	254
4.185	0.034	81.1	1841	266
4.187	0.034	81.4	1846	294
4.188	0.034	81.6	1900	297
4.189	0.034	81.8	1969	310

Age (ka BP) - from 1950	Age Error (ka)	Depth from top (mm)	REF-07 mean CT numbers >1000 HU	REF-07 mean CT number st.dev.
4.190	0.033	82.0	2022	301
4.192	0.033	82.2	2049	286
4.193	0.033	82.4	2056	263
4.194	0.033	82.6	2063	238
4.195	0.033	82.8	2054	246
4.196	0.033	83.0	2041	290
4.198	0.033	83.2	2085	233
4.199	0.033	83.4	2104	220
4.200	0.033	83.6	2124	222
4.201	0.033	83.8	2145	235
4.202	0.033	84.0	2150	230
4.204	0.033	84.2	2153	211
4.205	0.033	84.5	2095	297
4.207	0.033	84.7	2130	209
4.208	0.032	84.9	2156	200
4.209	0.032	85.1	2178	221
4.210	0.032	85.3	2194	233
4.211	0.032	85.5	2205	219
4.213	0.032	85.7	2208	194
4.214	0.032	85.9	2209	158
4.215	0.032	86.1	2206	136
4.216	0.032	86.3	2214	131
4.217	0.032	86.5	2234	126
4.219	0.032	86.7	2258	104
4.220	0.032	86.9	2261	96
4.221	0.032	87.1	2227	120
4.223	0.032	87.4	2146	150
4.224	0.032	87.6	2051	179
4.225	0.032	87.8	1981	222
4.226	0.032	88.0	1960	273
4.228	0.032	88.2	1984	298
4.229	0.032	88.4	2010	298
4.230	0.032	88.6	2024	282
4.231	0.032	88.8	2020	288
4.232	0.032	89.0	2010	340
4.234	0.031	89.2	2007	412
4.235	0.031	89.4	2144	274
4.236	0.031	89.6	2104	367
4.237	0.031	89.8	2096	397
4.238	0.031	90.0	2164	356
4.240	0.031	90.3	2209	301
4.241	0.031	90.5	2219	228
4.243	0.031	90.7	2191	160
4.244	0.031	90.9	2170	147

Age (ka BP) - from 1950	Age Error (ka)	Depth from top (mm)	REF-07 mean CT numbers >1000 HU	REF-07 mean CT number st.dev.
4.245	0.031	91.1	2166	144
4.246	0.031	91.3	2177	120
4.247	0.031	91.5	2176	115
4.249	0.031	91.7	2161	141
4.250	0.031	91.9	2136	175
4.251	0.031	92.1	2114	210
4.252	0.031	92.3	2109	233
4.253	0.031	92.5	2124	231
4.255	0.031	92.7	2152	204
4.256	0.031	92.9	2168	196
4.258	0.031	93.2	2160	213
4.259	0.031	93.4	2132	228
4.260	0.031	93.6	2106	232
4.261	0.031	93.8	2110	221
4.262	0.031	94.0	2142	201
4.264	0.031	94.2	2193	186
4.265	0.031	94.4	2225	186
4.266	0.031	94.6	2229	180
4.267	0.031	94.8	2192	188
4.268	0.031	95.0	2145	198
4.270	0.031	95.2	2101	203
4.271	0.031	95.4	2083	197
4.272	0.031	95.6	2076	200
4.273	0.031	95.8	2071	204
4.274	0.031	96.0	2048	214
4.276	0.031	96.3	2005	232
4.277	0.031	96.5	1964	255
4.279	0.031	96.7	1953	256
4.280	0.031	96.9	1976	243
4.281	0.031	97.1	2007	254
4.282	0.031	97.3	2093	215
4.283	0.031	97.5	2136	206
4.285	0.031	97.7	2167	203
4.286	0.031	97.9	2182	190
4.287	0.031	98.1	2179	170
4.288	0.031	98.3	2162	159
4.289	0.031	98.5	2109	213
4.291	0.031	98.7	2116	154
4.292	0.031	98.9	2102	144
4.294	0.032	99.2	2064	143
4.295	0.032	99.4	2010	155
4.296	0.032	99.6	1971	183
4.297	0.032	99.8	1953	211
4.299	0.032	100.0	1971	186

Age (ka BP) - from 1950	Age Error (ka)	Depth from top (mm)	REF-07 mean CT numbers >1000 HU	REF-07 mean CT number st.dev.
4.300	0.032	100.2	2001	141
4.301	0.032	100.4	2023	133
4.302	0.032	100.6	2028	165
4.303	0.032	100.8	2007	195
4.305	0.032	101.0	1972	229
4.306	0.032	101.2	1931	267
4.307	0.032	101.4	1899	293
4.308	0.032	101.6	1888	293
4.309	0.032	101.8	1894	272
4.311	0.032	102.1	1903	248
4.312	0.032	102.3	1917	224
4.314	0.032	102.5	1927	221
4.315	0.032	102.7	1958	216
4.316	0.032	102.9	1999	191
4.317	0.032	103.1	2053	161
4.318	0.032	103.3	2106	138
4.320	0.032	103.5	2160	138
4.321	0.033	103.7	2215	139
4.322	0.033	103.9	2275	146
4.323	0.033	104.1	2331	180
4.324	0.033	104.3	2374	231
4.326	0.033	104.5	2398	274
4.327	0.033	104.7	2404	267
4.328	0.033	104.9	2393	241
4.330	0.033	105.2	2373	209
4.331	0.033	105.4	2328	206
4.332	0.033	105.6	2270	215
4.333	0.033	105.8	2207	231
4.335	0.033	106.0	2161	219
4.336	0.033	106.2	2127	189
4.337	0.033	106.4	2107	175
4.338	0.034	106.6	2090	171
4.339	0.034	106.8	2086	163
4.341	0.034	107.0	2098	151
4.342	0.034	107.2	2111	167
4.343	0.034	107.4	2108	184
4.344	0.034	107.6	2069	195
4.345	0.034	107.8	2012	210
4.347	0.034	108.1	1956	235
4.348	0.034	108.3	1914	249
4.350	0.034	108.5	1889	266
4.351	0.034	108.7	1882	273
4.352	0.034	108.9	1901	267
4.353	0.035	109.1	1934	248

Age (ka BP) - from 1950	Age Error (ka)	Depth from top (mm)	REF-07 mean CT numbers >1000 HU	REF-07 mean CT number st.dev.
4.354	0.035	109.3	1972	213
4.356	0.035	109.5	2003	150
4.357	0.035	109.7	2011	104
4.358	0.035	109.9	2010	140
4.359	0.035	110.1	1993	199
4.360	0.035	110.3	1984	217
4.362	0.035	110.5	1973	204
4.363	0.035	110.7	1971	177
4.365	0.035	111.0	1945	181
4.366	0.036	111.2	1904	211
4.367	0.036	111.4	1840	226
4.368	0.036	111.6	1774	221
4.369	0.036	111.8	1707	217
4.371	0.036	112.0	1643	218
4.372	0.036	112.2	1594	204
4.373	0.036	112.4	1553	191
4.374	0.036	112.6	1522	185
4.375	0.036	112.8	1485	202
4.377	0.036	113.0	1447	233
4.378	0.037	113.2	1409	261
4.379	0.037	113.4	1390	278
4.380	0.037	113.6	1374	283
4.382	0.037	113.9	1360	290
4.383	0.037	114.1	1364	298
4.384	0.037	114.3	1343	317
4.386	0.037	114.5	1305	325
4.387	0.037	114.7	1281	321
4.388	0.038	114.9	1262	300
4.389	0.038	115.1	1240	279
4.390	0.038	115.3	1215	266
4.392	0.038	115.5	1249	273
4.393	0.038	115.7	1228	278
4.394	0.038	115.9	1251	285
4.395	0.038	116.1	1270	290
4.396	0.038	116.3	1246	285
4.398	0.038	116.5	1253	290
4.399	0.039	116.7	1285	308
4.401	0.039	117.0	1321	321
4.402	0.039	117.2	1316	333
4.403	0.039	117.4	1380	342
4.404	0.039	117.6	1407	349
4.405	0.039	117.8	1464	348
4.407	0.039	118.0	1487	361
4.408	0.039	118.2	1553	372

Age (ka BP) - from 1950	Age Error (ka)	Depth from top (mm)	REF-07 mean CT numbers >1000 HU	REF-07 mean CT number st.dev.
4.409	0.040	118.4	1603	385
4.410	0.040	118.6	1598	401
4.411	0.040	118.8	1623	386
4.413	0.040	119.0	1622	387
4.414	0.040	119.2	1676	365
4.415	0.040	119.4	1730	366
4.416	0.040	119.6	1724	390
4.418	0.041	119.9	1700	411
4.419	0.041	120.1	1636	417
4.420	0.041	120.3	1675	384
4.422	0.041	120.5	1761	347
4.423	0.041	120.7	1877	291
4.424	0.041	120.9	2003	208
4.425	0.041	121.1	2106	140
4.426	0.041	121.3	2169	140
4.428	0.042	121.5	2194	172
4.429	0.042	121.7	2194	186
4.430	0.042	121.9	2187	185
4.431	0.042	122.1	2175	180
4.432	0.042	122.3	2175	181
4.434	0.042	122.5	2190	190
4.435	0.043	122.8	2227	214
4.437	0.043	123.0	2255	237
4.438	0.043	123.2	2259	247
4.439	0.043	123.4	2229	246
4.440	0.043	123.6	2185	242
4.441	0.043	123.8	2139	240
4.443	0.043	124.0	2112	236
4.444	0.043	124.2	2102	223
4.445	0.044	124.4	2105	204
4.446	0.044	124.6	2113	168
4.447	0.044	124.8	2132	138
4.449	0.044	125.0	2141	142
4.450	0.044	125.2	2131	151
4.451	0.044	125.4	2085	159
4.452	0.044	125.6	2034	171
4.454	0.045	125.9	1993	196
4.455	0.045	126.1	1969	238
4.456	0.045	126.3	1947	261
4.458	0.045	126.5	1916	268
4.459	0.045	126.7	1881	265
4.460	0.045	126.9	1858	262
4.461	0.046	127.1	1844	252
4.462	0.046	127.3	1842	232

Age (ka BP) - from 1950	Age Error (ka)	Depth from top (mm)	REF-07 mean CT numbers >1000 HU	REF-07 mean CT number st.dev.
4.464	0.046	127.5	1849	211
4.465	0.046	127.7	1867	201
4.466	0.046	127.9	1896	211
4.467	0.046	128.1	1926	219
4.468	0.046	128.3	1959	220
4.470	0.047	128.5	1989	213
4.471	0.047	128.8	2010	196
4.473	0.047	129.0	2020	181
4.474	0.047	129.2	2020	178
4.475	0.047	129.4	2018	187
4.476	0.047	129.6	2016	210
4.477	0.048	129.8	2006	248
4.479	0.048	130.0	1982	281
4.480	0.048	130.2	1937	314
4.481	0.048	130.4	1880	343
4.483	0.048	130.6	1826	369
4.486	0.048	130.8	1778	357
4.489	0.048	131.0	1749	305
4.492	0.048	131.2	1733	260
4.495	0.047	131.4	1739	266
4.500	0.047	131.7	1746	305
4.503	0.047	131.9	1755	327
4.506	0.047	132.1	1764	324
4.509	0.047	132.3	1775	292
4.512	0.046	132.5	1787	268
4.516	0.046	132.7	1792	258
4.519	0.046	132.9	1797	253
4.522	0.046	133.1	1801	245
4.525	0.046	133.3	1810	250
4.528	0.046	133.5	1825	257
4.531	0.045	133.7	1836	264
4.534	0.045	133.9	1842	273
4.537	0.045	134.1	1844	273
4.540	0.045	134.3	1858	273
4.545	0.045	134.6	1882	279
4.548	0.045	134.8	1913	284
4.551	0.044	135.0	1936	278
4.554	0.044	135.2	1948	267
4.557	0.044	135.4	1934	250
4.560	0.044	135.6	1927	243
4.563	0.044	135.8	1934	238
4.567	0.044	136.0	1975	207
4.570	0.043	136.2	2031	170
4.573	0.043	136.4	2066	167

Age (ka BP) - from 1950	Age Error (ka)	Depth from top (mm)	REF-07 mean CT numbers >1000 HU	REF-07 mean CT number st.dev.
4.576	0.043	136.6	2069	187
4.579	0.043	136.8	2041	201
4.582	0.043	137.0	2006	208
4.585	0.043	137.2	1970	218
4.588	0.043	137.4	1934	228
4.593	0.042	137.7	1879	239
4.596	0.042	137.9	1811	261
4.599	0.042	138.1	1722	294
4.602	0.042	138.3	1627	319
4.605	0.042	138.5	1571	309
4.608	0.042	138.7	1498	310
4.611	0.041	138.9	1514	284
4.614	0.041	139.1	1480	303
4.618	0.041	139.3	1491	314
4.621	0.041	139.5	1468	344
4.624	0.041	139.7	1496	360
4.627	0.041	139.9	1463	384
4.630	0.041	140.1	1442	392
4.633	0.040	140.3	1441	382
4.638	0.040	140.6	1429	381
4.641	0.040	140.8	1402	395
4.644	0.040	141.0	1426	410
4.647	0.040	141.2	1466	400
4.650	0.040	141.4	1515	359
4.653	0.040	141.6	1545	331
4.656	0.040	141.8	1435	362
4.659	0.039	142.0	1366	351
4.662	0.039	142.2	1406	352
4.665	0.039	142.4	1482	367
4.669	0.039	142.6	1576	379
4.672	0.039	142.8	1617	369
4.675	0.039	143.0	1697	313
4.678	0.039	143.2	1774	255
4.682	0.039	143.5	1841	216
4.686	0.038	143.7	1880	198
4.689	0.038	143.9	1906	204
4.692	0.038	144.1	1915	218
4.695	0.038	144.3	1920	238
4.698	0.038	144.5	1919	254
4.701	0.038	144.7	1923	260
4.704	0.038	144.9	1919	252
4.707	0.038	145.1	1911	243
4.710	0.038	145.3	1897	235
4.713	0.038	145.5	1880	242

Age (ka BP) - from 1950	Age Error (ka)	Depth from top (mm)	REF-07 mean CT numbers >1000 HU	REF-07 mean CT number st.dev.
4.716	0.037	145.7	1860	262
4.720	0.037	145.9	1840	306
4.723	0.037	146.1	1838	331
4.726	0.037	146.3	1849	328
4.730	0.037	146.6	1875	300
4.733	0.037	146.8	1907	275
4.737	0.037	147.0	1943	220
4.740	0.037	147.2	1979	177
4.743	0.037	147.4	2013	162
4.746	0.037	147.6	2046	181
4.749	0.037	147.8	2079	194
4.752	0.036	148.0	2110	188
4.755	0.036	148.2	2134	160
4.758	0.036	148.4	2155	147
4.761	0.036	148.6	2167	164
4.764	0.036	148.8	2166	175
4.767	0.036	149.0	2144	160
4.771	0.036	149.2	2114	131
4.775	0.036	149.5	2090	113
4.778	0.036	149.7	2082	128
4.781	0.036	149.9	2080	161
4.784	0.036	150.1	2071	211
4.788	0.036	150.3	2057	259
4.791	0.036	150.5	2051	303
4.794	0.036	150.7	2069	320
4.797	0.036	150.9	2113	307
4.800	0.035	151.1	2162	271
4.803	0.035	151.3	2200	222
4.806	0.035	151.5	2217	188
4.809	0.035	151.7	2212	169
4.812	0.035	151.9	2194	168
4.815	0.035	152.1	2155	181
4.820	0.035	152.4	2118	206
4.823	0.035	152.6	2091	223
4.826	0.035	152.8	2077	213
4.829	0.035	153.0	2073	188
4.832	0.035	153.2	2071	181
4.835	0.035	153.4	2072	183
4.838	0.035	153.6	2077	172
4.842	0.035	153.8	2084	156
4.845	0.035	154.0	2088	149
4.848	0.035	154.2	2091	161
4.851	0.035	154.4	2083	183
4.854	0.035	154.6	2068	208

Age (ka BP) - from 1950	Age Error (ka)	Depth from top (mm)	REF-07 mean CT numbers >1000 HU	REF-07 mean CT number st.dev.
4.857	0.035	154.8	2039	220
4.860	0.035	155.0	1998	222
4.865	0.035	155.3	1950	216
4.868	0.035	155.5	1897	193
4.871	0.035	155.7	1856	179
4.874	0.035	155.9	1829	193
4.877	0.035	156.1	1833	211
4.880	0.035	156.3	1873	206
4.883	0.035	156.5	1931	195
4.886	0.035	156.7	1986	190
4.889	0.035	156.9	2016	191
4.893	0.035	157.1	2023	188
4.896	0.035	157.3	2009	186
4.899	0.035	157.5	1989	180
4.902	0.035	157.7	1964	166
4.905	0.035	157.9	1952	171
4.908	0.035	158.1	1940	203
4.913	0.035	158.4	1914	244
4.916	0.035	158.6	1878	264
4.919	0.035	158.8	1844	243
4.922	0.035	159.0	1848	192
4.925	0.035	159.2	1872	159
4.928	0.035	159.4	1919	176
4.931	0.035	159.6	1957	214
4.934	0.035	159.8	1992	227
4.937	0.035	160.0	2016	238
4.940	0.035	160.2	2047	269
4.944	0.035	160.4	2080	310
4.947	0.035	160.6	2115	324
4.950	0.035	160.8	2156	289
4.953	0.035	161.0	2193	225
4.957	0.035	161.3	2230	184
4.961	0.035	161.5	2251	187
4.964	0.035	161.7	2262	197
4.967	0.036	161.9	2262	202
4.970	0.036	162.1	2248	203
4.973	0.036	162.3	2219	214
4.976	0.036	162.5	2186	224
4.979	0.036	162.7	2166	219
4.982	0.036	162.9	2163	203
4.985	0.036	163.1	2170	194
4.988	0.036	163.3	2174	209
4.991	0.036	163.5	2173	238
4.995	0.036	163.7	2163	255

Age (ka BP) - from 1950	Age Error (ka)	Depth from top (mm)	REF-07 mean CT numbers >1000 HU	REF-07 mean CT number st.dev.
4.998	0.036	163.9	2151	251
5.002	0.036	164.2	2136	216
5.005	0.036	164.4	2127	180
5.008	0.036	164.6	2126	155
5.012	0.036	164.8	2134	143
5.015	0.037	165.0	2148	147
5.018	0.037	165.2	2159	161
5.021	0.037	165.4	2164	167
5.024	0.037	165.6	2166	168
5.027	0.037	165.8	2173	164
5.030	0.037	166.0	2187	156
5.033	0.037	166.2	2201	139
5.036	0.037	166.4	2202	129
5.039	0.037	166.6	2189	132
5.042	0.037	166.8	2148	159
5.046	0.037	167.0	2087	214
5.050	0.038	167.3	2017	283
5.053	0.038	167.5	1953	350
5.056	0.038	167.7	1918	389
5.059	0.038	167.9	1912	401
5.063	0.038	168.1	1935	386
5.066	0.038	168.3	2029	256
5.069	0.038	168.5	2045	257
5.072	0.038	168.7	2037	327
5.075	0.038	168.9	2103	268
5.078	0.038	169.1	2108	286
5.081	0.039	169.3	2116	278
5.084	0.039	169.5	2059	330
5.087	0.039	169.7	2075	258
5.090	0.039	169.9	2029	289
5.095	0.039	170.2	2036	250
5.098	0.039	170.4	2025	251
5.101	0.039	170.6	2016	259
5.104	0.039	170.8	2006	284
5.107	0.040	171.0	1989	330
5.110	0.040	171.2	2024	317
5.114	0.040	171.4	2056	330
5.117	0.040	171.6	1987	429
5.120	0.040	171.8	2062	319
5.123	0.040	172.0	2074	270
5.126	0.040	172.2	2061	223
5.129	0.040	172.4	1989	275
5.132	0.041	172.6	1957	244
5.135	0.041	172.8	1992	233

Age (ka BP) - from 1950	Age Error (ka)	Depth from top (mm)	REF-07 mean CT numbers >1000 HU	REF-07 mean CT number st.dev.
5.140	0.041	173.1	2010	255
5.143	0.041	173.3	2020	267
5.146	0.041	173.5	2014	245
5.149	0.041	173.7	2004	217
5.152	0.041	173.9	2005	198
5.155	0.042	174.1	2016	187
5.158	0.042	174.3	2044	184
5.161	0.042	174.5	2081	191
5.165	0.042	174.7	2132	205
5.168	0.042	174.9	2179	206
5.171	0.042	175.1	2215	211
5.174	0.042	175.3	2225	241
5.177	0.043	175.5	2202	310
5.180	0.043	175.7	2140	410
5.185	0.043	176.0	2143	428
5.188	0.043	176.2	2270	218
5.191	0.043	176.4	2271	227
5.194	0.043	176.6	2282	244
5.197	0.044	176.8	2281	289
5.200	0.044	177.0	2271	341
5.203	0.044	177.2	2134	473
5.206	0.044	177.4	2116	431
5.209	0.044	177.6	2165	299
5.212	0.044	177.8	2184	213
5.215	0.045	178.0	2185	172
5.219	0.045	178.2	2167	168
5.222	0.045	178.4	2140	176
5.225	0.045	178.6	2108	197
5.228	0.045	178.8	2074	228
5.232	0.045	179.1	2068	234
5.236	0.046	179.3	2074	248
5.239	0.046	179.5	2091	267
5.242	0.046	179.7	2099	272
5.245	0.046	179.9	2106	267
5.248	0.046	180.1	2119	250
5.251	0.046	180.3	2143	228
5.254	0.047	180.5	2164	226
5.257	0.047	180.7	2173	253
5.260	0.047	180.9	2170	290
5.263	0.047	181.1	2160	339
5.266	0.047	181.3	2225	296
5.270	0.047	181.5	2240	310
5.273	0.048	181.7	2261	332
5.277	0.048	182.0	2282	360

Age (ka BP) - from 1950	Age Error (ka)	Depth from top (mm)	REF-07 mean CT numbers >1000 HU	REF-07 mean CT number st.dev.
5.280	0.048	182.2	2241	459
5.283	0.048	182.4	2354	292
5.287	0.048	182.6	2377	269
5.290	0.049	182.8	2309	377
5.293	0.049	183.0	2316	350
5.296	0.049	183.2	2330	350
5.299	0.049	183.4	2347	369
5.302	0.049	183.6	2453	160
5.305	0.050	183.8	2391	366
5.308	0.050	184.0	2408	335
5.312	0.050	184.2	2435	289
5.318	0.049	184.4	2477	242
5.323	0.049	184.6	2520	222
5.331	0.048	184.9	2541	250
5.337	0.048	185.1	2520	320
5.342	0.047	185.3	2479	373
5.347	0.047	185.5	2429	376
5.353	0.046	185.7	2382	338
5.358	0.046	185.9	2340	330
5.363	0.046	186.1	2294	381
5.369	0.045	186.3	2271	438
5.374	0.045	186.5	2356	375
5.380	0.045	186.7	2401	370
5.385	0.044	186.9	2433	379
5.390	0.044	187.1	2412	420
5.396	0.044	187.3	2349	511
5.401	0.043	187.5	2263	649
5.406	0.043	187.7	2403	535
5.414	0.043	188.0	2328	514
5.420	0.042	188.2	2239	407
5.425	0.042	188.4	2224	258
5.431	0.042	188.6	2138	370
5.436	0.041	188.8	2131	336
5.441	0.041	189.0	2125	317
5.447	0.041	189.2	2106	301
5.452	0.041	189.4	2097	290
5.457	0.041	189.6	2094	294
5.463	0.040	189.8	2085	313
5.468	0.040	190.0	2067	340
5.474	0.040	190.2	2040	348
5.479	0.040	190.4	2022	337
5.484	0.040	190.6	2008	314
5.492	0.040	190.9	1999	295
5.498	0.039	191.1	1992	292

Age (ka BP) - from 1950	Age Error (ka)	Depth from top (mm)	REF-07 mean CT numbers >1000 HU	REF-07 mean CT number st.dev.
5.503	0.039	191.3	1972	298
5.508	0.039	191.5	1944	316
5.514	0.039	191.7	1905	344
5.519	0.039	191.9	1854	360
5.525	0.039	192.1	1819	360
5.530	0.039	192.3	1804	341
5.535	0.039	192.5	1798	331
5.541	0.039	192.7	1793	321
5.546	0.039	192.9	1773	295
5.551	0.039	193.1	1744	277
5.557	0.039	193.3	1718	275
5.562	0.039	193.5	1698	296
5.570	0.039	193.8	1673	294
5.576	0.039	194.0	1641	272
5.581	0.039	194.2	1607	274
5.586	0.039	194.4	1656	282
5.592	0.039	194.6	1724	298
5.597	0.040	194.8	1733	374
5.602	0.040	195.0	1769	411
5.608	0.040	195.2	1855	390
5.613	0.040	195.4	1882	391
5.618	0.040	195.6	1939	346
5.624	0.040	195.8	1974	284
5.629	0.040	196.0	1999	244
5.635	0.041	196.2	2017	234
5.640	0.041	196.4	2031	227
5.648	0.041	196.7	2042	196
5.653	0.041	196.9	2062	166
5.659	0.042	197.1	2086	142
5.664	0.042	197.3	2111	137
5.669	0.042	197.5	2131	141
5.675	0.043	197.7	2148	147
5.680	0.043	197.9	2161	148
5.686	0.043	198.1	2173	148
5.691	0.043	198.3	2189	144
5.696	0.044	198.5	2207	146
5.702	0.044	198.7	2221	148
5.707	0.044	198.9	2229	138
5.712	0.045	199.1	2233	126
5.718	0.045	199.3	2243	120
5.723	0.045	199.5	2255	120
5.731	0.046	199.8	2270	115
5.737	0.046	200.0	2285	103
5.742	0.047	200.2	2301	96

Age (ka BP) - from 1950	Age Error (ka)	Depth from top (mm)	REF-07 mean CT numbers >1000 HU	REF-07 mean CT number st.dev.
5.747	0.047	200.4	2313	98
5.753	0.048	200.6	2318	105
5.758	0.048	200.8	2312	111
5.763	0.048	201.0	2296	112
5.769	0.049	201.2	2275	117
5.774	0.049	201.4	2257	132
5.780	0.050	201.6	2248	136
5.785	0.050	201.8	2251	134
5.790	0.051	202.0	2270	136
5.796	0.051	202.2	2290	148
5.801	0.052	202.4	2301	150
5.809	0.052	202.7	2300	147
5.814	0.053	202.9	2285	147
5.820	0.053	203.1	2257	152
5.825	0.054	203.3	2222	159
5.831	0.054	203.5	2179	164
5.836	0.055	203.7	2139	166
5.841	0.055	203.9	2115	183
5.847	0.056	204.1	2097	213
5.852	0.056	204.3	2079	242
5.857	0.057	204.5	2050	281
5.863	0.057	204.7	2018	341
5.868	0.058	204.9	1984	421
5.874	0.058	205.1	2039	376
5.879	0.059	205.3	2058	376
5.887	0.060	205.6	2034	434
5.892	0.060	205.8	2079	416
5.898	0.061	206.0	2126	400
5.903	0.061	206.2	2178	378
5.908	0.062	206.4	2232	337
5.914	0.062	206.6	2291	283
5.919	0.063	206.8	2342	262
5.925	0.063	207.0	2372	281
5.930	0.064	207.2	2376	304
5.935	0.065	207.4	2361	294
5.941	0.065	207.6	2342	250
5.946	0.066	207.8	2333	199
5.951	0.066	208.0	2328	173
5.957	0.067	208.2	2319	180
5.962	0.067	208.4	2291	188
5.970	0.068	208.7	2259	181
5.976	0.069	208.9	2238	164
5.981	0.069	209.1	2234	144
5.986	0.070	209.3	2236	141

Age (ka BP) - from 1950	Age Error (ka)	Depth from top (mm)	REF-07 mean CT numbers >1000 HU	REF-07 mean CT number st.dev.
5.992	0.071	209.5	2235	152
5.997	0.071	209.7	2231	170
6.002	0.072	209.9	2235	186
6.008	0.072	210.1	2240	194
6.013	0.073	210.3	2241	188
6.018	0.074	210.5	2233	173
6.024	0.074	210.7	2221	154
6.029	0.075	210.9	2206	132
6.035	0.075	211.1	2189	112
6.040	0.076	211.3	2174	101
6.048	0.077	211.6	2161	108
6.053	0.078	211.8	2151	133
6.059	0.078	212.0	2142	151
6.064	0.079	212.2	2136	158
6.069	0.079	212.4	2135	164
6.075	0.080	212.6	2138	168
6.080	0.081	212.8	2133	167
6.086	0.081	213.0	2116	161
6.091	0.082	213.2	2087	167
6.096	0.082	213.4	2070	189
6.102	0.083	213.6	2073	207
6.107	0.084	213.8	2101	206
6.112	0.084	214.0	2134	181
6.118	0.085	214.2	2171	147
6.126	0.086	214.5	2199	124
6.131	0.087	214.7	2217	129
6.137	0.087	214.9	2226	157
7.292	0.091	215.1	2224	167
7.295	0.090	215.3	2219	159
7.298	0.090	215.5	2206	152
7.300	0.090	215.7	2188	153
7.303	0.089	215.9	2166	155
7.305	0.089	216.1	2144	172
7.308	0.089	216.3	2125	196
7.310	0.089	216.5	2105	218
7.313	0.088	216.7	2085	235
7.315	0.088	216.9	2071	263
7.318	0.088	217.1	2059	284
7.321	0.088	217.4	2047	301
7.324	0.087	217.6	2028	321
7.326	0.087	217.8	2002	352
7.329	0.087	218.0	1973	392
7.331	0.087	218.2	1944	428
7.334	0.086	218.4	2033	335

Age (ka BP) - from 1950	Age Error (ka)	Depth from top (mm)	REF-07 mean CT numbers >1000 HU	REF-07 mean CT number st.dev.
7.336	0.086	218.6	2021	330
7.339	0.086	218.8	2005	335
7.341	0.086	219.0	1997	336
7.344	0.085	219.2	1993	319
7.346	0.085	219.4	1942	359
7.349	0.085	219.6	1969	281
7.351	0.085	219.8	1962	280
7.354	0.084	220.0	2012	220
7.356	0.084	220.2	2042	184
7.360	0.084	220.5	2048	155
7.363	0.083	220.7	2039	140
7.365	0.083	220.9	2035	146
7.368	0.083	221.1	2041	165
7.370	0.083	221.3	2055	173
7.373	0.082	221.5	2058	177
7.375	0.082	221.7	2049	215
7.378	0.082	221.9	2033	278
7.380	0.082	222.1	2085	211
7.383	0.081	222.3	2096	221
7.385	0.081	222.5	2068	286
7.388	0.081	222.7	2123	223
7.390	0.081	222.9	2168	183
7.393	0.080	223.1	2201	149
7.397	0.080	223.4	2211	143
7.399	0.080	223.6	2210	162
7.402	0.080	223.8	2195	179
7.404	0.079	224.0	2182	179
7.407	0.079	224.2	2183	175
7.409	0.079	224.4	2187	167
7.412	0.079	224.6	2188	167
7.414	0.078	224.8	2173	179
7.417	0.078	225.0	2152	193
7.419	0.078	225.2	2122	205
7.422	0.078	225.4	2102	218
7.424	0.078	225.6	2090	225
7.427	0.077	225.8	2100	212
7.429	0.077	226.0	2128	186
7.433	0.077	226.3	2161	165
7.436	0.077	226.5	2191	161
7.438	0.076	226.7	2211	162
7.441	0.076	226.9	2221	158
7.443	0.076	227.1	2223	148
7.446	0.076	227.3	2227	136
7.448	0.075	227.5	2230	140

Age (ka BP) - from 1950	Age Error (ka)	Depth from top (mm)	REF-07 mean CT numbers >1000 HU	REF-07 mean CT number st.dev.
7.451	0.075	227.7	2233	157
7.453	0.075	227.9	2228	165
7.456	0.075	228.1	2225	161
7.458	0.075	228.3	2224	152
7.461	0.074	228.5	2225	138
7.463	0.074	228.7	2216	113
7.466	0.074	228.9	2203	80
7.468	0.074	229.1	2188	69
7.472	0.073	229.4	2171	92
7.474	0.073	229.6	2156	117
7.477	0.073	229.8	2143	135
7.479	0.073	230.0	2142	155
7.482	0.072	230.2	2139	181
7.484	0.072	230.4	2140	199
7.487	0.072	230.6	2150	188
7.489	0.072	230.8	2159	165
7.492	0.072	231.0	2158	164
7.494	0.071	231.2	2129	169
7.497	0.071	231.4	2089	169
7.500	0.071	231.6	2046	165
7.502	0.071	231.8	2017	174
7.505	0.071	232.0	2004	177
7.508	0.070	232.3	2001	169
7.511	0.070	232.5	2005	152
7.513	0.070	232.7	2020	149
7.516	0.070	232.9	2039	154
7.518	0.070	233.1	2055	164
7.521	0.069	233.3	2065	166
7.523	0.069	233.5	2068	168
7.526	0.069	233.7	2067	176
7.528	0.069	233.9	2059	194
7.531	0.069	234.1	2047	210
7.533	0.068	234.3	2037	213
7.536	0.068	234.5	2029	204
7.538	0.068	234.7	2025	193
7.541	0.068	234.9	2030	189
7.545	0.068	235.2	2040	178
7.547	0.067	235.4	2067	171
7.550	0.067	235.6	2092	185
7.552	0.067	235.8	2114	211
7.555	0.067	236.0	2123	238
7.557	0.067	236.2	2127	264
7.560	0.066	236.4	2134	285
7.562	0.066	236.6	2142	294

Age (ka BP) - from 1950	Age Error (ka)	Depth from top (mm)	REF-07 mean CT numbers >1000 HU	REF-07 mean CT number st.dev.
7.565	0.066	236.8	2155	288
7.567	0.066	237.0	2179	278
7.570	0.066	237.2	2215	268
7.572	0.066	237.4	2254	246
7.575	0.065	237.6	2281	219
7.577	0.065	237.8	2294	192
7.581	0.065	238.1	2291	178
7.584	0.065	238.3	2278	170
7.586	0.065	238.5	2261	175
7.589	0.064	238.7	2256	171
7.591	0.064	238.9	2264	163
7.594	0.064	239.1	2269	156
7.596	0.064	239.3	2257	163
7.599	0.064	239.5	2234	193
7.601	0.064	239.7	2217	221
7.604	0.063	239.9	2203	220
7.606	0.063	240.1	2192	184
7.609	0.063	240.3	2177	149
7.611	0.063	240.5	2170	138
7.614	0.063	240.7	2167	147
7.616	0.063	240.9	2159	164
7.620	0.062	241.2	2138	181
7.622	0.062	241.4	2120	185
7.625	0.062	241.6	2111	189
7.627	0.062	241.8	2112	194
7.630	0.062	242.0	2112	202
7.632	0.062	242.2	2112	218
7.635	0.062	242.4	2110	238
7.638	0.061	242.6	2105	248
7.640	0.061	242.8	2095	251
7.643	0.061	243.0	2083	249
7.645	0.061	243.2	2075	244
7.648	0.061	243.4	2077	226
7.650	0.061	243.6	2087	218
7.653	0.061	243.8	2096	222
7.656	0.061	244.1	2103	229
7.659	0.060	244.3	2112	231
7.661	0.060	244.5	2137	214
7.664	0.060	244.7	2177	191
7.666	0.060	244.9	2220	168
7.669	0.060	245.1	2247	164
7.671	0.060	245.3	2244	165
7.674	0.060	245.5	2221	164
7.676	0.060	245.7	2201	159

Age (ka BP) - from 1950	Age Error (ka)	Depth from top (mm)	REF-07 mean CT numbers >1000 HU	REF-07 mean CT number st.dev.
7.679	0.059	245.9	2195	157
7.681	0.059	246.1	2204	159
7.684	0.059	246.3	2218	158
7.686	0.059	246.5	2239	160
7.689	0.059	246.7	2259	160
7.693	0.059	247.0	2278	157
7.695	0.059	247.2	2286	135
7.698	0.059	247.4	2287	116
7.700	0.059	247.6	2276	108
7.703	0.058	247.8	2262	114
7.705	0.058	248.0	2244	121
7.708	0.058	248.2	2235	131
7.710	0.058	248.4	2236	145
7.713	0.058	248.6	2246	153
7.715	0.058	248.8	2251	166
7.718	0.058	249.0	2249	185
7.720	0.058	249.2	2240	199
7.723	0.058	249.4	2233	194
7.725	0.058	249.6	2229	180
7.728	0.058	249.8	2222	176
7.732	0.057	250.1	2213	184
7.734	0.057	250.3	2206	191
7.737	0.057	250.5	2202	195
7.739	0.057	250.7	2193	197
7.742	0.057	250.9	2174	193
7.744	0.057	251.1	2155	186
7.747	0.057	251.3	2147	179
7.749	0.057	251.5	2155	172
7.752	0.057	251.7	2168	173
7.754	0.057	251.9	2176	177
7.757	0.057	252.1	2182	185
7.759	0.057	252.3	2190	202
7.762	0.057	252.5	2200	224
7.764	0.057	252.7	2213	236
7.768	0.057	253.0	2223	236
7.771	0.057	253.2	2231	227
7.773	0.056	253.4	2240	211
7.776	0.056	253.6	2250	208
7.778	0.056	253.8	2259	210
7.781	0.056	254.0	2265	213
7.783	0.056	254.2	2268	209
7.786	0.056	254.4	2268	205
7.788	0.056	254.6	2270	197
7.791	0.056	254.8	2273	179

Age (ka BP) - from 1950	Age Error (ka)	Depth from top (mm)	REF-07 mean CT numbers >1000 HU	REF-07 mean CT number st.dev.
7.793	0.056	255.0	2279	173
7.796	0.056	255.2	2286	179
7.798	0.056	255.4	2297	182
7.801	0.056	255.6	2316	188
7.804	0.056	255.9	2340	189
7.807	0.056	256.1	2358	183
7.809	0.056	256.3	2364	170
7.812	0.056	256.5	2356	169
7.814	0.056	256.7	2340	174
7.817	0.056	256.9	2320	178
7.819	0.056	257.1	2295	177
7.822	0.056	257.3	2263	171
7.824	0.056	257.5	2234	170
7.827	0.056	257.7	2215	167
7.829	0.056	257.9	2210	162
7.832	0.056	258.1	2214	153
7.834	0.056	258.3	2217	145
7.837	0.056	258.5	2214	139
7.841	0.056	258.8	2203	142
7.843	0.056	259.0	2190	145
7.846	0.056	259.2	2174	146
7.848	0.056	259.4	2159	146
7.851	0.056	259.6	2143	154
7.853	0.056	259.8	2128	168
7.856	0.056	260.0	2114	163
7.858	0.056	260.2	2110	128
7.861	0.056	260.4	2113	104
7.863	0.056	260.6	2121	127
7.866	0.056	260.8	2127	153
7.868	0.056	261.0	2133	159
7.871	0.056	261.2	2150	145
7.873	0.056	261.4	2170	121
7.876	0.056	261.6	2185	96
7.880	0.056	261.9	2189	85
7.882	0.056	262.1	2183	95
7.885	0.056	262.3	2170	110
7.887	0.056	262.5	2154	119
7.890	0.057	262.7	2149	110
7.892	0.057	262.9	2150	101
7.895	0.057	263.1	2151	96
7.897	0.057	263.3	2153	95
7.900	0.057	263.5	2169	96
7.902	0.057	263.7	2198	106
7.905	0.057	263.9	2228	113

Age (ka BP) - from 1950	Age Error (ka)	Depth from top (mm)	REF-07 mean CT numbers >1000 HU	REF-07 mean CT number st.dev.
7.907	0.057	264.1	2239	123
7.910	0.057	264.3	2224	125
7.912	0.057	264.5	2203	116
7.916	0.057	264.8	2196	111
7.919	0.057	265.0	2208	123
7.921	0.057	265.2	2223	134
7.924	0.057	265.4	2225	142
7.926	0.057	265.6	2214	145
7.929	0.057	265.8	2204	155
7.931	0.058	266.0	2200	164
7.934	0.058	266.2	2198	159
7.936	0.058	266.4	2185	135
7.939	0.058	266.6	2159	130
7.941	0.058	266.8	2127	148
7.944	0.058	267.0	2096	160
7.946	0.058	267.2	2080	165
7.949	0.058	267.4	2062	167
7.952	0.058	267.7	2043	170
7.955	0.058	267.9	2012	172
7.957	0.058	268.1	1983	197
7.960	0.059	268.3	1965	223
7.962	0.059	268.5	1957	237
7.965	0.059	268.7	1953	228
7.967	0.059	268.9	1945	203
7.970	0.059	269.1	1939	175
7.973	0.059	269.3	1942	164
7.975	0.059	269.5	1959	174
7.978	0.059	269.7	1987	180
7.980	0.059	269.9	2018	174
7.983	0.059	270.1	2047	153
7.985	0.060	270.3	2069	137
7.988	0.060	270.5	2086	146
7.991	0.060	270.8	2086	184
7.994	0.060	271.0	2063	235
7.996	0.060	271.2	2015	301
7.999	0.060	271.4	2040	186
8.001	0.060	271.6	2014	183
8.004	0.061	271.8	1995	177
8.006	0.061	272.0	1980	177
8.009	0.061	272.2	1929	245
8.011	0.061	272.4	1955	169
8.014	0.061	272.6	1984	133
8.016	0.061	272.8	2013	158
8.019	0.061	273.0	2033	205

Age (ka BP) - from 1950	Age Error (ka)	Depth from top (mm)	REF-07 mean CT numbers >1000 HU	REF-07 mean CT number st.dev.
8.021	0.061	273.2	2044	235
8.024	0.062	273.4	2055	241
8.028	0.062	273.7	2074	237
8.030	0.062	273.9	2105	236
8.033	0.062	274.1	2141	226
8.035	0.062	274.3	2168	196
8.038	0.062	274.5	2184	182
8.040	0.063	274.7	2193	194
8.043	0.063	274.9	2205	202
8.045	0.063	275.1	2219	198
8.048	0.063	275.3	2230	194
8.050	0.063	275.5	2234	197
8.053	0.063	275.7	2227	200
8.055	0.063	275.9	2216	197
8.058	0.064	276.1	2199	180
8.060	0.064	276.3	2184	169
8.064	0.064	276.6	2170	169
8.067	0.064	276.8	2166	166
8.069	0.064	277.0	2163	160
8.072	0.064	277.2	2160	164
8.074	0.065	277.4	2157	184
8.077	0.065	277.6	2154	218
8.079	0.065	277.8	2160	249
8.082	0.065	278.0	2173	256
8.084	0.065	278.2	2193	236
8.087	0.065	278.4	2202	199
8.089	0.066	278.6	2191	163
8.092	0.066	278.8	2160	150
8.094	0.066	279.0	2116	169
8.097	0.066	279.2	2079	190
8.100	0.066	279.5	2053	205
8.103	0.067	279.7	2051	215
8.105	0.067	279.9	2072	231
8.108	0.067	280.1	2114	238
8.111	0.067	280.3	2155	225
8.113	0.067	280.5	2174	207
8.116	0.068	280.7	2170	187
8.118	0.068	280.9	2161	187
8.121	0.068	281.1	2165	199
8.123	0.068	281.3	2178	216
8.126	0.068	281.5	2185	231
8.128	0.068	281.7	2178	221
8.131	0.069	281.9	2160	192
8.133	0.069	282.1	2132	159

Age (ka BP) - from 1950	Age Error (ka)	Depth from top (mm)	REF-07 mean CT numbers >1000 HU	REF-07 mean CT number st.dev.
8.136	0.069	282.3	2099	135
8.139	0.069	282.6	2076	106
8.142	0.070	282.8	2075	86
8.144	0.070	283.0	2103	103
8.147	0.070	283.2	2141	139
8.149	0.070	283.4	2182	162
8.152	0.070	283.6	2212	166
8.154	0.071	283.8	2227	158
8.157	0.071	284.0	2231	146
8.159	0.071	284.2	2234	133
8.162	0.071	284.4	2240	122
8.164	0.071	284.6	2245	112
8.167	0.072	284.8	2246	111
8.169	0.072	285.0	2250	113
8.172	0.072	285.2	2262	120
8.176	0.072	285.5	2281	124
8.178	0.073	285.7	2297	129
8.181	0.073	285.9	2314	129
8.183	0.073	286.1	2332	125
8.186	0.073	286.3	2346	116
8.188	0.073	286.5	2350	114
8.191	0.074	286.7	2344	109
8.193	0.074	286.9	2339	97
8.196	0.074	287.1	2334	89
8.198	0.074	287.3	2327	98
8.201	0.074	287.5	2317	114
8.203	0.075	287.7	2310	128
8.206	0.075	287.9	2308	140
8.208	0.075	288.1	2314	159
8.212	0.075	288.4	2319	177
8.215	0.076	288.6	2315	189
8.217	0.076	288.8	2305	179
8.220	0.076	289.0	2291	163
8.222	0.076	289.2	2279	148
8.225	0.077	289.4	2269	146
8.227	0.077	289.6	2259	145
8.230	0.077	289.8	2244	152
8.232	0.077	290.0	2229	160
8.235	0.077	290.2	2206	174
8.237	0.078	290.4	2181	205
8.240	0.078	290.6	2139	283
8.243	0.077	290.8	2163	234
8.246	0.077	291.0	2140	252
8.248	0.077	291.2	2139	229

Age (ka BP) - from 1950	Age Error (ka)	Depth from top (mm)	REF-07 mean CT numbers >1000 HU	REF-07 mean CT number st.dev.
8.253	0.076	291.5	2155	183
8.255	0.076	291.7	2114	290
8.258	0.076	291.9	2125	277
8.261	0.076	292.1	2167	193
8.264	0.075	292.3	2138	243
8.267	0.075	292.5	2104	290
8.269	0.075	292.7	2083	304
8.272	0.074	292.9	2027	351
8.275	0.074	293.1	2073	251
8.278	0.074	293.3	2124	208
8.281	0.074	293.5	2167	205
8.283	0.073	293.7	2205	199
8.286	0.073	293.9	2231	183
8.289	0.073	294.1	2254	162
8.293	0.072	294.4	2285	143
8.296	0.072	294.6	2318	139
8.299	0.072	294.8	2339	150
8.302	0.072	295.0	2344	174
8.304	0.071	295.2	2336	195
8.307	0.071	295.4	2329	199
8.310	0.071	295.6	2330	184
8.313	0.070	295.8	2337	153
8.316	0.070	296.0	2345	127
8.318	0.070	296.2	2349	99
8.321	0.070	296.4	2354	85
8.324	0.069	296.6	2361	93
8.327	0.069	296.8	2365	120
8.330	0.069	297.0	2362	164
8.334	0.069	297.3	2354	202
8.337	0.068	297.5	2344	228
8.340	0.068	297.7	2336	221
8.342	0.068	297.9	2328	211
8.345	0.068	298.1	2316	205
8.348	0.067	298.3	2293	215
8.351	0.067	298.5	2256	228
8.354	0.067	298.7	2215	242
8.356	0.067	298.9	2178	238
8.359	0.066	299.1	2148	222
8.362	0.066	299.3	2114	208
8.365	0.066	299.5	2073	209
8.368	0.066	299.7	2037	221
8.370	0.066	299.9	2017	234
8.375	0.065	300.2	2021	243
8.377	0.065	300.4	2037	272

Age (ka BP) - from 1950	Age Error (ka)	Depth from top (mm)	REF-07 mean CT numbers >1000 HU	REF-07 mean CT number st.dev.
8.380	0.065	300.6	2059	324
8.383	0.065	300.8	2151	207
8.386	0.064	301.0	2178	192
8.389	0.064	301.2	2197	169
8.391	0.064	301.4	2209	164
8.394	0.064	301.6	2144	284
8.397	0.063	301.8	2139	236
8.400	0.063	302.0	2110	232
8.403	0.063	302.2	2066	266
8.406	0.063	302.4	2017	315
8.408	0.063	302.6	1972	364
8.411	0.062	302.8	1939	383
8.414	0.062	303.0	1923	360
8.418	0.062	303.3	1916	317
8.421	0.062	303.5	1928	272
8.424	0.062	303.7	1954	241
8.427	0.061	303.9	2002	220
8.429	0.061	304.1	2051	204
8.432	0.061	304.3	2089	193
8.435	0.061	304.5	2106	191
8.438	0.061	304.7	2093	200
8.441	0.061	304.9	2058	217
8.443	0.060	305.1	2000	245
8.446	0.060	305.3	1932	293
8.449	0.060	305.5	1932	252
8.452	0.060	305.7	1898	327
8.455	0.060	305.9	1884	441
8.459	0.059	306.2	1897	536
8.462	0.059	306.4	2054	336
8.464	0.059	306.6	2056	372
8.467	0.059	306.8	2110	338
8.470	0.059	307.0	2115	362
8.473	0.059	307.2	2078	428
8.476	0.059	307.4	2168	309
8.478	0.058	307.6	2023	536
8.481	0.058	307.8	2003	431
8.484	0.058	308.0	2073	298
8.487	0.058	308.2	2075	324
8.490	0.058	308.4	2103	299
8.493	0.058	308.6	2091	295
8.495	0.058	308.8	2062	309
8.500	0.057	309.1	2031	328
8.502	0.057	309.3	2001	353
8.505	0.057	309.5	1957	377

Age (ka BP) - from 1950	Age Error (ka)	Depth from top (mm)	REF-07 mean CT numbers >1000 HU	REF-07 mean CT number st.dev.
8.508	0.057	309.7	1905	441
8.511	0.057	309.9	1948	395
8.514	0.057	310.1	1943	377
8.516	0.057	310.3	1940	351
8.519	0.057	310.5	1930	326
8.522	0.057	310.7	1922	301
8.525	0.057	310.9	1914	280
8.528	0.056	311.1	1909	269
8.530	0.056	311.3	1903	259
8.533	0.056	311.5	1897	267
8.536	0.056	311.7	1896	315
8.539	0.056	311.9	1889	376
8.543	0.056	312.2	2001	356
8.546	0.056	312.4	2049	396
8.549	0.056	312.6	2074	412
8.551	0.056	312.8	2029	438
8.554	0.056	313.0	2047	377
8.557	0.056	313.2	2072	327
8.560	0.056	313.4	2100	310
8.563	0.056	313.6	2135	315
8.566	0.056	313.8	2163	335
8.568	0.055	314.0	2176	361
8.571	0.055	314.2	2172	385
8.574	0.055	314.4	2168	406
8.577	0.055	314.6	2186	422
8.580	0.055	314.8	2232	395
8.584	0.055	315.1	2278	354
8.587	0.055	315.3	2304	323
8.589	0.055	315.5	2300	326
8.592	0.055	315.7	2281	336
8.595	0.055	315.9	2266	330
8.598	0.055	316.1	2268	311
8.601	0.055	316.3	2290	284
8.603	0.055	316.5	2315	253
8.606	0.055	316.7	2324	244
8.609	0.055	316.9	2315	267
8.612	0.055	317.1	2302	292
8.615	0.055	317.3	2302	295
8.617	0.055	317.5	2321	274
8.620	0.055	317.7	2336	270
8.624	0.055	318.0	2337	286
8.627	0.055	318.2	2324	297
8.630	0.055	318.4	2316	289
8.633	0.055	318.6	2318	270

Age (ka BP) - from 1950	Age Error (ka)	Depth from top (mm)	REF-07 mean CT numbers >1000 HU	REF-07 mean CT number st.dev.
8.636	0.055	318.8	2326	265
8.638	0.055	319.0	2340	250
8.641	0.055	319.2	2356	213
8.644	0.055	319.4	2367	185
8.647	0.055	319.6	2352	219
8.650	0.055	319.8	2325	290
8.653	0.056	320.0	2305	345
8.655	0.056	320.2	2327	316
8.658	0.056	320.4	2370	243
8.661	0.056	320.6	2412	159
8.665	0.056	320.9	2422	128
8.668	0.056	321.1	2409	130
8.671	0.056	321.3	2389	132
8.674	0.056	321.5	2381	128
8.676	0.056	321.7	2389	134
8.679	0.056	321.9	2403	149
8.682	0.056	322.1	2410	167
8.685	0.056	322.3	2404	194
8.688	0.056	322.5	2387	225
8.690	0.056	322.7	2371	242
8.693	0.057	322.9	2360	248
8.696	0.057	323.1	2361	250
8.699	0.057	323.3	2380	221
8.702	0.057	323.5	2407	180
8.704	0.057	323.7	2436	137
8.709	0.057	324.0	2456	115
8.711	0.057	324.2	2464	93
8.714	0.057	324.4	2459	77
8.717	0.057	324.6	2443	97
8.720	0.058	324.8	2422	129
8.723	0.058	325.0	2405	144
8.725	0.058	325.2	2397	138
8.728	0.058	325.4	2402	116
8.731	0.058	325.6	2407	104
8.734	0.058	325.8	2406	98
8.737	0.058	326.0	2395	105
8.740	0.058	326.2	2379	122
8.742	0.059	326.4	2362	135
8.745	0.059	326.6	2339	141
8.749	0.059	326.9	2331	138
8.752	0.059	327.1	2343	136
8.755	0.059	327.3	2379	126
8.758	0.059	327.5	2403	136
8.761	0.060	327.7	2402	175

Age (ka BP) - from 1950	Age Error (ka)	Depth from top (mm)	REF-07 mean CT numbers >1000 HU	REF-07 mean CT number st.dev.
8.763	0.060	327.9	2381	216
8.766	0.060	328.1	2366	248
8.769	0.060	328.3	2362	239
8.772	0.060	328.5	2353	212
8.775	0.060	328.7	2328	202
8.777	0.061	328.9	2285	231
8.780	0.061	329.1	2243	277
8.783	0.061	329.3	2205	323
8.786	0.061	329.5	2180	357
8.790	0.061	329.8	2160	379
8.793	0.062	330.0	2142	389
8.796	0.062	330.2	2120	400
8.798	0.062	330.4	2102	416
8.801	0.062	330.6	2090	436
8.804	0.062	330.8	2091	444
8.807	0.063	331.0	2109	427
8.810	0.063	331.2	2138	392
8.813	0.063	331.4	2168	343
8.815	0.063	331.6	2181	306
8.818	0.063	331.8	2177	294
8.821	0.064	332.0	2163	298
8.824	0.064	332.2	2152	301
8.827	0.064	332.4	2152	300
8.829	0.064	332.6	2158	293
8.834	0.064	332.9	2161	281
8.836	0.065	333.1	2152	277
8.839	0.065	333.3	2129	285
8.842	0.065	333.5	2096	290
8.845	0.065	333.7	2060	286
8.848	0.066	333.9	2030	283
8.850	0.066	334.1	2014	291
8.853	0.066	334.3	2008	306
8.856	0.066	334.5	2071	181
8.859	0.066	334.7	2077	175
8.862	0.067	334.9	2079	184
8.864	0.067	335.1	2092	190
8.867	0.067	335.3	2105	181
8.870	0.067	335.5	2131	183
8.874	0.068	335.8	2123	238
8.877	0.068	336.0	2177	210
8.880	0.068	336.2	2200	209
8.883	0.069	336.4	2198	202
8.885	0.069	336.6	2188	201
8.888	0.069	336.8	2183	211

Age (ka BP) - from 1950	Age Error (ka)	Depth from top (mm)	REF-07 mean CT numbers >1000 HU	REF-07 mean CT number st.dev.
8.891	0.069	337.0	2183	225
8.894	0.070	337.2	2184	238
8.897	0.070	337.4	2177	247
8.900	0.070	337.6	2179	255
8.902	0.070	337.8	2183	261
8.905	0.071	338.0	2185	250
8.908	0.071	338.2	2179	223
8.911	0.071	338.4	2169	202
8.915	0.071	338.7	2165	197
8.918	0.072	338.9	2167	215
8.921	0.072	339.1	2173	251
8.923	0.072	339.3	2191	270
8.926	0.073	339.5	2213	271
8.929	0.073	339.7	2242	260
8.932	0.073	339.9	2260	265
8.935	0.073	340.1	2267	280
8.937	0.074	340.3	2256	289
8.940	0.074	340.5	2241	292
8.943	0.074	340.7	2232	288
8.946	0.074	340.9	2241	282
8.949	0.075	341.1	2266	272
8.951	0.075	341.3	2294	259
8.956	0.075	341.6	2316	249
8.958	0.076	341.8	2326	241
8.961	0.076	342.0	2327	227
8.964	0.076	342.2	2320	214
8.967	0.077	342.4	2305	217
8.970	0.077	342.6	2285	219
8.973	0.077	342.8	2261	212
8.975	0.077	343.0	2244	203
8.978	0.078	343.2	2251	205
8.981	0.078	343.4	2286	209
8.984	0.078	343.6	2335	211
8.987	0.079	343.8	2379	216
8.989	0.079	344.0	2402	231
8.992	0.079	344.2	2412	250
8.995	0.080	344.4	2413	266
8.999	0.080	344.7	2405	290
9.002	0.080	344.9	2395	301
9.005	0.081	345.1	2383	295
9.008	0.081	345.3	2379	268
9.010	0.081	345.5	2388	237
9.013	0.082	345.7	2394	217
9.016	0.082	345.9	2399	204

Age (ka BP) - from 1950	Age Error (ka)	Depth from top (mm)	REF-07 mean CT numbers >1000 HU	REF-07 mean CT number st.dev.
9.019	0.082	346.1	2390	204
9.022	0.082	346.3	2381	219
9.024	0.083	346.5	2365	239
9.027	0.083	346.7	2337	254
9.030	0.083	346.9	2292	267
9.033	0.084	347.1	2238	281
9.036	0.084	347.3	2188	296
9.040	0.084	347.6	2158	307
9.043	0.085	347.8	2151	327
9.045	0.085	348.0	2159	356
9.048	0.085	348.2	2241	232
9.051	0.086	348.4	2234	218
9.054	0.086	348.6	2197	231
9.057	0.086	348.8	2130	288
9.060	0.087	349.0	2069	353
9.062	0.087	349.2	2030	388
9.065	0.087	349.4	2026	389
9.068	0.088	349.6	2046	355
9.071	0.088	349.8	2066	337
9.074	0.088	350.0	2078	334
9.076	0.089	350.2	2073	344
9.081	0.089	350.5	2062	348
9.083	0.089	350.7	1993	397
9.086	0.090	350.9	1999	339
9.089	0.090	351.1	2002	298
9.092	0.090	351.3	2004	268
9.095	0.091	351.5	2005	251
9.097	0.091	351.7	2008	245
9.100	0.091	351.9	2004	241
9.103	0.092	352.1	1998	231
9.106	0.092	352.3	1986	218
9.109	0.092	352.5	1970	216
9.111	0.093	352.7	1950	203
9.114	0.093	352.9	1936	184
9.117	0.093	353.1	1931	169
9.120	0.094	353.3	1938	173
9.124	0.094	353.6	1946	209
9.127	0.095	353.8	1944	254
9.130	0.095	354.0	1930	281
9.133	0.095	354.2	1893	283
9.135	0.096	354.4	1848	277
9.138	0.096	354.6	1860	190
9.141	0.096	354.8	1843	169
9.144	0.097	355.0	1841	159

Age (ka BP) - from 1950	Age Error (ka)	Depth from top (mm)	REF-07 mean CT numbers >1000 HU	REF-07 mean CT number st.dev.
9.147	0.097	355.2	1838	168
9.149	0.097	355.4	1837	194
9.152	0.098	355.6	1839	225
9.155	0.098	355.8	1813	290
9.158	0.098	356.0	1849	276
9.161	0.099	356.2	1888	273
9.165	0.099	356.5	1919	290
9.168	0.100	356.7	1940	292
9.170	0.100	356.9	1947	288
9.173	0.100	357.1	1945	280
9.176	0.101	357.3	1929	293
9.179	0.101	357.5	1898	341
9.182	0.101	357.7	1880	382
9.184	0.102	357.9	1873	351
9.187	0.102	358.1	1845	368
9.190	0.102	358.3	1783	369
9.193	0.103	358.5	1756	362
9.196	0.103	358.7	1720	260
9.198	0.103	358.9	1644	230
9.201	0.104	359.1	1730	260
9.205	0.104	359.4	1834	149
9.208	0.105	359.6	1812	168
9.211	0.105	359.8	1606	343
9.214	0.105	360.0	1635	249
9.217	0.106	360.2	1627	268
9.220	0.106	360.4	1719	186
9.222	0.106	360.6	1742	223
9.225	0.107	360.8	1783	246
9.228	0.107	361.0	1842	272
9.231	0.108	361.2	1809	395
9.234	0.108	361.4	1885	343
9.236	0.108	361.6	1852	354
9.239	0.109	361.8	1993	436

Appendix C

H.E. Ridley, J.U.L. Baldini, K.M. Prufer, I.W. Walczak, and S.F.M. Breitenbach – High-resolution monitoring of Yok Balum Cave, Belize: An investigation of seasonal ventilation regimes and the atmospheric and drip-flow response to a local earthquake. *Journal of Cave and Karst Studies*, v. 77, no. 3, p. 183–199, DOI: 10.4311/2014ES0117

HIGH-RESOLUTION MONITORING OF YOK BALUM CAVE, BELIZE: AN INVESTIGATION OF SEASONAL VENTILATION REGIMES AND THE ATMOSPHERIC AND DRIP-FLOW RESPONSE TO A LOCAL EARTHQUAKE

Harriet E. Ridley[1]*, James U.L. Baldini[1], Keith M. Prufer[2], Izabela W. Walczak[1], and Sebastian F.M. Breitenbach[3]

Abstract: The nature of cave ventilation is of interest to cavers, speleologists, and paleoclimatologists working with stalagmites. Because cave ventilation systematics may change over the growth span of a stalagmite, understanding what factors affect them is critical for determining events that may have affected climate proxies within the stalagmite. Similarly, understanding how the hydrology of the drips feeding a stalagmite evolves through time is key to building robust records of paleoclimate, particularly because stalagmite records have become critical archives of climate change information of the last 500,000 years. Here we present data from an extensive, on-going monitoring effort at Yok Balum Cave, Belize, initiated in 2011, that characterizes high-resolution ventilation dynamics at this site. Clear seasonal ventilation regimes exist, driven by thermally induced inside-outside air density differences. The winter regime is dominated by air inflow into the cave, decreased drawdown from the epikarst into the cave, and a limited diurnal signal. Conversely, summer ventilation is dominated by air outflow from the cave, greater CO_2 drawdown and drip water degassing, and a strong diurnal signal. Active monitoring during a large (M7.4) earthquake in November 2012 provides a unique opportunity to assess the response of the cave atmosphere and hydrology to substantial seismic activity. Cave atmosphere dynamics and hydrology are found to be highly resilient to seismic activity, with no observable disturbance occurring around the earthquake, despite there being considerable evidence of physical disruption in the cave. Monitoring included different kinds of drips, and the earthquake affected none of the monitored drip types. This suggests that stalagmite-derived paleoclimate records are not affected by seismic activity, except in extreme cases where the stalagmite or conjugate stalactite is damaged or reoriented.

Introduction

Characterizing caves in terms of their unique ventilation processes is important, as it has a first-order control on atmosphere composition, can potentially lead to seasonal bias in speleothem growth; and consequently, has significant implications when interpreting paleoclimate proxy signals from speleothems (Kowalczk and Froelich, 2010; Baldini, 2010; Sanchez-Canete et al., 2013). Cave atmosphere data are also useful when characterizing cave ecosystems (Oh and Kim, 2011; De Freitas et al., 1982) and assessing the suitability of caves for industry and tourism (De Freitas et al., 1982; Smithson, 1991; Dueñas et al., 1999; Dueñas et al., 2011; Virk et al., 1997). Estimation of cave ventilation is possible directly via anemometers, indirectly via measurement of levels of radon gas (^{222}Rn) (Kowalczk and Froelich, 2010; Hakl et al., 1997; Faimon et al., 2006; Oh and Kim, 2011) and other tracer gases (De Freitas et al., 1982), or by studies of air density contrasts and thermal patterns within the cave (Faimon et al., 2012; Smithson, 1991; Sanchez-Canete et al., 2013). The importance of understanding specific cave ventilation mechanisms has been well highlighted in recent studies (Kowalczk and Froelich, 2010; Cowan et al., 2013; Mattey et al., 2010; Baker et al., 2014), as the distinct nature of ventilation in individual caves can negate general assumptions regarding the seasonality of carbonate precipitation. For example, Mattey et al. (2010) identified unusual seasonal ventilation regimes in New St. Michaels Cave, Gibraltar, where the summer season was typified by low cave-air pCO_2. This proved important when linking seasonal regimes to calcite fabric, paired annual laminae, and stable isotope and trace element variability, and highlighted the importance of understanding particular cave environments. Studies like this become increasingly important as speleothem-based paleoclimate

* Corresponding author: h.e.ridley@durham.ac.uk
[1] Department of Earth Sciences, University of Durham, Durham, DH1 3LE, UK.
[2] Department of Anthropology, University of New Mexico, Albuquerque, NM 87106, USA.
[3] Department of Earth Science, University of Cambridge, Cambridge, CB2 3EQ, UK.

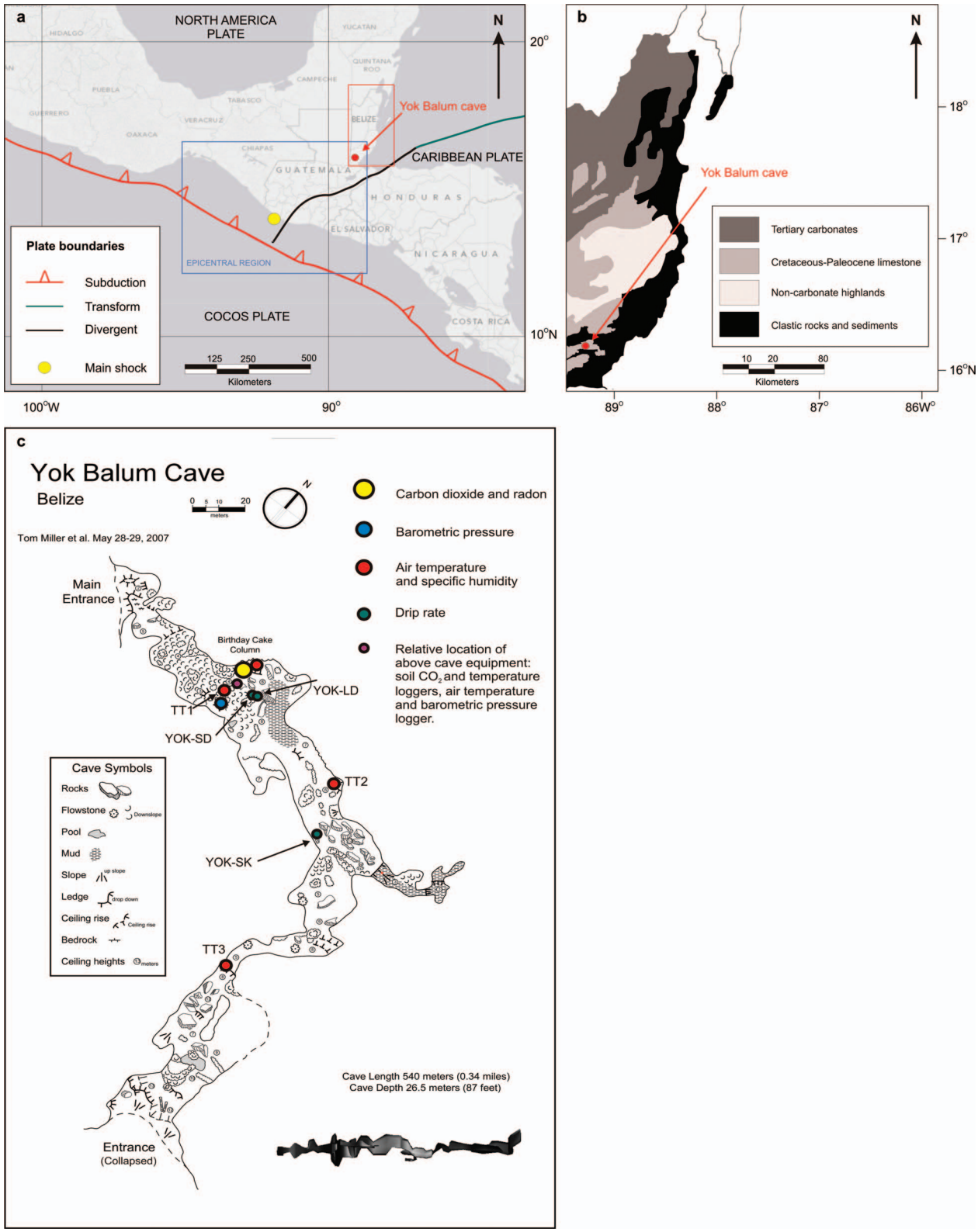

Figure 1. (a) Tectonic setting of Belize region, including tectonic boundaries (adapted from the U. S. Geological Survey). Estimated epicenter (yellow dot) and epicentral region (blue rectangle) of 7th November 2012 earthquake. Red box identifies Belize, Yok Balum Cave (red dot) and the area covered in (b), which is a geological schematic of Belize (adapted from Miller, 1996) with the location of Yok Balum Cave (red dot). (c) Map of Yok Balum Cave with equipment locations and drip sites monitored in this study.

research continues to develop higher-resolution records that are resolved to a seasonal or sub-seasonal level.

Caves in seismically active regions can display considerable evidence of past seismic activity, such as broken speleothems, speleothem growth anomalies and deformation, displacement, and rock-fall events (Becker et al., 2006; Gilli, 1999; Gilli and Serface, 1999; Gilli and Delange, 2001). A limited number of studies have attempted to quantify the effect seismic activity may have on the atmosphere in a karst cave (Sebela et al., 2010; Virk et al., 1997), particularly with regard to CO_2 variability. Such information is pertinent when interpreting proxy paleoclimate evidence from speleothems in caves that may have been subject to substantial tectonic activity, as seismic activity affects cave ^{222}Rn and CO_2 levels through pro-/co-seismic degassing and increased influx to the cave (Sebela et al., 2010; Wu et al., 2003; Virk et al., 1997; Menichetti, 2013). Crushing of material during seismic activity increases the rock's permeability for ^{222}Rn gas and CO_2, leading to higher in-cave concentrations. Cave-air pCO_2 levels exert a strong control on carbonate-precipitation rates (Baldini, 2010; Kowalczk et al., 2008; Palmer, 2007; Banner et al., 2007); and therefore, substantial crustal degassing has the potential to stagnate speleothem growth, particularly in deep, poorly ventilated passages. This can complicate paleoclimate-proxy interpretations from speleothems for weeks to years, depending on site-specific ventilation regimes. ^{222}Rn is a radioactive yet inert tracer gas frequently used to assess cave ventilation (Kowalczk and Froelich, 2010; Oh and Kim, 2011), but it can also pose a health risk in confined, poorly ventilated caves (Field, 2007; Virk et al., 1997); therefore, its relation to seismic activity warrants assessment, particularly in caves used for commercial or tourism purposes. It is also largely unknown how seismic activity may affect karst hydrology and stalagmite-drip regimes. Changes in the hydrological regime feeding a stalagmite can affect speleothem growth rates and the transmission of geochemical signals from overlying climate to the speleothem carbonate; consequently, changes in hydrology can have important implications when interpreting paleoclimate-proxy data in speleothems.

This study presents high-resolution cave monitoring data from Yok Balum Cave, Belize. These data provide detailed information regarding seasonal cave ventilation mechanisms by demonstrating cave pCO_2 and air density relationships and examination of thermal gradients as evidence of internal-external air exchange. An understanding of the subtle seasonally variable fluxes of cave air CO_2 allows improved interpretations from not only Yok Balum, but also other tropical sites. Additionally, active monitoring during a large (M7.4) earthquake in November 2012 provides a unique opportunity to assess the response of cave atmosphere and hydrology to substantial seismic activity.

Study Site

Yok Balum Cave (Mopan Mayan for Jaguar Paw Cave) is located in the Toledo District of southern Belize, approximately 3 km south of the modern Mopan Maya village of Santa Cruz (16°12′30″ N, 89°4′24″ W; 366 m above sea level) (Fig. 1a). The cave is developed within the tectonically uplifted Cretaceous Campur Limestone formation that originated from massive limestone deposition around the granite intrusions composing the Maya Mountains to the north (Miller, 1996; Kennett et al., 2012). The cave is one of several that occur in a southwest-to-northeast-trending limestone-karst ridge (Fig. 1b), and its formation was likely associated with the vertical flow of chemically aggressive allogenic water originating on the highlands of the Maya Mountains (Miller, 1996), although no stream exits within the cave today. Yok Balum extends approximately 540 m as a main trunk passage from a small opening in the west, the main entrance, to a larger, more elevated opening to the south, the second entrance (Fig. 1c). The second entrance resulted from cave collapse probably associated with tectonic activity. U-series dating of the base of a stalagmite growing on a breakdown block associated with the creation of the second entrance dates the collapse at a minimum of 44,000 $\pm$ 3300 years BP. There is also considerable evidence of seismic activity within the cave, including large faulted flowstones and displaced speleothems. U-series dating of carbonate precipitated within a faulted flowstone provided a date of 26,400 $\pm$ 170 years BP.

The western coast of Central America displays relatively high seismic-hazard potential due to the subduction of the Cocos Plate beneath the North American and Caribbean Plates (Fig. 1a). A divergent boundary exists between the North American and Caribbean Plates approximately 100 km south of the southern Belize border. The dominant source of seismic activity felt in southern Belize, however, results from intermediate depth earthquakes occurring within the subducted Cocos Plate.

Monitoring Instrumentation

Tropical environments provide a challenging environment for electronic monitoring instrumentation, especially for long term monitoring studies in remote areas. In this study, the threat of malfunction due to high humidity and water was minimized by keeping non-waterproof equipment in airtight boxes and sealed plastic bags with a silica desiccant where applicable. Above-cave soil temperature was recorded hourly using a Tiny tag temperature logger buried at a 0.4 m depth. Cave-air CO_2 was monitored every three hours between April 2011 and January 2013 (with a four month break from June 2012 to October 2012 due to equipment failure) using a Vaisala Carbocap carbon-dioxide probe DMP343 ($\pm$ 3 ppmv + 1% of reading) linked to a Vaisala MI70 indicator and powered by two Duracell MN918 lantern batteries. A Radon Scout Plus, powered by two D-cell batteries and a four-D-cell external battery pack was

Table 1. Summary of equipment used in this study, including equipment accuracy, sampling interval, and additional comments.

Parameter	Equipment	Accuracy	Monitoring Interval	Comment
Cave Air CO_2	Vaisala CARBOCAP Carbon Dioxide GMP343 Probe with Vaisala MI70 Indicator (plus two Duracell MN918 Lantern batteries)	± 3 ppmv ± 1% of reading	Three-Hourly	Tested upon installation.
Temperature	Tinytag Logger	± 0.1°C	Hourly	Data compared to Barotoll temperature data.
^{222}Rn	Radon Scout Plus (plus 4 × D-cell External battery pack)	…	Three-Hourly	Ten days of data discarded after data download due to anomalously high ^{222}Rn counts after opening the box.
Pressure and Temperature	Barotroll	± 0.1%	Hourly	Data compared to Tinytag temperature data.
Rainfall	Pluvimate Rain Gauge	± 0.01 mm	Hourly	Located at Santa Cruz village.
Drip Rate	Stalagmate Drip Logger	…	Hourly	Tested upon installation.

set up next to the within-cave CO_2 logger to measure radon fluctuations every three hours for the same time interval. The Radon Scout, being extremely sensitive to moisture, was kept in a watertight box. This resulted in a muted radon measurement, because fewer α particles reached the alpha counter. For qualitative assessment of ^{222}Rn fluctuations this was not considered an issue. However, ^{222}Rn values peaked following a data download when the logger was removed from the box. To account for this, ten days of data were removed after each data download to allow ^{222}Rn values to return to normal levels. Combined Barotroll pressure and temperature loggers were installed both inside and above the length of the cave to measure hourly barometric pressure and temperature (precision ± 0.1% and ± 0.1°C). Tinytag temperature loggers were placed in transect along the cave to measure hourly temperature. Stalagmate automated drip-loggers recorded hourly rates of drips feeding three stalagmites of potential paleoclimate interest. Data were downloaded and the equipment maintained every four months. A summary of all monitoring equipment is shown in Table 1. The location of all equipment and monitored stalagmites is shown in Figure 1c.

CAVE VENTILATION

Cave ventilation (air exchange with the outside atmosphere) has a first-order control on cave atmosphere composition and is dependent on a number of factors, including fluctuations in temperature and pressure, cave geometry, and susceptibility to external winds (Cowan et al., 2013; Bourges et al., 2001; Spötl et al., 2005; Baldini et al., 2006; Denis et al., 2005; Kowalczk and Froelich, 2010). Pflitsch and Piasecki (2003) classify cave passages in terms of air movement as being dynamic, transitional, or static. However, the static state is very rarely observed, aside from in deep passages (Pflitsch and Piaseki, 2003; Przylibski and Ciezkowski, 1999). Convective air circulation, driven by internal versus external air density differences, is a dominant ventilation mechanism in caves with more than one entrance at different elevations (Gregoric et al., 2013; Kowalczk and Froelich, 2010; Wigley, 1967; Badino, 2010). In tropical caves, where cave air temperatures do not vary significantly on seasonal timescales, air density differences will be predominantly controlled by surface temperature and barometric-pressure variations (Fairchild et al., 2006). Air density responds primarily to temperature (Faimon et al., 2012; Gregoric et al., 2013; Gregoric et al., 2011) and to a lesser extent pressure and humidity as expressed in Equation (1) below (after Kowalczk (2009)):

$$\rho_{air} = \frac{P}{R_d T_v} \quad (1)$$

where R_d is the universal gas constant and P is barometric pressure in mb. T_v is virtual temperature, calculated via Equation (2), in which both T and dew point T_d are in K.

$$T_v = \frac{T + 237.15}{1 - 0.379\left(\frac{6.11 \times 10^{\frac{7.5T_d}{237.3+T_d}}}{P}\right)} \quad (2)$$

If cave pCO_2 is more than an order of magnitude greater than that of the free atmosphere, T_v is affected. This can lead to errors of up to 9°C when calculating cave T_v (Sanchez-Canete et al., 2013), and consequently, errors in air density calculations. At Yok Balum the maximum recorded pCO_2 is 770 ppm and the summertime mean is ~ 500 ppm. This is less than an order of magnitude greater

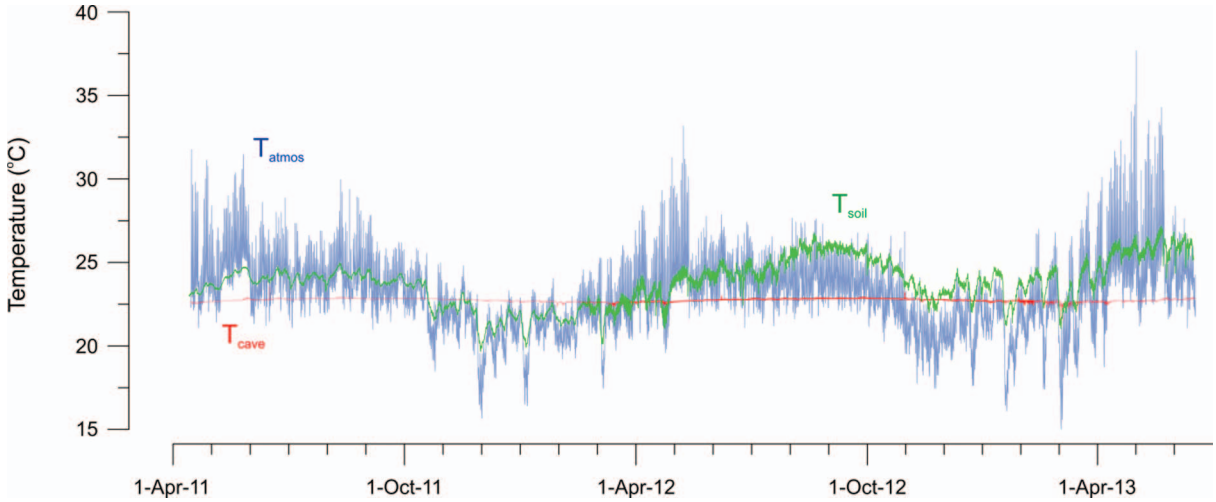

Figure 2. Time series for 26.5 months of hourly cave temperature (T_{cave}) (using the Barotroll logger), soil temperature (T_{soil}) (measured using a TinyTag), and outside air temperature (T_{atmos}) (using the Barotroll logger).

than the free atmosphere; and therefore, this CO_2 exerts a negligible effect on cave air density.

Typically, during the winter months external air temperature will be cooler than that of the cave and a positive air density difference will dominate, i.e, external air will be denser, although a diurnal signal will also exist. Alternatively, during the summer typically warmer external temperatures will result in largely negative air density differences. Local weather may result in short-lived reversals in cave/atmosphere air density differences. The particular ventilation influence of seasonal air density differences between cave and free atmosphere is governed by the cave geometry (e.g., passage orientation and size), the distance from cave entrances, and total cave volume (Batiot-Guilhe et al., 2007; Cowan et al., 2013).

Results and Discussion of Ventilation

The diurnal and seasonal patterns of airflow at Yok Balum are a direct response to a thermally induced disequilibrium in air density between the cave and outside air, similar to other caves (De Freitas et al., 1982; Kowalczk and Froelich, 2010). Within-cave temperature is nearly constant at 22.4°C ($\pm$ 0.5°C) year-round, although a low-amplitude diurnal signal is present. Within-cave temperature is equivalent to the average yearly external temperature (Fig. 2) and is likely a result of moderation of outside temperatures by the epikarst. External air temperature can affect cave air pCO_2 by both inducing density-driven ventilation associated with inside-outside air density differences (De Freitas et al., 1982) (Fig. 3a) and by causing higher soil pCO_2 by stimulating biological activity in the soil zone (Baldini et al., 2008; Bond-Lamberty and Thomson, 2010; Hess and White, 1993; Murthy et al., 2003; Sherwin and Baldini, 2011).

The simple structure of Yok Balum Cave, with two entrances at either end of a single main trunk passage, results in a well-ventilated dynamic cave system, evidenced by the low annual mean CO_2 values (461ppm) (Fig. 3b). However, CO_2 displays clear seasonal trends in both mean concentration and variability. Summer (April–October) is characterized by higher mean pCO_2 ($\sim$ 500 ppm) and high temporal variability (standard deviation of 72.5 ppmv) whereas winter (November–March) has lower pCO_2 ($\sim$ 420 ppm) and displays lower temporal variability (standard deviation 24.3 ppmv). Here, we use the theory of entropy of curves to highlight the differences between summer and winter ventilation. Entropy (E) is a measure of variance within a dataset. It is described as the mean cumulative sum of absolute first differences of a time or spatial derivative (Denis et al., 2005; Denis and Crémoux, 2002), or specifically, in this case, the average change in pCO_2 values at 3-hour intervals. Higher entropy values indicate a greater change in subsequent pCO_2 measurements; and therefore, an indication of variance within subsets of the dataset. CO_2 displays entropy of approximately 430 during the summer and 150 during the winter (Fig. 3b), indicating that the variance is nearly three times greater during the summer months. These trends in pCO_2 mean values and variance are controlled by seasonal CO_2 flux into the cave and ventilation, most likely controlled by external temperatures and infiltrating rainfall. The following sections will use high-resolution-monitoring data to describe the seasonal ventilation regimes occurring in Yok Balum. It should be noted that the summer and winter seasons are not synonymous with the wet and dry seasons.

Summer Regime

Air density differences between the cave and the free atmosphere, controlled predominantly by external

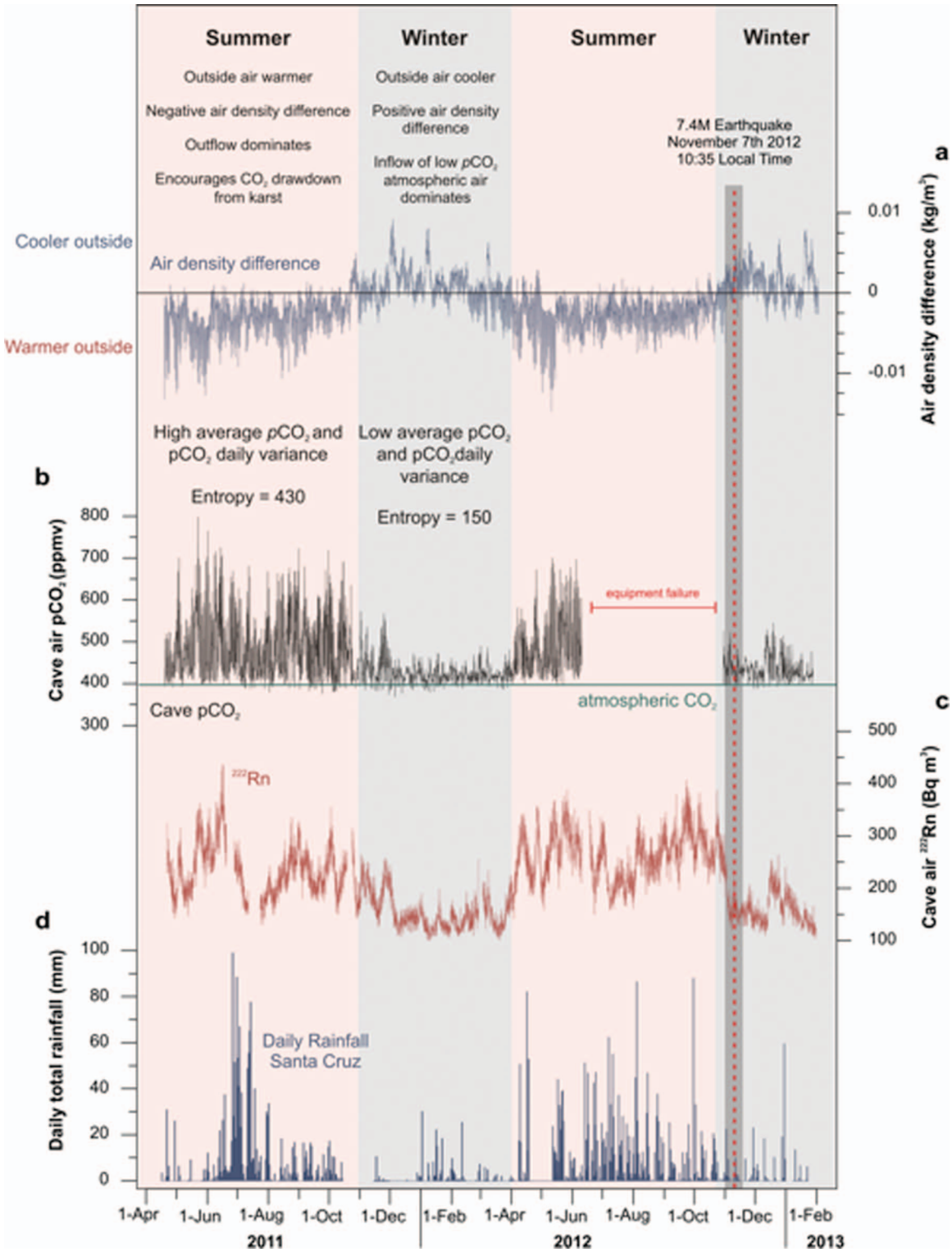

Figure 3. Seasonal regimes and dominant characteristics of (a) hourly inside versus outside air density difference. (b) Three-hourly cave pCO_2 and summer (April through October) and winter (December through March) pCO_2 entropy values. Horizontal line at about 400 ppmv is CO_2 content of outside air, presumed constant. Three hourly ^{222}Rn (c) and daily rainfall at Santa Cruz (d). November 7 earthquake indicated by the red dashed line and surrounding two-week period by the gray-shaded section.

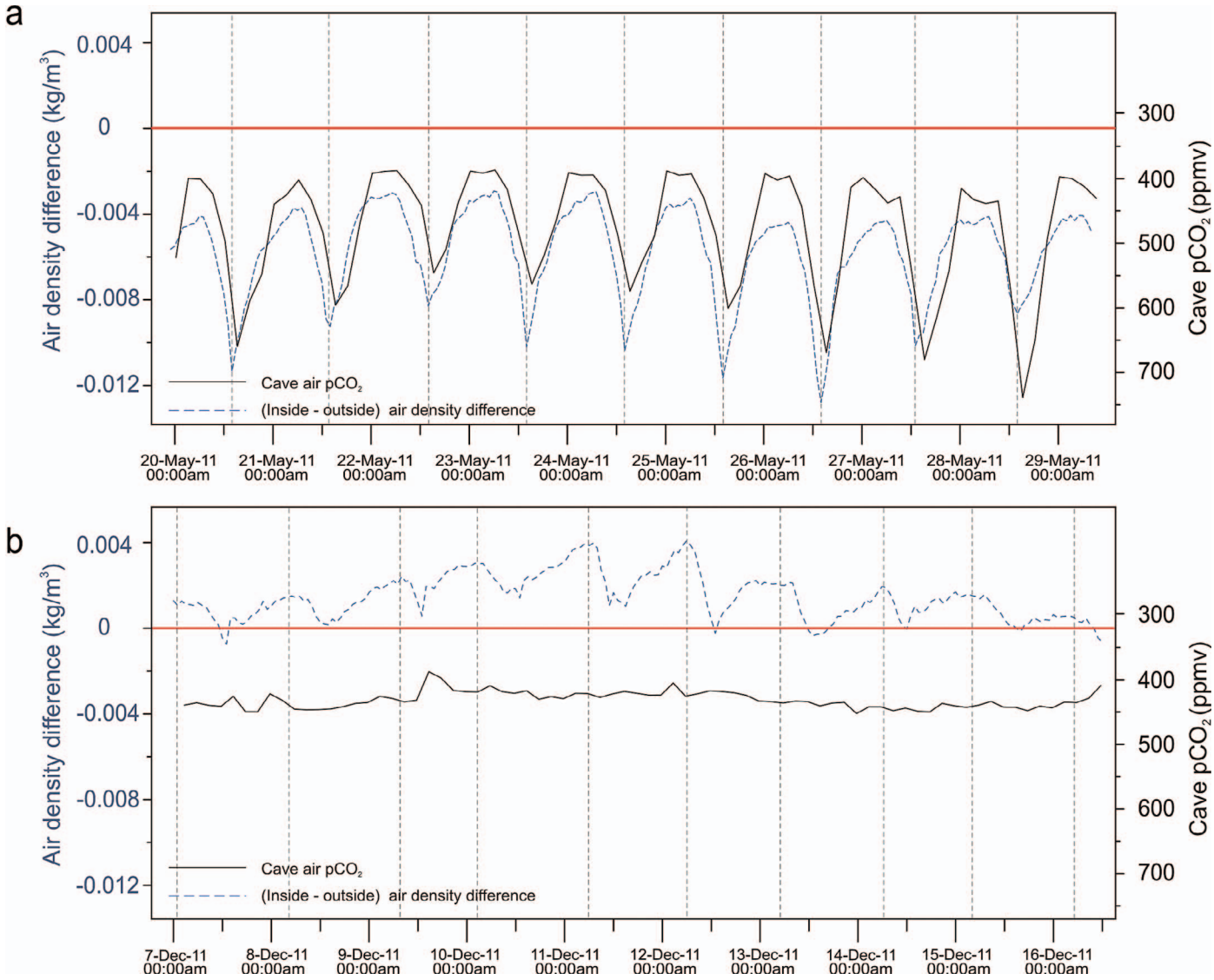

Figure 4. Hourly density difference between cave and outside air and cave pCO_2 over (a) December 7–16, 2011 (winter) and (b) May 20–39, 2011 (summer).

temperature, drives the summer season diurnal ventilation regime. Outside air temperatures (T_{atmos}) are higher on average than that inside the cave (T_{cave}) producing an almost constant negative air density difference (Fig. 3b). In a typical one-entrance cave system this could cause severe season-long stagnation and consequently very high pCO_2 as the cooler, denser cave air becomes trapped at the lowest point of elevation in the cave (Cowan et al., 2013; Spötl et al., 2005). At Yok Balum complete stagnation does not occur because the dual-entrance system provides for density-driven flow from the more elevated southern entrance to the lower western entrance.

Outside air temperature begins to rise around 0600 and reaches a maximum in the early afternoon. At this point cave/atmosphere air density difference is greatest and air outflow is at a maximum (Fig. 4a). As the air density difference increases during this period, outflow occurs at both entrances; CO_2 concentrations will simultaneously increase as high pCO_2 air is drawn out of the overlying epikarst and soil zones (Fig. 5a). During the day, biological activity in the soil will also be at a diurnal maximum, producing higher soil pCO_2. By late afternoon the cave/atmosphere air density difference begins to decrease and the volume of outflowing air decreases, reducing CO_2 drawdown from the epikarst. Outflow at the lower main entrance weakens or ceases completely. As the cave/atmosphere air density difference reaches a minimum, around 0100, cave air pCO_2 reaches minimal values. This is most likely due to minimized CO_2 drawdown and inflow of low-pCO_2 atmospheric air from the second entrance if T_{cave} reaches or surpasses T_{atmos}, flushing through the cave from the second entrance to the lower main entrance (Fig. 5b). If the

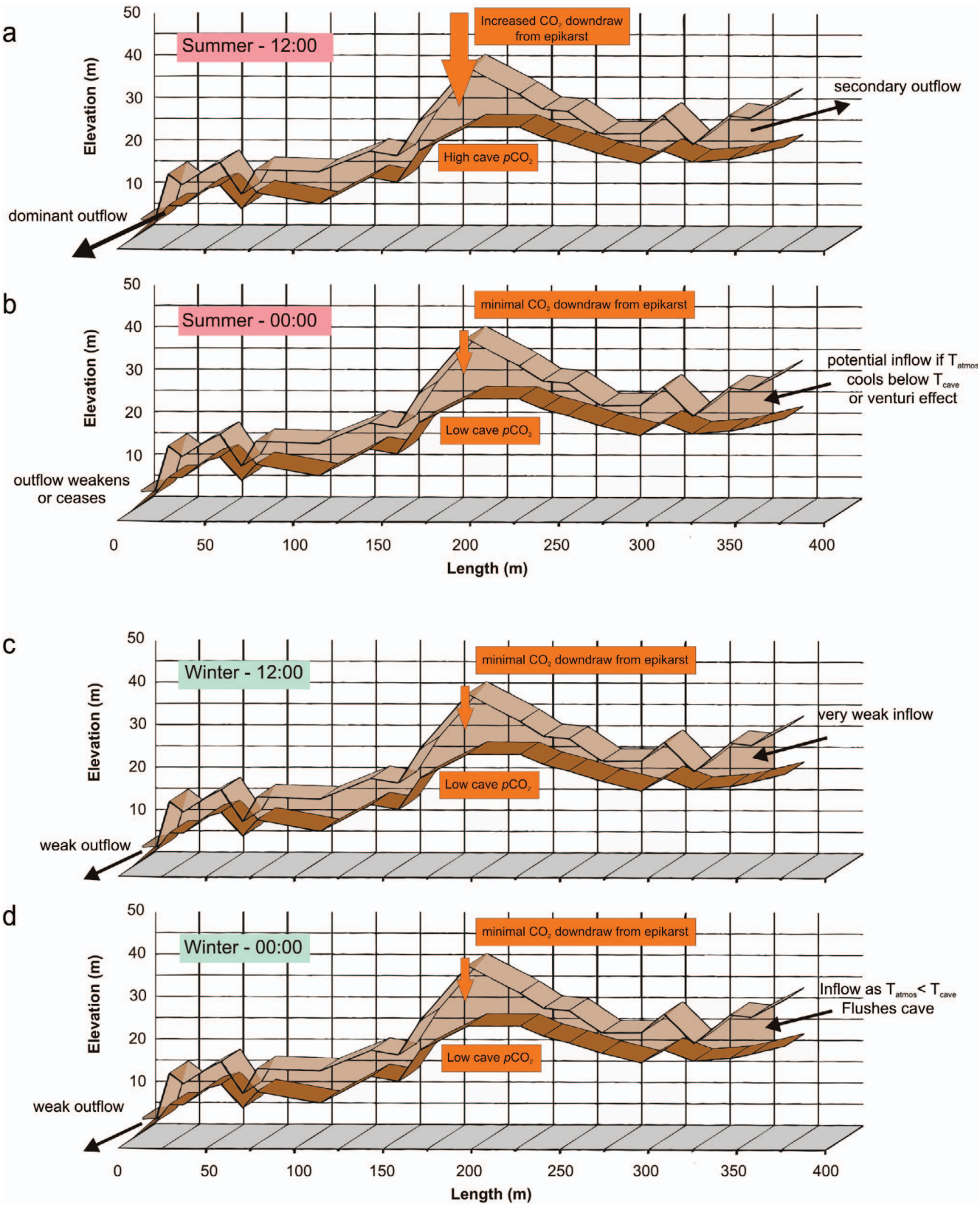

Figure 5. Yok Balum long profile with schematic of theorised primary air flows and CO_2 flux during the summer at noon (a) and midnight (b). Schematic of theorised primary air flows and CO_2 flux during the winter at 1200 (c) and 0000 (d).

outside air density remains considerably higher than that of the cave, then pCO_2 may remain elevated, but will decrease somewhat due to decreased CO_2 drawdown from the epikarst, lower soil activity, and some air movement driven by the venturi effect (Fig. 5b). Areas closest to the entrances can be expected to undergo the most ventilation, particularly at the second entrance, which is larger. Increased water through-flow during the wet season is undoubtedly an additional driver of higher average summer pCO_2, as it increases dissolved CO_2 transport to the cave, increasing degassing, and consequently, producing higher cave pCO_2.

Winter Regime

During the winter season, outside air temperatures are generally cooler than those inside the cave, producing a positive air density difference and a ventilation regime dominated by inflow. Ventilation is therefore more continuous than during the summer.

Maximum air density difference occurs at night (around 0300) when T_{atmos} is at a minimum (Fig. 4b). Cooler outside air flushes into the cave, predominantly through the more elevated second entrance, but also from the main entrance. Cave-air pCO_2 will therefore approximate that of the external atmosphere. Outside air temperatures begin to rise at about 0600 and reaches a maximum at about 1400, as in the summer season. However, as the outside temperature increases, it approaches that of the cave air, reducing the air density difference to near zero, or to negative values if T_{cave} surpasses T_{atmos}. This reduces air inflow to the cave, and if a negative air density difference occurs, then outflow may occur during this time (Fig. 5c). This variation of air density difference over a threshold value results in a daily ventilation regime whereby the cave inhales during the day and exhales at night. The inhalation during the day draws low-pCO_2 air into the cave, flushing the cave and keeping pCO_2 values similar to atmospheric levels (Fig. 5d). Any weak exhalation at night continues effective air turnover and maintains low pCO_2 concentrations. Again, it is the areas close to the entrances that will undergo the most rigorous air turnover.

A combination of inflow-dominated ventilation and less CO_2 from drip-water degassing keeps winter cave-air pCO_2 at near atmospheric levels. A less distinct diurnal regime is observed in CO_2 and air density difference variability. During the summer, increased water through-flow, strong air outflow and large CO_2 drawdown increase average pCO_2 and daily variability.

Temperature Observations

Hourly temperature data are used as an indicator of air movement to determine seasonal modes of ventilation and to understand exactly how air moves through the cave. We use Tinytag (TT) temperature loggers at different sites to assess thermal variability. TT3, a temperature logger located about 50 m from the second entrance, shows more variance than TTI, located about 50 m from the main entrance, and TT2, located in the midsection of the cave about 100 m from the main entrance and about 140 m from the second entrance (Fig. 6e). TT2 displays the least variance and most moderated temperature (Fig. 6b). Entropy (see section 5) can be illustrated graphically through time as a cumulative curve, the slope of which indicates variability within the dataset. Entropy curves are calculated for each temperature dataset from the three loggers (Fig. 6a), thus facilitating comparison of their variance with time. TT3 displays the greatest variability over the whole time series, suggesting that this region of the cave is most strongly coupled with external air temperatures via air exchange. During the summer months TT3 increases by 0.4°C, as air in this region responds to warmer external temperatures. TT2 is stable through the same period, and TT1 displays an increase similar to that of TT3, but of only 0.3°C. This thermal variability decreasing with distance from a cave entrance is in accordance with a traditional cave temperature models (Wigley, 1967) and previous thermal profile studies of caves (Sanchez-Canete et al., 2013; De Freitas et al., 1982).

During the winter, TT3 displays greater variance than the other two loggers, again indicating that this section of the cave is more closely coupled to the outside air during winter than summer (Fig. 6). This is consistent with the ventilation mechanism described in the previous section, where inflow of cooler atmospheric air dominates the winter ventilation regime, simultaneously lowering long-term cave-air temperature in this area of the cave and mimicking the diurnal external temperature cycle in the cave. TT2 remains the least variable, due to its location in the midsection of the cave. TT1 decreases, indicating that cooler atmospheric air flows in, but that ventilation at the main entrance is less rigorous than at the second entrance. Furthermore, short-lived decreases in temperature recorded by TT1 (and to a lesser extent in TT2) are in anti-phase with TT3. This could be an indication of air entering at the main entrance and flushing through the cave, forcing warmer air from the less dynamic mid-section of the cave through to the second entrance, where it is recorded as a small increase in temperature at TT3. This thermal-pulse process would also operate in reverse, with cooler air entering at the second entrance and forcing air through the cave to the main entrance.

Data collected through high-resolution temperature experiments, conducted over two 14-hour intervals in June and late October 2012, are used to characterize ventilation on short time scales. A transect of three temperature loggers placed in the cave recorded temperature every 10 seconds to capture very short-term thermal fluctuations overnight, from 1800 to 0800. Failure of one of the loggers during the June experiment limits the number of loggers to two, but does not affect data interpretation for this project. During the June experiment (Fig 8) the two temperature loggers, TT5 and TT7, record essentially static temperature, supporting the idea that air density driven outflow dominates during this season. During the logging interval, the cave air density difference does not drop below zero and so

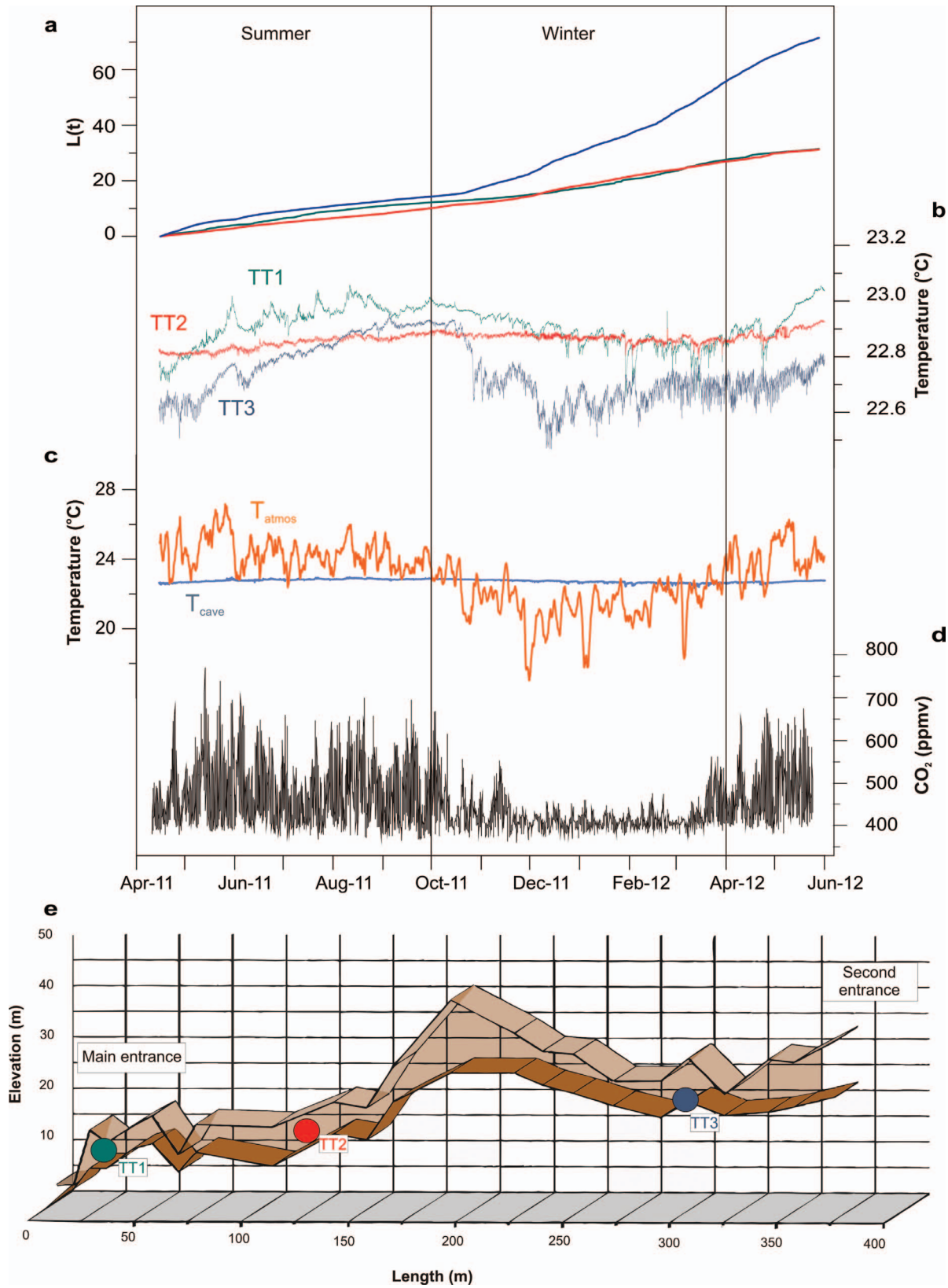

Figure 6. Time series for 14 months of (a) variability L(t) of three temperature time-series expressed as entropy (cumulative sum of the absolute first differences) against time, (b) hourly temperature from the three temperature loggers in the cave, (c) hourly record of temperatures inside (TT2) and outside the cave, (d) three hourly cave air pCO_2, and (e) location of temperature loggers within the cave.

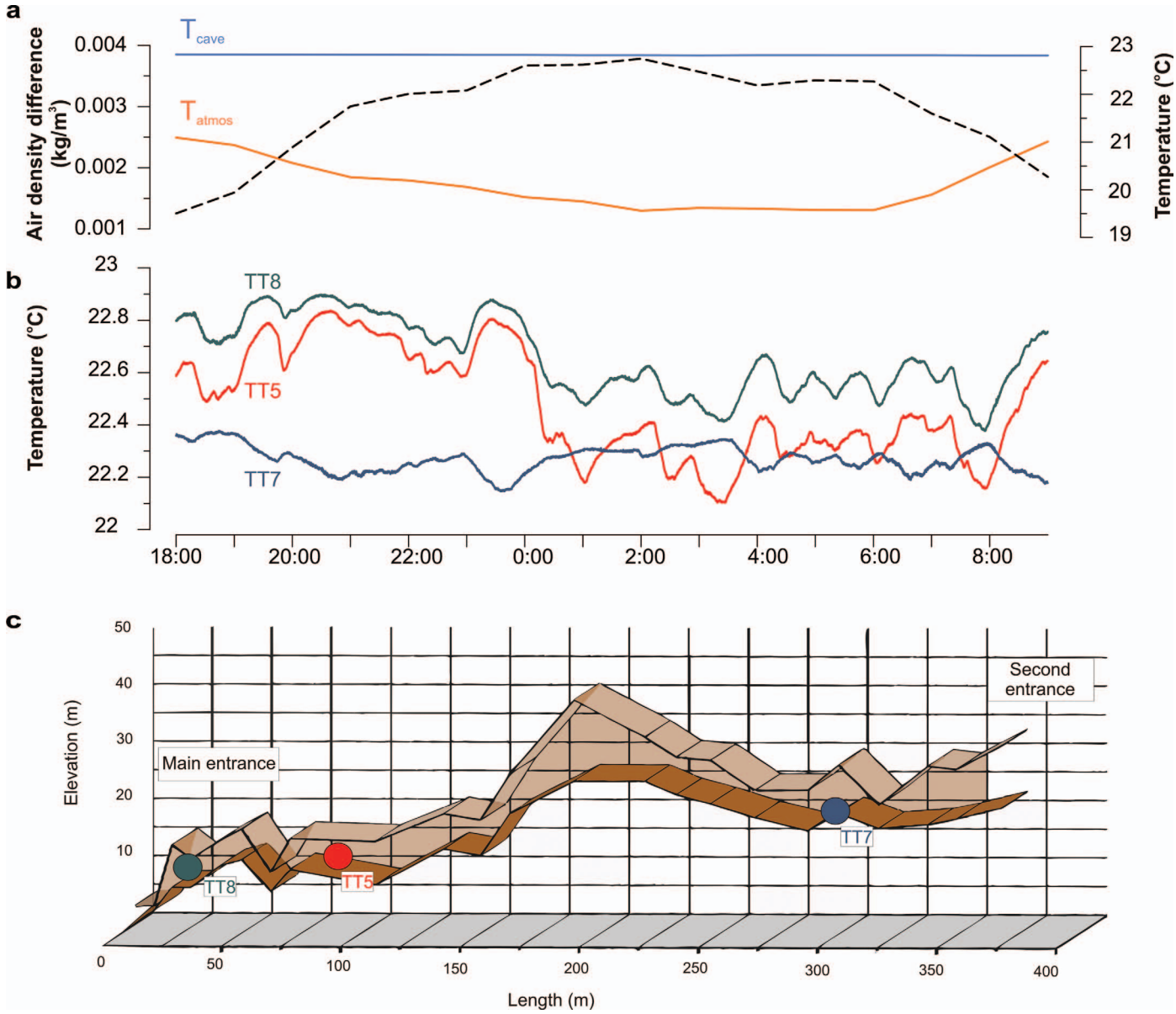

Figure 7. High-resolution winter experiment. Fourteen-hour time series of (a) hourly cave temperature, external air temperature, and internal/external air density difference and (b) 10-second temperature measurements of TT8, TT5, and TT7. (c) shows location of TT8, TT5, and TT7 in the cave.

inflow does not occur. During the late-October experiment, thermal variance at all three sites is much greater (Fig. 7). TT5 and TT8 record more thermal variability than TT7, suggesting that air inflow close to the main entrance is less persistent. TT5 and TT7 both record cooler temperatures than TT8, presumably due to their proximity to a cave entrance. TT8 and TT5 track each other, roughly in accordance with cave/atmosphere air density difference and are weakly in anti-phase with TT7. This is similar to what we see in the longer-term record (Fig. 6), where cooler external air enters the main entrance and forces air along the main passage, which is recorded as a pulse of warmer deep-cave air at the second entrance. It would appear from this high-resolution time series that this occurs in both directions. The limited temporal timeframe of these two experiments hinders making firm conclusions about the diurnal movement of air at Yok Balum Cave, but it is encouraging that the results acquired are in agreement with the longer, hourly-resolution time series.

November 7 Earthquake

On November 7, 2012, at 1635 (UTC; 1035 local time) a 7.4 magnitude earthquake struck off the coast of Guatemala (Fig. 1a). The epicentre was estimated to be at a depth of 24.0

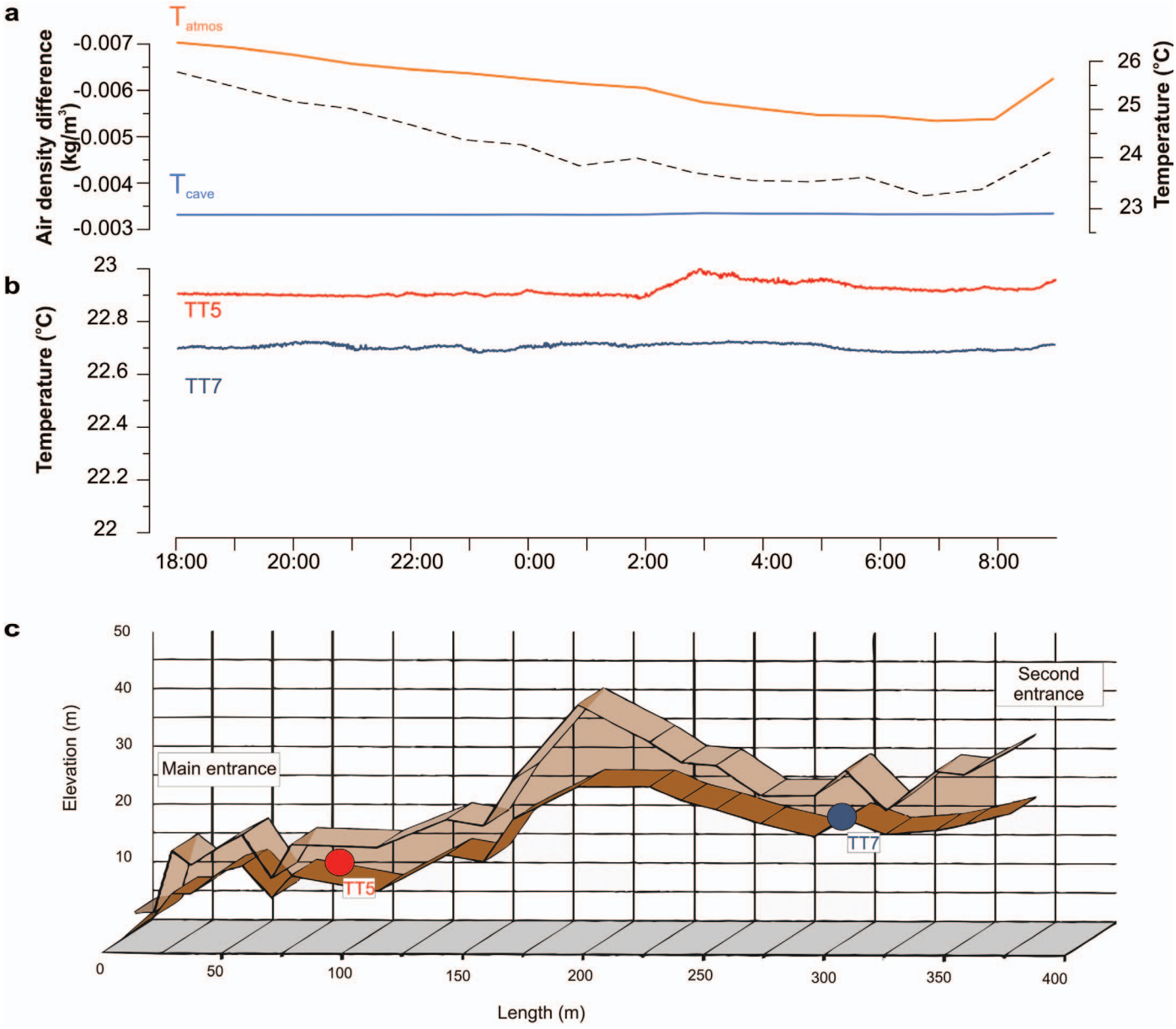

Figure 8. High-resolution summer experiment. Fourteen-hour time series of (a) hourly cave temperature (from Tinytag loggers), external air temperature, and calculated internal/external air density difference and (b) 10-second temperature measurements of TT5 and TT7. (c) shows location of TT5 and TT7 in the cave.

km and occurred as a result of thrust faulting on or near the subduction zone of the Cocos plate and the overlying Caribbean and North American plates. Tremors were felt in parts of Belize, and villagers from Santa Cruz village, 5 km from Yok Balum Cave, reported feeling the tremors. According to United States Geological Survey estimates, this shock would result in a seismic hazard, measured in peak ground acceleration at the cave site of 1.6 to 2.4 m s^{-2}. A field crew returned to the cave in January 2013 to find large fallen blocks at the cave's main entrance and numerous displaced and freshly broken stalagmites and stalactites within the cave. Reasonable evidence therefore suggests that the cave was subject to seismic activity on or around November 7, 2012. There are only a handful of published studies reporting earthquake damage to caves (Gilli, 1999; Gilli and Delange, 2001; Renault, 1970), and so direct monitoring observations of the effect of seismic activity are pertinent to the science of speleology, in general, and have implications for reconstructing climate from cave deposits. It will be particularly useful to determine how environmental variables that affect speleothem growth and carbonate deposition, such as drip hydrology and cave ventilation, may be affected be seismic

activity. For example, if seismic activity causes considerable water re-routing, we might expect subsequent changes in speleothem growth for days to months, which can confuse a climate record. Similarly, atypical speleothem growth or carbonate isotopes could be produced from significant seismically induced changes in cave pCO_2.

Cave Atmosphere Response

No clear change occurred in cave-air pCO_2 or ^{222}Rn during or for the week following the earthquake (Fig. 9). Two ^{222}Rn peaks occur around the earthquake (Fig. 9a) and although fracture dilation induced by seismic activity may cause such peaks in cave-atmosphere ^{222}Rn, these peaks are not significant, in terms of magnitude or duration, when the entire ^{222}Rn dataset is considered (Fig. 3c). A sharp increase in both ^{222}Rn and CO_2 occurs on December 20 (Fig. 3 b and c) but given the short half-life of radon (3.8 days) it is extremely unlikely that this is a delayed signal of the November 7 event. This increase could be explained instead by a coincident decrease in air density difference associated with a moderate rainfall event that temporarily reduced air inflow to the cave and resulted in a short-lived increase in CO_2 and ^{222}Rn.

A significant change in cave atmosphere may not have been observed due to the seasonal timing of the earthquake. As previously observed, cave ventilation during the winter is dominated by inflow, which acts to keep pCO_2 levels low. Seismic activity of a similar magnitude occurring during the summer season, when outflow is dominant, may lead to a discernible increase in cave air ^{222}Rn and CO_2. Potentially a clearer influence could be observed in a less well ventilated cave. Prior to the collapse and opening of the second entrance at Yok Balum, ventilation would have been less effective and cave air pCO_2 and ^{222}Rn higher. Considerable seismic activity at that time may have created uncharacteristically high pCO_2 and ^{222}Rn values as a result of limited ventilation and should be a consideration when studying speleothems from Yok Balum deposited prior to the collapse of the second entrance, when ventilation would have been restricted. Similarly, in any cave where ventilation is less efficient it may be pertinent to assess the impact of seismic activity on cave-atmospheric composition, particularly when speleothems from the cave are being considered for palaeoclimate reconstruction.

Hydrological Response

Three drip loggers were deployed during the November 2012 earthquake: YOK-SK, YOK-SD, and YOK-LD. Of these drips, two (YOK-LD and YOK-SD) were static in nature (Smart and Friederich, 1987; Baker et al., 1997), because they displayed low drip rates and low variability (Fig. 10a), indicative of a diffuse-flow-dominated hydrology. YOK-SK is classified as a seasonal drip (Baker et al., 1997), because it responds to local rainfall events and seasonal climate variability (Fig. 10a), suggesting that a fracture flow pathway is activated once a threshold rainfall rate or epikarst saturation is achieved. YOK-SK responds to local rainfall with a lag time of less than 6 days, but displays greater variability during the wet season, when the epikarst and soil are closer to saturation.

None of these three loggers recorded any clear drip response to the seismic activity on November 7 (Fig. 10b). YOK-LD and YOK-SD, the two static drips, show no response, suggesting that diffuse flow regimes are not affected by seismic activity of substantial magnitude. Similarly, YOK-SK, which at the time of the earthquake was displaying a peak in drip rate in response to rainfall events in the preceding days, shows no response outside what would be expected from the longer time series. These data suggest that preferential flow routes are not necessarily altered by seismic activity of this nature. This observation is of significant value for speleothem-based paleoclimate studies, as it suggests that seismic activity does not affect hydrological flow pathways or alter carbonate geochemistry.

Conclusions

Yok Balum is an extremely well ventilated cave system that displays distinct seasonal ventilation regimes, consistent with changes in air density differences between the cave and outside atmosphere. The winter regime is dominated by air inflow, low pCO_2, and lower epikarstic drawdown and CO_2 flux into the cave. Conversely, air outflow, high epikarstic CO_2 drawdown, increased drip-water degassing, and a strong diurnal signal dominates the summer regime. Based on air-temperature changes, the degree of air exchange increases from the center of the cave to the entrances, and the second entrance experiences greater air exchange than the main entrance, presumably due to its size. By looking at thermal fluctuations of cave air on a ten-second timescale, the direction of air movement is identified during summer and winter nights, respectively, and both entrances are found to display active dual-directional connections to the free atmosphere. The three datasets presented here: long term three-hour CO_2, hourly temperature, and the two high-resolution studies all help to build a comprehensive understanding of ventilation at Yok Balum Cave. This will be pertinent as on-going paleoclimate research at this cave. Continued monitoring will help to discern inter-annual fluctuations and identify long-term links between cave pCO_2 and local climate.

Cave pCO_2 and ^{222}Rn did not show any discernable response to the November 7 earthquake. Likewise, none of the three drips displayed any discernible hydrological response to the earthquake, suggesting that seismic activity, even of considerable magnitude, has minimal hydrological repercussions at Yok Balum and is insufficient to result in perturbations in speleothem petrographical or geochemical records. It is noteworthy that the three loggers recorded two end members of standard drip types, from highly

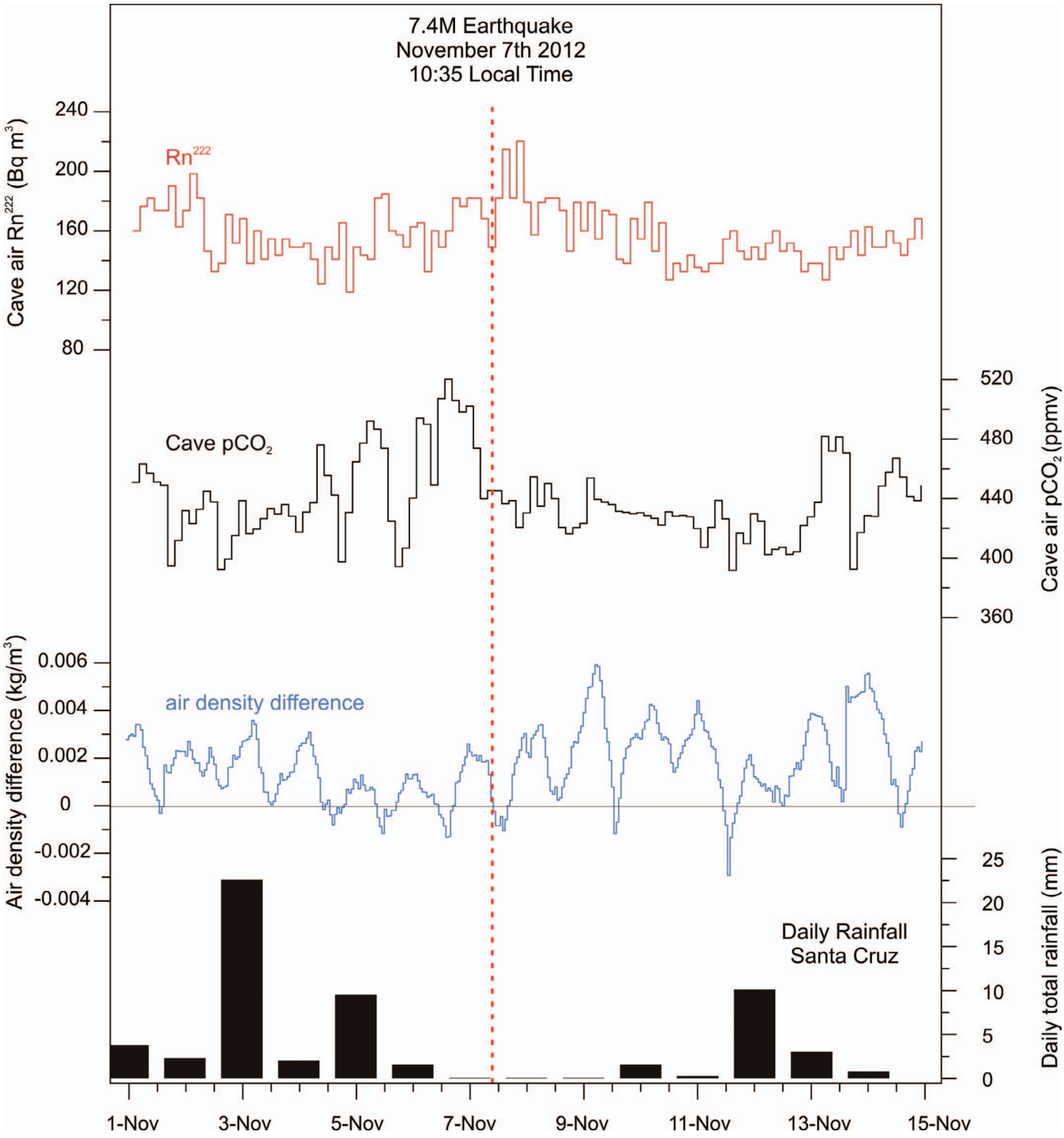

Figure 9. Traces of (a) cave-air Rn^{222}, (b) CO_2, (c) calculated inside cave versus outside air density difference, and (d) daily rainfall at Santa Cruz village during a 15-day period surrounding the November 7 earthquake (red dashed line).

diffuse, slow, and static drip rates (YOK-LD and YOK-SD), to highly variable and relatively fast drip rates (YOK-SK). This suggests that intermediate drip types would probably be similarly unaffected by seismic activity of a similar magnitude. The primary effect seismic activity may have on a speleothem record is by altering the growth-axis position or orientation, rather than a direct disruption of the overlying hydrology. This could appear as a hiatus or sudden shift in isotope values if the growth axis movement was not accounted for during milling.

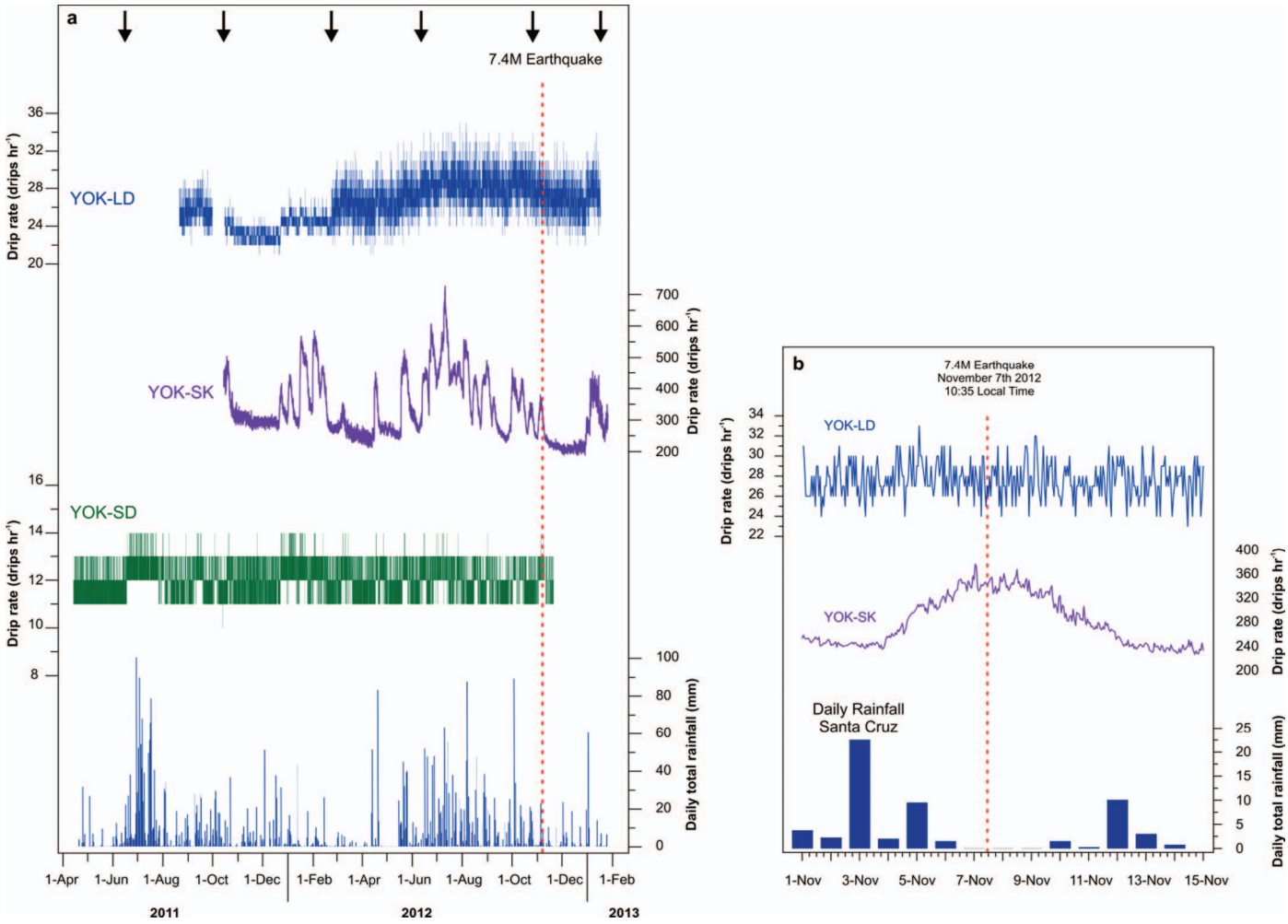

Figure 10. (a) Time series for 22 months of drip regimes of YOK-LD, YOK-SK, and YOK-SD against Santa Cruz daily rainfall; note different scales. November 7 earthquake indicated by red dashed line. Black arrows indicate visits to the cave. b) YOK-LD and YOK-SK drip- rates and Santa Cruz daily rainfall from 1 through 15 November, with time of earthquake indicated by red dashed line.

This study provides real-time data on the effect of seismic activity on cave hydrology and atmosphere. In seismically active regions, determining this site-specific response is a desirable outcome of cave monitoring studies designed to aid speleothem paleoclimate proxy interpretation. These data provide encouraging evidence that seismic activity of this level does not have implications for speleothem paleoclimate proxy interpretations from caves with similar ventilation dynamics as Yok Balum.

References

Badino, G., 2010, Underground Meteorology – "What's the Weather Underground?": Acta Carsologica, v. 39, p. 427–448.

Baker, A., Barnes, W.L., and Smart, P.L., 1997, Variations in the discharge and organic matter content of stalagmite drip waters in Lower Cave, Bristol: Hydrological Processes, v. 11, p. 1541–1555. doi:10.1002/(SICI)1099-1085(199709)11:11<1541::AID-HYP484>3.0.CO;2-Z.

Baker, A.J., Mattey, D.P., and Baldini, J.U.L., 2014, Reconstructing modern stalagmite growth from cave monitoring, local meteorology, and experimental measurements of dripwater films: Earth and Planetary Science Letters, v. 392, p. 239–249. doi:10.1016/j.epsl.2014.02.036.

Baldini, J.U.L., 2010, Cave atmosphere controls on stalagmite growth rate and paleoclimate records, *in* Pedley, H.M., and Rogerson, M, eds., Tufas and Speleothems: Unravelling the Microbial and Physical Controls: Geological Society London, Special Publications 336, p. 283–294. doi:10.1144.SP336.15.

Baldini, J.U.L., McDermott, F., and Clipson, N., 2006, Effects of high-frequency cave atmosphere P-CO_2 variability on stalagmite climate proxy records [abstract]: Geochimica et Cosmochimica Acta, v. 70, p. A30–A30. doi:10.1016/j.gca.2006.06.169.

Baldini, J.U.L., McDermott, F., Hoffmann, D.L., Richards, D.A., and Clipson, N., 2008, Very high-frequency and seasonal cave atmosphere PCO_2 variability: Implications for stalagmite growth and oxygen isotope-based paleoclimate records: Earth and Planetary Science Letters, v. 272, p. 118–129. doi:10.1016/j.epsl.2008.04.031.

Banner, J.L., Guilfoyle. A., James, E.W., Stern, L.A., and Musgrove, M. L., 2007, Seasonal variations in modern speleothem calcite growth in Central Texas, USA: Journal of Sedimentary Research, v. 77, p. 615–622. doi:10.2110/jsr.2007.065.

Batiot-Guilhe, C., Seidel, J-L., Jourde, H., Hébrard, O, and Bailly-Comte, V., 2007, Seasonal variations of CO_2 and ^{222}Rn in a mediterranean sinkhole - spring (Causse d'Aumelas, SE France): International Journal of Speleology, v. 36, p. 51–56.

Becker, A., Davenport, C.A., Eichenberger, U., Gilli, E., Jeannin, P.-Y., and Lacave, C., 2006, Speleoseismology: A critical perspective: Journal of Seismology, v. 10, p. 371–388. doi:10.1007/s10950-006-9017-z.

Bond-Lamberty, B., and Thomson, A., 2010, Temperature-associated increases in the global soil respiration record: Nature, v. 464, p. 579–582. doi:10.1038/nature08930.

Bourges, F., Mangin, A., and d'Hulst, D., 2001, Le gaz carbonique dans la dynamique de l'atmosphère des cavités karstique: l'exemple de l'Aven d'Orgnac (Ardèche): Earth and Planetary Sciences, v. 333, p. 685–692.

Cowan, B.D., Osborne, M.C., and Banner, J.L,. 2013, Temporal variability of cave-air CO_2 in Central Texas: Journal of Cave and Karst Studies, v. 75, p. 38–50. doi:10.4311/2011ES0246.

De Freitas, C.R., Littlbjohn, R.N., Clarkson, T.S., and Kristament, I.S., 1982, Cave climate: Assessment of airflow and ventilation: Journal of Climatology, v. 2, p. 383–397. doi:10.1002/joc.3370020408.

Denis, A., and Crémoux, F., 2002, Using the entropy of curves to segment a time or spatial series: Mathematical Geology, v. 34, p. 899–914. doi:10.1023/A:1021302922108.

Denis, A., Lastennet, R., Huneau, F., et al., 2005, Identification of functional relationships between atmospheric pressure and CO_2 in the cave of Lascaux using the concept of entropy of curves: Geophysical Research Letters, v. 32, L05810, 4 p., doi:10.1029/2004GL022226. [articles are numbered and then paged individually]

Dueñas, C., Fernández, M.C., Cañete, S., Carretero, J., and Liger, E., 1999, ^{222}Rn concentrations, natural flow rate and the radiation exposure levels in the Nerja Cave: Atmospheric Environment, v. 33, p. 501–510. doi:10.1016/S1352-2310(98)00267-2.

Dueñas, C., Fernández, M.C., Cañete, S., Pérez, M., and Gordo, E., 2011, Seasonal variations of radon and the radiation exposure levels in Nerja cave, Spain: Radiation Measurements, v. 46, p. 1181–1186. doi:10.1016/j.radmeas.2011.06.039.

Faimon, J., Štelcl, J., and Sas, D., 2006, Anthropogenic CO_2-flux into cave atmosphere and its environmental impact: A case study in the Císařská Cave (Moravian Karst, Czech Republic): Science of the Total Environment, v. 369, p. 231–245. doi:10.1016/j.scitotenv.2006.04.006.

Faimon, J., Troppová, D., Baldik, V., and Novotný, 2012, Air circulation and its impact on microclimatic variables in the Císařská Cave (Moravian Karst, Czech Republic): International Journal of Climatology, v. 32, p. 599–623. doi:10.1002/joc.2298.

Fairchild, I.J., Smith, C.L., Baker, A., Fuller, L., Spötl, C., Mattey, D., McDermott, F., and E.I.M.F., 2006, Modification and preservation of environmental signals in speleothems: Earth-Science Reviews, v. 75, p. 105–153. doi:10.1016/j.earscirev.2005.08.003.

Field, M.S., 2007, Risks to cavers and cave workers from exposures to low-level ionizing α radiation from ^{222}Rn decay in caves: Journal of Cave and Karst Studies, v. 69, p. 207–228.

Gilli, E., 1999, Evidence of palaeoseismicity in a flowstone of the Observatoire cave (Monaco): Geodinamica Acta, v. 12, p. 159–168. doi:10.1080/09853111.1999.11105339.

Gilli, E., and Delange, P., 2001, Utilisation des spéleothemes comme indicateurs de néotectonique ou de la paléosismicité, *in* Gille, E., and Audra, P. eds., Tectonique Active et Géomorphologie, Revue d'Analyse Spatiale Quantitative et Appliquée, Special Publication 2001, p. 79–90.

Gilli, E., and Serface, R., 1999, Evidence of palaeoseismicity in the caves of Arizona and New Mexico (USA): Earth and Planetary Sciences, v. 329, p. 31–37. doi:10.1016/S1251-8050(99)80224-9.

Gregoric, A., Vaupotic, J., and Gabrovsek, F., 2013, Reasons for large fluctuation of radon and CO_2 levels in a dead-end passage of a karst cave (Postojna Cave, Slovenia): Natural Hazards and Earth System Sciences, v. 13, p. 287–297.

Gregorič, A., Zidanšek, A., and Vaupotič, J., 2011, Dependence of radon levels in Postojna Cave on outside air temperature: Natural Hazards and Earth System Sciences, v. 11, p. 1523–1528. doi:10.5194/nhess-11-1523-2011.

Hakl, J., Hunyadi, I., Csige, I., Géczy. G., Lénárt, L., and Várthegyi, A., 1997, Radon transport phenomena studied in karst caves - International experiences on radon levels and exposures: Radiation Measurements, v. 28, p. 675–684. doi:10.1016/S1350-4487(97)00163-7.

Hess, J.W., and White, W.B., 1993, Groundwater geochemistry of the carbonate karst aquifer, south-central Kentucky, USA: Applied Geochemistry, v. 8, p. 189–204. doi:10.1016/0883-2927(93)90034-E

Kennett, D.J., Breitenbach, S.F.M., Aquino, V.V., Asmerom, Y, Awe, J. Baldini, J.U.L., Bertlein, P., Culleton, B.J., Ebert, C., Jazwa, C., Macri, M.J., Marwan, N., Polyak, V., Prefer, K., Ridley, H.E., Sodemann, H., Winterhalder, B., and Haug, G. H., 2012, Development and disintegration of Maya political systems in response to climate change: Science, v. 338, p. 788–791. doi:10.1126/science.1226299.

Kowalczk, A., 2009, High resolution microclimate study of Hollow Ridge Cave: Relationships between cave meteorology, air chemistry, and hydrology and the impact of speleothem deposition [MS thesis]: Department of Earth, Ocean and Atmospheric Sciences, Florida State University, Thallahasse, 238 p.

Kowalczk, A., and Froelich, P., 2010, Cave air ventilation and CO_2 outgassing by radon-222 modeling: How fast do caves breathe?: Earth and Planetary Science Letters, v. 289, p. 209–219. doi:10.1016/j.epsl.2009.11.010.

Kowalczk, A.J., Froelich, P.N., Gaffka, C., and Tremaine, D., 2008, High resolution time series cave ventilation processes and the effects on cave air chemistry and drip waters: Speleoclimatology and proxy calibration [abstract]: EOS Transactions American Geophysical Union, v. 89, fall meeting supplement, abstract PP51C-1521.

Mattey, D.P., Fairchild, I.J., Atkinson, T.C., et al., 2010, Seasonal microclimate control of calcite fabrics, stable isotopes and trace elements in modern speleothem from St Michaels Cave, Gibraltar, *in* Pedley, H.M., and Rogerson, M, eds., Tufas and Speleothems: Unravelling the Microbial and Physical Controls: Geological Society London, Special Publications 336, p. 323–344. doi:10.1144/SP336.17.

Menichetti, M., 2013, Karst processes and carbon flux in the Frasassi Caves, Italy, *in* Filippi, M., and Bosák, P., eds, 16th International Congress of Speleology Proceedings, v. 3, p. 376–378.

Miller, T.E., 1996, Geologic and hydrologic controls on karst and cave development in Belize: Journal of Cave and Karst Studies, v. 58, p. 100–120.

Murthy, R., Griffin, K.L., Zarnoch, S.J., Dougherty, P.M., Watson, B., Van Haren, J., Patterson, R.L., and Mahato, T., 2003, Carbon dioxide efflux from a 550 m^3 soil across a range of soil temperatures: Forest Ecology and Management, v. 178, p. 311–327. doi:10.1016/S0378-1127(02)00480-2.

Oh, Yong Hwa, and Kim, Guebuem, 2011, Factors controlling the air ventilation of a limestone cave revealed by ^{222}Rn and ^{220}Rn tracers: Geosciences Journal, v. 15, p. 115–119. doi:10.1007/s12303-011-0010-3.

Palmer, A.N., 2007, Cave geology and speleogenesis over the past 65 years: Role of the National Speleological Society in advancing the science: Journal of Cave and Karst Studies, v. 69, p. 3–12.

Pflitsch, A., and Piaseki, J., 2003, Detection of an airflow system in Niedzwiedia (Bear) Cave, Kletno, Poland.: Journal of Cave and Karst Studies, v. 65, p. 160–173.

Przylibski, T.A., and Ciezkowski, W., 1999, Seasonal changes of radon concentration in the Niedzwiedzia Cave (SW Poland): Nuovo Cimento Della Societa Italiana Di Fisica C—Geophysics and Space Physics, v. 22, p. 463–469.

Renault, P., 1970, La Eormation des Cavernes: Paris, Presses universitaires de France, 128 p.

Sánchez-Cañete, E.P., Serrano-Ortiz, P., Domingo, F., and Kowalski, A.S., 2013, Cave ventilation is influenced by variations in the CO_2-dependent virtual temperature: International Journal of Speleology, v. 42, p. 1–8. doi:10.5038/1827-806X.42.1.1.

Šebela, S., Vaupotič, J., Košťak, B., and Stemberk, J., 2010, Direct measurement of present-day tectonic movement and associated radon flux in Postojna Cave, Slovenia: Journal of Cave and Karst Studies, v. 72, p. 21–34. doi:10.4311/jcks2009es0077.

Sherwin, C.M., and Baldini, J.U.L., 2011, Cave air and hydrological controls on prior calcite precipitation and stalagmite growth rates: Implications for paleoclimate reconstructions using speleothems: Geochimica et Cosmochimica Acta, v. 75, p. 3915–3929. doi:10.1016/j.gca.2011.04.020.

Smart, P.L., and Friederich, H., 1987, Water movement and storage in the unsaturated zone of a maturely karstified carbonate aquifer, Mendip Hills, England, *in* Proceedings of the Environmental Problems in Karst Terranes and their Solutions Conference, October 28–30, 1986, Bowling Green, Kentucky: Dublin, Ohio, National Water Well Association, p. 59–87.

Smithson, P.A., 1991, Inter-relationships between cave and outside air temperatures: Theoretical and Applied Climatology, v. 44, p. 65–73. doi:10.1007/BF00865553.

Spötl, C., Fairchild, I.J., and Tooth, A.F., 2005, Cave air control on dripwater geochemistry, Obir Caves (Austria): Implications for speleothem deposition in dynamically ventilated caves: Geochimica et Cosmochimica Acta, v. 69, p. 2451–2468. doi:10.1016/j.gca.2004.12.009.

Virk, H.S., Singh, M., and Ramola, R.C., 1997, Radon monitoring for uranium exploration, earthquake prediction and environmental health hazard in Himachal Pradesh, India: an appraisial, *in* Virk, H.S., ed., Rare Gas Geochemistry - Applications in Earth and Environmental Sciences: Amritsar, Indian, Guru Nanak Dev University, p. 89–99.

Wigley, T.M.L., 1967, Non-steady flow through a porous medium and cave breathing: Journal of Geophysical Research, v. 72, p. 3199–3205. doi:10.1029/JZ072i012p03199.

Wu, Y., Wang, W., Xu, Yonhxin, Liu, H., Zhou, X., Wang, L., and Titus, R., 2003, Radon concentration: A tool for assessing the fracture network at Guanyinyan study area, China: Water SA, v. 29, p. 49–53.